Doctoral theses at NTNU, 2021:277

Erlend Lunnan Bjørnstad

Oxidative Ladle Refining of Metallurgical Grade Silicon

Refining of Ca and Al Impurities

NTNU
Norwegian University of
Science and Technology

Doctoral thesis

Erlend Lunnan Bjørnstad

ISBN 978-82-326-6550-1 (printed ver.)
ISBN 978-82-326-6676-8 (electronic ver.)
ISSN 1503-8181 (printed ver.)
ISSN 2703-8084 (online ver.)

NTNU
Norwegian University of
Science and Technology

Thesis for the Degree of
Philosophiae Doctor
Faculty of Natural Sciences
Department of Materials Science and Engineering

NTNU

Doctoral theses at NTNU, 2021:277

NTNU

Erlend Lunnan Bjørnstad

Oxidative Ladle Refining of Metallurgical Grade Silicon

Refining of Ca and Al Impurities

Thesis for the Degree of Philosophiae Doctor

Trondheim, August 2021

Norwegian University of Science and Technology
Faculty of Natural Sciences
Department of Materials Science and Engineering

NTNU
Norwegian University of
Science and Technology

NTNU
Norwegian University of Science and Technology

Thesis for the Degree of Philosophiae Doctor

Faculty of Natural Sciences
Department of Materials Science and Engineering

ISBN 978-82-326-6550-1 (printed ver.)
ISBN 978-82-326-6676-8 (electronic ver.)
ISSN 1503-8181 (printed ver.)
ISSN 2703-8084 (online ver.)

Doctoral theses at NTNU, 2021:277

Printed by NTNU Grafisk senter

Preface

This thesis is submitted in partial fulfillment of the degree of philosophiae doctor to the Norwegian University of Science and Technology, detailing the findings and scientific contributions made during this doctoral work.

The doctoral work has been performed at the Department of Materials Science and Engineering, Faculty of Natural Sciences, Norwegian University of Science and Technology, Trondheim, Norway, between August 2016 and April 2021, under the guidance of professor Gabriella Tranell as the supervisor of this doctoral work, with professor Hugo Atle Jakobsen and Dr. Jan Erik Olsen as co-supervisors.

This research work has been funded by the SFI Metal Production, (Centre for Research-based Innovation, 237738). The author gratefully acknowledges the financial support from the Research Council of Norway and the partners of the SFI Metal Production. Part of the work was also conducted at NorFab, and the Research Council of Norway is acknowledged for the support to the Norwegian Micro- and Nano-Fabrication Facility, NorFab, project number 295864/F50.

Trondheim, May 2021

Erlend Lunnan Bjørnstad

Abstract

Metallurgical grade silicon (MG-Si) is used as an alloying agent, raw material, or as a precursor compound, in the production of aluminum alloys, silicones, photovoltaics, and electronics. Access to clean and affordable energy and deep-water ports, have been competitive advantages for the Norwegian metallurgical industry, with Norway hosting several of the world's leading producers of metallurgical grade silicon. During the production of MG-Si the liquid alloy needs to undergo refining, where the amount of impurities in the alloy are reduced to meet customer specification. Of the different refining methods available, oxidative ladle refining (OLR) is the most commonly used, primarily to reduce the amount of Ca and Al impurities in the alloy. OLR consists of tapping the liquid alloy into a refining ladle, while oxygen-enhanced air is purged through a bottom mounted porous plug. When the alloy comes into contact with oxygen in the gas, the silicon and impurities form a SiO_2-CaO-Al_2O_3 slag, where the slag and alloy are immiscible, thus allowing the alloy to be separated from the slag.

This thesis investigates the mass transfer of Ca and Al in this process. The first part of the thesis presents a theoretical framework, describing the nucleation of SiO_2-CaO-Al_2O_3 slag on the bubbles created by the purge gas, using classical macroscale thermodynamics. Classical macroscale thermodynamics requires the slag nucleus to exhibit a "well defined" surface, which cannot generally be assumed at nanoscale. The work describes how liquid silica should retain its "well defined" surface structure, even while the slag nucleus is small. Silica is highly surface active in SiO_2-CaO-Al_2O_3 slags, which the work uses to extend the "well defined" surface structure of silica to SiO_2-CaO-Al_2O_3 slags as a whole, as long as its silica content is high. Experiments were also conducted which confirm the surface active nature of silica in the SiO_2-CaO-Al_2O_3 system. The framework also shows the impact of calcia and alumina on the interfacial properties of the slag.

The second part of the thesis concerns itself with the macroscale mass transfer of Ca and Al. Laboratory experiments were conducted for the purpose of understanding the mass transfer kinetics of Ca and Al from a synthetic SiO_2-CaO-Al_2O_3 slag to pure silicon. Laboratory-scale experiments were also conducted to evaluate the refining path Ca and Al, simulating industrial OLR of MG-Si. The results suggest that OLR of MG-Si occurs in three primary steps. Initially, surface oxidation, due to an initial high contact area between the alloy and latent atmospheric oxygen during tapping, is the most prominent refining effect, resulting in a high calcia SiO_2-CaO-Al_2O_3 slag. When the ladle reaches a critical fill height, slag formation by gas purging becomes the prominent refining effect, due to the increased residence time of a bubble. This results in the subsequent formation of new SiO_2-CaO-Al_2O_3 slag dominating the refining process. Finally, a critical amount of slag has been formed by gas purging and amassed in the ladle. An equilibrium between the bulk SiO_2-CaO-Al_2O_3 slag and alloy is approached by mass transfer of Ca and Al, both to and from the slag.

The final part of the thesis consists of a model for locating slag contaminated samples in industrial measurement sets.

Acknowledgments

I would like to thank my supervisor professor Gabriella Tranell for her invaluable guidance, engagement, and support throughout the whole doctoral period. Especially, I would like to thank professor Tranell for her insights and discussions on the industrial applications of the theoretical and experimental findings, and her patience in teaching how to present and depict these findings to reach the target industrial and academic audience. I am very grateful to my co-supervisor professor Hugo Atle Jakobsen for introducing me to the field of statistical experimental design and analysis, and for helping me better understand how mathematics is used to describe and depict physical process and the nature of mathematical models. Great thanks also go out to my co-supervisor Dr. Jan Erik Olsen for discussions on the previous work done on oxidative ladle refining of silicon, and for allowing me to utilize his technical experience on the subject.

The support and openness from the industrial partners at SFI Metal Production have been instrumental in merging the scientific academic work with the industrial process. I would especially like to thank the industry representatives attached to this doctoral work, Dr. Lars Klemet Jakobsson and Dr. Birger Andresen, for their engagement, support, and invaluable insight and discussions on the industrial process.

My thanks go out to professor In-Ho Jung and research professor Marie-Aline Van Ende at Seoul National University, contributing their vast knowledge on thermodynamic modeling and FactSage know-how for our collaboration on describing the refining stages of oxidative ladle refining. While the raging pandemic kept me from visiting Korea, I hope for further collaborations in the future.

Further, I would like to thank the people at the Department of Materials Science and Engineering and REM group. A big thanks goes out to the professors, researchers, PhD candidates, and students in the SiManTiAl group, for the academic discussions, seminars, social events, and gatherings. The employees at SINTEF have also been open for discussions and questions, sharing their experiences and knowledge, and I am very grateful for their assistance, with special thanks to Dr. Anne Kvithyld and Dr. Martin Syvertsen.

My deepest gratitude goes to the engineers and technical personnel at NTNU and SINTEF, without you the experimental work would not have been possible. I especially wish to thank Dr. Dmitry Slizovskiy for help and guidance during the experimental work, Eva Rise for instructing me in how to perform my possibly fatal experiments in a safe manner, and Trygve Lindahl Schanche, Torild Korgstad, Ove Darel, John Inge Edvardsen, Dr. Øystein Dahl, Dr. Sigurd Wenner, and Aksel Alstad for help with material processing, sample preparation, and sample analysis. Your patience and dedication allowed even someone without any practical background to attain proficiency in many complex aspects of experimental work.

I would be remiss if I did not mention the PhD candidates who helped me along the way. Håkon Aleksander Hartvedt Olsen Myklebust for his academic discussions and friendship throughout all five years, Ivar Andre Ødegår and Arman Hoseinpur Kermani for their invaluable help and experience on designing and building experiments, combined with their deep knowledge on the theoretic and experimental behavior of silicon melts, and Egil Grøndal Krystad for mentoring me during the initial phase of my PhD period. A special thanks also goes out to Kamilla Arnesen, Daniel Perez Clos, Hossein Saleh, Massoud Hassabadi, Dr. Katarina Jakovljevic, Dr. Trine Asklund Larssen, Cathrine Kyung Won Solem, and Dr. Nicholas Smith-Hanssen, for having had the fortitude and patience to share an office with me for all these years, and I greatly appreciate our academic and social interactions.

At last, I would like to thank SFI Metal Production for giving me this great opportunity, and I wish the center all luck during the years it has left.

Contents

List of Publications

Paper 1

E. L. Bjørnstad and G. M. Tranell: *Nucleation of SiO_2-CaO-Al_2O_3 Slag in Oxidative Ladle Refining of Metallurgical Grade Silicon*
In: Met. Trans. B. 2021, 52(3), 1392–1412

Statement of Contribution:

Bjørnstad:	Theoretical analysis, thermodynamic modeling, experimental work, figures, data analysis, discussed of the results, and writing.
Tranell:	Discussed results and writing.

Paper 2

E. L. Bjørnstad and G. M. Tranell: *Investigation of the Surface Oxide Layer of Metallurgical Grade Silicon*
Extended abstract for the 11th International Conference on Molten Slags, Fluxes and Salts 2021.

Statement of Contribution:

Bjørnstad:	Experimental work, figures, discussed results, and writing.
Tranell:	Discussed results and writing.

Paper 3

E. L. Bjørnstad and G. M. Tranell: *Mass Transfer of Al and Ca Between Silicon and Synthetic SiO_2-CaO-Al_2O_3 Slags*
In: Materials Processing Fundamentals 2017, pp. 85–96

Statement of Contribution:

Bjørnstad:	Experimental work, data analysis, figures, discussed results, and writing
Tranell:	Discussed results and writing.

Paper 4

E. L. Bjørnstad, G. Solbakk, Ø. Mosevoll, and G. M. Tranell: *The Effect of Calcium Alloy Content on the Mass Transfer of Boron Between Silicon and SiO_2-CaO slag*
Extended abstract for the 11th International Conference on Molten Slags, Fluxes and Salts 2021.

Statement of Contribution:

Bjørnstad:	Figures, data analysis, discussed results, and writing.
Solbakk:	Experimental work.
Mosevoll:	Experimental work.
Tranell:	Discussed results and writing.

Paper 5

E. L. Bjørnstad, I.-H. Jung, M.-A. Van Ende, and G. M. Tranell: *Oxidative Refining of Metallurgical Grade Silicon: Lab-scale Measurements and Description of Ca and Al Mass Transfer*
Manuscript to be submitted.

Statement of Contribution:

Bjørnstad:	Experimental work, data analysis, figures, thermodynamic modeling, discussed results, and writing.
Jung:	Thermodynamic modeling and database creation.
Van Ende:	Thermodynamic modeling and database creation.
Tranell:	Discussed results and writing.

Paper 6

E. L. Bjørnstad and G. M. Tranell: *Statistical Model for Locating Micro Slag Droplets in MG-Si Production*
In: Silicon for the Chemical Industry XIV, pp. 349–356

Statement of Contribution:

Bjørnstad:	Data analysis, statistical modeling, figures, discussed results, and writing.
Tranell:	Discussed results and writing.

List of Tables

List of Figures

List of Symbols and Abbreviations

Species Phase Location

[El]	Species El is in the alloy phase
(El)	Species El is in the slag phase
{El}	Species El is in the gas phase

Symbols

#	"Number of"
#N	Purity (0 . "number of 9's")
$\sim$	"Similar to"

Latin Script

A_s	Surface area	[m^2]
$\overline{A}_i$	Surface molar coverage of species i	[m^2/mol]
a	Activity	[-]
Reference state:	Dissolved species	1 wt%
	Gaseous species	1 bar
	Solid/Liquid	X=1
b	Model parameter	
c	Dimensionless concentration	[-]
D	Diameter	[m]
OD/ID	Outer/Inner Diameter	[m]
d	Diameter	[m]
$\overline{d}_0$	Initial Sauter mean diameter	[m]
e	Residual	

f	Henrian activity coefficient	[-]
f	Function	
f(α_{ij},$\alpha_{k\ell}$)	Volume correction factor for a lens	[-]
f_α	Critical value for the fisher distribution	[-]
ΔG	Gibbs energy	[J/mol]
H	Height	[m]
OH/IH	Outer/Inner Height	[m]
h	Droplet height	[m]
i	Specific entry in a set	
j	Specific entry in a set	
K	Thermodynamic distribution coefficient	[-]
k	Total entries in a set	
k_B	Boltzmann constant	[J/#particles·K]
k_t	Total mass transfer coefficient	[m/s]
L	Length	[m]
m	Mass	[kg]
M	Molar mass	[g/mol]
NL	Normal liter	[L]
n	Amount of moles	[mol]
n	Sample size	[#samples]
$n^\star$	Initial/Critical amount of moles in nucleus	[mol]
P	Total pressure	[Pa], [bar]
p	Partial pressure	[Pa], [bar]
R	Ideal gas constant	[J/(molK)]
r	Radius	[m]
r_{curv}	Surface curvature	[m^{-1}]
r_G	Radius of droplet	[m]
$r_G^\star$	Initial/Critical radius of nucleus	[m]
s^2	Sample variance	
s_p^2	Pooled sample variance	
s_{comp}^2	Combined sample variance	
t	Time	[s], [min], [hr]
t_{alpha}	Critical value for the t-distribution	[-]
T	Temperature	[K], [°C]
V	Volume	[m^3]
V_m	Molar volume	[m^3/mol]
V_p	Phase volume	[m^3/#particles]
W	Width	[m]
X	Mole fraction	[-]
X	Model input	
x	Distance	[m]
x	Model input	
x	General input	
x	Cartesian coordinate	
y	Model Response	
y	Cartesian coordinate	
z	Cartesian coordinate	

Greek Script

α	Type I error	[-]
α_{sg}	Angle between slag and gas	[°, rad]
α_{sm}	Angle between slag and melt	[°, rad]
β	Fitting coefficient	[-]
χ	Thermodynamic relative molar fraction	[-]
Δ	Denotes parameter differential	[-]
ℓ	Specific entry in a set	
Γ	Surface Excess	[#particles/m^2]
γ	Raoultian activity coefficient	[-]
γ°	Raoultian activity coefficient at infinite dilution	[-]
Λ	Displacement	
μ	Dynamic viscosity	[Pa·s]
μ	Thermodynamic chemical potential	[J/mol], [J/#particles]
$\Delta\mu$	Thermodynamic chemical potential change	[J/mol]
ν	Normalized molar reaction marker	[-]
ν	Statistical degrees of freedom	[-]
ω	Mass fraction	[-]
Π	Solute product	[-]
Φ	Dividing surface	[m]
φ	Segregation Boundary	
$\Delta\varphi_p$	Nucleation Energy Term	[J/m^3]
$\psi(\alpha_{ij}$	Volume correction factor for a spherical cap	[-]
ρ	Mass density	[kg/m^3]
$\overline{\rho}$	Bulk mass density	[kg/m^3]
ϱ	Particle density	[#particles/m^3]
$\varrho(x)$	Particle density function	[#particles/m^3]
σ_i°	Surface energy density/tension of species i	[J/m^2]
σ_i	Surface energy density/tension of phase i	[J/m^2]
σ_{ij}	Interfacial energy density/tension between phases i and j	[J/m^2]
ς_p	Number of particles in a phase	[particles]
$\varsigma^\star_{molecules}$	Critical number of molecules in a nucleus	[#molecules]
τ	Rate constant	[s]
θ	Contact angle of a phase	[°, rad]
θ	Fitting parameter	
ϑ	Normalized concentration minima	[-]
$\vartheta(\alpha_{ij})$	Surface area correction factor for a spherical cap	[-]
Υ	Mass transfer parameter	[-]
$\Xi(\alpha_{ij},\alpha_{k\ell})$	Surface area correction factor for a lens	[-]
ζ	Mass transfer parameter	[-]

Delimiters

$\overline{x}$	Arithmetic average/mean	
$\overline{\overline{x}}$	Arithmetic mean of means	
$\hat{x}$	Estimated	
$\dot{x}$	Rate/Time derivative	[s^{-1}]
$\underline{x}$, $\mathbf{x}$	Vector	

Subscripts and Superscript

	Subscripts
0	Initial
b	Bubble or Bulk
g	Gas
lens	The whole lens
m	Alloy melt
s	Slag
sat	Saturated
	Superscript
$\circ$	At some equilibrium/reference state
b	Bulk
eq	Equilibrium
ox	Oxidize
s	Surface
T	Transposed

Abbreviations

AAS	Atomic Adsorption Spectroscopy
Ar 5.0/6.0	5N/6N (by volume) Argon Gas
CA	Cluster Approach
CI	Confidence Interval
DFA	Density Functional Approach
EDS	Energy-Dispersive X-ray Spectra
EELS	Electron Energy-Loss Spectroscopy
FIB	Focused Ion Beam Emitter
FN	False Negative
FP	False Positive
H_0	Initial Hypothesis
ICP-MS	Inductively Coupled Plasma Mass Spectrometry
JCI	Joined Confidence Interval
MG-Si	Metallurgical Grade Si
MSE	Mean Residual Sum of Square Error
MSR	Mean Regression Sum of Square Error
OLR	Oxidative Ladle Refining
PI	Prediction Interval
RHS	Right Hand Side
RSD	Relative Standard Deviation
SSE	Residual Sum of Square Error
SSR	Regression Sum of Square Error
STEM	Scanning Transmission Electron Spectroscopy
TEM	Transmission Electron Spectroscopy
XRF	X-ray Fluorescence Spectroscopy

Chapter 1

Introduction

1.1 Oxidative Ladle Refining of Metallurgical Grade Silicon

The production of aluminum alloys, silicones, photovoltaics, and electronics, all rely on MG-Si (metallurgical grade silicon) as an alloying agent, raw material, or as a precursor compound for further purification. "Metallurgical grade", usually refers to a group of silicon alloys which contains between 98.5 and 99.5 [wt%Si][1], even though it is generally defined as alloys containing more than 96 [wt%Si][2][3]. MG-Si is produced from quartz (SiO_2), which together with other silicates accounts for more than 25% of the Earth's continental crust[1]. When compared to other metallurgically relevant minerals, quartz is commonly found worldwide in very high purity deposits, providing the industry with an abundant source of high-quality feed stock. The typical industrial production route for MG-Si sees quartz carbothermally reduced in a SAF (submerged arc-furnace), at temperatures above 2200 K, following the overall reaction:

$$\text{R1)}\ \ \mathrm{SiO}_{2(qrtz)} + 2\mathrm{C}_{(s)} = \mathrm{Si}_{(l)} + 2\mathrm{CO}_{(g)}$$

After carbothermal reduction, the molten silicon alloy contains a range of impurities, entering the process as part of the carbon sources, electrodes, quartz, and furnace lining. In high concentrations, these impurities may negatively impact the alloy's further use, requiring the alloy to undergo refining to meet customer specification. Typical compositions are outlines in Schei et al.[4] or Bjørnstad and Tranell[5]. The exact refining schemes may change from plant to plant and the target alloy composition, but will most commonly involve OLR (oxidative ladle refining), either as the only refining step or as part of a series of steps.

OLR is a batch reactor process, where the alloy is typically continuously tapped from the furnace into a ladle over a span of 1 to 3 hours, depending on the furnace capacity and ladle size, where furnace capacity and ladle size are normally correlated. A typical industrial ladle for continuous large scale production contains more than 7 tonnes of liquid alloy when full, towering over 2.2 m in height and 1.5 m in breadth, as illustrated in figure 1.1. The temperature of the alloy will change throughout the refining process, but typically lies between 1773-1973 K, with a desired temperature between 1773 and 1873 K.

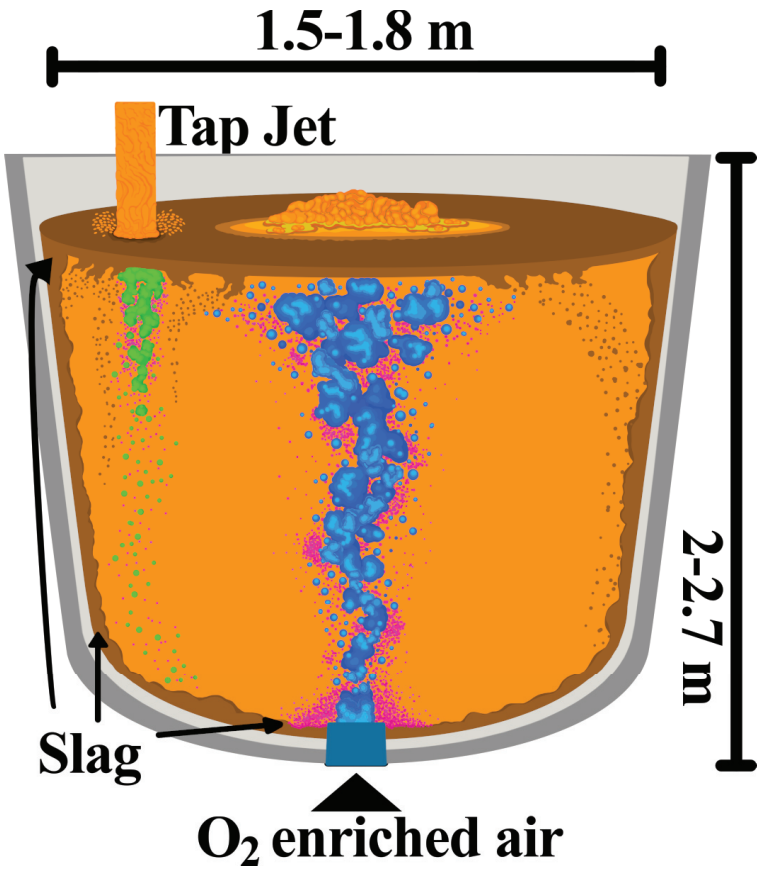

Figure 1.1: A ladle in which a silicon alloy is refined by gas purging, illustrating the OLR process. The falling molten jet from the furnace, or "tap jet", carries molten alloy from the furnace into the ladle. Green bubbles represent entrapped air from the jet, while the central bubble column is in blue. Pink dots indicate slag recently formed on the bubbles, while already settled slag is in brown. From Bjørnstad and Tranell[5].

During the tapping process, alloy in the ladle is constantly purged by an air-oxygen gas-mixture from a bottom-mounted porous plug. The porous plug releases the purge gas as bubbles into the liquid alloy. These bubbles will interact with each other, coalescing and breaking up into a wide range of different bubble sizes, shown in figure 1.2(a), in the turbulent flow field created by the central bubble column. As oxygen from the gas bubbles reacts with the alloy, a slag is produced, containing mainly strong oxide forming impurity elements, such as Ca and Al. The slag and alloy are immiscible, allowing the alloy and impurity-rich slag to be separated, at the cost of a small portion of the final product ending up as silica in the slag, metal droplets retained in the slag, and silica and silicon monoxide vapor. In the production of MG-Si, OLR is primarily used to reduce the Ca and Al content of the alloy, with Ca and Al both being found in the quartz and ash[1] from the carbon reductants. Concentrations of Ca and Al lie between 0.5 and 2 wt% in a typical unrefined alloy tapped directly from the furnace, with refined commercially available products containing approximately 0.01 to 0.5 [wt%Ca] and 0.1 to 1.2 [wt%Al][5]. The quantity and number of other impurities will vary among different raw materials and alloy processing, where typical raw material compositions can be found in Martello[6] and Myrhaug[7].

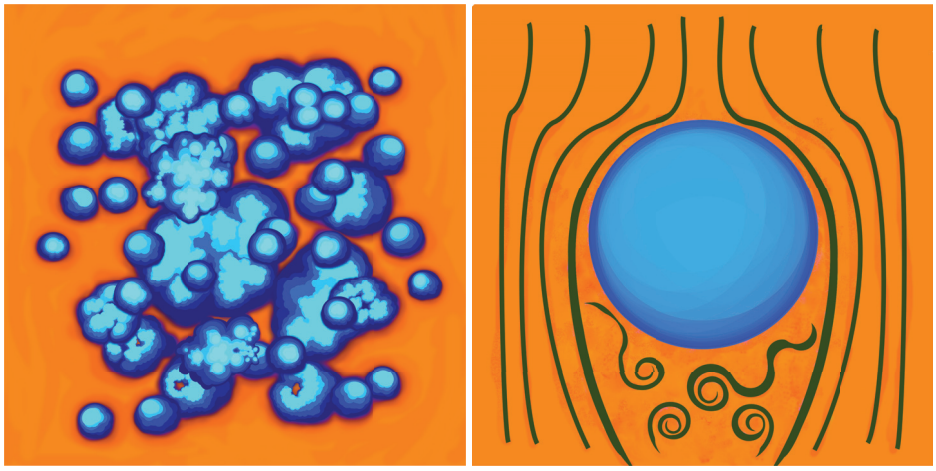

(a) **(b)**

Figure 1.2: a) Range of bubble sizes and shapes. **b)** Spherical bubble with lines indicating the flow field. The bubble's turbulent wake is marked with swiveling eddies.

[1] As clay residues.

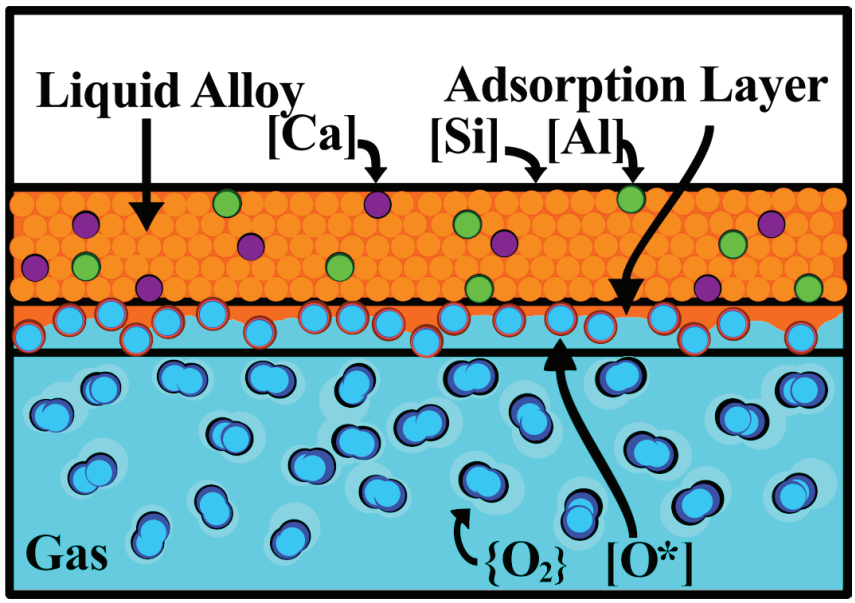

Figure 1.3: Schematic representation of the melt/gas interface. From Bjørnstad and Tranell[5].

After a gas bubble is formed by the porous plug, it will start to react with the alloy through the liquid alloy/gas interface, seen in figure 1.3. During its ascent, [Si] (Si in the liquid alloy phase) will react with $\{O_2\}$ (O_2 in the gas phase) to form (SiO_2) (SiO_2 in the slag phase) and $\{SiO\}$. (SiO_2) is formed as $\{O_2\}$ dissolved into the alloy, where the local over-saturation of [O] leads to the formation of $[SiO_2]$. This results in the alloy becoming locally over-saturated with $[SiO_2]$, initiating nucleation of (SiO_2) nuclei on the bubble surface. These initial seeds will grow as they adsorb more (SiO_2), [Ca], and [Al], resulting in a predominantly SiO_2-CaO-Al_2O_3 slag droplet. The overall reactions can be written as follows:

$$
\begin{aligned}
&\text{R2)} \quad 2[Si] + \{O_2\} = 2\{SiO\} \\
&\text{R3)} \quad [Si] + \{O_2\} = (SiO_2) \\
&\text{R4)} \quad 2[Ca] + (SiO_2) = 2(CaO) + [Si] \\
&\text{R5)} \quad 4[Al] + 3(SiO_2) = 2(Al_2O_3) + 3[Si] \\
&\text{R6)} \quad 2[Al] + 3(CaO) = (Al_2O_3) + 3[Ca]
\end{aligned}
$$

After the slag droplet reaches a certain size and shape, it will extend beyond the laminar boundary layer of the bubble and get affected by the external flow field, causing slag to detach from the bubble surface. Due to the shape of the flow field surrounding the bubble, it is expected that most of the slag droplets will end up in the turbulent wake of the bubble, seen in figure 1.2(b), and that the exact detachment condition may change depending on the bubble geometry and location of the slag droplet on the bubble surface. Regardless, by the time the bubble exits the ladle, the slag will detach from the bubble surface, coalescing with other slag droplets and further reacting with the alloy. Up until this point, it is unlikely that the slag droplet has existed for more than a second, considering the rapid reaction kinetics and high flow rates associated with the refining process. The flow field perceived by the slag droplet, and the thermophysical-properties/composition of the slag, will determine its path through the alloy. However, it will eventually settle on the ladle walls, floor, or as a floating slag (if its density is low enough).

OLR is performed in open air, which results in air bubbles being entrapped by the falling molten tap-jet, and the plume, also known as the "open eye", which is formed by the bubble column breaching the liquid alloy surface. Both the tap-jet and plume create surface convection currents which may emulsify floating slag. These surface currents also increase the interaction between the alloy and latent oxygen in the air by changing the surface topology, and drawing oxygen-saturated alloy into the bulk while replacing it with alloy which is not.

Gas-purging will continue after the ladle is full, until the alloy composition is within customer specification. The alloy and slag are then separated. Most of the slag will stick to the ladle walls and floor, but skilled operators are required to make sure that the product is free of floating slag or other contaminants.

1.2 Motivation

Norway hosts several of the world's leading producers of MG-Si[2], with the metallurgical industry as one of the largest land-based industries in Norway. In refining, the focus is generally on attaining target impurity concentrations as efficiently and consistently as possible, not necessarily to go as low as possible. For both producers of MG-Si and their customers, there is a big difference between having [wt%Ca]$\leq$0.1 and knowing that [wt%Ca]$\leq$0.1. Attaining high compositional accuracy may in it of itself be a goal, as some markets have more stringent demands than others. This work aims to aid in achieving greater compositional control by expanding the current knowledge pertaining to the mass transfer mechanisms and kinetics of [Ca] and [Al] in refining of MG-Si trough theoretical considerations, laboratory experiments, and evaluation of industrial data.

1.3 Thesis Outline

This thesis summaries and expands upon the work presented in papers 1–6. Chapter 2 contains the findings from paper 1[5] and 2[8], expanding on the thermodynamic framework for describing SiO_2-CaO-Al_2O_3 slag nucleation on gas bubbles in OLR of MG-Si using classical macroscale thermodynamics. Chapter 3 describes macroscale mass transfer, and contains the findings from paper 3[9], paper 4[10], paper 5[11], and paper 6[12]. The first part of the chapter investigates experimentally the slag to pure metal mass transfer, with respect to Ca, Al, and B. After the slag to metal mass transfer has been considered, the chapter covers the experimental work to simulate industrial OLR of MG-Si at laboratory-scale and includes a description of the refining regimes found in OLR. Lastly, chapter 4 contains the work carried out to develop a mathematical model to locate samples contaminated by micro slag droplets in industrial measurement campaigns.

Chapter 5 lists the main conclusions over all of the work, with chapter 6 proposing future work on the covered topics.

Chapter 2

Fundamental Description of SiO_2-CaO-Al_2O_3 Slag Nucleation in OLR

2.1 Nucleation of SiO_2-CaO-Al_2O_3 Slag in Oxidative Ladle Refining of Metallurgical Grade Silicon

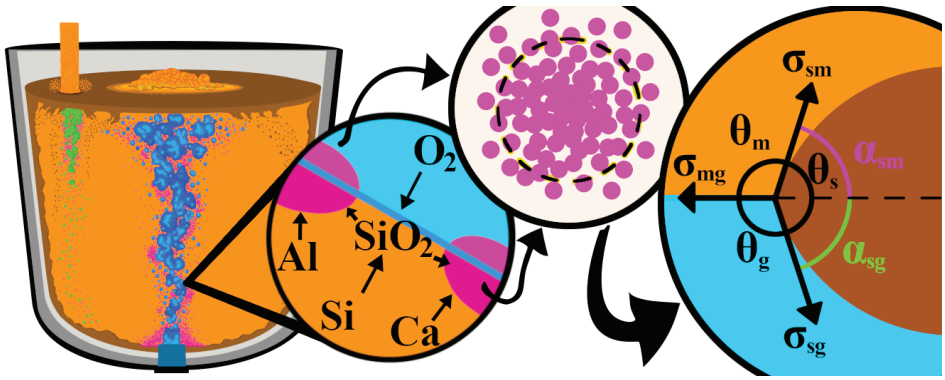

Figure 2.1: Graphical summary of the nucleation and formation of SiO_2-CaO-Al_2O_3 slag in OLR of MG-Si.

2.1.1 Summary

Paper 1[5] gives a comprehensive theoretical description of the nucleation and formation of SiO_2-CaO-Al_2O_3 slag in OLR of MG-Si, at nano/microscale using classical macroscale thermodynamics. This is supported by experimental evidence in both paper 1 and 2[8]. Paper 1 argues that the liquid structure of silica allows its nuclei to exhibit a "well defined" surface, which means that the cluster approach (CA) can adequately describe the silica surface, even at nanoscale. CA is an assumption established by Gibbs in his magnum opus "On the Equilibrium of Heterogeneous Substances"[13][14], and is tacitly assumed by the majority of classical macroscale thermodynamic literature concerned with surfaces. If CA can be used on silica nuclei at nanoscale, then this allows the different spatial regimes to be bridged, using a mathematical language and thermophysical properties familiar to the metallurgical community at large. This would also validate a large body of work already published within condensation and solidification of silica nanoclusters, as this should apply to silica nucleation in general regardless of driving force. Paper 1 then argues that since silica is highly surface active in SiO_2-CaO-Al_2O_3 slags, this should result in the slag retaining the surface properties of silica at high silica contents. It is further argued that in OLR of MG-Si, the SiO_2-CaO-Al_2O_3 slag will always exhibit a "well defined" surface, as the point where silica loses its surface dominance is only likely to occur after the slag nuclei/droplet becomes large enough to satisfy the assumption regardless. Paper 1 further discusses some of the ramifications this has on the geometries of slag droplets, and relates this to behaviors seen in the industrial process.

Most importantly, paper 1 shows that the calcia concentration of the slag has much greater impact on the droplet geometry than its alumina concentration, providing a mechanism to describe why industrial refining becomes inefficient when the dissolved concentration of Ca in the alloy, [Ca], becomes too low.

Experimental work in paper 1 and 2 strongly supports the theory that silica is surface active, while alumina is not. These works used imaging by TEM/STEM (scanning transmission electron microscopy), and concentration mapping with electron energy-loss spectroscopy (EELS) and energy-dispersive X-ray spectra (EDS), on an oxidized industrial unrefined alloy sample to study the location of different elements in the generated surface oxide, validating the hypothesis.

2.1.2 Theoretical Framework

2.1.2.1 Nucleation Thermodynamics at Nanoscale and Silica's Surface Structure

When discussing slag nucleation as a first step in slag formation, it is first important to find the spatial size regime at which it occurs. The lower spatial boundary is the initial slag nucleus size, which is the nuclei size a system must be able to support for the nucleus to be stable, and subsequently grow. Paper 1 calculates an upper spatial boundary from the total amount of silica a characteristic bubble with diameter 1 cm[15] can produce, which is approximately 0.11 mg, corresponding to a sphere with a diameter of 0.46 mm[5]. Neither changing system properties or slag composition has any significant impact on these values. Further, it is argued that since this is the total amount of slag a bubble can produce over its ascent, it is reasonable to assume that the actual size of a slag droplet leaving the bubble may be considerably smaller than the calculated maximum value.

The initial slag nucleus size is most likely near, or at nanoscale, where many common macro/microscale assumptions are no longer generally valid. Gibbs[13][14] makes one such assumption in his magnum opus "On the Equilibrium of Heterogeneous Substances", where he lays down the foundation for the classical macroscale thermodynamic framework commonly used in metallurgy today. A large portion of the 2nd part of his work is dedicated to integrating a phase's surface properties into Gibbs' thermodynamic framework. In the section "Influence of Surfaces of Discontinuity Upon the Equilibrium of Heterogeneous Masses - Theory of Capillary"[14, pp.380–391], Gibbs describes a surface as a geometrical plane which cleanly separates two phases into distinct volumes, without any transition-region between them, named a dividing surface[1].

[1] Marmur[16] has proposed a method which allows for a simplified transition region, which might be applicable in the future after extensive experimental validation.

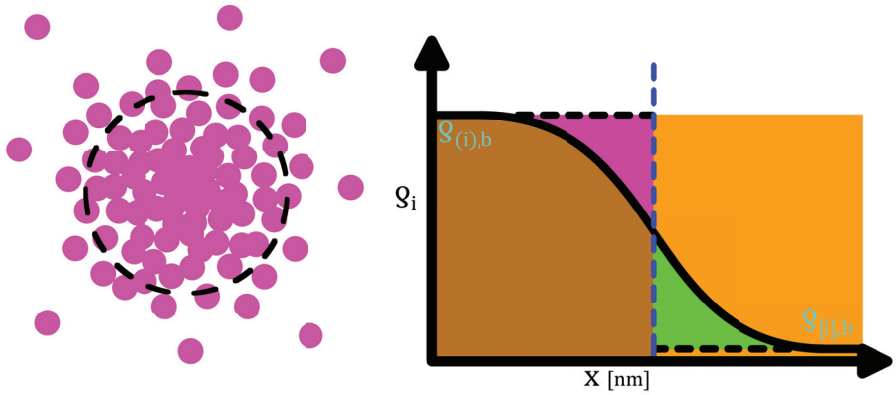

(a) (b)

Figure 2.2: a) The cluster approach. Particles shown in pink and the phase's surface is shown by the dotted line. **b)** How particle density ϱ_i of a species i changes as one passes from the bulk of the slag in brown to the melt in orange. The dotted line indicates the equimolar dividing surface, where the green and pink areas show the particles which are removed and added respectively, due to the placement of said dividing surface. Both from Bjørnstad and Tranell[5].

All of the thermodynamic properties of a phase which are defined by the surface, like surface tension, phase volume, surface area, etc., are properties of this mathematical construct. In the modern literature, this methodology of separating phases is named the cluster approach (CA)[17][18][19], and is illustrated in figure 2.2(a).

A surface is more accurately described as a transitional region, where the particle density of a species i, ϱ_i, transitions from its bulk density in one phase $\varrho_{(i),b}$ to that of its neighbor $\varrho_{[i],b}$, as shown in figure 2.2(b).

$$\varrho_i(x) = \begin{cases} \varrho_{(i),b} & \text{if } x \text{ is within the slag} \\ \varrho_{[i],b} & \text{if } x \text{ is within the alloy} \end{cases} \tag{2.1}$$

In CA, ϱ_i is a boolean function, shown in equation 2.1, which means that any part of the actual particle density curve is set to the bulk value of whichever phase it falls within after the dividing surface has been placed. Thus, depending on the dividing surface placement, the amount of particles in a phase may change. Total phase and species mass/particle count is still conserved by other means, but this is not reflected in the bulk mass/particle count, as these may change freely[18, pp.59–61]. However, this author has found no literature relevant to this work on the practical application of dividing surfaces, which does not assume an equimolar dividing surface.

Most of the commonly used thermodynamic properties one wishes to investigate rely on a thermodynamic bulk phase and its physical counterpart having the same number of particles, thus assuming an equimolar dividing surface is reasonable. An equimolar dividing surface can be seen in figure 2.2(b), where the number of particles lost and gained by placing the dividing surface is equal. At macroscale, the surface region will be so small compared to the bulk, that any discrepancies caused by different mass/particle counts between the thermodynamic and physical states are negligible.

While often neglected in metallurgical literature, it is by no means a given that thermodynamic properties reflect their physical counterparts[2]. The only requirement from a thermodynamic point of view, is that it needs to be internally consistent. Thermodynamic volume for instance, reflects the energy potential this volume represents, and not an actual physical size. This is partly why thermodynamics is so useful, as many problems are easier to solve in thermodynamic space, but it also means that one needs to ensure that the thermodynamic properties we calculate in thermodynamic space can be transformed to equal/approximate their physical counterparts. In Gibbs' thermodynamic framework, the placement of the dividing surface[3] is what allows thermodynamic and physical space to align, but by Gibbs' own words "the position of this plain is as yet to a certain extent arbitrary"[14, pp.380]. While thermodynamics itself is internally consistent with an arbitrary placement of the dividing surface, there seems to be no universal method for placing them such that thermodynamics adequately reflects the physical world. Although in this case, if a phase exhibits certain physical properties, an adequate dividing surface can be placed.

The goal is to align the thermodynamic dividing surface with the "surface of tension", where this "surface of tension" has a superficial tension σ, also known as thermodynamic surface tension[14, pp.391]. Surface tension is interlinked with the position of the "surface of tension", as this is the only place where physically measurable surface normal-tension is equal to the thermodynamic surface tension[18, pp.57–58]. The dividing surface is at the "surface of tension" if a surface can be proven to exhibit the "well defined" property. A surface is considered to be "well defined" when the surface tension σ_{ii} [J/m^2] is independent of the surface curvature r_{curv}, which is not generally the case at small spatial regimes[20].

[2] A point discussed in Gibbs[13][14], but more fleshed out in books like [17][18][19].

[3] Multiple dividing surfaces can potentially be placed to better represent different aspects of a physical system, but in this work only one will be considered.

Commonly, the number of particles the phase consists of ς_p is used instead of curvature, as they both related to size:

$$\frac{d\sigma_{ii}}{d\varsigma_p} \approx 0, \;\; \varsigma_p \propto r_{curv} \tag{2.2}$$

This is also called the capillary approximation, as thermodynamic surface tension is technically only defined for a planar surface and is only approximated for a curved one[18, pp.61]. Kashchiev[17, pp.81] states that σ_{ii} is affected less and less as ς_p increases, and calculates that for water droplets, if $\varsigma_p{>}1000$ then their surface tension will not vary more than 10%. He generally uses $\varsigma_p{<}100$ as the range where the use of CA is absolutely not generally valid, and as $\varsigma_p{>}1000$ is in the same order as that found in Thompson et al.[20], it is assumed to be an adequate benchmark for how large a slag nuclei/droplet needs to be before CA can be assumed as a generally applicable approximation. This is due to both Kashchiev and Thompson et al.'s results pertaining to simple liquids, and that the proposed framework requires the slag to exhibit complex behaviors while the nuclei are small.

In the OLR of MG-Si the alloy manly consists of Si, and the initial slag nuclei are expected to consist of pure SiO_2, which further reacts with [Ca] and [Al]. Molten silica is a non-ideal liquid, having both short and intermediate range structure[21]. Silica has a very strong surface structure, which can be seen by its low surface tension, as surface tension represents the energy difference between the surface and bulk structures[22]. Molten silica is also a part of a select group of liquid species which have surface tensions that increase with temperature. While there are different theories for why this is, it is generally accepted that this is due to a change in the surface structure[23].
This agrees with the molecular modeling work by Schweigert et al.[24], who found that the surface tension of silica, when liquid, does not change significantly down to clusters of 24 SiO_2 molecules over T=1500–2800 K. They propose that a SiO_2 cluster may be viewed as an outer surface shell encompassing the bulk, where the low energy state of the shell structure allows it to be "well defined" even at a very small cluster size. A similar silica shell structure is also found in Roder et al.[25], but the study only covers higher temperatures and larger cluster sizes than Schweigert et al., and Vaccaro et al.[26] who measured the shell thickness experimentally at room temperature to be $\sim$1 nm, where Schweigert et al.'s model predicts it to be closer to 0.3 nm. Critically, for the fumed silica particles from 7 to 40 nm created by Vaccaro et al., they found that the shell thickness was independent of the particle diameter, which further supports that the silica surface is "well defined". Thus, it seems prudent to assume that the surface structure of silica is "well defined" in all spatial regimes relevant to OLR.

2.1.2.2 "Well Defined" Surfaces in SiO_2-CaO-Al_2O_3 Slags

While the previous section showed that it is prudent to assume that the surface structure of silica is "well defined" even at nanoscale, this section mostly concerns itself with how this property can be extended to SiO_2-CaO-Al_2O_3 slags, at least those with high silica contents. It is normally assumed that the "surface of tension" is aligned with the equimolar dividing surface for one component systems[18, pp.59], as:

$$\text{Surface of Tension: } \frac{d\sigma_{ii}}{d\varsigma_p} = -\frac{d\Delta\varphi(\varsigma_p)}{d\varsigma_p}\sum_{\ell=1}^{k}\Gamma_\ell V_{p,\ell} = 0 \tag{2.3}$$

$$\text{Equimolar Dividing Surface: } \sum_{\ell=1}^{k}\Gamma_\ell V_{p,\ell} = 0 \tag{2.4}$$

$$\text{One Component: } k = 1 \Rightarrow \Gamma_1 = 0 \tag{2.5}$$

Here Γ_ℓ [#particles/m^2] is the surface excess for species ℓ, which is a correction factor which keeps the total amount of particles in a phase constant regardless of dividing surface. Γ_ℓ is often confused with the surface concentration found in Butler[27], as Butler uses both properties in his work, although he is careful to separate between them. $V_{p,\ell}$ [m^3/#particles] is the volume species ℓ occupies in the phase. $\Delta\varphi$ [J/m^3] is a term which depends on the type of nucleation (in [18, pp.59] partial pressure is used) per unit volume.

If the phase consists of multiple species, then placing the equimolar dividing surface becomes a much greater challenge, as it is rare to find a system where the trivial case (all Γ_ℓ=0) is possible[18, pp.60]. In the case of SiO_2-CaO-Al_2O_3 slags it becomes even worse, as the species are surface active to different degrees, with the issue illustrated in figure 2.3. Tanaka[28][29] contains a slag surface tension model, based on the work by Butler[27], which shows that calcia and alumina are both not surface active, while silica is very surface active. The high surface activity of silica is in this specific case what allows the equimolar dividing surface to be placed, solving the previously noted multicomponent issue.

To show the differences in surface activity among the slag species, Tanaka's[29] model framework uses the equation set:

$$\sigma_s = \sigma_i^\circ + \frac{RT}{\overline{A}_i}\ln\left(\frac{a_i^s}{a_i^b}\right) \tag{2.6}$$

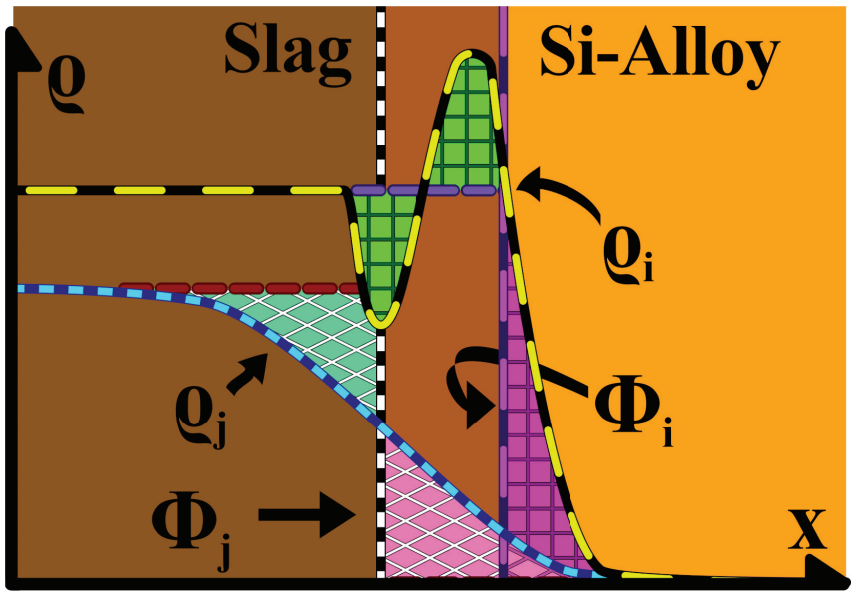

Figure 2.3: Particle density functions ($\varrho(x)$) of the surface active species i with lines in black and yellow, and the non surface active species j in blue, where x represents distance from the bulk slag phase. Φ_i (purple and pink) and Φ_j (black and white) indicate the equimolar dividing surface for each species. From Bjørnstad and Tranell[5].

Here $\overline{A}_i$ [m^2/mol] is the surface molar coverage for species i, and a_i is the Raoultian activity, with reference state as pure species in mole fractions, where superscripted b or s designate either surface or bulk respectively. Figure 2.4 was calculated using equation 2.6, with species surface tension σ_i°, and surface molar coverage $\overline{A}_i$ were taken from Arutyunyan et al.[30].

Comparing figure 2.4(a) and 2.4(b), shows that the concentration of silica must change drastically before it has any large impact on the surface concentration. Figure 2.4(a) also shows that the surface tension of the slag σ_s, is affected more by the calcia than alumina, which also reflects how they impact the surface structure. Nakamoto et al.[31][32], Fabritius et al.[33], and Hanao et al.[34], all show that this model approximates the slag surface tension σ_s adequately for a wide range of slag compositions, and also compares well with Arutyunyan et al.[30] and values from Slag Atlas[35, pp.430], at least in the high silica region shown in figure 2.4.

Since the initial slag nuclei is assumed to consist of pure silica, the nuclei will only take on calcia and alumina as it grows. Silica will therefore define the slag surface structure until the concentration of calcia and alumina becomes such that they are able to disrupt said structure.

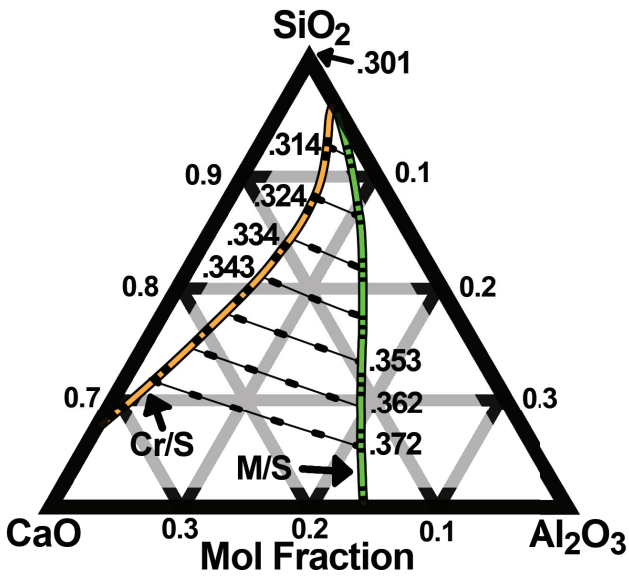

(a)

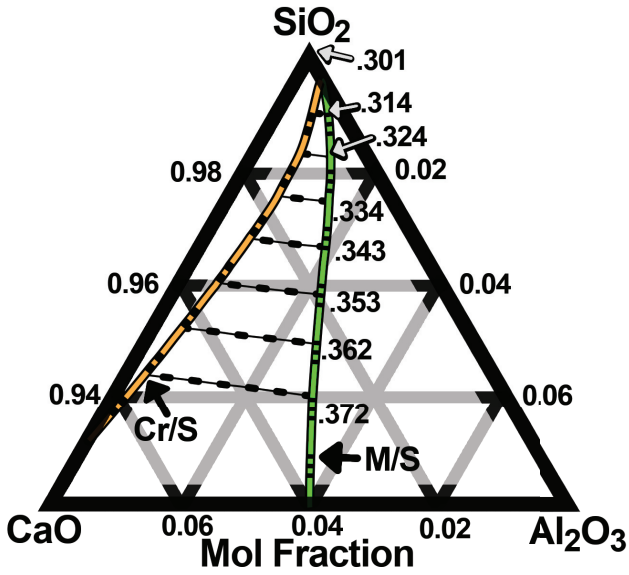

(b)

Figure 2.4: Slag surface tension σ_s [J/m^2] at different surface/bulk slag concentrations, calculated with the model from Tanaka[29] at 1873 K. The iso-tension lines cover the concentrations where the slag is liquid, and is flanked by the cristobalite/slag(liq) (Cr/S) line and the mullite/slag(liq) (M/S) line. **a)** σ_s at different bulk slag concentrations. **b)** Shows the surface concentrations corresponding with the iso-tension, Cr/S, and M/S lines in a). Both from Bjørnstad and Tranell[5].

As calcia and alumina are not surface active, their concentration will be over-represented in the bulk, thus making $\Gamma_{(CaO)}$, $\Gamma_{(Al_2O_3)}$ negative, with $\Gamma_{(SiO_2)}$ being positive, making the equimolar condition in equation 2.4 possible. This should be seen as an approximation, which will be at its worst when the nucleus is very small. However, when the nucleus is very small, then the silica concentration is at its highest, meaning this is when the approximation is least relied upon. The silica surface shell structure is also very thin (>0.2 nm[24], $\sim$1 nm[26]), which means that the bulk concentrations of each species should not be distorted significantly by the equimolar dividing surface's placement.

Further, it is important to note at which concentrations calcia and alumina disrupt the surface structure. The higher the concentrations of calcia and/or alumina are required, the larger the slag nuclei can become before they lose the "well defined" silica surface property, which is only required while the nucleus is small. Silica is a strong network-forming oxide, while calcia is a network-modifier, and alumina is amphoteric[4][21], which designates calcia as the slag component which will degrade the silica surface structure most actively, agreeing with figure 2.4. While the exact concentration at which the silica surface structure collapses is unknown for SiO_2-CaO-Al_2O_3 slags, it is stated in Waseda and Toguri[36, pp.5] that "any addition of alkali metal oxide[5] beyond 10 mol% will gradually change the fragmented random covalent network of silica into an ionic liquid".
Bockris et al.[37] also provides a similar range from their experimental work, which states that the silica framework will "collapse" when 10–12 mol% metal oxide is added. Richardson[38, pp.92–99] later expands on Bockris et al., but keeps Bockris et al.'s concentration range, even though Richardson includes more of the then available literature. Linh and Hoang[39] also shows that CA is not valid for amorphous and liquid $Al_2O_3{\cdot}2SiO_2$ nanoparticles of size 2–4 nm in their modeling work, but even at 33.33 mol% Al_2O_3 does not seem to collapse the surface shell structure.
Litton and Garofalini[40] have performed molecular modeling work on the atomic structure of sodium/calcium-silicate intergranular-films in alumina at 300 K, where soda (Na_2O) is a network modifier like calcia. While the system is a quite different, their model forms the phases by placing silica, calcia/soda, and alumina in a special configuration at very high temperatures, before cooling down the system. Their results show that if the concentration of calcia/soda was 0 mol%, the interfacial energy of the silica film did not depend on the number of atoms in the film (300, 450, 600, 750 atoms), with a big drop in interfacial energy between 8–15 mol% calcia/soda.

[4] Alumina can act as both a network-former and -modifier, but in alumina's case it tends more towards a network-former.

[5] Also known as a network-modifier.

The interfacial energy curves also follow each other reasonably well for both the 600 and 750 atom case, with the 450 atom case close as well before 13 mol%CaO. While caution must be taken in directly drawing conclusions from Litton and Garofalini's[40] work, the fact that it provides similar ranges as the more similar sources must be noted. It also does not contradict the previously stated assumption that CA is valid when $\varsigma_p > 1000$, and shows values in the same range as Kashchiev[17, pp.81] and Thompson et al.[20].

Based upon what has been covered in this section, it seems prudent to assume that if the concentration of silica dips below 88–90 mol%, then it cannot be presumed that silica defines the slag surface structure. However, figure 2.4 shows that there is very big difference between surface and bulk concentrations, and from the sources mentioned it is judged likely that the bulk concentration of silica can be lower than 88–90 mol%, while retaining the "well defined" surface. This might not extend as far as figure 2.4 implies, if one assumes that the 88–90 mol% only applies to the surface concentration, but it provides a solid upper bound, with a bulk concentration of 90 mol% silica as the lower bound. Calcia will affect the surface slag structure to a greater extent than an equal amount of alumina, and it is more likely that the structural "collapse" condition runs parallel to the surface tension lines in figure 2.4, and is found between the stated lower and upper bounds. In either case, this means that the slag nuclei/droplet needs to grow quickly to $\varsigma_p > 1000$, such that it retains its "well defined" surface.

2.1.2.3 Slag Droplet shape and Critical Nucleus Size

This section will cover the shape a liquid slag droplet condensing on a gas substrate in a liquid alloy takes, which is necessary to express the critical nucleus size. Only heterogeneous nucleation will be considered, due to it being substantially more energy efficient than its homogeneous counterpart. It also contains some elucidations on the nature of slag growth in OLR of MG-Si.

Up until now it has always been specified that the slag is a liquid, even though silica does not melt before $\sim$1725°C, and it has previously been stated that the relevant temperature range for OLR of MG-Si is 1500–1700°C. Silica has a gradual transition from its amorphous state to liquid form, one reason for why the glassy-representation is often used to describe the liquid structure of silica[21]. Molecular modeling, like that of Schweigert et al.[24], shows that silica starts to gradually behave more like a liquid well below its bulk melting-point. Another effect which must be considered is melting-point depression at nanoscale, a very well documented effect where the melting-point can decrease by several hundred degrees centigrade, due to the high curvatures at micro/nanoscale[41, pp.184][42][43].

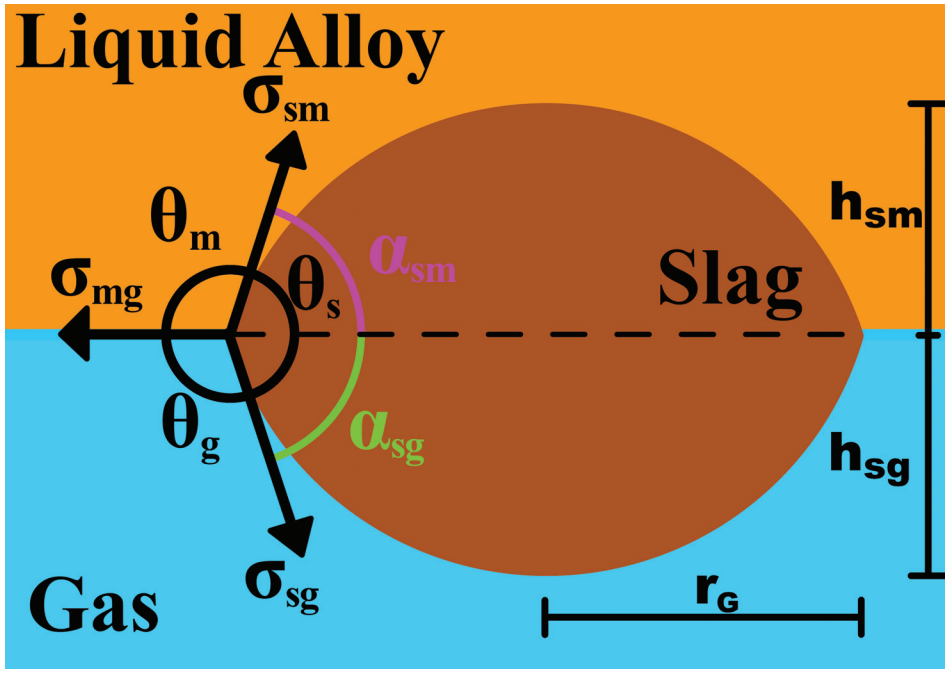

Figure 2.5: The slag-bubble-alloy three-fluid system with relevant parameters; Interfacial tension σ_{ij}, contact angles θ_i, α_{ij}, lens ground radius r_G, and height of each spherical cap h_{sm}, h_{sg}. Subscripts s, m, and g denote the slag, alloy, and gas phase respectively. From Bjørnstad and Tranell[5].

This is also consistent with Broggi[44], where silica was observed experimentally to undergo melting-point depression during condensation of liquid silica nano-droplets, with the melting-point within the relevant temperature interval for OLR. It is also assumed that this is true for SiO_2-CaO-Al_2O_3 slags at very high silica contents, as long as the droplet size is at nanoscale. Even so, this work is also consistent for solid particles, but a different set of geometric equations would need to be used. Paper 1[5] also notes that the exothermic nature of the formation reactions may cause the slag nuclei/droplets to experience temperatures greater than what stated here[45][6].

A liquid droplet forming on a fluid substrate in a fluid atmosphere is a three-fluid system (slag(liq)-bubble(gas)-alloy(liq)), where the liquid droplet takes a lens shape[22]. Since it already has been shown that silica exhibits a "well defined" surface, the critical nucleus size can be calculated from the nucleation theory based on classical macroscale thermodynamics.

[6]If this is the case, the modeled effects seen later in this work are predicted to be more pronounced.

The droplet is shown in figure 2.5, with its geometric properties, nucleation equations, and some thermodynamic relations in appendix sections A.1 to A.4. A.1 describes that the solute condensation caused by over-saturation/supersaturation can be expressed by the activity difference between the current oxygen in the gas $a_{\{O_2\}}$, and saturation limit of oxygen in silicon $c_{[O],sat}$, as:

$$\Delta\mu = -RT \ln\left(\frac{a_{\{O_2\}}}{a_{[O]}^2}\right) \tag{2.7}$$

$$\lim_{[wt\%O]\to 0} a_{[O]} = c_{[O],sat} \tag{2.8}$$

Here, $\Delta\mu$ [J/mol] is the change in chemical potential, representing the system relieving its over-saturation by initiating nucleation. $a_{[O]}$ is assumed to equal to the dimensionless oxygen saturation in liquid silicon $c_{[O],sat}$, with reference state 1 wt% dissolved species in liquid silicon. $a_{\{O_2\}}$ is the oxygen activity in the gas bubble, with 1 bar reference state. This allows the critical nucleus size $r_G^\star$ to be expressed as:

$$r_G^\star = -\frac{2\sigma_{sm}V_{0,mol}}{RT\ln\left(c_{[O,sat]}^2/a_{\{O_2\}}\right)}\frac{\sigma_{sg}}{\sigma_{mg}}\sin(\theta_s) \quad [m] \tag{2.9}$$

Contact angles, like θ_s, will be locked to a single value for a given thermodynamic state, shown in A.3. While σ_{sg} and σ_{mg} can be approximated as their respective surface tensions σ_s and σ_m respectively, this does not work for σ_{sm}. An approximation by Girifalco and Good[46] is commonly used in the metallurgical literature, but Girifalco and Good clearly state that their model is not well suited for high structure liquids, like the slag compositions relevant to this work. Instead, it is seen as more useful to look at how the system behaves over the whole parameter space. By plotting equation 2.9 with respect to θ_s and $a_{\{O_2\}}$[7], figure 2.6 and 2.7 are produced.

Figure 2.6 and 2.7 allows predictions to be made about the critical silica nuclei, even though many of the parameters are not known, due to how changing the parameters influence the total behavior. There are for instance, clear restrictions on the geometry and size of the critical nuclei, with respect to $a_{\{O_2\}}$.

[7] $a_{\{O_2\}}$ is used instead of the dimensionless oxygen partial pressure in the bulk gas $p_{\{O_2\}}$, due to the oxygen seen by the alloy not necessarily reflecting the bulk gas. Næss[45] covers this in more detail.

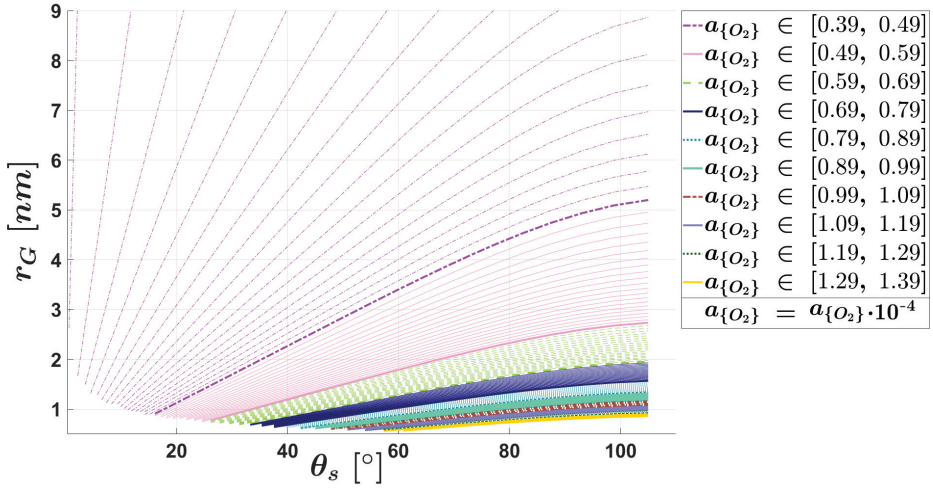

Figure 2.6: $r_G^\star$ as a function of the slag's contact angle θ_s and the oxygen activity in the gas $a_{\{O_2\}}$ ($a_{\{O_2\}}$ in the legend must be multiplied by 10^{-4} to get the actual value). Each line represents a different activity, and lines are grouped together by color/line style, where where each color/line style represents a span of 10^{-5}. Parameters used can be found in table 2.1. From Bjørnstad and Tranell[5].

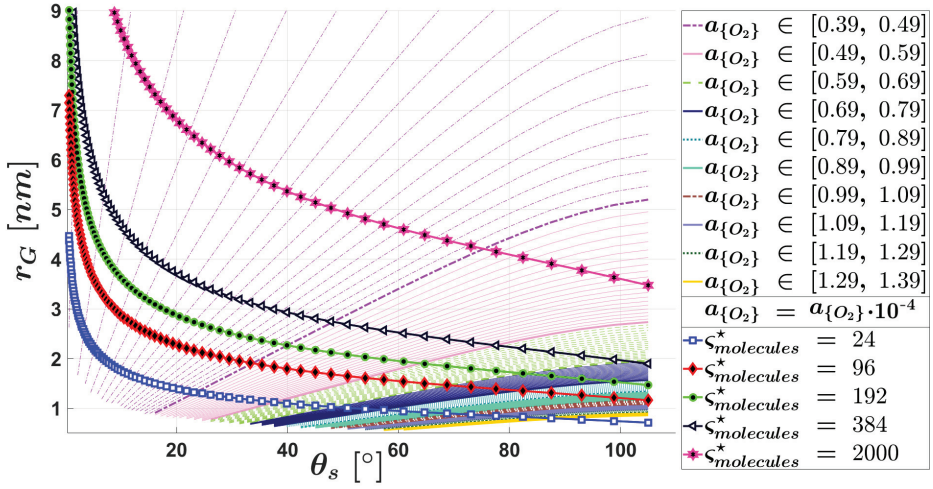

Figure 2.7: Figure 2.6 with lines indicating the number of SiO_2 molecules in the critical nucleus. These lines use densities from Sweigert et al.[24] and transforms a sphere with said density into a lens. For a lens r_G is a function of θ_s which is then plotted. From Bjørnstad and Tranell[5].

Table 2.1: Values used to generate figure 2.6.

$V_{0,mol}$	$27.516(1+(T-1773)\cdot10^{-4})\cdot10^{-6}$	$\frac{m^3}{mol}$	[47]
$\log_{10}\left(c_{[O],sat}\right)$	$-\frac{4620}{T}+0.332$	$-$	[48]
σ_{sg}	$(243.2+0.031T)\cdot10^{-3}$	$\frac{J}{m^2}$	[28]
σ_{mg}	$0.82-3\cdot10^{-4}(T-1685)$	$\frac{J}{m^2}$	[49]
T	1823	K	

The span of $a_{\{O_2\}}$ was chosen as it covers the relevant size range, and clearly shows that increasing the oxygen activity on the bubbles gives smaller nuclei, thus providing a larger surface area, which results in a higher refining efficiency. In the industrial case, it is more likely that $a_{\{O_2\}}$ is high, but this most likely changes during the bubbles ascent, with it being high initially and lower towards the end of its path. Something which is of interest for further study, is if a drop in $a_{\{O_2\}}$ would lead to larger nuclei which retain their geometry, or if the critical nuclei retain their size but change their geometry.

Figure 2.7 shows the critical nucleation size as a function of oxygen activity in the gas $a_{\{O_2\}}$, and geometry by the slags primary contact angle θ_s, but due to its shape, a lens may distribute its volume between its two spherical caps(figure 2.5), where only one is in contact with the alloy. Figure 2.8 and 2.9 shows that most of the critical nucleus' volume is not towards the alloy, but rather the bubble, even though the slag/alloy surface area to size ratio remains fairly constant. While the proportion of volume facing the bubble increases more rapidly with θ_s than that towards the alloy, the volume size fraction facing the alloy still increases until it reaches its maximum at θ_s=90°. This is also where the slag/alloy surface area to size ratio peaks, and is the point where the contact angle between slag and alloy α_{sm} reaches its maximum. At this point, refining efficiency for any given nucleus size should be at its maximum, as this is the maximum contact area that can be gained between the slag and alloy. This may be the key to reduce the possible critical size values in figure 2.7 further in the future. Næss[45] concludes that there is a maximum bulk oxygen partial pressure for active oxidation of a still silicon surface, at $2\cdot10^{-3}$ atm. Since surface geometry and oxygen activity are clearly correlated with nucleus size in figure 2.7, the effect described by Næss might be the same as the one described here, where oxygen activities similar to $2\cdot10^{-3}$ only occur at temperatures above 2000 K. Further investigations of this would require thermodynamic parameters for higher temperature, which are not documented to the same extent as those for lower temperatures.

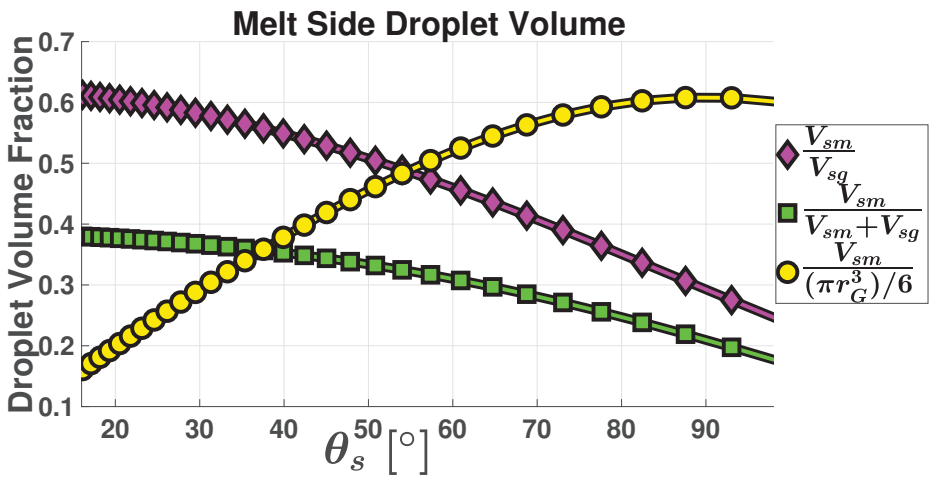

Figure 2.8: Melt side volume fractions with respect to the contact angle θ_s, for critical nuclei in figure 2.6.

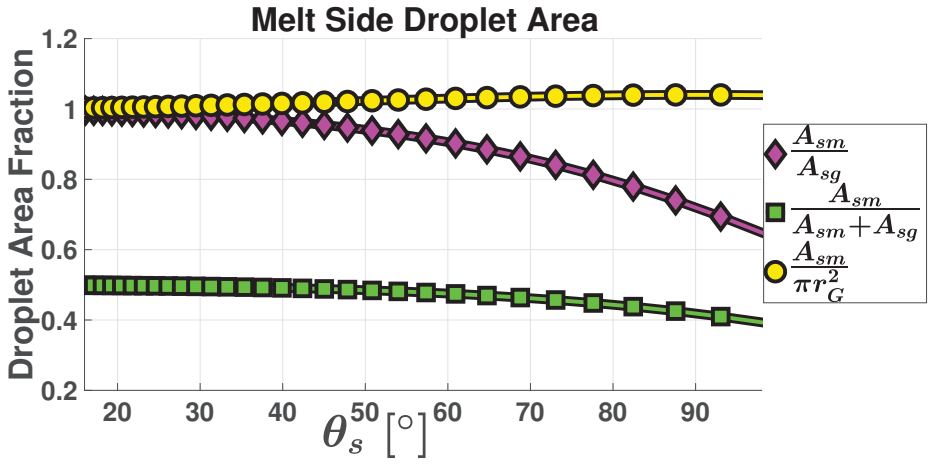

Figure 2.9: Melt side surface area fractions with respect to the contact angle θ_s, for critical nuclei in figure 2.6.

Some Reflections on Slag Nucleation and Growth

How a nuclei distributes its volume depends on how the different interfacial tensions relate to each other. In figure 2.7, $\sigma_{sg} \approx \sigma_{SiO_2}$ is assumed, which is always low ($\sim$0.3), explaining why the lens volume is shifted towards the gas bubble. It is also assumed that $\sigma_{mg} \approx \sigma_{Si}$, which is comparatively high ($\sim$0.7–0.8), and due to how it decreases with dissolved oxygen content and temperature, is the property which has the greatest ability to shift the lens' volume distribution towards the alloy. How the surface tension of silicon behaves regarding dissolved oxygen content and temperature can be found in among others: Mills and Su[50], Keene[51][52], Shishkin and Basin[49], Narushima et al.[48], Yuan et al.[53], and Gheribi et al.[54].

An important aspect of nucleation in high temperature environments is that it occurs very rapidly. Thus, it makes little sense that the slag nuclei/droplet will change its shape to accommodate a local equilibrium at any given time, but rather the local equilibrium dictating the path of further growth. If an initial silica nucleus is formed at high oxygen activities then it is predicted to form with most of its volume not visible to the alloy, but while its projection towards the alloy is small, it still forms a seed which to other silica molecules/sub critical clusters can attach. The silica nuclei should now grow very rapidly, and if the surface tension of the alloy changes due to temperature increase from to the highly exothermic interactions between silicon and oxygen, the alloy being saturated with oxygen, and/or other unknown nanoscale effects, then the slag nuclei will start to favor contact with the alloy more, and making it more likely that it comes into contact with the impurity elements. Since the nuclei initially project little of their volume towards the alloy, it is not seen as likely that they are able to take up enough Ca and Al before they become large enough for their surface to be assumed as "well defined".

The surface structure of silica consists of a highly coordinated ring structure, with some oxygen atoms protruding out of the surface, seen in Roder et al.[25], Schweigert et al.[24], and Vaccaro et al.[26]. From Bromley et al.[55], it follows that these protruding oxygen atoms serve as the primary attachment points, both for adding new silica molecules and for "reacting" with [Ca] and [Al].

Calcia and alumina do not have the same structural properties as silica, so when Ca and Al attach onto the oxygen atoms they cause defects in the future surface structure, by locally reducing the availability of surface oxygen atoms for new silica molecules to attach to. There are also indications that Marangoni effects may allow the silica surface to efficiently transfer any species with disrupt its surface structure into the bulk, which will cause similar defects in the surface structure as those discussed above, but this needs further study.

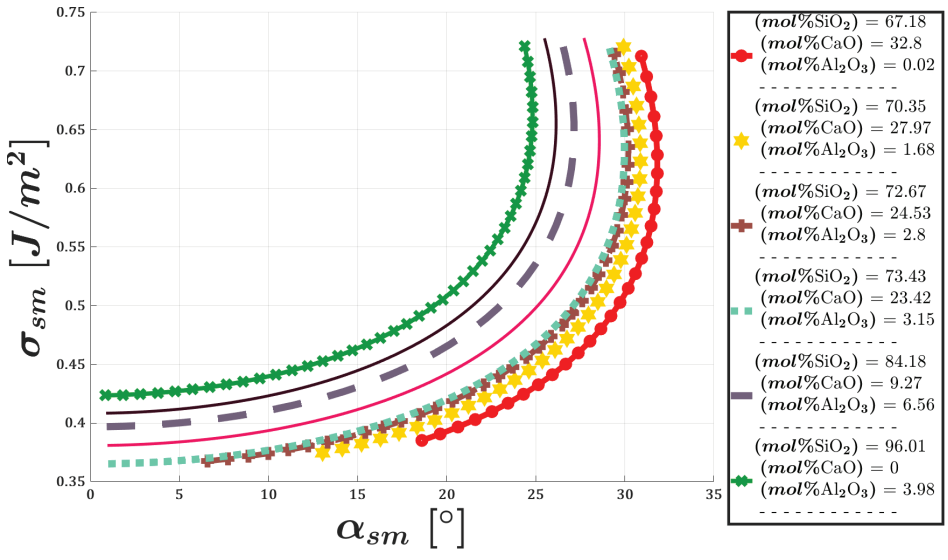

(a)

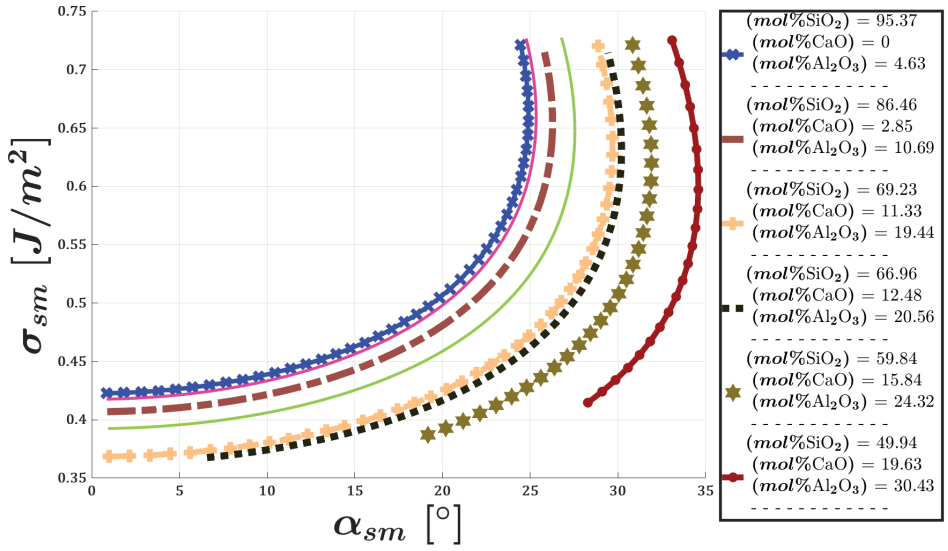

(b)

Figure 2.10: Interfacial tension between slag and melt as a function of contact angle and bulk slag composition along the **a)** cristobalite/slag(liq) and **b)** mullite/slag(liq) line. The lines are produced by the procedure shown in paper 1[5], with σ_{sg} from Tanaka's model[29] at T=1873 K, and σ_{mg} set equal to 0.73 J/m^2. Both from Bjørnstad and Tranell[5].

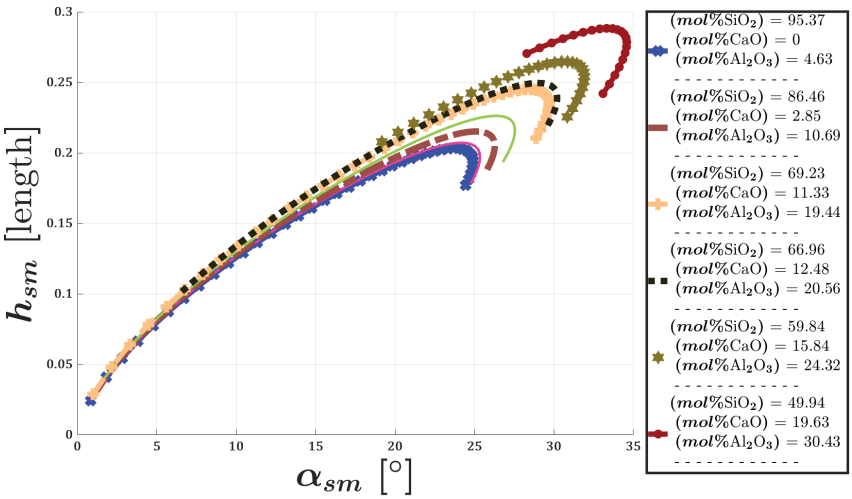

Figure 2.11: Height of the slag droplet between the slag and melt h_{sm} as a function of wetting angle between slag and melt α_{sm} and slag composition following the mullite/slag(liq) line. The slag droplet is assumed to have a constant volume of 1 with an arbitrary cubed length unit. From Bjørnstad and Tranell[5].

While the slag nuclei have been able to protrude into the melt due to changes in the alloys surface tension, this is no longer required as it takes on more calcia and alumina, as these increase the slags surface tension. However, if the alloy surface tension does not change, then this will make it much easier for the slag droplet to detach. This can be seen in figures 2.10(a) and 2.10(b), where the valid solutions for the interfacial tension between the alloy and slag σ_{sm} is plotted against the contact angle α_{sm}. From these figures it is clear that the slag composition strongly affects the range of values σ_{sm} can take.

Figures 2.10(a) and 2.10(b) show that calcia has a much greater effect on the slag behavior than alumina, which is expected from previous sections. As such, as the slag droplet grows and its composition changes, it protrudes ever further into the alloy, shown in figure 2.11. When the droplet reaches a critical point, it gets affected by the external flow field, which causes the whole droplet to detach, or just some parts of it, freeing up space for more slag to formed on the bubble surface in its wake.

2.1.3 Experimental Investigation of Slag Surfaces

Parts of the theoretical framework relies on the notion that silica is surface active, while alumina and calcia are not. This was investigated by melting two $\sim$1.5 mm cubes, cut from an unrefined industrial alloy, on an ISO-88 graphite substrate. They were then held at 1600°C for 15 min, under an oxygen-scrubbed Ar 6.0 ($p_{O_2} < 10^{-15}$ ppmV) atmosphere, where one of them was subjected to 1 min of regular Ar 6.0 to promote surface oxidation. The samples were then rapidly cooled, had selected cross sections extracted by a focused ion beam emitter (FIB), which were then imaged by scanning transmission electron microscopy (TEM/STEM) and chemically mapped by electron energy spectroscopy (EELS), simultaneously collecting the energy-dispersive X-ray spectra (EDS).

2.1.3.1 Experimental Results and Discussion

In paper 1, the concentration maps of a single slag droplet on a SiC formation on the silicon surface from the exposed sample were compared. Figure 2.12 shows the EELS concentration maps for Al, O, Si, and Ca respectively. The strongest signals from Si and Al were extracted from both the EELS and EDS maps by increasing the signal contrast in each image, with the Al signal superimposed on that of Si. Figure 2.13 shows these strongest signal maps for the central portion of the droplet. Ca could not be compared in this manner as its spectra is close to that of C. The coating used during FIB extraction to protect the sample surface contains C, which introduces noise into the concentration maps of Ca, making it unsuited for this type of image manipulation. There also seems to be very little silicon in figure 2.12(c), but as EELS and EDS show relative concentrations of elements, it is assumed that the silicon signal from the SiC surface overshadows the silicon signal from the slag. This is a known problem which might occur when using EELS and EDS in TEM, as these analysis methods are better suited for finding which elements are present rather than quantifying them.

Both figure 2.13(a) and 2.13(b) support the theoretical claims that silica is surface active while alumina is not. This can be seen by how the concentration of red pixels (Si) is higher towards the slag surface, while Al has its highest concentration towards the bulk slag, as the green color is brightest there and becomes dimmer (lower concentration) towards the surface.

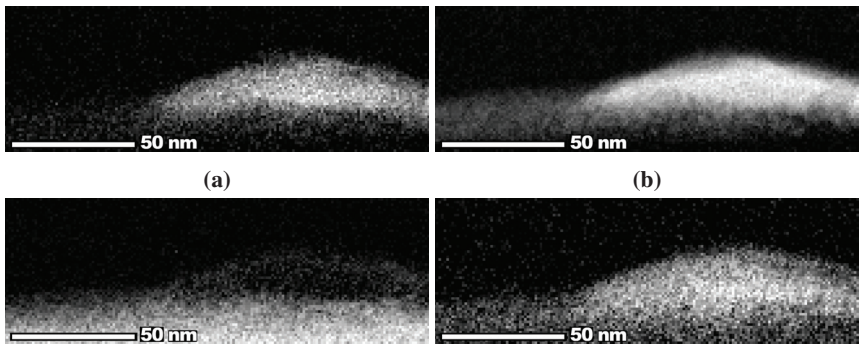

Figure 2.12: EELS maps of **a)** Aluminum, **b)** Oxygen, **c)** Silicon, and **d)** Calcium. All from Bjørnstad and Tranell[5].

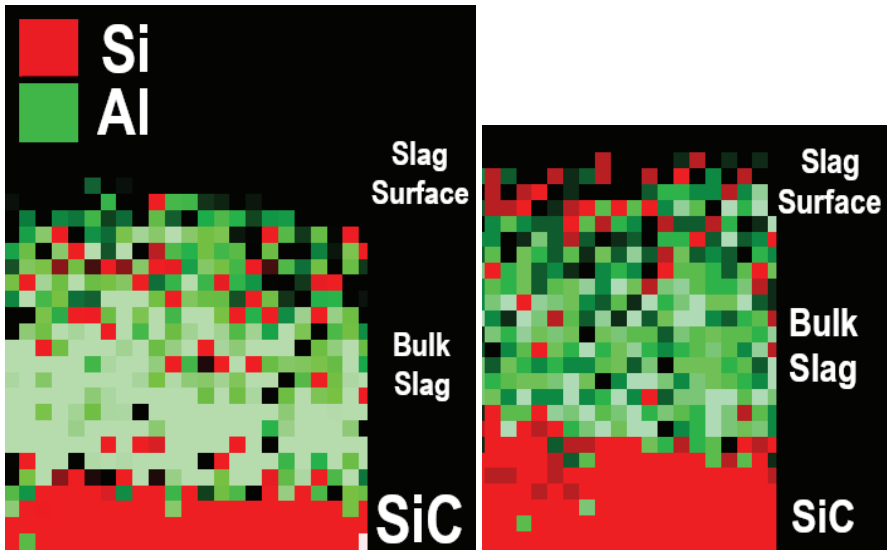

Figure 2.13: a) EELS map retaining only the strongest concentration signal for Al(Green) and Si(Red) in the middle portion of the slag droplet in figure 2.12. The sidebar shows where the slag surface, center, and SiC are located. **b)** EDS map of the same area as in a). Al is colored in green and Si in red. All from Bjørnstad and Tranell[5].

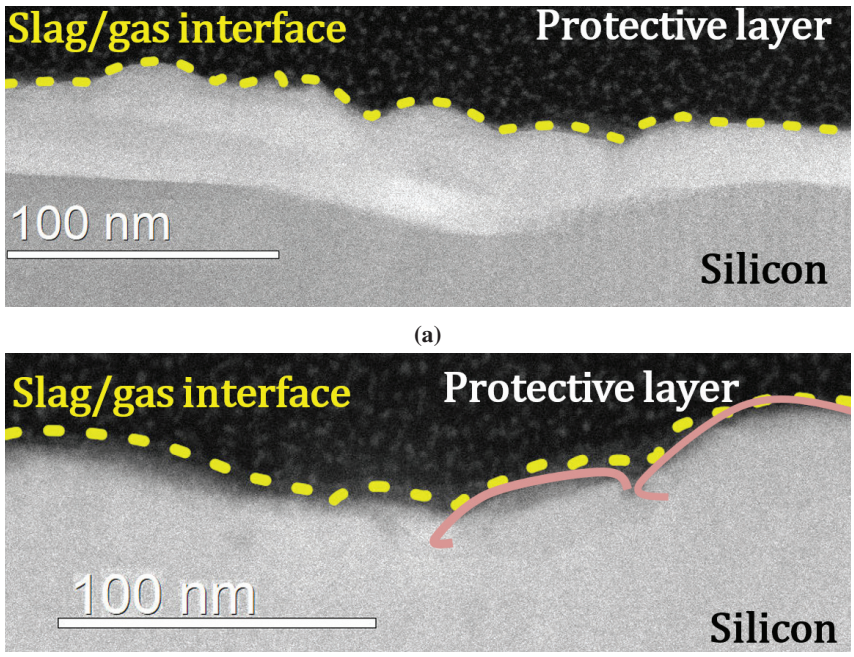

Figure 2.14: TEM images of the **a)** un-exposed and **b)** exposed sample surfaces. Slag/gas interface marked with yellow dotted line. Two of the droplets are outlined in pink in the exposed sample. The protective gallium-carbon layer forms the dark backdrop. Both from Bjørnstad and Tranell[8].

Paper 2[8] looks at two sections of the silicon surface, one for the sample which was not exposed to regular Ar 6.0, and one for the sample that was exposed, both seen in figure 2.14. In both figures 2.14(a) and 2.14(b), it can be observed that regardless if the sample was exposed to oxygen during melting or not, there was still enough bound oxygen on the silicon surface to form a slag layer with an approximate thickness of 10 nm. The difference between the samples, is in the geometric configuration of the slag. In the exposed case there are individual slag droplets, outlined in pink in figure 2.14(b), while the un-exposed sample is like a thin slag film with droplet-like protrusions. Differences in surface geometry are likely due to changes in the surface tension of the slag, which paper 1 shows can occur from changes in slag composition[5]. It is likely that if the surface is subjected to oxygen the surface slag film becomes unstable due to slag forming reactions at the interface, changing the slag composition, and with it the surface tension.

Concentration maps of Al and O were also compared, here sections of the concentration maps in paper 2 were prepared in the same manner as in figure 2.13, and are shown in figure 2.15. Figure 2.15 shows that both the exposed and un-exposed sample exhibits a behavior indicating that alumina is not surface active, supporting both the theoretical claim and experimental result from paper 1.

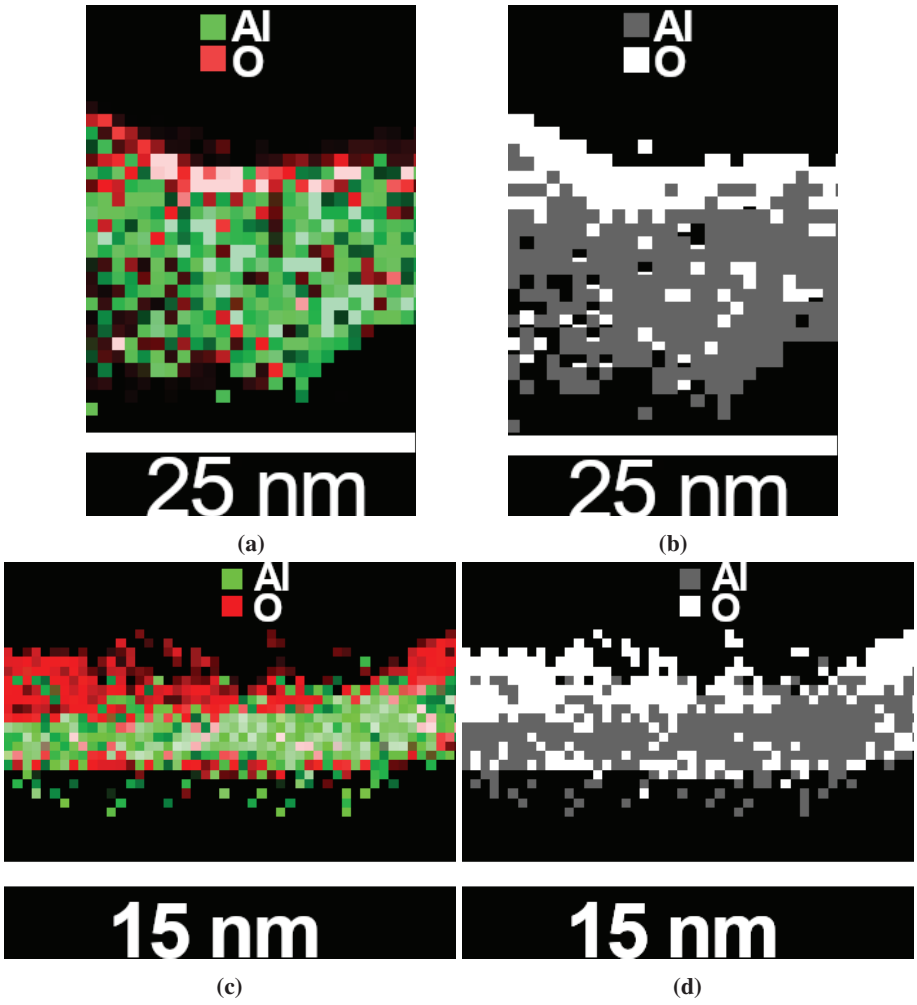

Figure 2.15: a) EELS map retaining only the strongest concentration signal for Al(Green) and O(Red) along the surface of figure 2.14(a). **b)** Is a map of a) where the elements are given a single gray-scale color value to give better contrast. **c)** EELS map retaining only the strongest concentration signal for Al(Green) and O(Red) along the surface of figure 2.14(b). **d)** Is a map of c) where the elements are given a single gray-scale color value to give better contrast.

2.1.4 Conclusions and Industrial Implications

1) The proposed theoretical framework for the nucleation of SiO_2-CaO-Al_2O_3 slag can form a foundation for building more in-depth process models for OLR of MG-Si.

2) The framework uses parameters which are challenging to measure, but since the framework links these together with multiple measurable parameters, it can also be used as a basis to better estimate these parameters.

3) It is predicted that a purge gas with high oxygen content will improve refining efficiency. Since there is an oxidation limit of silicon, the oxygen content in the purge gas can be tailored such that it will promote the formation of small nuclei throughout the bubble's ascent. Higher temperatures are also predicted to increase the oxidation limit, but will also promote SiO formation, thus a critical temperature cut-off for efficient refining exists.

4) Calcia has a much greater effect on slag growth than alumina, which means that the amount of dissolved Ca in the melt is an important control parameter. If the concentration of [Ca] becomes too low, it is expected that the refining will slow down.

5) Since calcia plays such a big role in the refining, it might be more efficient with respect to refining dissolved Al to lower the oxygen concentration in the refining gas, while there is a low amount of alloy in the ladle. [Ca] should react faster than [Al], with calcia facilitating the uptake of alumina, such that if the slag droplets do not stay long enough on the bubble, they might not be able to take up the maximum amount of alumina possible. While paper 5 shows that an eventual alloy/slag equilibrium is expected, reactions on the bubbles are expected to be faster than those with the bulk slag.

6) While the framework is tailored to OLR of MG-Si there is no reason why it should not be applicable for refining of FeSi or steels, as these produce similar slags, but these process may exhibit a different set of behaviors which must be accounted for before use.

7) Experiments were performed which showed that there are strong indications that silica is surface active, and that alumina is not surface active in SiO_2-CaO-Al_2O_3 slag. While a surface slag was found in both the un-exposed and exposed sample, the slag geometry was different. This may be due to the slag film becoming unstable due to interfacial slag formation reactions changing the slag composition, and with it the surface tension of the slag.

Chapter 3

OLR at Macroscale: Experimental and Modeling Work

3.1 Mass Transfer of Al and Ca Between Silicon and Synthetic SiO_2-CaO-Al_2O_3 Slags

3.1.1 Summary

Paper 3[9] aims to experimentally investigate the mass transfer kinetics of Ca and Al, from liquid SiO_2-CaO-Al_2O_3 slags of different compositions to pure liquid Si at 1873 K. Experiments were performed by placing 12g silicon (5N) and 11g SiO_2-CaO-Al_2O_3 slag in a in a graphite crucible, at 1873 K for a given amount of time, followed by rapid cooling of the crucible. The target ((wt%SiO_2), (wt%CaO), (wt%Al_2O_3)) slag compositions were (55, 25, 20), (40, 25, 35), and (40, 40, 20). Kinetic measurement series[1] were performed for each target slag composition, with each slag composition reacting for 5, 10, 20, 30, and 180 min. The metal was separated from the slag and crucible, crushed in a wolfram carbide puck mill, and analyzed for its Ca and Al content by inductively coupled plasma mass spectrometry (ICP-MS). Kinetic analysis determined the total mass transfer coefficient $k_{t,Ca}$ to $3{\cdot}10^{-6}$ and $k_{t,Al}$ to $1{\cdot}10^{-5}$ [m/s]. Measured equilibrium compositions were compared with expected equilibrium compositions calculated with FactSage 7.3[56], using FactPS, FT-oxid, and a custom database. This comparison shows among other, that the interaction between the silicon and graphite crucible is significant, such that a different crucible material should be considered for these types of experiments.

3.1.2 Experimental Investigation of the Slag to Si Mass Transfer Kinetics of Ca and Al in OLR

3.1.2.1 Experimental Work

Furnace

This experiment was performed in a tube furnace, seen in figure 3.1, which was capable of holding a consistent internal temperature and atmosphere while crucibles are inserted and retracted. This was achieved by separate chamber located below the main furnace chamber, where the two chambers could be sealed off from one another or equalized with each other. The separate chamber could additionally be equalized with the external atmosphere and opened, allowing insertion of new crucibles and/or extraction of old ones. After a crucible had been inserted, the chamber was sealed, evacuated, and equalized with the main furnace chamber. The crucible lay inside a graphite crucible holder situated at the end of a long molybdenum rod, which allowed the crucible to be rapidly inserted into the main chamber's hot-zone by pushing the rod laterally.

[1] 3 additional replicate sets were performed with the (40, 25, 35) slag, and are included here.

Inserting the cold crucible into the hot-zone did affected the temperature and pressure inside the furnace chamber, taking approximately 1 min to regain its original state. The crucible was extracted by retracting the molybdenum rod, rapidly cooling the crucible, crucible holder, and rod. A top mounted B-type thermocouple was used to control the furnace temperature, which was placed 5 cm above the top of the crucible. An additional B-type thermocouple was also mounted on the side of the furnace next to the hot-zone, to ensure that the crucible did not experience any significant temperature gradient.

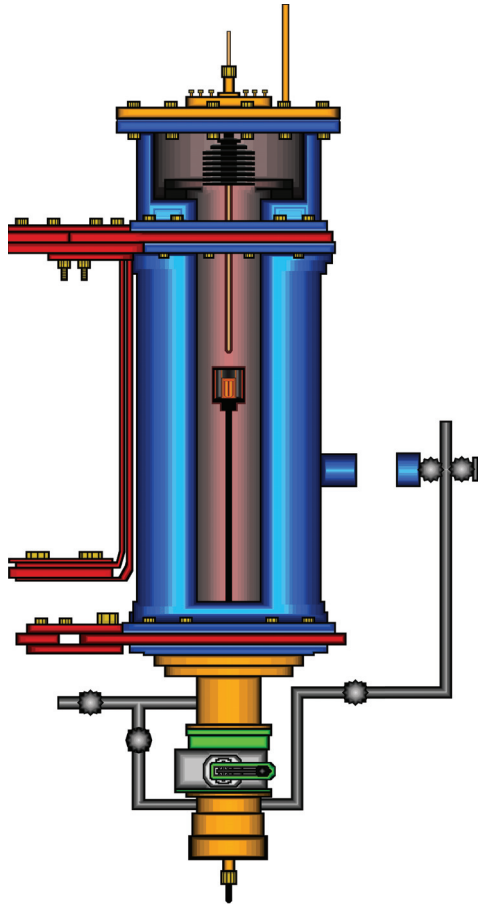

Figure 3.1: Tube Furnace.

Execution

Prior to the kinetic experiments, 12g Si (8N) was melted in an IG-110 graphite crucible (OD: 30mm, ID: 22mm, OH: 45mm, IH: 40mm), under an Ar 5.0 atmosphere (1.15–1.30 bar). After cooling, the solidified silicon provided a consistent contact area between each sample, which was close to that reflected by the crucible's inner diameter. 11g of slag was then placed on top, covering the silicon. Three different slags, table 3.1, were mixed from a set of SiO_2-CaO-Al_2O_3 master slags intended for high purity use. These had been analyzed by XRF to contain approximately 0.1 wt% Fe_2O_3, with other impurity oxides totaling less than 0.1wt%. Homogenization was ensured by heating the slag mixture to 1873 K for 1 hour, before rapid cooling and subsequent crushing.

Table 3.1: Target slag concentrations.

Slag ID	SiO_2 [wt%]	CaO [wt%]	Al_2O_3 [wt%]
SCA-1	55	25	20
SCA-2	40	25	35
SCA-3	40	40	20

A kinetic series with 5 holding times was performed with each target slag concentration, totaling 15 samples. The holding times were 5, 10, 20, 30, and 180 min, where Jakobsson[57] proposed that a holding time of 180 min was sufficient for approaching equilibrium between SiO_2-CaO-Al_2O_3 slags and liquid silicon at 1873 K. After cooling, the crucibles were removed with a rotary grinder, and the slag and metal subsequently separated. Great care was taken to ensure that no slag was present in the metal sample, with an approximate metal retention of 95 wt%. The samples were then crushed in wolfram carbide puck mill, and prepared for ICP-MS. Each sample was split into two sub-samples, which were measured individually, together with 3 NIST MG-Si standard reference samples and 3 blanks.

3.1.2.2 Kinetic Model

Kero et al.[3] propose that the oxidation and general mass transfer of Ca and Al from metal to slag in OLR, behaves according to a standard batch reactor model:

$$-m_m \frac{d\omega_{[i]}}{dt} = k_{t,i}\overline{\rho}_m A_s \left(\omega_{[i]} - \omega_{[i]}^{eq}\right) \tag{3.1}$$

Here $\omega_{[i]}$ is the mass fraction of species i in the liquid metal phase, and m_m [kg], $\overline{\rho}_m$ [kg/m^3], A_s [m^2], and $k_{t,i}$ [m^2/s] denoting the bulk metal mass, bulk density, contact area, and total mass transfer coefficient[2] of species i respectively. Kero et al. only show the mass transfer from liquid metal to slag, but equation 3.1 may be modified to express slag to metal transfer, resulting in equation 3.2.

$$\begin{aligned}
&(MeO_y) + \frac{y}{2}[Si] \rightarrow [Me] + \frac{y}{2}(SiO_2) \\
&\omega_{[Me]}(t) = \omega_{[Me]}^{\infty}\left(1 - \exp\left(-(\frac{k_{t,Me}\overline{\rho}_s A_s}{m_m}\beta)t\right)\right) \\
&\beta = \frac{m_m}{m_s} + \left(M_{Me}\sum_j \frac{\omega_{(jOX)}}{M_{jOX}}\right)\frac{100 f_{[Me]}}{K_{Me}\gamma_{(MeO_y)}}\left(\frac{a_{(SiO_2)}}{a_{[Si]}}\right)^{\frac{y}{2}}
\end{aligned} \tag{3.2}$$

How the expressions were generated is detailed in A.5.

[2] This is not the actual mass transfer coefficient, but a term representing the total combined resistance against mass transfer. A more detailed description can be found in Engh[58, pp.176] and Bjørnstad[59].

3.1.3 Results and Discussion

The results of the ICP-MS analysis of slag and metal samples can be found in B.1. The measurements, normalized with respect to their arithmetically combined 180 min means from equation 3.3, can be seen in figure 3.2 and 3.3. In figure 3.2 and 3.3, the mean and variance were generated by an unbiased combination of the inputs, unlike the biased combination in the paper[9], and duplicate scans[3] of a single sub-sample were pooled[4], as to retain the unbiased nature of the inputs, and making all n_i equal. Populations were assumed normally distributed, such that the samples are t-distributed, giving:

$$\overline{\overline{X}} = \frac{\sum_{i=1}^{k} n_i \overline{X}_i}{\sum_{j=1}^{k} n_j}, \quad s^2_{comb} = \frac{\sum_{i=1}^{k} (n_i - 1)\left(s_i^2 + (\overline{X}_i - \overline{\overline{X}})^2\right)}{\sum_{j=1}^{k} (n_j - 1)} \tag{3.3}$$

$$s_p^2 = \frac{\sum_{i=1}^{k} (n_i - 1)\, s_i^2}{\sum_{j=1}^{k} (n_j - 1)} \tag{3.4}$$

$\overline{\overline{X}}$ is the mean of means $\overline{X}_i$, s^2_{comb} is the combined variance of the sample variances s_i^2, s_p^2 is the pooled variance, and n_i the sample size of sample set i, with k as the total number of sets. This case has sample populations which are expected to overlap in their entirety, which should allow the estimated variance s^2_{comb}, from combining overlapping sub-populations into a general overarching population, to be a suitable estimate of the actual combined variance. However, it can be shown that s_p^2 would also be serviceable, but it under-represents the variance by up to several orders of magnitude when the sub-sample values are very far apart, compared to s^2_{comb}.

[3] The verification protocol of the ICP-MS machine would sometimes scan a sample twice to ensure that it measured the correct concentration.

[4] In this specific case the pooling relations collapse into a simple arithmetic mean.

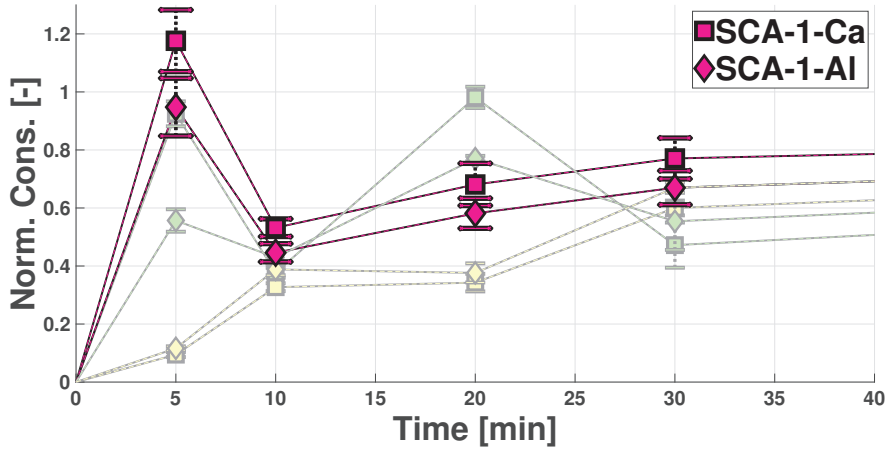

(a)

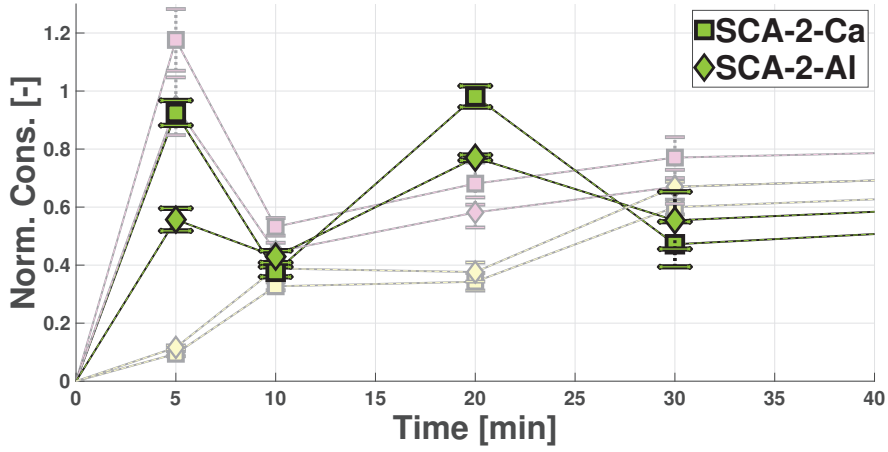

(b)

Figure 3.2: Normalized mean Ca and Al concentrations, with respect to their mean end value (180 min sample), against their holing times at 1873 K. The 180 min sample is not shown but has the value 1 in all cases. Error bars show the 95% confidence interval.

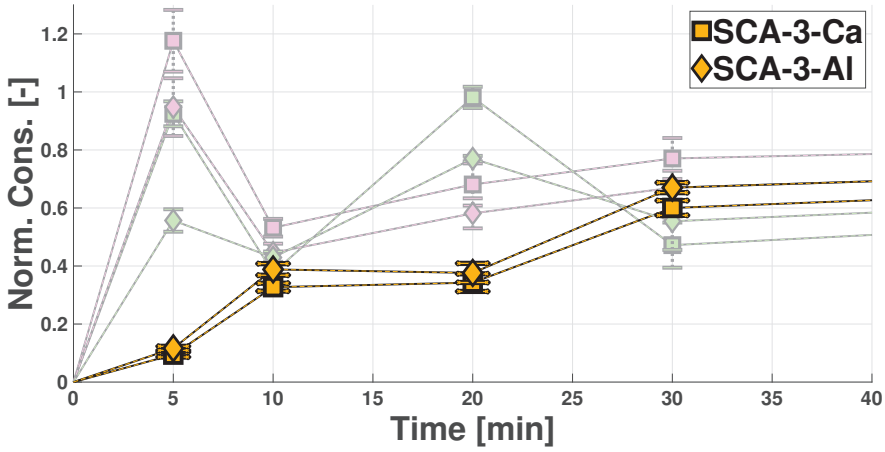

Figure 3.3: Normalized mean Ca and Al concentrations, with respect to their mean end value (180 min sample), against their holing times at 1873 K. The 180 min sample is not shown but has the value 1 in all cases. Error bars show the 95% confidence interval.

Figures 3.2 and 3.3 show that the mass transfer of Al and Ca for each slag exhibit highly similar behaviors. This can for instance be seen by the rank[5] being equal for both species of a specific set after a given hold time. The species additionally share consistent deviation with respect to time, where the Al samples see less variance than that of Ca, which is thought to be due to how Ca interacts with the digestive acids used in ICP-MS[57]. Some samples do deviate greatly from their neighbors, with the deviation mainly being positive, suggesting that they may have been contaminated by small amounts of slag. That the contamination is small, comes from the sub-samples showing a high degree of homogeneity, excluding the final SCA-3 measurements, which suggest that the slag was spread evenly within the sample, during crushing, and no visible slag pieces were seen before crushing. The normalized values also do not exhibit deviations reflecting the difference in mass of both Al and Ca between the metal and slag, which is of several orders of magnitude. This is a likely candidate for these samples not being able to significantly express the exponentially decaying behavior resulting from equation 3.2, as omitting the outliers decreases the statistical resolution below the validity threshold of the regression.

[5]Rank is the sample order from smallest to highest, so after a hold time of 5 min, SCA-3 has rank 1, as it is the lowest value, SCA-2 has rank 2, and SCA-1 has rank 3. This is a very common parameter in statistical non-parametric tests.

Table 3.2 compares the 180 min samples with the calculated dissolved equilibrium concentrations of Al and Ca in Si using FactSage 7.3[56]. To warrant further investigation into their similarity, both calculated concentrations should fall within the 95% confidence interval, which is not the case for any of the given sets. Since the crucibles were made from graphite, including graphite in the FactSage calculations was also tested, but no adequate solution could be found. While not included

Table 3.2: Measured composition at 180 min, compared with equilibrium calculations between 100g Si and 100g slag from FactSage 7.3 at 1873 K, with the FT-oxid, FT-lite, and FactPS databases[56].

	Measured 180 min					
	SCA-1	(55,25,20)	SCA-2	(40,25,35)	SCA-3	(40,40,20)
	Mean	95% CI	Mean	95% CI	Mean	95% CI
[wt%Ca]	0.40	$\pm$ 0.009	0.47	$\pm$ 0.016	1.62	$\pm$ 0.420
[wt%Al]	0.32	$\pm$ 0.012	0.98	$\pm$ 0.076	0.79	$\pm$ 0.183
	FactSage					
[wt%Ca]	0.10	*	0.18	*	1.21	*
[wt%Al]	0.12	*	0.46	*	0.30	*

in the paper 3, samples from the slag were also analyzed by ICP-MS, where the measurement data can be found in B.1. This was performed as a general test to see if ICP-MS could adequately express slag compositions. The results clearly show why ICP-MS is generally not used for this task, as when the specie measurements are converted to their respective oxide, there is a high probability that they do not show proper coherence (sum to 100%), even when including the confidence intervals. However, with the sample size present, it is adequate for assuming that the measured slag composition reflects the target composition, except for in SCA-2.

Unpublished SCA-2 Replicate Sets

The experiments follow from the work done by Jakobsson[57], among others, but the measurements stray very far from the calculated thermodynamic equilibrium compositions. As the furnace and experimental methodology in this work are frequently employed, 3 replicate kinetic series were performed to verify the replicability of the findings. SCA-2 was the sample set which exhibited the greatest deviation from its expected behavior, seen from both metal and slag measurements, so it was selected as the slag composition for the replicate sets. Almost all parameters were kept the same, except that 10g Si and 10g slag was used, instead of 12g Si and 11g slag. 3 replicate sets were performed, with hold times of 5, 10, 30, 60, 180, and 210 min. From each sample, 3 metal sub-samples were sent for ICP-MS and another 3 were analyzed by atomic adsorption spectroscopy (AAS).

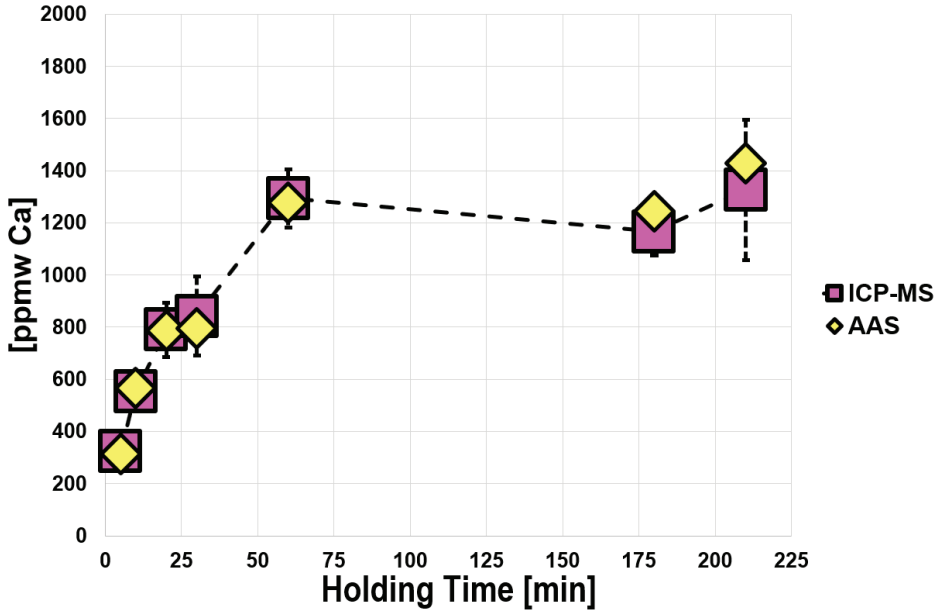

(a)

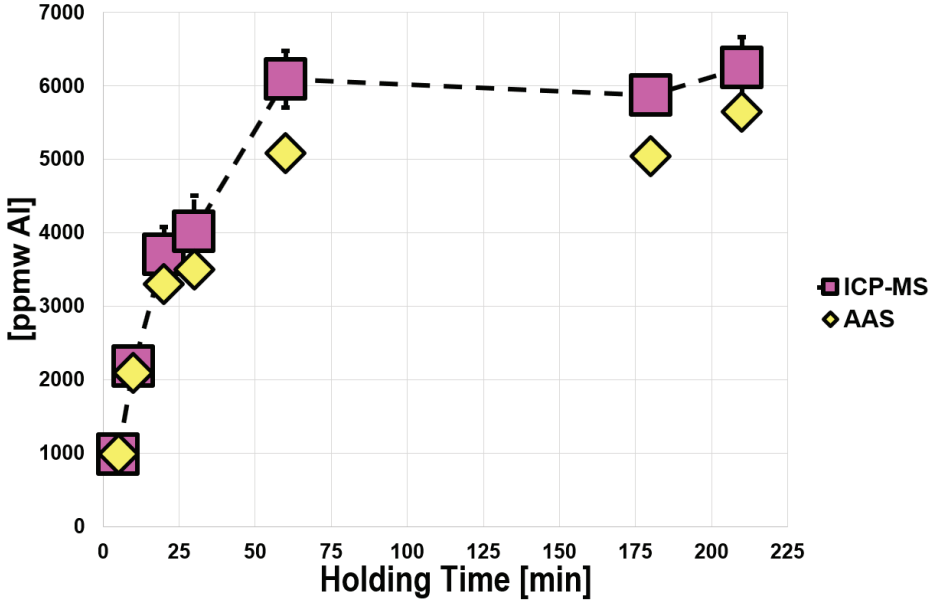

(b)

Figure 3.4: Total combined mean [ppmw Ca] and [ppmw Al] for all replicate sets at each hold time for the ICP-MS and AAS measurements. The error bars represent the 95% confidence intervals from the ICP-MS measurements.

The raw measurement data can be found in B.1, where the total combined means for the means of the three replicate sets can be found in figure 3.4. The replicate sets show good agreement, but the AAS values for Al are lower than its ICP-MS counterparts from 60 min and onward. It will also be shown by kinetic modeling that the replicate sets exhibits the dependent mass transfer behavior for both Ca and Al, as is seen in figure 3.2 and 3.3 for the previous sets.
The concentration of both Ca and Al in the replicate sets are very different from the first SCA-2 set, and the calculated equilibrium composition in table 3.2. New equilibrium calculations were made using a custom FactSage database to replace FT-lite[56], as the literature indicates that the activity coefficient of Ca at infinite dilution in Si at high temperatures, is inadequate in the current database. The custom database uses the activity coefficient from Jakobsson and Tangstad[60] instead, and while the equilibrium calculations still do not give values close to the ones measured here, if a small amounts of carbon is added to the system, a proper fit can be found, as listed in table 3.3. The custom database also allows equilibrium values to be calculated for SCA-2 and SCA-3, with 6.6g C and 4.2g C respectively. This indicates that the experimental methodology is sound and equipment is sufficiently adequate, but that the interaction between the graphite crucible and silicon is significant, and the extent of this interaction adds an extra layer of uncertainty to the output.

Table 3.3: 60, 180, and 210 min total combined mean of the measurement data from ICP-MS and AAS. Equilibrium composition calculations from FactSage 7.3[56], where 100g Si, 100g slag, and the denoted amount of C was used as inputs at 1873 K. Calculated with the custom and FT-lite databases, with the shown values being representative fits.

	Replicate SCA-2				
		ICP-MS		AAS	
	Hold Time	Mean	95% CI	Mean	95% CI
[ppmw Ca]	60	1293	±111	1278	±128
[ppmw Ca]	180	1165	±89	1244	±98
[ppmw Ca]	210	1327	±269	1430	±339
[ppmw Al]	60	6092	±384	5078	±247
[ppmw Al]	180	5875	±240	5044	±207
[ppmw Al]	210	6250	±411	5644	±415
		FactSage			
		Custom		FT-lite	
		2.1g C	0g C	3g C	0g C
[ppmw Ca]	*	1328	833	3887	1790
[ppmw Al]	*	5856	4613	5839	4575

Kinetic Model

The replicate sets allows the total mass transfer coefficients k_{Ca} and k_{Al} to be estimated by a non-linear regression, without necessitating a natural-logarithmic transformation of equation 3.2 commonly used in the literature. This removes the propagation of model errors resulting from transforming the natural-logarithmic equation back to regular parameter space. The mean ICP-MS values at each hold time from the three replicate sets were fitted by the normalized equation:

$$\hat{c}_{[Me]}(t) = \theta_1 \left(1 - \exp(\text{-}\theta_2 t)\right), \quad c_{[Me]} = \frac{\overline{\omega}_{[Me]}}{\overline{\overline{\omega}}^{\infty}_{[Me]}} \tag{3.5}$$

Here θ_1 and θ_1 are the estimated parameters, t is the input, while $\hat{c}_{[Me]}$ is the estimated response. θ_1 represents $\overline{\omega}^{\infty}_{[Me]}/\overline{\overline{\omega}}^{\infty}_{[Me]}$, and should thus be approximately equal to 1, while θ_2 is the parameter we wish to estimate. Including known parameters like θ_1 to be estimated is common in non-linear regression, as such parameters aid in model validation by providing information about the parameter covariance and general regression behavior. The normalization was carried out using the total combined mean of the 210 min samples, and the optimization regression for the non-linear regression was the minimization of the residual sum of square error, resulting in table 3.4.

Table 3.4: Estimated parameters for Ca and Al with their individual 95% confidence interval.

	θ_1	95% CI	θ_2	95% CI
Ca	0.938	±0.099	0.051	±0.016
Al	1.017	±0.046	0.044	±0.006

The estimated and measured responses with a 95% prediction interval with respect to Ca and Al can be found in figure 3.5(a) and 3.6(a), with their respective performance indicators in figures 3.5(b) and 3.6(b). Table 3.4 shows that θ_1 is not different than 1 at a 95% confidence for both Ca and Al, and that θ_2 for both Ca and Al cannot be assumed different at a 95% confidence. That θ_2 is similar for both Ca and Al is expected, and further underlines the similarity between the relative mass transfer behavior of the two species. With Gibbs energies and activities of the slag species from the FactSage 7.3[56] databases FactPS and FT-oxid, Raoultian activity coefficients at infinite dilution for dissolved Ca and Al in Si from Jakobsson and Tangstad[60], and $\overline{\rho}_s \approx 2500$ [kg/m^3][4, pp.237], the mass transfer coefficients can be estimated and are listed in table 3.5. The contact area A_s was calculated both as a circle and spherical cap[6] with the inner crucible diameter, but it did not change the result significantly.

[6] Some surface distortion was seen in some of the samples. Heights of the spherical cap up to 1 cm were tested.

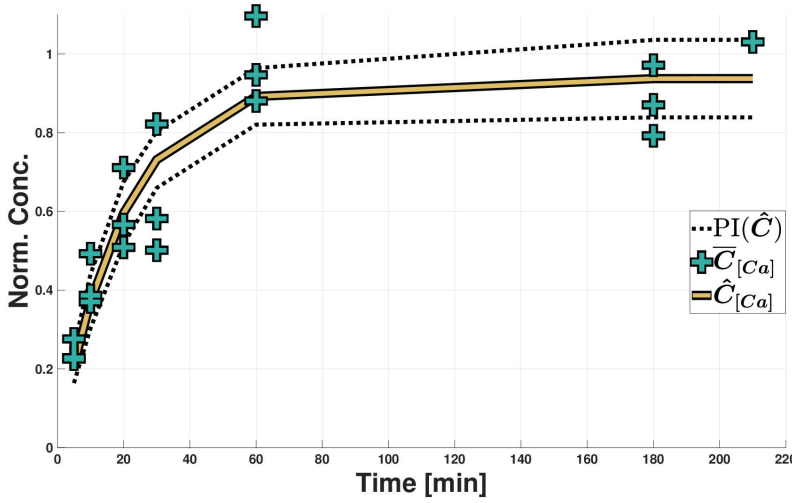

(a)

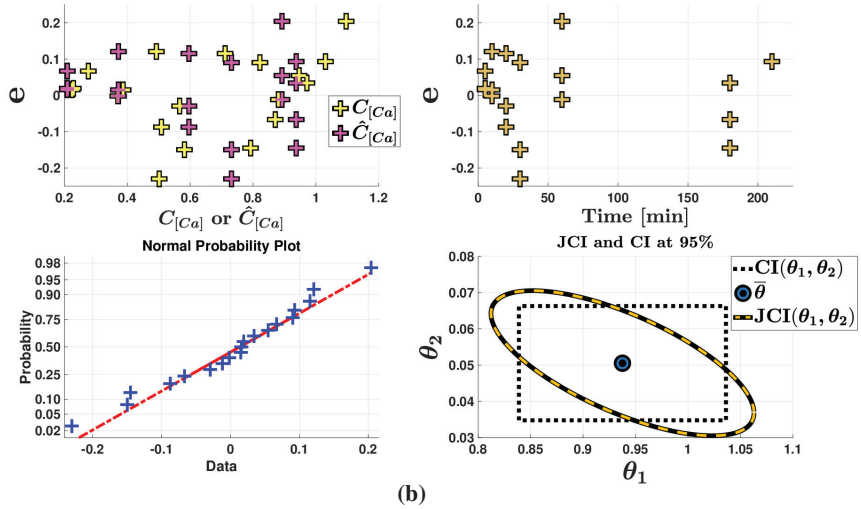

(b)

Figure 3.5: a) Estimated and measured responses with a 95% prediction interval with respect to the normalized Ca concentration for the model parameters in table 3.4. **b)** Regression performance indicators which show that the regression is valid. The two upper graphs show that the residuals are random with respect to the input, and the estimated and measured response. In the lower left graph the crosses follow the line, showing that the residuals are normally distributed. The lower right graph shows the joint confidence intervals of the model parameters. This interval does not contain zero, thus being significantly different than zero, but it does show high elliptical eccentricity, indicating high parameter covariance. The curvature at the elliptical vertex shows that the covariance is not high enough to invalidate the regression.

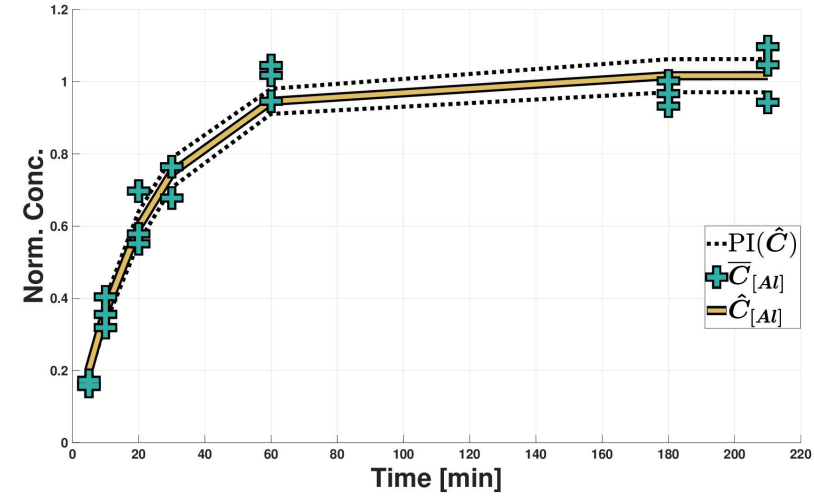

(a)

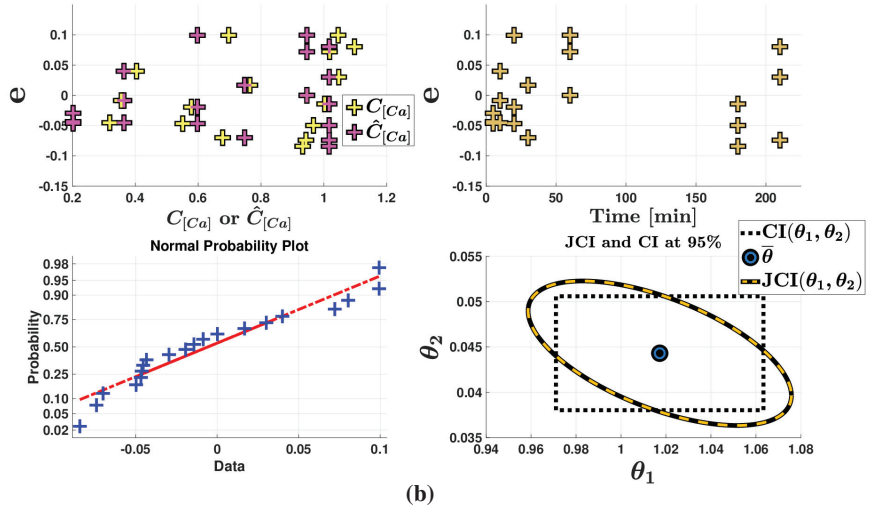

(b)

Figure 3.6: a) Estimated and measured responses with a 95% prediction interval with respect to the normalized Al concentration for the model parameters in table 3.4. **b)** Regression performance indicators which show that the regression is valid. The two upper graphs show that the residuals are random with respect to the input, and the estimated and measured response. In the lower left graph the crosses follow the line, showing that the residuals are normally distributed. The lower right graph shows the joint confidence intervals of the model parameters. This interval does not contain zero, thus being significantly different than zero, it does show medium elliptical eccentricity, indicating medium parameter covariance. The curvature at the elliptical vertex shows that the covariance is not high enough to invalidate the regression.

Table 3.5: Reactions, correction factor β from equation 3.2, and total mass transfer coefficients for Ca and Al, $k_{t,Ca}$ and $k_{t,Al}$[7].

	$CaO(s) + 0.5Si(l) = [Ca] + 0.5SiO_2(cr)$
β	135.54
$k_{t,Ca}$ [m/s]	$\approx 3 \cdot 10^{-6}$
	$AlO_{1.5}(s) + 0.75Si(l) = [Al] + 0.75SiO_2(cr)$
β	30.64
$k_{t,Al}$ [m/s]	$\approx 1 \cdot 10^{-5}$

3.1.4 Conclusions and Industrial Implications

Kinetic experiment series were performed to investigate the mass transfer of Ca and Al between Si and synthetic SiO_2-CaO-Al_2O_3 slag compositions (55,25,20), (40,25,35), and (40,40,20) at 1873 K. Hold times of 5, 10, 20, 30, and 180 min were used. 3 replicate measurements series with the (40,25,35) slag were also performed to verify the experimental procedure. Conclusions from the work were:

1) The measured values show similarity between the mass transfer behavior of both Al and Ca, indicating that their individual mass transfer is dependent of the other.

2) The measurement series to not reach compositions reflected by the calculated equilibrium composition with the FT-oxid, FT-lite, and FactPS databases in FactSage 7.3[56]. If activity data from Jakobsson and Tangstad[60] was used instead of that in FT-lite, and a small amount of C was added to the system, the calculated equilibrium composition reflected those measured.

3) A general mass transfer model was used to estimate the total mass transfer coefficient $k_{t,i}$ in the 3 replicate sets. $k_{t,Ca} \approx 3 \cdot 10^{-6}$ and $k_{t,Al} \approx 1 \cdot 10^{-5}$ [m/s].

4) The FactSage comparison between the equilibrium compositions shows that the interaction between the silicon and graphite crucible is significant, such that a different crucible material should be considered for these types of experiment.

[7] This is not the actual mass transfer coefficient, but a term representing the total combined resistance against mass transfer. A more detailed description can be found in Engh[58, pp.176] and Bjørnstad[59].

Industrial Implications

Paper 3[9] contains the first piece of work performed during the PhD period. Much has been learned since then, and this work is hence presented in light of what is currently known. These experiments were performed to separately investigate one of the mass transfer effects expected to be present in the oxidative ladle refining (OLR) of metallurgical grade silicon (MG-Si), namely the mass transfer to reach an equilibrium between alloy[8] and slag, aiding in dissecting complex industrial behaviors. Thus, while the paper focuses on estimating the mass transfer coefficients for a kinetic model, a key industrial implication is that the mass transfer behavior of Ca and Al show high similarity, as they are highly statistically correlated, when the mass transfer occurs by slag/alloy equilibriation. The similarity persists while the mass transfers are of different orders, and does not depend on the selected slag composition.

This indicates that a SiO_2-CaO-Al_2O_3 slag will continually adjust its calcia and alumina content when in contact with a silicon alloy, providing experimental evidence for the global bulk slag equilibrium refining behavior in paper 5[11]. If the bulk slag constantly adjusts its calcia and alumina composition towards an equilibrium with the alloy, then to achieve a greater refining effect it is desirable to keep the bulk slag and alloy away from an equilibrium as long as possible. This is achieved by constantly producing new silica[9], like in OLR, which will ensure that the calcia and alumina concentration in the slag cannot reach their equilibrium levels until a critical mass of slag has been reached, such that its composition remains unaffected by the influx of new silica. This is in accordance with the theoretical work in the paper 1[5], as silica creates and grows the slag phase, while calcia and alumina modify it.

[8] Pure Si was used instead of a silicon alloy to get larger effect-sizes.

[9] This is not a general case for SiO_2-CaO-Al_2O_3 slags, but is rather an effect of the slag being in contact with a silicon alloy. Thus, there is always an excessive amount of Si available to form silica, while this is not true for alumina and calcia.

3.2 The Effect of Calcium Alloy Content on the Mass Transfer of B Between Si and SiO_2-CaO slag.

3.2.1 Summary

A large body of literature has documented that during high temperature liquid metal/liquid slag reactions, dynamic interfacial phenomena such as interfacial turbulence, emulsification, and subsequent changes in apparent interfacial area may occur[61][62][63][64][65]. Krystad et al.[66] have previously documented that the Fe content of FeSi had an impact on the mass transfer rate of B, for FeSi in contact with SiO_2-CaO slags at 1873 K. SiO_2-CaO slags are often utilized when B is refined from Si alloys by slag refining, where influencing the B mass transfer kinetics by manipulating the interfacial properties would be beneficial in industrial process control. The mass transfer of Ca between slag and alloy is many orders of magnitude higher than that of B, so it was deemed a good candidate for investigating the interfacial effects, with Kline et al.[67] showing that for the slag network to incorporate B as B_2O_3 it must be charge compensated, where Ca can perform this role.

Paper 4[10] investigates how the simultaneous mass transfer of Ca affects the mass transfer of B between liquid silicon and SiO_2-CaO slag. The mass transfer of [B] was compared between B-doped Si, with an initial [wt%Ca] of either 0 or 0.7, and SiO_2-CaO slag (45:55 mass ratio) at 1873 K. 2 parallels were performed for each initial [Ca] concentration, with each kinetic series consisting of 6 different holding times at 1873 K, of 5, 8, 12, 20, 30, and 60 min, in graphite crucibles under an Ar 5.0 atmosphere. Each crucible was subsequently rapidly cooled, metal was separated from the crucible and slag, to then be crushed in a wolfram carbide puck mill, and analyzed for its [Ca] and [B] content by ICP-MS.

Statistical analysis was used to show that there was no significant kinetic effect from the initial Ca content of the alloy on the mass transfer of B from Si to the SiO_2-CaO slag, at a 95% confidence.

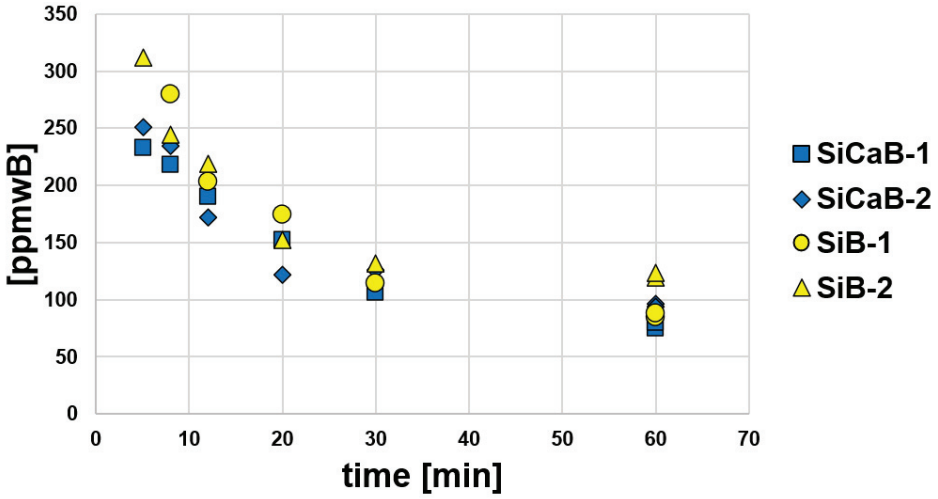

(a)

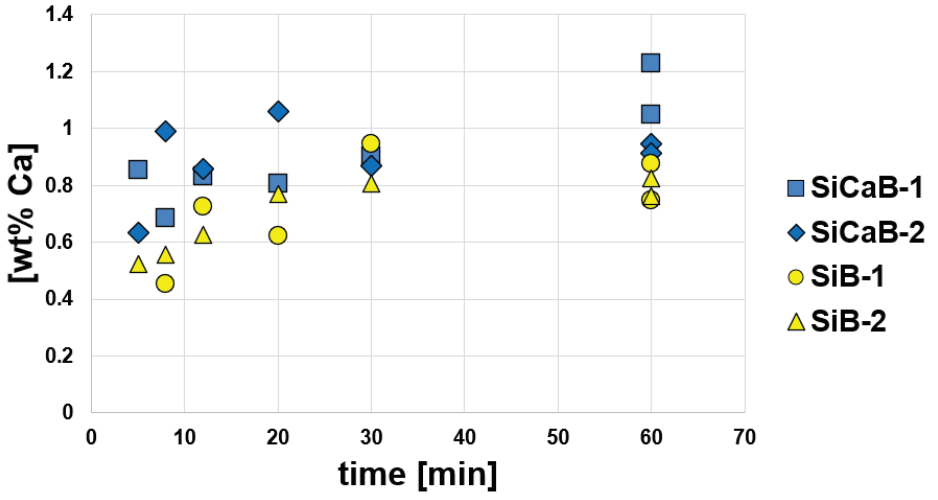

(b)

Figure 3.7: Measured **a)** B and **b)** Ca concentration in liquid silicon as a function of time. Marker color denotes the alloy, and marker shape denotes the parallel. Measurement data can be found in B.2. Based on figures from Bjørnstad et al.[10].

3.2.2 Experimental Work

The execution is was similar to than in section 3.1.2.1, except with different materials. Two silicon alloys with different amounts of B, 300 and 360 ppmw respectfully, were synthesized by a similar process to that in B.3, where the 300 [ppmwB] alloy had an additional 0.7[10] [wt%Ca] alloyed in. A master slag, consisting of 45 (wt%SiO_2) and 55 (wt%CaO), was produced by repeatedly melting and crushing pure oxides to ensure homogenization. The slag and metal were held at 1873 K for 5, 8, 12, 20, 30, and 60 min. 2 parallel kinetic series were performed with each Si alloy. 10g of both alloy and slag were used.

3.2.3 Results and Discussion

The kinetic series for both [Ca] and [B] can be seen in figure 3.7, where they exhibit similar but opposite exponentially decaying behaviors. After 30 min the concentrations have mostly converged, regardless of initial composition. Literature values for the distribution coefficient between slag and metal, L_B=(wt%B)/[wt%B], at 1873 K are about 2 to 2.1[57]. Assuming no external losses of B, the silicon contains around 100 [ppmwB], and the slag about 200 to 240 (ppmwB), depending on the initial [B] concentration, giving L_B values close to that in the literature.

This can be shown more rigorously by using the same statistical methodology as in section 3.1.3, with the model in equation 3.1. The metal to slag mass transfer expression can then be expressed as in equation 3.8.

$$[\text{ppmwB}] = [\text{ppmwB}]_\infty + ([\text{ppmwB}]_{in} - [\text{ppmwB}]_\infty) \cdot \exp\left(-\frac{t}{\tau}\right) \tag{3.6}$$

$$\frac{[\text{ppmwB}]}{[\text{ppmwB}]_{in}} = \frac{[\text{ppmwB}]_\infty}{[\text{ppmwB}]_{in}} + \left(1 - \frac{[\text{ppmwB}]_\infty}{[\text{ppmwB}]_{in}}\right) \cdot \exp\left(-\frac{t}{\tau}\right) \tag{3.7}$$

$$\tau \approx \text{Constant}$$

$$\Rightarrow \hat{C}_{[B]} = \theta_1 + (1 - \theta_1) \cdot \exp(-\theta_2 t) \tag{3.8}$$

[10] 0.7 [wt%Ca] is close to the equilibrium concentration of Ca in Si, in contact with the said slag[57].

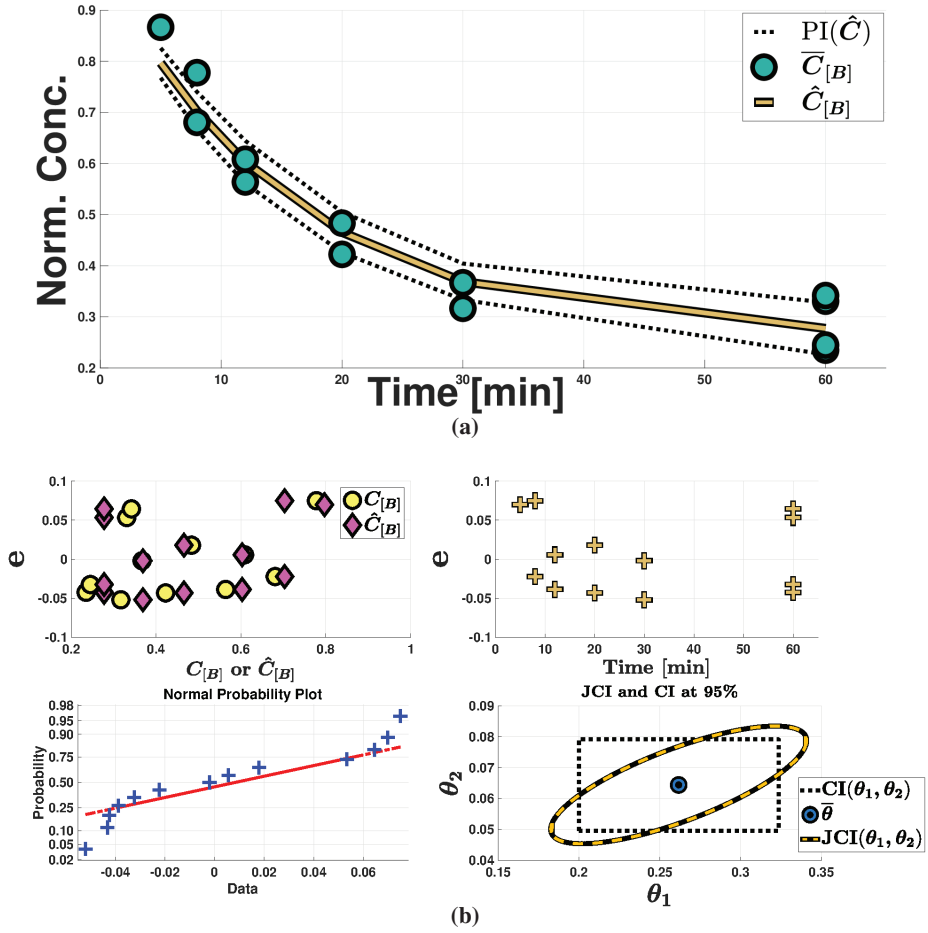

Figure 3.8: a) Estimated and measured responses with a 95% prediction interval with respect to the normalized [B] concentration for the SiB alloy. Both replicate sets have been combined and are treated as a single set. **b)** Regression performance indicators which show that the regression is valid. The two upper graphs show that the residuals are random with respect to the input, and the estimated and measured response. In the lower left graph the crosses follow the line, but curve towards the edges. This does not impact the other performance indicators, so even though the residuals cannot be said to be entirely normally distributed, but the task at hand does not require high precision, so it is an ok approximation in this specific case. The lower right graph shows the joint confidence intervals of the model parameters. This interval does not contain zero, thus being significantly different than zero, it does show high elliptical eccentricity, indicating high parameter covariance. The curvature at the elliptical vertex shows that the covariance is not high enough to invalidate the regression.

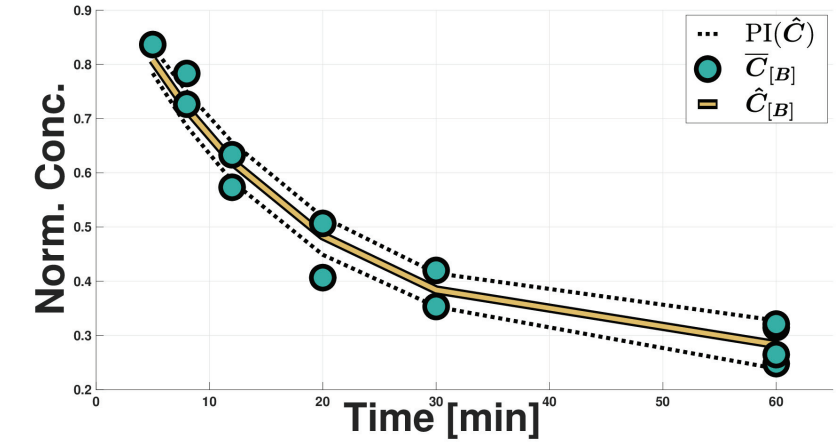

(a)

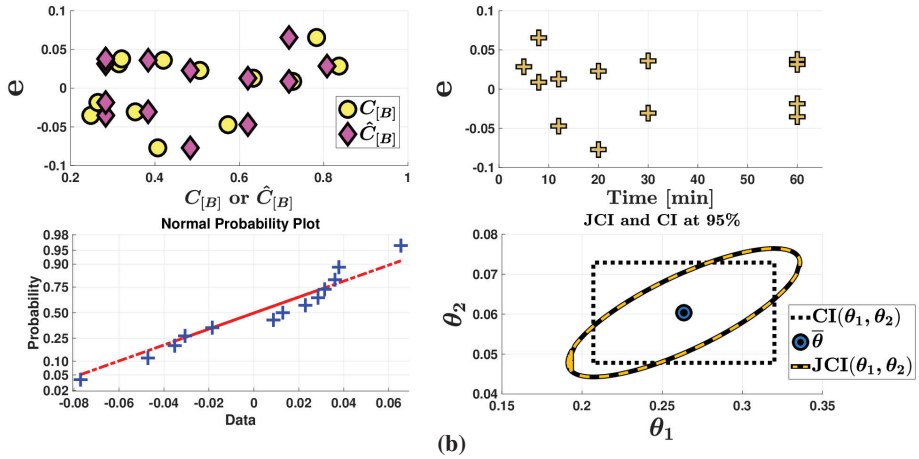

(b)

Figure 3.9: a) Estimated and measured responses with a 95% prediction interval with respect to the normalized [B] concentration for the SiCaB alloy. Both replicate sets have been combined and are treated as a single set. **b)** Regression performance indicators which show that the regression is valid. The two upper graphs show that the residuals are random with respect to the input, and the estimated and measured response. In the lower left graph the crosses follow the line, but curve towards the edges. This does not impact the other performance indicators indicating the residuals are normally distributed. The lower right graph shows the joint confidence intervals of the model parameters. This interval does not contain zero, thus being significantly different than zero, it does show high elliptical eccentricity, indicating high parameter covariance. The curvature at the elliptical vertex shows that the covariance is not high enough to invalidate the regression.

Regression by equation 3.8 for the SiB and SiCaB case, can be seen in figures 3.8(a) and 3.9(a) respectively, with their statistical performance indicators in figures 3.8(b) and 3.9(b). From figures 3.8(b) and 3.9(b) it can be noted that the joint confidence intervals (JCI) (lower right graph) for both regressions overlap to such an extent that further analysis is deemed superfluous, and it can be stated to a 95% confidence (the JCI confidence) that they are similar. However, this might be due to the amount of B being too low, such that the effect size becomes lower than the statistical resolution of the experiment.

It is well documented that the activity of [Ca] is strongly affected by the Fe content in FeSi[4]. Since charge compensation is needed to incorporate (B_2O_3) into the slag network[67], the dynamic mass transfer effects documented by Krystad et al.[66] may instead be due to differences in the calcia availability on the slag surface, which is related to the [Ca] activity[11], than an increase in the interfacial area. This would not occur in the current experimental work, as the [Ca] activity will be similar for both alloys.

3.2.4 Conclusions and Industrial Implications

The effect of simultaneous Ca mass transfer on the kinetics of boron mass transfer from Si to a 45 (wt%SiO_2) and 55 (wt%CaO) slag was investigated experimentally.

1) It was found that the boron transfer was not significantly affected by simultaneous mass transfer of Ca to a 95% confidence.

2) After a holding time of 30 min, the concentrations of both [B] and [Ca] have mostly converged, regardless of initial composition, with B converging towards the L_B predicted by the literature ($\approx$2–2.1).

3) For the industry, this means that the mass transfer of Ca will not alone change the dynamic surface area between slag and alloy to such an extent that the B mass transfer is significantly affected.

[11] Combine R4) and equation 2.6.

3.3 Oxidative Refining of Metallurgical Grade Silicon: Lab-scale Measurements and Description of Ca and Al Mass Transfer

3.3.1 Summary

Paper 5[11] contains experimental work aiming to reproduce similar refining behaviors as in industrial oxidative ladle refining (OLR) of metallurgical grade silicon (MG-Si), at lab-scale. The experimental work was conducted by purging synthetic alloys with synthetic air for 15 min at 1873 K, with alloy samples being taken after 0, 5, 7, 10, and 15 min. 5 different alloy compositions were used, with the chosen compositions forming a 2^2 factorial design, with center-points and a replicate set. In total 11 measurement sets were performed. From the experimental measurements, paper 5 proposes that the refining progression in OLR occurs in three overarching stages. Before the purge gas is initiated, surface oxidation is seen from the alloy reacting with latent oxygen in the atmosphere through the melt surface. This forms a protective oxide layer which pacifies the surface, stopping further surface oxidation, which favors reducing the amount of dissolved calcium in the melt [Ca], by forming SiO_2-CaO-Al_2O_3 slags with higher calcia contents. After gas purging is initiated, the refining behavior becomes controlled by slag formation on the gas bubbles, as the refining shifts to favor the production of more slag. Towards the end of the refining process, the amount of slag accumulated in the ladle becomes so high that a global equilibrium between the slag and alloy is established. At this point, the melt composition should be close to the target composition, as any compositional changes from this point on carries with it an exponentially compounding product loss (Si alloy), negatively impacting the profit margin. In comparing lab-scale and industrial measurement data, paper 5[11] uses a novel method for normalizing vectors in ternary space, allowing the refining behaviors to be compared separately, accounting for the statistical resolution of the lab-scale experiments by limiting the scope. The analysis shows that the lab-scale and industrial measurement data compare favorably under similar operating conditions. A thermodynamic model running FactSage[56] was also employed to help explore the slag behaviors, indicating the importance of the oxygen "source", i.e. oxygen in the gas versus that of oxides in the slag, for how the refining occurs. The paper also includes a ternary solute diagram of Ca and Al in equilibrium with a SiO_2-CaO-Al_2O_3 slags at 1873 K, calculated using a [Ca] activity coefficient at infinite dilution from Jakobsson and Tangstad[60].

3.3.2 Experimental Work and Kinetic Model

3.3.2.1 Experimental Work

Experiment Setup

An induction furnace setup represented schematically in figure 3.10, with dimensions of major components in table 3.6, was utilized for the experiments. A graphite crucible, clad in graphite wool, was used to facilitate even heating. An inner quartz crucible was used to separate the liquid alloy and the graphite crucible. A thin layer of refractory cement was poured into the graphite crucible ensuring that the two crucibles were properly aligned, with a thin layer around the quartz crucible, securing it in place. It was found that the quartz crucible could be replaced by a quartz tube (similar dimensions), capped towards the bottom of the graphite crucible with a 1 cm layer of refractory cement. It should in theory be possible to only use refractory cement, but it is not trivial to fully line the graphite crucible and leave enough room for the charge, while retaining a strong clean wall lining. The cement used was a mullite-based low-cement supplied by Pyrotek Scandinavia AB, able to withstand the combination of molten silicon and air at high temperatures without any significant reaction between the cement and silicon alloy[12]. As an extra precaution, all initial target alloy compositions contained at least one measurement set with a full quartz crucible. This allows the two cases to be statistically tested for potential consistent deviations afterwards, where no significant consistent effect was found to a 95% confidence.

A lid was placed to cover the furnace opening, as illustrated in figure 3.10, while resting on mineral wool. This mineral wool served many a purpose, from providing a tighter seal between the furnace and lid, allowing the thermocouple wire to rest safely, to catching small metal droplets that erupt from the melt while purging. The lid served as a multipurpose platform, from securing the lance, funneling fumes, and shielding both melt and operators. The lance was fastened to the head protruding from the lid body, on a detachable top, by a 9 mm ring clamp beneath, and a 10 mm industrial wire clamp (normally used for restraining steel cable) above the detachable top. This configuration did not put the lance under too much stress (SiC is very brittle) while still heavily restricting its movement. Two holes were placed on the lid's body, one for taking samples (D: 40 mm), and the other for allowing fumes to escape.

[12]This cement was chosen after lengthy dialog with the supplier, as it should be able to withstand the combination of molten silicon and air at high temperatures without any significant reaction between the cement and silicon alloy. Its use in a lab scale environment necessitated different processing, handling, and curing than in the industrial case. To ensure proper use and consistent performance, any use of the cement in this work was done based on instructions from the supplier

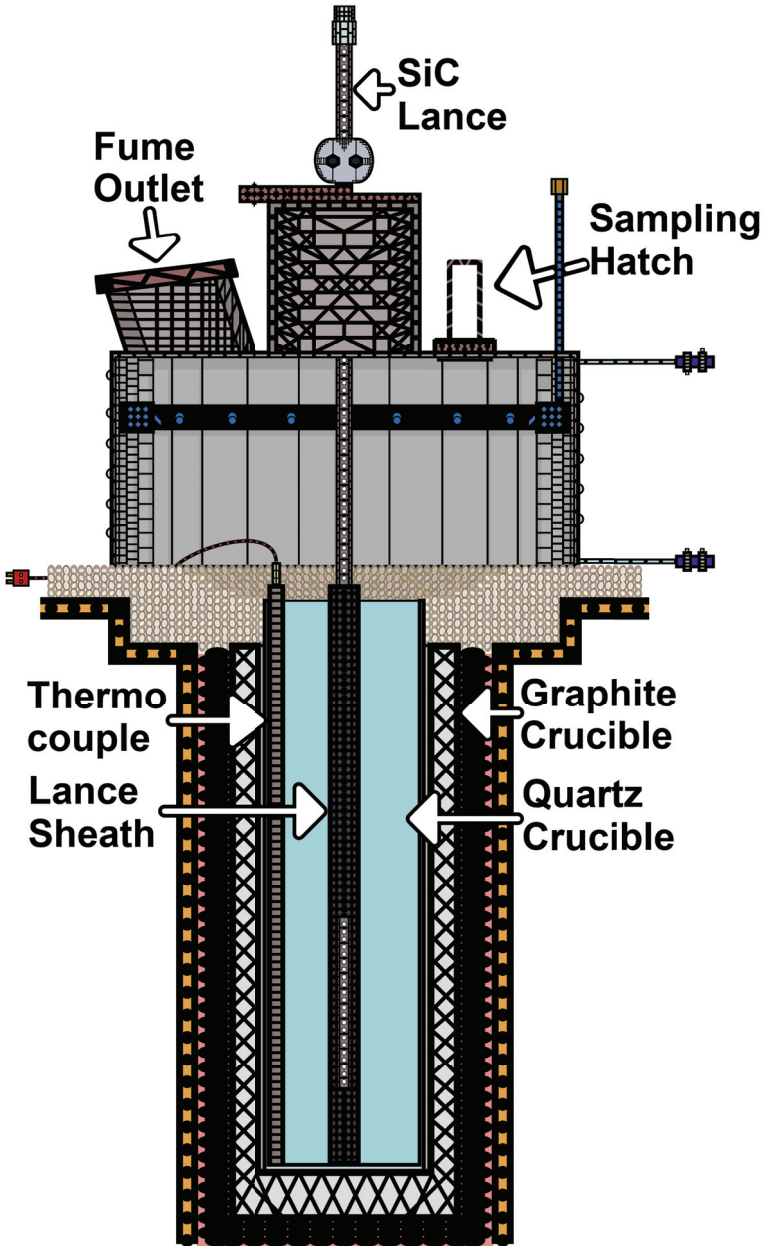

Figure 3.10: Schematic representation of the relevant parts concerning the experimental setup described in this section. An effort has been made to make sure that the sizes are consistent relative to each other. Dimensions of different components can be found in table 3.6. From Bjørnstad et al.[11].

Table 3.6: Dimensions [mm] of the major components used in the experimental setup.

Component	OH	IH	OD	ID
Gr. Crucible	400	370	150	115
Qrtz. Crucible	380	375	105	100
Lid	140	135	310	305
Lid Head	100	100	100	90
Fume Outlet	60	60	95	83
SiC Lance			9	6
Gr. Sheath	380	330	20	10
SiC Sheath	380	377	9	6
Qrtz. Tubes	330	330	6	3

The fume outlet was kept open, as silicon production/refining fumes heavily. To reduce the effect of atmospheric oxygen, an argon gas shield was mounted underneath the lid body. This shield consisted of 16 evenly spaced nozzles on a ring, angled towards the melt. 4 NL(1bar, 298K)/min of Ar 5.0 was continuously purged onto the crucible throughout the heating, alloying, and sampling process. The whole system was water-cooled to reduce thermal wear.

A SiC tube, designed as a cover for high performance temperature sensors in high-temperature high-purity alloys, was used for the lance. From the literature on aeronautics[68][69][70], it is expected that a protective layer of SiO_2 will form when SiC and O_2 are in contact at high temperatures, reducing its deterioration rate. The lance rested inside a graphite sheath during heating. As the lower portion of the charge melted first, it caused the top portion to collapse, subjecting the lance to unwanted stress. These stresses also occurred during alloying, and the sheath protected the lance not only from these stresses, but also insured that the lance tip was positioned properly and removed the possibility of clogging before initiating the purge gas.

Multiple other lance geometries and materials were tried. Overall, it was only the high performance SiC tubes that were able to retain a level of mechanical strength (unlike zirconia, quartz, alumina, and filters of these materials), while being resistant to thermal shock (unlike zirconia) and did not react violently with the melt or oxygen (unlike graphite).

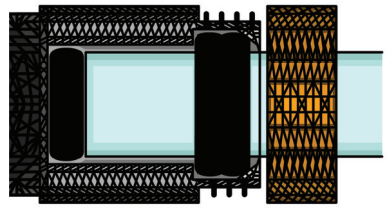

Figure 3.11: Sample tube fastening mechanism.

Temperature was measured by a c-type thermocouple inside the quartz crucible. The thermocouple was protected by an alumina tube, placed inside a SiC tube of similar material as that of the lance, with the top covered by cement, and wires protected with thermal plastic. These thermocouples still failed at a high rate, so they were only used for a maximum of two experiments each, together with their shielding, as previous tests showed an unacceptably high risk of failure after this point.

Quartz tubes were used to extract samples from the melt, with the tubes fastened to a sampler made with steel gas tubing and gas pipe connectors packed with O-rings. A normal rubber bulb (Peleus-ball) provided and under-pressure to facilitate rapid sample extraction. Sampling had to occur quickly, as the samplers could not endure prolonged exposure to the melt, with the quartz tubes degrading quickly in contact with the melt, or in its close vicinity. To facilitate rapid sampling, a fastening mechanism between the quartz tubes and samplers was designed, seen in figure 3.11. Figure 3.11 shows the quartz tube being held by O-rings resting on a shelf which curves up slightly towards the quartz tube, holding the O-rings in place such that they do not jam, with an O-ring at the bottom to cushion the quartz tube during insertion. The commercially available fastening mechanisms between glass tubes and steel piping are designed to achieve a tight seal, and not to allow the two to be separated quickly. This new design provides a seal which is tight enough for sampling, allows rapid extraction of the quartz tube without damaging it, and can be efficiently operated while wearing protective equipment.

The raw materials and alloying agents used can be seen in table 3.7, with the SiCa-alloy covered more in depth in B.3.

Table 3.7: Raw material and alloying materials used in the experiment. The relative standard deviation (RSD) noted for the SiCa-alloy came from 3 replicate meta-samples, made by crushing 0.5g from 5 different SiCa-ingots together, all of which had a similar target concentration.

Material	Purity	Notes
Silicon	≥99.999 wt% (5N)	Used as bars (L: 100-200 mm, W: 30-50 mm)
SiCa-alloy	2.80-5.20 wt% Ca ± 0.073 wt%	Produced as approx. 600g ingots. Sample RSD, with n = 3
Aluminum	≥99.0 wt% (2N) [wt%Ca]<0.05	Food grade aluminum foil[13]

Table 3.8: Table listing the randomly generated experiment order, and the target wt% of dissolved Ca and Al in the liquid silicon for each experiment.

Replicate	1	1	1	2	2	1	2	1	2	2	3
$[wt\%\text{Ca}]$	0.5	0.5	1	0.5	1	1.5	1.5	1.5	0.5	1.5	1
$[wt\%\text{Al}]$	0.5	1.5	1	1.5	1	0.5	0.5	1.5	0.5	1.5	1

Execution

The thermocouple and graphite lance sheath were positioned inside the crucible, and kept in place by smaller pieces of silicon, followed by larger silicon bars. Target alloy compositions are listed in table 3.8, with the estimated composition in B.4. The charge was adjusted such that it should total 3000g in the end, as the SiCa-ingots did vary in Ca-content.

The crucible was heated to the melting point of Si (≈1685 K) over 30-40 min. When fully molten and T > 1753 K, the alloying elements were added. This temperature was more used as a guide to discern the correct power setting for the furnace, as it had to be high enough to melt the alloying agents quickly, but still not so high that the temperature would spike when the alloying agent became molten. The alloying process itself took between 15 to 30 min, depending primarily on alloying amount.

[13] EU standard EN 602:2004, 2nd ed., Accessed 21.09.2020 from Standard Norge as Norwegian Standard NS-EN 602:2004.

It was especially important to submerge the aluminum-foil quickly to limit oxidation, which was accomplished by wrapping the foil around chunks of SiCa-alloy, shown in figure 3.12(a). No noticeable amount of foil was seen after it became submerged.

After alloying the temperature was increased to 1873 K. At 1873 K, an initial sample was taken, the graphite sheath covering the lance was removed, and the purge gas was initiated before the lance was lowered into the liquid alloy. The purge gas consisted of synthetic air ($\{mol\%O_2\}$=21), and was delivered at 2 [NL(1bar, 298K)/min]. As the lance was inserted into the melt it would immediately start to bubble and fume, with small molten droplets ejecting from the surface from time to time, reminiscent of an industrial ladle. A clearly visible slag phase forming on the surface was seen in some of the experiments. Alloy samples were taken after 5, 7, 10, and 15 min, and if replicate samples were taken, multiple samplers would be used to reduce the time between each replicate. To attain representative samples, the quartz tubes were plunged deep into the melt and lifted upwards in a controlled fashion while extracting. From each sample between 0.3-1.5g alloy was extracted, with such a sample shown in figure 3.12(b) after the quartz tube was removed, and before it was crushed to a power in a wolfram carbide puck mill. To avoid cross contamination, the milling chamber and puck were cleaned after every sample, firstly by brush and pressurized air, and subsequently with ethanol. After crushing, 0.3-1g was sent for analysis by ICP-SFMS, which in the case of dissolved Ca and Al in Si, allows for a higher measurement sensitivity than regular ICP-MS by employing a sector field (SF) to "double-focus".

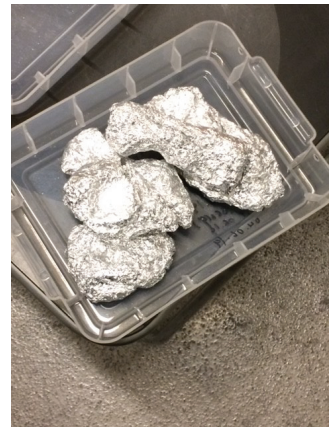

(a)

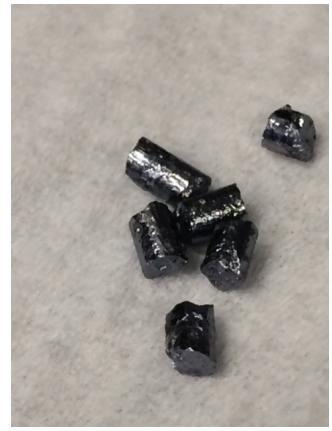

(b)

Figure 3.12: a) Chucks of SiCa-alloy wrapped in aluminum foil. **b)** Alloy samples extracted from the sampling tubes.

3.3.2.2 Model Overview and Predicted Behavior

A thermodynamic model was constructed to explore how a simple melt/slag/gas system responds to different initial conditions, and indicate which conditions are necessary to attain specific refining effects. The model was run in FactSage 7.3[56] in the Equilib module's macro processing environment using the FactPS and FT-oxid databases, including a costume database which replaced FT-lite's activity coefficient at infinite dilution at 1873 K to $\ln(\gamma^{\circ}_{[Ca]})$=-7[60]. Model parameters were tuned using a non-linear statistical model validation algorithm, minimizing the model residual sum of square error, using the "fminunc" environment in Matlab 2019b. The thermodynamic model considered three different processes to occur in the given order at each time step:

R1) Reaction between part of the Si-alloy and the gas bubbles.

R2) Reaction between part of the Si-alloy and the slag/inclusions.

R3) Homogenization of the Si-alloy.

The primary assumptions made are that all the slag/inclusions are at equilibrium with each other and with part of the Si-alloy, all reactions are performed at equilibrium, all oxygen that is purged into the liquid alloy is consumed, all of the slag/inclusions remain in the liquid alloy, and that all three reactions occur within the same time interval at every time step. More specific detail on the model is provided in the paper[11].

The most impactful result from the modeling work was how different the model behaved, depending on which phase acted as the oxygen source. If the initial amount of slag in the ladle is low and silica poor, then the tuning algorithm favored solutions where the purge gas was the primary oxygen source. This resulted in new slag constantly being produced, which would be of a different composition to a slag in global equilibrium with the alloy, keeping the alloy from attaining equilibrium with the slag. As more slag was formed, the reactions between the bulk slag and alloy became more dominant, indicating that a global equilibrium between the bulk slag and alloy would eventually be attained. If large amounts of silica were initially present in the crucible, the tuning algorithm instead favored solutions which favored reactions between the silica and alloy, throttling any refining performed by the purge gas, except for producing a small amount of pure silica. This resulted in a case where the refining would only be controlled by the bulk slag, and would slowly move towards a global equilibrium between the bulk slag and alloy. These two cases show how the slag and purge gas compete for control over the overarching refining of the alloy, but that they move towards the same final state, a global equilibrium between the bulk slag and alloy.

3.3.2.3 Solute Equilibrium Diagram

The tuning algorithm could not find any plausible solutions using only commercially available databases with FactSage 7.3[56]. This experience is shared by several previous authors[71][60][72], which indicate that the activity coefficient of Ca at infinite dilution in liquid silicon, is not correct at high temperatures. A new custom database was created using the activity coefficient from Jakobsson and Tangstad[60] at 1873 K, $\ln(\gamma^{\circ}_{[Ca]})$=-7, which resolved the problem. With the new database, a new solution diagram for Ca and Al dissolved in Si and in equilibrium with a SiO_2-CaO-Al_2O_3 slag at 1873 K was calculated. This diagram can be seen in figure 3.13.

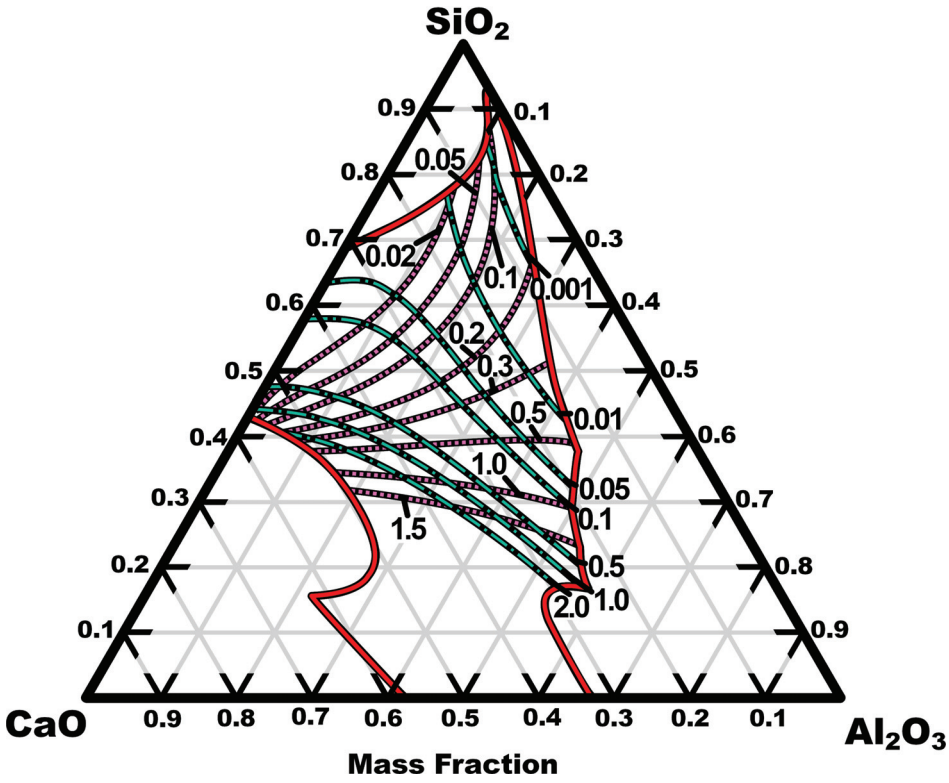

Figure 3.13: Solution diagram for Ca and Al dissolved in Si(l), where the silicon alloy is in equilibrium with a SiO_2-CaO-Al_2O_3 slag, at 1873 K. The dissolved concentrations of Ca(blue line with dot) and Al(pink stippled lines) are in wt%. From Bjørnstad et al.[11].

3.3.3 Results and Discussion

The measured alloy compositions throughout the refining cycle, with respect to Ca and Al, are shown in context of their equilibrium SiO_2-CaO-Al_2O_3 slag composition in figure 3.15. This summary will mainly cover the general overarching behaviors, with the behavioral deviations being covered in greater detail within paper 5[11].

In figure 3.15 there is a clear discrepancy between the initial target (□) and measured (⬡) compositions. This deviation is presumed to be the result of surface oxidation, resulting from surface reactions between the alloy and atmospheric oxygen, during alloying and subsequent heating. A protective silica layer will first form, to then react with dissolved Ca and Al to a SiO_2-CaO-Al_2O_3 slag. As the slag composition becomes lower in silica it disrupts the slag structure[5], and the pacifying effect of the surface layer is reduced[73]. To regain full surface passivation the surface layer grows thicker, where the thickness is a function of the surface slag composition, which depends on the alloy composition. This results in the pre-purging refining effect being directly correlated with the target alloy composition, which is seen in figure 3.14. A comprehensive statistical investigation of the behavior of this effect can be found in A.6.

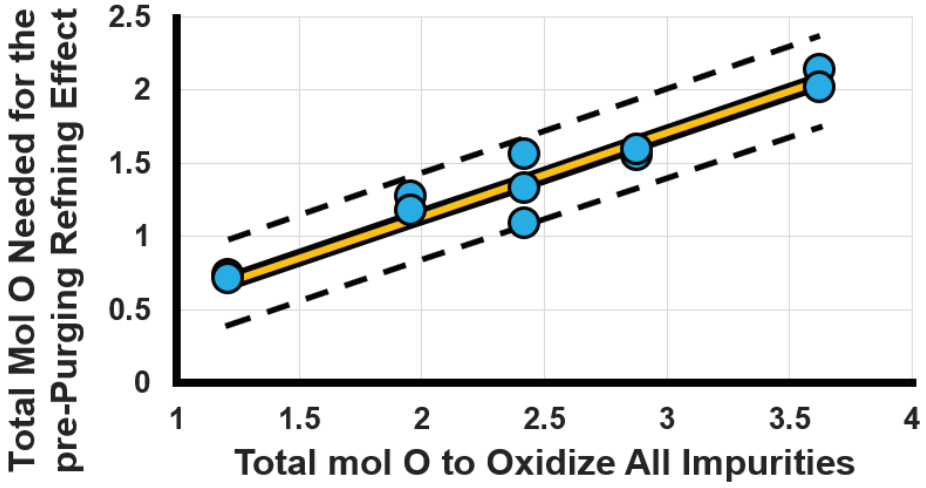

Figure 3.14: Linear regression, where $\hat{y}=b_1x$, $b_1=0.568$ with 95% CI $[0.534,\ 0.602]$. Full yellow line shows the regression, with its 95% prediction intervals as stippled black lines. From Bjørnstad et al.[11].

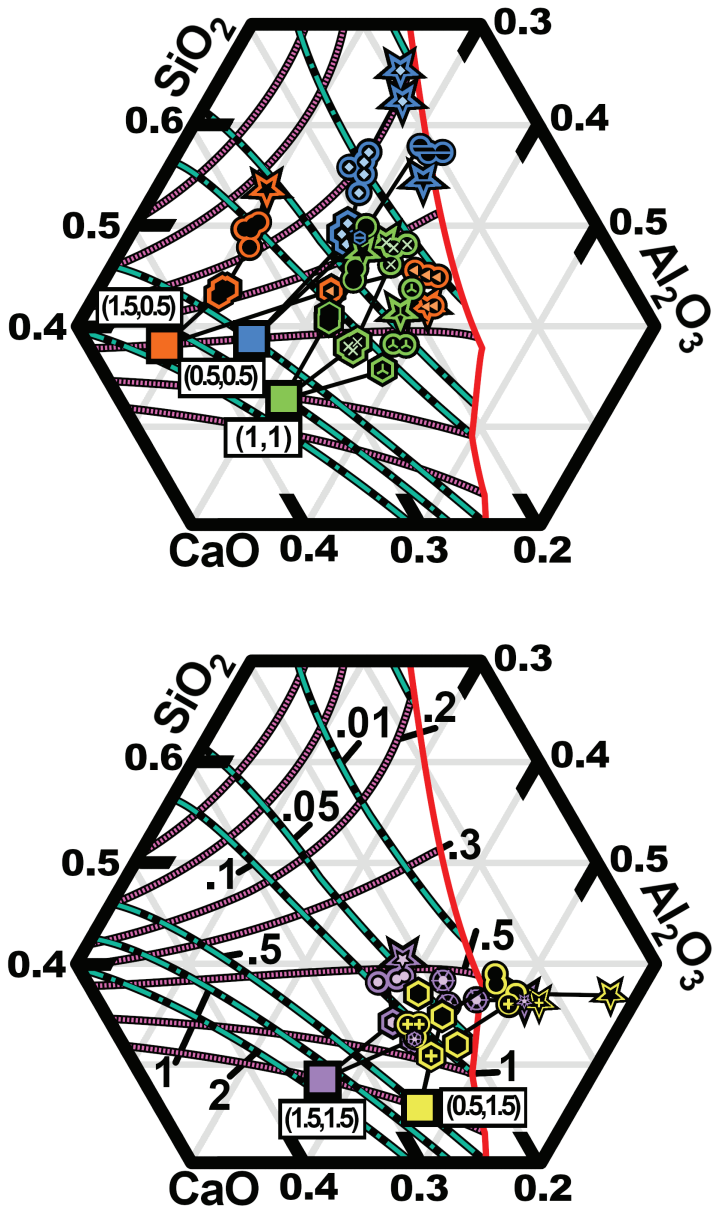

Figure 3.15: Measured alloy compositions [wt%] with respect to Ca and Al throughout each refining cycle, as if in equilibrium with a SiO_2-CaO-Al_2O_3 slag at 1873 K. Iso-concentration lines for dissolved Ca (blue line with dot) and Al (pink stippled line) are from figure 3.13. Each measurement set is color coded according to, and marked with, its initial target concentration. □ represent the target initial concentrations, while ⬡ and ⋆ mark the measured initial and end concentrations respectively. Every other sample during the refining cycle is marked with a ○. Experimental data can be found in B.4. From Bjørnstad et al.[11].

From the modeling work, it follows that the refining behavior is a combined effect between the reduction of [Ca] and [Al], and the production of SiO_2-CaO-Al_2O_3 slag. This is expressed in figure 3.15, as the measured refining behavior can be thought of as a change in the composition of an imaginary slag, which is always in equilibrium with the alloy. The change in the composition of the imaginary slag thus reflects the actual slag being produced, as this is what causes said change. Figure 3.15 shows that a decrease in the [Ca] concentration is reflected by a decrease in the calcia concentration of the imaginary slag, which must result in an increase in the amount of calcia in the real bulk slag. Increasing the amount of silica in the imaginary slag represents a reduction in both [Ca] and [Al], which in OLR can only be accomplished by producing more silica. Thus, an increase in silica for the imaginary slag can be thought as representing the production of more real slag. Alumina is an amphoteric oxide, which can be seen by how the iso-concentration lines of [Al] in figure 3.13 are more similar to that of the iso-concentration line of calcia than alumina at [wt%Al]$\geq$1.0, while [wt%Al]$\leq$0.5 has iso-concentration lines behaving closer to those of alumina. This means that increasing/decreasing the amount of alumina in the imaginary slag will reflect different refining behaviors depending on the amount of [Al], where the divide will be shown to occur approximately at [wt%Al]$\geq$1.0. These relations are summed up in table 3.9.

Table 3.9: Relations between an imaginary slag in equilibrium with the measurement sets, and the real slag in the crucible.

Imaginary Slag			Real Slag	Notes	
Δ(wt%CaO)	$<$	0	$\Delta m_{(CaO)}>0$		
Δ(wt%Al_2O_3)	$<$	0	$\Delta m_{(Al_2O_3)}>0$	if [wt%Al]	<1
	$>$	0			≥ 1
Δ(wt%SiO_2)	$>$	0	$\Delta m_{(SiO_2)}>0$ $\Rightarrow m_{Slag}>0$		

Normalized Ternary Vector Representation of the Measured Refining Behaviors.

To describe the general refining behaviors seen from the measured sets in figure 3.15, the compositional change in the imaginary slag can be displayed as ternary normal vectors. This allows the measured sets to be compared by their change in imaginary slag composition, as this change reflects the formation, growth, and accumulation of the real bulk slag.

In practice, normalizing the ternary vectors describing the compositional change of the imaginary slag consists of taking the black lines between the points in figure 3.15, normalizing them to all be of equal length, while retaining their direction (angle and sign). It is also useful to displace them such that they all originate at the same point, as this makes it easier to compare their specific directions, and most crucially allows for the discussion of behavioral similarity between the measurement sets. Figure 3.16 will be used to compare the normalized vectors, and while it will be covered in brief here, it, along with a detailed description of how ternary vectors operate, is covered in A.7.

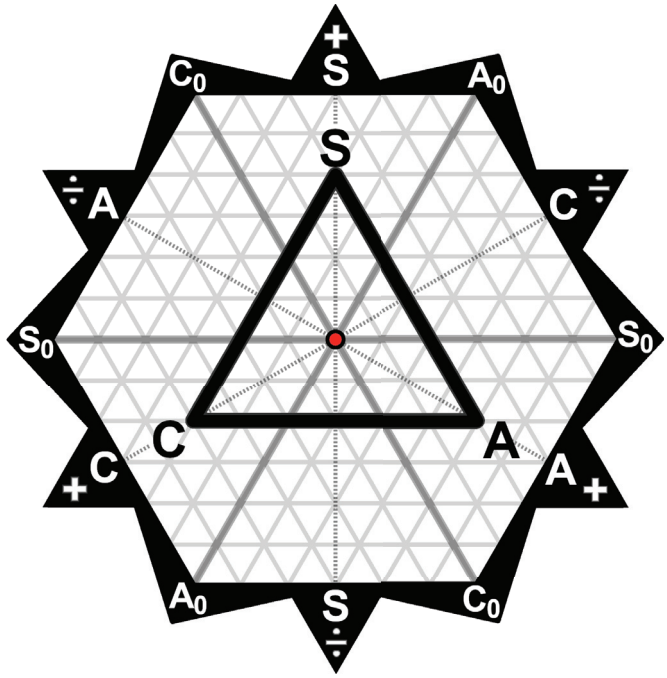

Figure 3.16: Diagram for describing what compositional changes a ternary SCA (SiO_2-CaO-Al_2O_3) vector describes, here a SCA ternary phase diagram has been placed in the center to show how the two diagrams relate. The protruding arrow denoting the species which controls the general direction and sign, with the border providing an indication of the size of the fraction between the two other subservient species. S_0, C_0, and A_0 are the iso-concentration lines of the given species (SiO_2-CaO-Al_2O_3). From Bjørnstad et al.[11].

The properties of the ternary space a ternary phase diagram inhabits allows any straight line to be uniquely denoted by the change in one of the slag species, and a constant fraction between the two others. Thus, a straight line in a ternary phase diagram can be said to have a species which "controls" the overarching movement direction, or in the terms of figure 3.16, determines which of the hexagonal segments the vector falls into, marked by the outermost protruding arrowheads. The hexagonal shape comes from there being 3 possible commanding species (SCA), and that they can either increase or decrease (+,÷), giving 6 distinct behaviors, which in 2D requires a hexagon. This makes it easier to see the differences in the relative compositional change between normalized ternary vectors, all originating from the center of the diagram. Inside each hexagonal section the specific direction is determined by the ratio between the two remaining "subservient" species. This ratio/fraction is constant and can take any positive value, but the mathematics simplify greatly if the ratio is restricted to values of 1 or greater, by always making the subservient species which sees the largest change (the "dominant") the numerator, and the subservient species which sees the least change as the denominator. In figure 3.16, each hexagonal slice is subdivided by a stippled line, which shows where the ratio is equal to 1, where each subsection is marked by its respective dominant species, and contains white arrowhead showing which direction increases the ratio with respect to said dominant species.
While the diagram contains a great deal of information shown in A.7, for the measured refining behaviors it must also be noted that changes in the calcia and silica concentrations in the imaginary slag from table 3.9, are expressed to various degrees by any vector in figure 3.16 within the marked areas in figure 3.17.

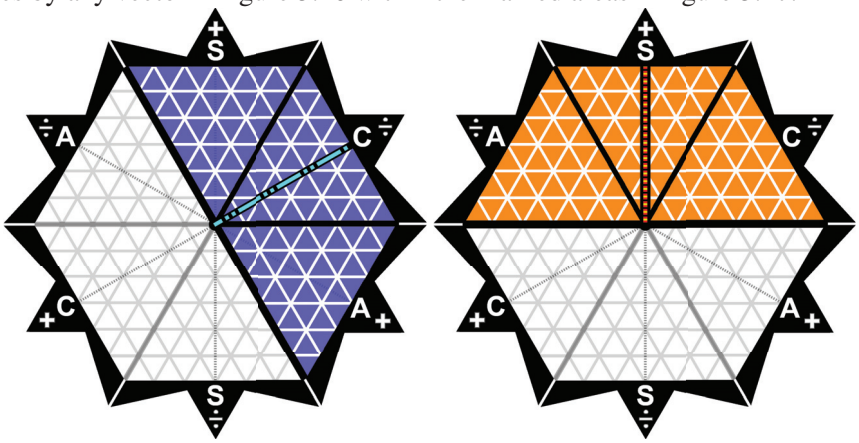

Figure 3.17: a) All vectors within the dark blue area describe a decrease in calcia content, with the decrease being greater towards the central teal spotted line. **b)** All vectors within the light orange area describe an increase in silica content, with the increase being greater towards the central maroon stippled line.

The normalized ternary vectors given by the measured refining sets in figure 3.15 can be divided into 3 distinct general refining behaviors, where vectors showing the same general refining behavior have been combined for the sake of simplifying the upcoming figures. Figure 3.18 shows the initial behavior, where all of the measured sets exhibit an initial general behavior favoring a decrease of calcia in the imaginary slag, which amounts to an increasing the amount of calcia in the actual slag. As the duration of the refining behavior is also of interest, each normalized vector has been scaled to show what fraction of the total refining time it represents, with the pre-purging refining effect set to 5 min for each set. This initial calcia controlled behavior is exhibited by the pre-purging refining effect in every set, with the exception of 1 set which lies just within the border of being silica controlled, and coincidentally belongs to one of the (0.5,1.5)[14] sets. All sets additionally show behaviors which suggest that slag is being produced, showing the importance of calcia in the formation of SiO_2-CaO-Al_2O_3 slag, which is consistent with that found in the paper 1[5], and is expected to result in rapid slag growth.

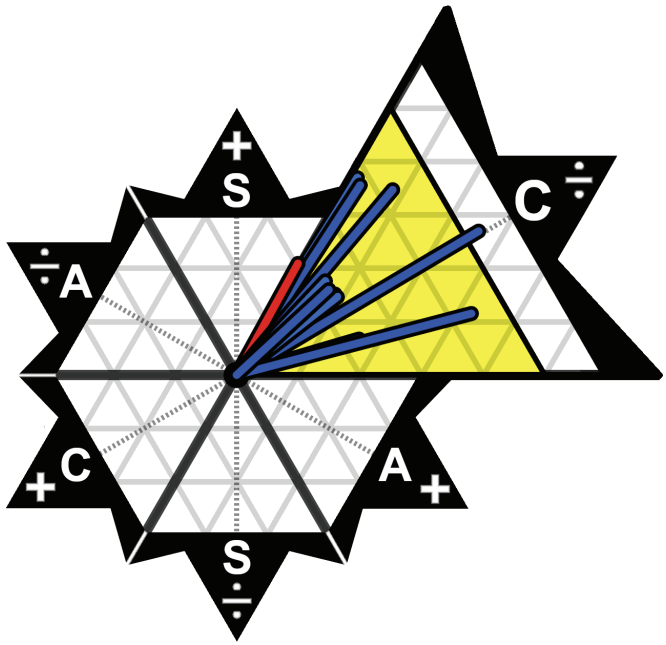

Figure 3.18: Simplified version of figure 3.16, containing the initial refining behaviors from figure 3.15 as normalized ternary vectors, and highlighting the relevant hexagonal slice. The vectors have been scaled to show the relative duration of the refining behavior, with the pre-purging refining effect set to 5 min for each set. All vectors describing the pre-purging refining effect are contained with this figure. Vectors in the calcia and silica controlled sections are colored blue and red respectively.

[14] A reminder that the samples are denoted by their target alloy composition in ([wt%Ca],[wt%Al])

Some sets in figure 3.18 continue to exhibit the calcia controlled behavior also after purging is initiated, but the closeness of these to the silica region suggests that the calcia controlled behavior ends somewhere between the 0 and 5 min samples. The others are deviating sets which are discussed in the current paper[11]. After initiating the purge gas, the refining behavior shifts from being calcia controlled to silica controlled, giving the second refining behavior, seen in figure 3.19.

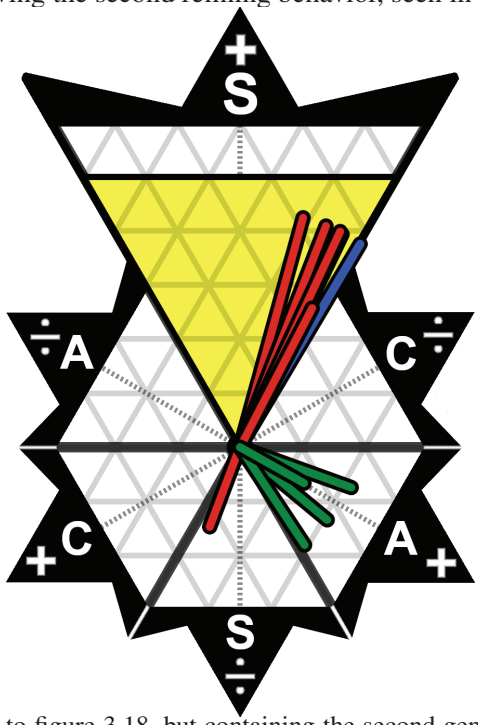

Figure 3.19: Similar to figure 3.18, but containing the second general refining behavior. It must be noted that vector length, here representing relative time, have not been scaled with the highlighted hexagonal slice. Vectors in the calcia, silica, and alumina controlled sections are colored blue, red, and green respectively.

Figure 3.19 shows that when the purge gas is initiated, the refining behavior starts favoring increasing the amount of slag in the crucible. However, the refining behaviors strongly favor the calcia dominant region, indicating that calcia is most important in the formation of more bulk slag, second to silica. Those not in the silica controlled section exhibit an alumina controlled behavior, which is expressed by all of the refining sets which interact with the liquidus line between slag(liq)/mullite, thought to indicate the formation of solid alumina-rich inclusions. Every set where this occurs further refining seems to slow down, which is expected by figure 3.19 as these vector are not within the area shown in figure 3.17 to favor slag formation. The silica decreasing behavior is an outlier, further discussed in paper 5[11].

Towards the end of the refining cycle there seems to be no single refining direction which is favored, as seen in figure 3.20. The modeling work implies that a global equilibrium between the bulk slag and alloy will set in eventually, which should occur when the imaginary slag aligns with the actual slag, thus becoming one and the same. As the sets do not seem to favor any single refining behavior, it is thought that this indicates that the amount of slag in crucible has become large enough to cause a transition from refining by slag formation to refining by global slag equilibrium.

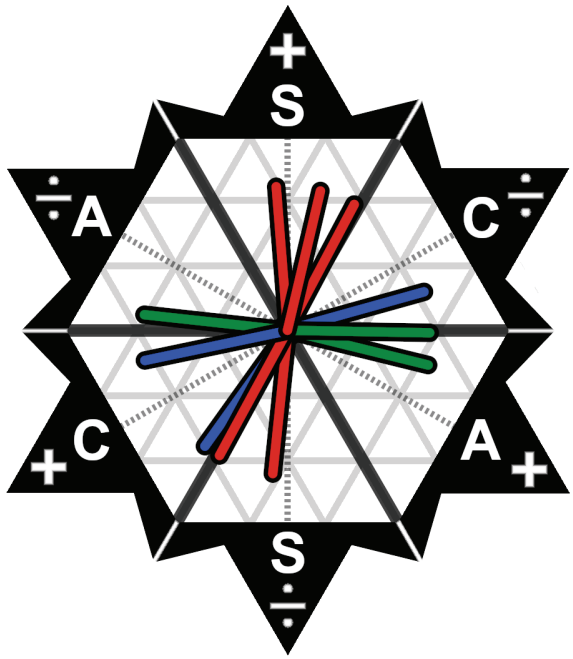

Figure 3.20: Similar to figure 3.18, but containing the final general refining behavior. Vectors in the calcia, silica, and alumina controlled sections are colored blue, red, and green respectively.

This point is of critical importance, as any further changes to the alloy composition will require a change in the global slag composition, resulting in product losses (i.e., excess oxidation of the Si alloy). I.e., the problem becomes that the more slag is present in the ladle, the more slag must be generated to change its composition. To produce this slag, silica is needed, resulting in an exponentially cumulative loss of silicon to silica formation. Preferably, the desired slag composition is reached before the critical slag amount is attained, thus locking the desired composition in place. The industry influence this by adding oxides and changing the temperature.

If a mass balance is performed on the slag formed by the different refining stages, it is clear that the slag formed by surface oxidation cannot share the same composition of the bulk slag. This traps a large portion of the initial [Ca] in the calcia-rich surface slag, which thus does not contribute to the equilibrium bulk slag composition. However, the mass balance suggests that there are unknown interaction effects between the surface and bulk slag, but the specifics of the effects could not be specified by the current experimental work.

The overarching refining behavior seen from the measurements can thus be summed up in table 3.10.

Table 3.10: Description of the refining progression, showing which refining effect, oxygen source, and formation of which slag species dominate the refining path of Al and Ca in MG-Si at a given refining stage. From Bjørnstad et al.[11].

	Time	Start ⟶ End		
	Refining Stage	Start-Early	Early-Late	Late-End
Dominant	**Refining Effect**	Surface Oxidation	Gas Purging	Slag Equilibrium
	Oxygen Source	Latent Oxygen	Gas Bubbles	Slag
	Slag Species	CaO	SiO_2	SiO_2/CaO/Al_2O_3

The Role of Activity

Refining behaviors during the experimental refining sets have been illustrated above without discussing the driving force. Figure 3.21(a) shows the general behaviors from figure 3.15, but with the iso-activity lines for silica and calcia instead of the iso-concentration lines. The figure shows that the refining effects are related to the activity, as most of the refining behaviors move perpendicular to the iso-activity lines of the species given as important for that particular refining stage given in table 3.10.

If the lines perpendicular to the two extreme tangent-lines of the iso-activity lines of silica, calcia, and alumina are drawn at 1873 K, and allow these to serve as confidence regions for the activity-controlled refining behavior, then figure 3.21(b) is generated. The figure shows that almost every vector from the measured refining sets falls within the activity regions of one of the slag species, with most of them falling within the narrow activity regions of silica and calcia. The importance of calcia in the refining of MG-Si is also made clear in this figure, as the regions were calcia sees the least change, close to the C_0 line, is almost vacant of any vectors, and not covered by the activity regions of any slag species.

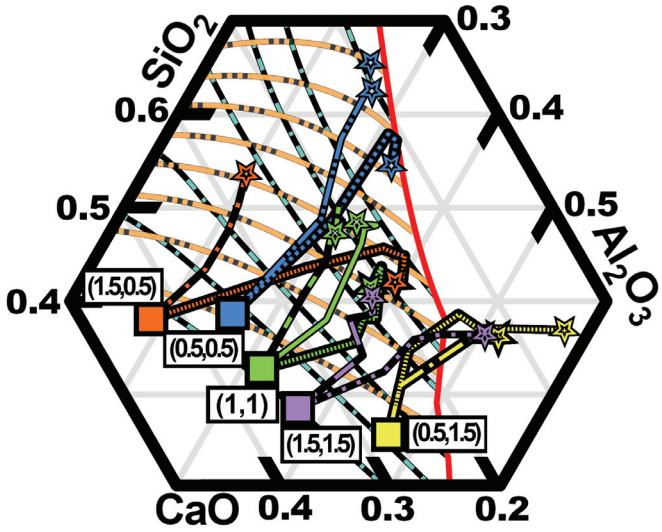

(a)

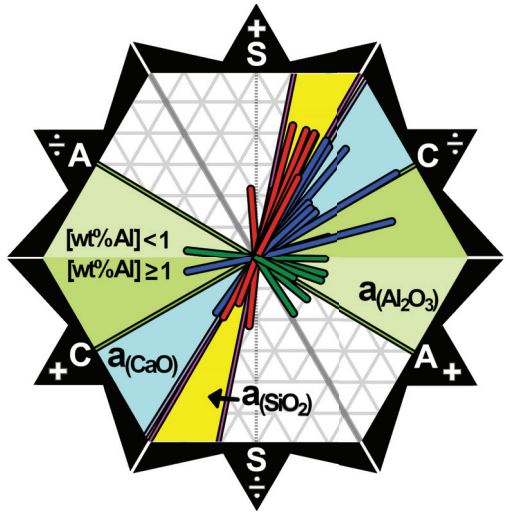

(b)

Figure 3.21: a) Measurements plotted against the activity of SiO_2 (full line with double dots) and CaO (stippled line) at 1873 K. From Bjørnstad et al.[11]. **b)** All of the vectors from figures 3.18, 3.19, and 3.20, together with areas between the two perpendicular lines to the two tangent-lines of the iso-activity lines of silica, calcia, and alumina at 1873 K with the greatest difference. These areas act as confidence regions for an activity controlled refining behavior. Vectors in the calcia, silica, and alumina controlled sections are colored blue, red, and green respectively. The activity region of alumina is divided into two parts, due to its amphoteric nature giving it a wide range for behaviors.

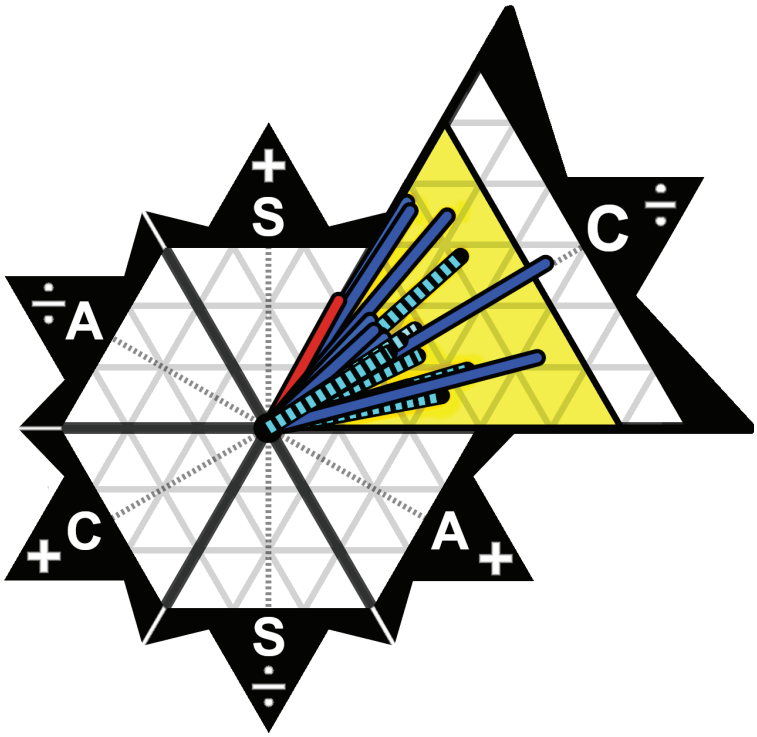

Figure 3.22: Data from an industrial measurement campaign marked with stippled lines, and the measurements from this work in full lines. Lines in blue, red, and green line colors show calcia, silica, and alumina controlled directions respectively, where the hexagonal section housing the most sets in each case is enlarged and highlighted in yellow. Shows the initial refining stage. From Bjørnstad et al.[11].

Industrial Comparison

The measurements in this work were also compared with a large set of data from an industrial measurement campaign, supplied by industrial partners, and can be seen in figure 3.22 and 3.24. Here each set has been normalized with respect to the ternary phase diagram, and each line-segment has been rescaled to indicate what portion of the total refining time it represents. It must be noted that the figure represents the imaginary slag which is always in equilibrium with the alloy. Thus, a reduction of calcia in the imaginary slag represents an increase of calcia in the actual slag, resulting from the oxidation of dissolved Ca in the liquid Si alloy. An increase in the amount of silica represents increasing the amount of slag in the ladle, and the closer the line points towards the (S+) protrusion the more the behavior is controlled by the formation of new slag.

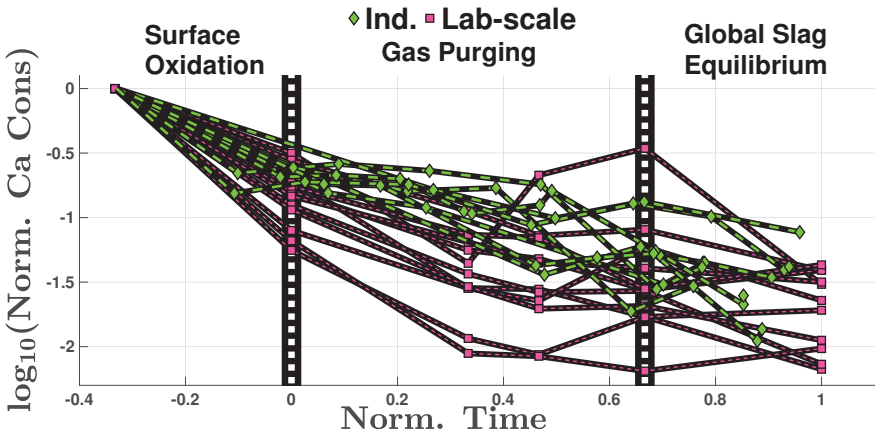

(a)

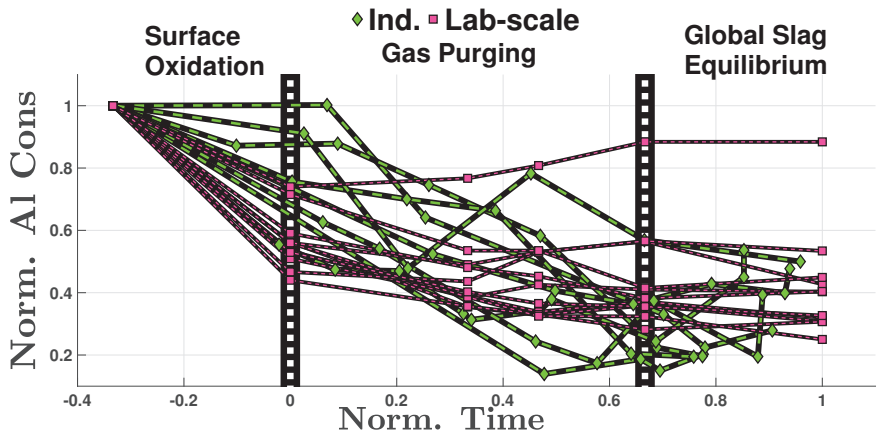

(b)

Figure 3.23: Normalized industrial (green dashed lines) and laboratory-scale (pink stippled lines) refining measurements with respect to **a)** [Ca] and **b)** [Al], with the same data used in figures 3.22 and 3.24. In both figures, the time axis was normalized by the total purge time (15 min), and mapped such that gas purging occurs from 0 to 1, with the pre-purging refining occurring before 0 (negative time), where the pre-purging refining was arbitrarily set to have lasted for 5 min in each set (-5/15=0.33..). The industrial measurements were then normalized with respect to their total refining time, and subsequently mapped to fit within the normalized time ([-0.33.., 1]) of the lab-scale experiments. The refining stages from table 3.10 have been marked. Both from Bjørnstad et al.[11].

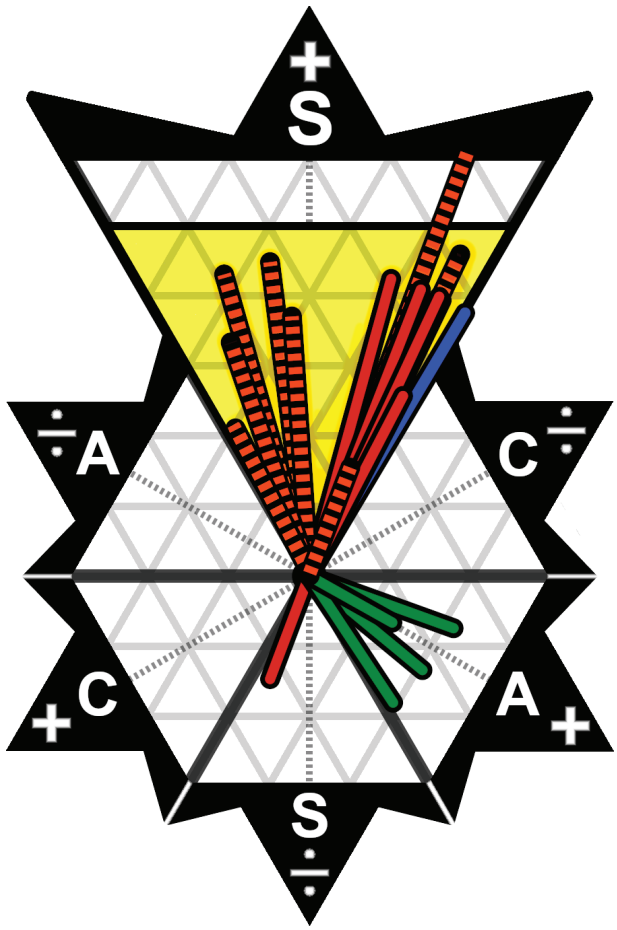

Figure 3.24: As with figure 3.22, but showing the second refining stage. From Bjørnstad et al.[11].

The formation of new slag is present in both of the stages depicted in figures 3.22 and 3.24, but it is clear that it is weaker in the initial stage than the second refining stage. Alumina behaves interestingly, as when the Al concentration is high (>0.5wt%) figure 3.13 shows that the refining of Al occurs above the iso-concentration line of silica, but at lower concentrations it changes to oxidize when the alumina content in the slag reduces.
From the figure there are clear similarities between the lab-scale and industrial measurements initially, as they both exhibit the same initial calcia controlled behavior and subsequent silica controlled behavior during the second refining stage. About half of the industrial measurement sets exhibit angles favoring reducing its alumina content over calcia during the second stage, indicating a greater relative refining of Al during this period than in the lab-scale measurements.

As the industrial measurements show similar initial refining behavior to those at lab-scale, it is possible to assume that industrial ladle refining also experiences surface oxidation. In the industrial case, when the liquid alloy is tapped into the ladle, the falling molten jet will first be scattered as it is deflected by the ladle floor, and later by impacting the liquid alloy surface as the ladle fills. The impinging jet flow caused by the jet impacting the ladle floor, creates ample opportunities for an exposed liquid alloy surface to come into contact with latent oxygen. Purging at low fill heights additionally contributes to increase the contact area between the air and melt, where the falling jet and gas plume additionally break and emulsify the surface oxide layer, causing it to continuously reform. It might also explain why the industrial sets show an initial refining behavior leaning somewhat more towards alumina than that of silica in the lab-scale measurement sets, as the industrial case may experience more surface interaction.

3.3.4 Conclusions and Industrial Implications

Laboratory-scale experiments simulating industrial OLR of MG-Si were performed. This was conducted by purging synthetic silicon alloys with synthetic air (2 NL/min) for 15 min at 1873 K, where the alloys differ with respect to their initial target Ca and Al content. A kinetic measurement series was performed for each alloy, sampling at 0, 5, 7, 10, and 15 min. Conclusions from the work were:

1) The discrepancy between the initial target and measured compositions indicate that there was a consistent pre-purging refining effect. This effect was shown to be directly correlated with the target composition, and was attributed to surface oxidation.

2) The general refining behavior indicated by the lab-scale measurements moved perpendicular to the iso-activity lines of calcia and silica, belonging to an imaginary SiO_2-CaO-Al_2O_3 slag in equilibrium with the alloy.

3) Three of the refining sets with high initial target Al content exhibited a different refining behavior than the other refining sets. This deviation was attributed to the formation of solid alumina-rich inclusions, which occurs when the refining path intersects the SiO_2-CaO-Al_2O_3 slag(liq)/mullite liquidus line.

4) A thermodynamic model was established to look at how a simple Si alloy-SiO_2-CaO-Al_2O_3 slag-gas system reacts to different initial conditions. The model was used to indicate which initial conditions leads to a specific response.

5) The overall refining behavior, which was also seen in the industrial measurements, may be described as:

   – Initially the refining occurs by the formation of a surface slag layer, controlled by the formation of calcia-rich SiO_2-CaO-Al_2O_3 slag. If this surface slag layer is not disrupted, then it will hinder any further surface oxidation.
   – After a critical amount of alloy has been tapped into the ladle, gas purging becomes the primary refining effect. Here, refining primarily occurs by slag formation on the gas bubbles, controlled by the formation of new silica-rich SiO_2-CaO-Al_2O_3 slag.
   – Towards the end of the refining cycle, enough slag has been amassed in the ladle to form a global equilibrium between the bulk slag and alloy. This is seen by a change in the general refining path. It is assumed that this change reflects a final compositional adjustment in the alloy to reach an equilibrium with the bulk slag.

Industrial Implications

Since there is a high degree of similarity in the refining behavior between the laboratory-scale measurements and the industrial measurement campaign, this indicates that the general refining behavior described above also applies to industrial ladles. Thus, when starting production of a new alloy, figure 3.15 provides vital information on which refining behavior one may expect from a given initial alloy composition. Viewing the refining path as normalized ternary vectors is also valuable. As shown, the proposed diagrams allow refining paths to be analyzed in a manner which highlights their relative similarity/difference, which is useful to assess performance and refining behaviors between different industrial measurement sets. For instance, comparing the refining behavior of different batches of a similar alloy across different furnaces or plants could provide valuable insights for locating potential operational inefficiencies or errors.

Since the initial refining stage sees rapid depletion of Ca, it might be more efficient to keep the initial gas purging to a minimum, and rather ramp it up when a greater melt volume is present in the ladle. If the concentration of Ca dips too low in the alloy, then the refining efficiency of other impurities goes down, like Al.

Chapter 4

Industrial Modeling

4.1 Statistical Model for Locating Micro Slag Droplets in MG-Si Alloy Sample Sets

4.1.1 Summary

Paper 6[12] investigates deviations found in data sets from industrial measurement campaigns on OLR of MG-Si, and presents a statistical model for locating samples taken during tapping and ladle refining which have been contaminated by micro slag droplets (MSDs). The silicon refining ladle is a system of immiscible phases, primarily different phases of liquid SiO_2-CaO-Al_2O_3 slag and alloy with different compositions, and other minor phases like solid inclusions. These phases contain many of the same elements, but in different quantities. Thus, a sample contaminated by small amounts of other phases is difficult to detect, and may require detailed microscopic analysis to not be discarded as an outlier with regards to the other samples in a set.

Both scientific research and industrial operations rely on a small number of industrial measurement campaigns, comprised of samples taken during the refining of different batches/ladles of silicon alloy. It is therefore desirable to separate out the ladles which behave in a similar manner, and to locate the samples within these ladles which do not conform to the general refining behavior.

The work looks at the alloy content and refining behavior of the two primary slag forming impurities [Ca] and [Al][1], from a published[3] industrial measurement campaign containing 8 individual refining sets, with samples at different points during the refining process. A model was developed which estimates statistical properties, based on the behavioral minima, from the equilibrium region, as there is more likely to be a higher number of values representing the same composition in this area. The model then uses these statistical properties to develop an upper bound for the concentrations of [Ca] and [Al] which adhere to the general refining behavior along the whole refining process. Simulated measurement sets were also used to test the stability and sensitivity of the statistical model, and was found to represent the system adequately, with a type I error (false positive) less than 2.5%, and a realistic type II error (false negative) below 15%.

[1]Reminder: [El] means that El is in the liquid metal phase.

4.1.2 Model

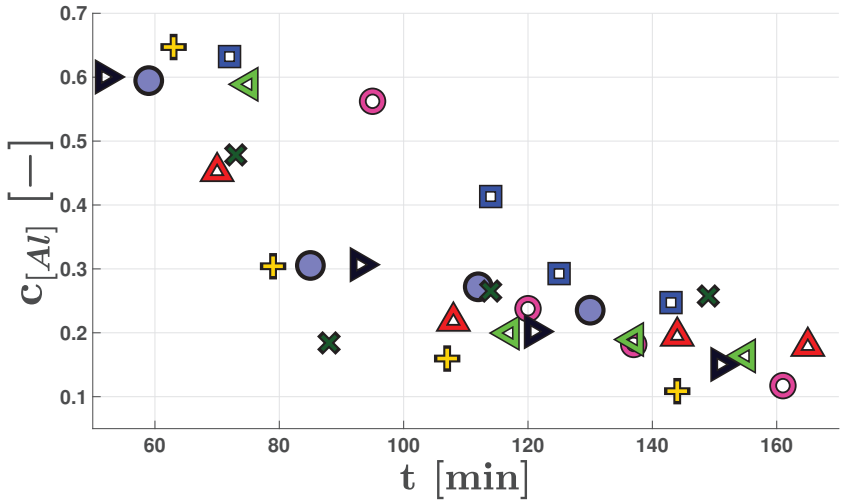

Figure 4.1: Normalized concentration of [Al], $c_{[Al]}$, from the industrial measurement campaign in Kero et al.[3]. The industrial measurement campaign consists of several refining batches, each distinguishable by a unique marker and marker-color. Based on figure from Bjørnstad and Tranell[12].

The model is based on 7 assumptions, which here will be used to find the similar sets on the raw data from Kero et al.[3] in figure 4.1.

Since an industrial measurement campaign will contain measurements from multiple refining batches, it is necessary to assume that the refining process was performed in a similar manner for each batch/ladle, as the model does not in this form account for external factors. This is indicated by the alloy tapped into the ladle having been found to have a constant composition, thus the refining needed to reach its target composition should also be similar. While specifics cannot be disclosed, industrial measurement data from an industrial partner, comprising of samples from the alloy tapped into the refining ladle from the furnace, with respect to their [Ca] and [Al] composition, were investigated for different alloys and batches. Statistical analysis found that the alloy tapped into the ladle had a constant composition with respect to [Ca] and [Al] for a given alloy, though there was high sample in-homogeneity.

All statistical calculations were performed at a 95% confidence level for each target MG-Si alloy, within each industrial measurement campaign. The statistical tests used were: Grubbs test[74] for locating outliers, and Runs-test[2] which found no sampling order bias. Spearman's rank correlation coefficient[75], Pearson's ρ[76], and Kendall's τ[77], all found a positive constant correlation between the [Al] and [Ca] content. This indicated that the furnace operation was consistent between batches, as both [Ca] and [Al] should be correlated, a common theme throughout this thesis, and as the correlation was consistent, the "furnace effects" on the [Ca] and [Al] composition can be seen as similar between different batches. An Anderson-Darling test[78] stated that there was no reason to believe that the concentration data was not normally distributed. Thus, all samples of the furnace taping jet belonging to specific alloy could be combined into a single t-distributed set, regardless of when it was sampled, with a single mean and variance for each species respectively. All statistical tests can among others be found in the libraries of Minitab 18, Matlab 2019b, and the R programming language, or in NIST/SEMATECH e-Handbook of Statistical Methods[79].

Before applying any assumptions, the measurement data from each refining batch in Kero et al.[3] were normalized with respect to their initial value $c_{[El]}$, as in equation 4.1. Here $\omega_{[El]}$ is the mass fraction of [El], and t_0 is the time where refining is initiated. Normalization highlights the relative refining behavior by suppressing any size effects.

$$c_{[El]} = \frac{\omega_{[El]}(t)}{\omega_{[El]}(t_0)} \tag{4.1}$$

The model was based on the following assumptions:

Assumption 1

Contamination by MSDs has a large effect on the metal analysis.

This assumption states that the contamination must produce an effect which does not significantly overlap with the distribution given by the process and model variance of an uncontaminated set, as large effect sizes are easier to locate. Additionally, if the contamination is so low that it cannot be distinguished from the uncontaminated case, then there is no reason to locate it, with respect to locating a representative refining behavior.

[2]Explained in A.6.

Assumption 2 and 3

> **Contamination by MSDs produce a positive deviation in both $\omega_{[\mathbf{Ca}]}$ and $\omega_{[\mathbf{Al}]}$.**

The maximum amount of impurities in MG-Si is in the order of 4 wt%[1], which is lower than the Ca and Al content in the SiO_2-CaO-Al_2O_3 slag[3]. Thus, any slag contamination in the metal sample should produce a positive deviation in both $\omega_{[Ca]}$ and $\omega_{[Al]}$. Necessitating a deviation in both $\omega_{[Ca]}$ and $\omega_{[Al]}$ also greatly reduces the type II error, were an extreme concentration in one of the species will not flag the sample as contaminated, as this might result from natural compositional variance.

Assumption 4

> **The lowest measured normalized concentration from all of the refining batches in each specified time interval can be combined into a single set $\vartheta_{[\mathbf{El}]}$(t). This set can be decently[4] represented by equation 4.3.**

$$\vartheta_{[El]}(t_i) = \min\left(c_{[El]}(t_j)\right), \;\; t_j \in {}^5t_i \pm \Delta t, \; i{=}1, 2, ...k \tag{4.2}$$

$$\hat{\vartheta}_{[El]}(t) = \theta_1 + (\theta_2 - \theta_1)\exp(\text{-}\theta_3 t) \tag{4.3}$$

θ_1, θ_2, and θ_3 are fitting parameters, with the model similar to that in Kero et al.[3]. $\vartheta_{[El]}$ and $\hat{\vartheta}_{[El]}$ are the measured and estimated concentration minima within each time interval.

Assumption 2 indicates that the lowest measured concentrations are least likely to be contaminated, allowing the measurement values in $\vartheta_{[El]}$ to aid in estimating the uncontaminated refining behavior. Equation 4.3 is used as a 1st order approximation of the refining behavior, to indicate if the selected set of values in $\vartheta_{[El]}$ can represent the desired refining behavior, as assumption 1 states that there is no need to know the uncontaminated refining behavior very accurately.

---

[3] When looking at a ternary SiO_2-CaO-Al_2O_3 phase diagram, the amount of Si, Ca, and Al can be estimated by: about 50% of the mass of silica and alumina comes from Si and Al respectively, while approximately 70% of the mass of calcia is Ca.

[4] The wording was changed from "adequately" in paper 6[12], to "decently". This is to not confuse the ball-park representation needed here, with the more ingrained use of "adequate" as a level of statistical validity, which is used elsewhere in this thesis and in the statistics literature.

[5] This symbol denotes that t_j is a value within the bounds defined by $t_i \pm \Delta t_i$.

To increase the odds of $\vartheta_{[El]}$ being decently represented by equation 4.3, the model uses a moving time interval, covered in paper 6[12]. This accounts for a possible nonuniform sampling density, which may lead to situations where there are too few samples in a given time interval to find a minima not at odds with those already located.

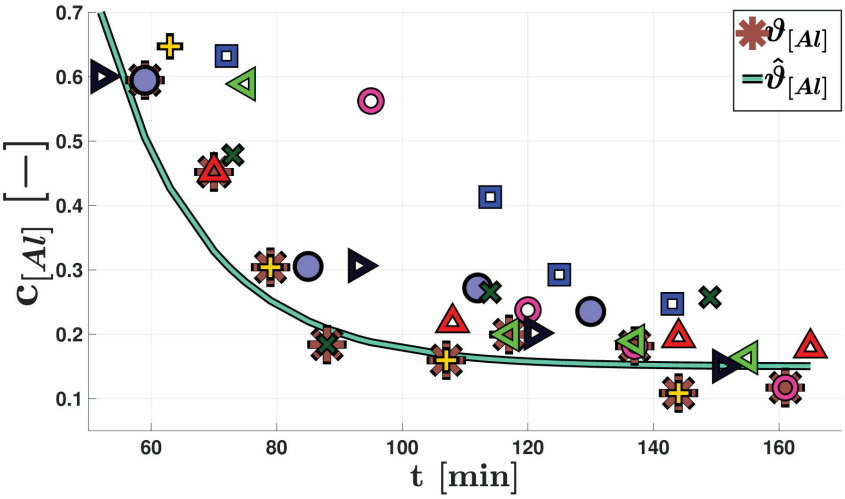

Figure 4.2: Figure 4.1 with the normalized concentration minima within each time interval $\vartheta_{[El]}$, marked with a *, with the estimated concentration minima $\hat{\vartheta}_{[El]}$. Based on figure from Bjørnstad and Tranell[12].

Assumption 5

> **The normalized refining profiles should eventually converge towards the same target end concentration, where the final samples all represent the same population value.**

For practical and operational reasons, industrial measurement campaigns will typically contain more measurements towards the end of the refining process. Since similar refining profiles should converge towards the same value, it can be assumed that all these samples belong to the same population. The size of this section allows rudimentary outlier analysis to be performed, such that a sample variance for this section can be calculated. This outlier analysis will increase the probability that the samples used to estimate the variance are uncontaminated.

For larger sample sizes (n≥15) the Generalized Extreme Studentized Deviate test (EDS), described by Rosner[80], is advised, but as such high sample sizes are not necessarily always available, like in the industrial set in Kero et al.[3], a different method will be used here. The 95% confidence interval (CI) is calculated, using the t-distribution with respect to the mean. If the CI does not contain the lowest point, then the point with the largest positive deviation is discarded and the process repeats. This creates an interval which is biased towards the minima, which from assumption 2 are less likely to be contaminated.

Assumption 6

The actual variance is the same over the whole refining curve.

This assumption is heavily reliant on assumption 1 but it allows the variance from assumption 5 to be projected along the whole refining profile. The model then takes the 95% CI interval from assumption 5, and adds it to each entry in $\vartheta_{[El]}$ from assumption 4 forming a segregation boundary (equation 4.4). Each measurement above this boundary is then flagged as a potentially contaminated, and if it flagged for both species then it is marked as contaminated.

$$\varphi_{[El],i} = \vartheta_{[El],i} + (\max(\text{CI}) - \min(\text{CI})) \tag{4.4}$$

From figures 4.3 and 4.4, it is clear that the measurement set, represented by the blue squares, deviate from the rest, together with the initial point from the pink circles and green left-arrow. These were all flagged by the model as contaminated, together with the final forest-green cross.

Assumption 7

The value normalized against is not contaminated.

This is an important assumption, and if the measurements from a single batch are much lower than the others, then a different normalization value may be considered.

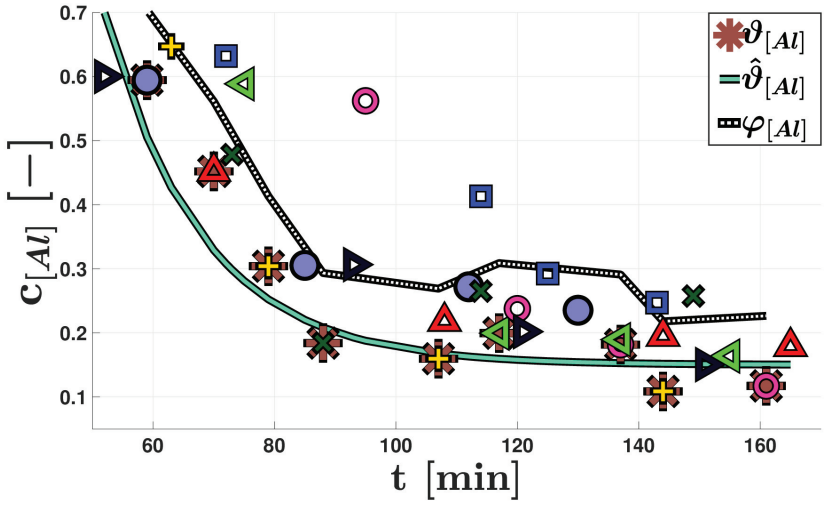

Figure 4.3: Figure 4.1 with the normalized concentration minima within each time interval $\vartheta_{[El]}$, marked with a *, with the estimated concentration minima $\hat{\vartheta}_{[El]}$, and segregation boundary $\varphi_{[Al]}$. Based on figure from Bjørnstad and Tranell[12].

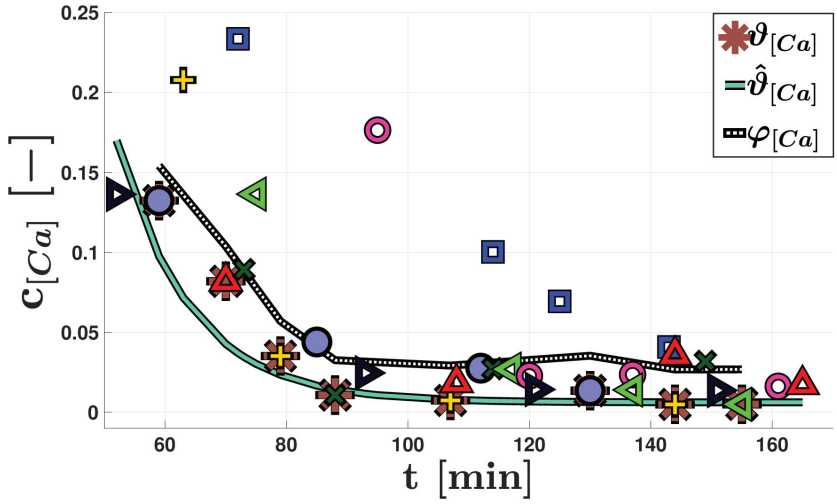

Figure 4.4: Like figure 4.3, but for [Ca]. Here with the normalized concentration minima within each time interval $\vartheta_{[Ca]}$, marked with a *, with the estimated normalized concentration minima $\hat{\vartheta}_{[Ca]}$, and segregation boundary $\varphi_{[Ca]}$. Based on figure from Bjørnstad and Tranell[12].

4.1.3 Performance and Discussion

Simulated normalized sets[6] were used to estimate the general performance of the model, for different probabilities of sample contamination, and general concentration fluctuation in the liquid silicon alloy, with respect to [Ca] and [Al], shown in figure 4.5. Here, the population variance was additionally made relative to the simulated mean, though specifying the population's relative standard deviation (RSD), where 5, 15, 25, 30, and 40% were tested for both [Ca] and [Al]. This was to include the case where the projected variance is lower than the actual variance earlier in the set. Figure 4.5 shows how the natural measurement population variation for both [Ca] and [Al] affects how well the model distinguishes between a contaminated and uncontaminated sample from 10^4 simulated sets, each consisting of 100 virtual samples. The figure also shows that there is a substantial performance increase in requiring both [Ca] and [Al] to be flagged as contaminated, instead of just considering one of the species.

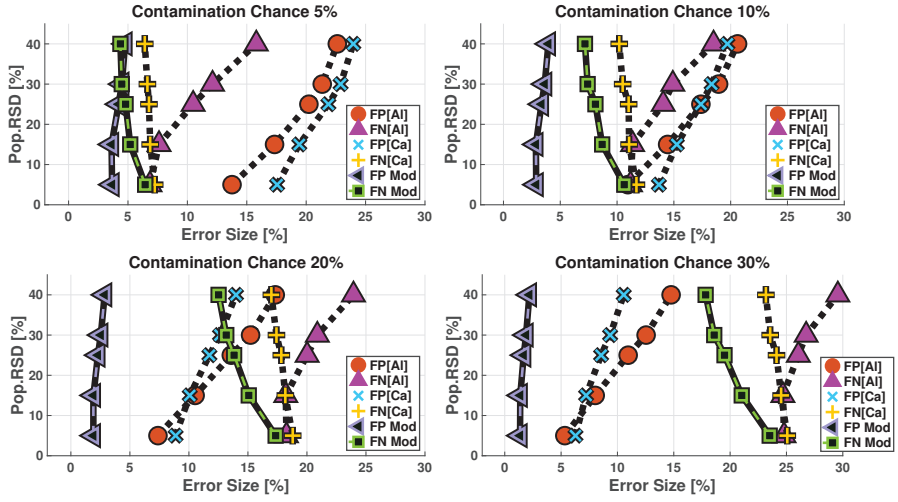

Figure 4.5: Model performance from simulated sets, described by the percent (Effect Size) of false negatives (FN) and positives (FP) flagged by the model, with respect to the actual population variance, represented as an RSD, and the probability that any single sample is contaminated by micro slag droplets. It shows the performance if either [Ca], [Al], or both, are used to determine of a virtual sample is contaminated or not. Each point represents 10^4 simulated sets consisting of 100 virtual samples, where the final 10 points were used to generate the CI in each set.

[6] Specifics on the simulated sets can be found paper 6[12]

Figure 4.5 shows that the model performance is highly dependent on the number of contaminated samples in the measurement set, but that this primarily affects the false negative rate. This mainly occurs due to there being more samples which are less contaminated, thus having a greater chance of being included when determining the segregation boundary, increasing the contamination degree required before being flagged as contaminated. Higher population variance also reduces the false negative rate, which is explained by more extreme minima, which lower the segregation boundary significantly. This is considered as a beneficial property, as it is seen as more important to perform well in the high variance range, due to industrial measurement campaigns being more likely to occupy this range.
The proposed model can be expanded if more relations between the mass transfer of [Al] and [Ca] are found, or if more industrial measurement campaigns were published. More specific sampling designs would also be welcome, but this would require each industrial site to change their sampling routines. However, the current model has been shown to be apt at discovering if a measurement sample is significantly contaminated by micro slag droplets or not.

4.1.4 Conclusions and Industrial Implications

A statistical model for locating slag-contaminated samples in industrial measurement campaigns, based on the industrial measurement [Ca] and [Al] data from Kero et al.[3], has been proposed.

1) The model was shown to be apt at discovering if a measurement sample is significantly contaminated by micro slag droplets or not.
   - The model was shown to work with the experimental [Ca] and [Al] data from Kero et al.[3].
   - Simulated sets were used to estimate that the model has a type I error (false positive) less than 2.5%, and a realistic type II error (false negative) below 15%.

Industrial Implications

While the presented statistical model is used to locate micro slag droplets, it actually looks for any measurement samples or sets which see a positive deviation from the norm. The flagged sets or samples might actually be flagged for a reason unrelated to slag contamination, which makes the model more generally applicable.

It can often be difficult to discern between natural local compositional fluctuations in the measurements and an actual behavioral deviation, especially when the variance is high. The real benefit of a statistical model, like the one proposed here, is that it aids in identifying potential problems, which can then be flagged for further analysis.

An example of how this model can be used in an industrial setting, other than general data analysis, is if something has gone wrong during the refining of a specific batch. If an industrial measurement campaign was performed when the alloy first went into production[7], then when the operators discover the problem they could start frequent sampling of the alloy throughout the remainder of the refining cycle. This model could then aid in deciding if the alloy is still fit for the customers use or if it should be withheld.

[7] According to the industrial focused representative sampling standard DS 3077:2013 (2nd ed. was consulted in this work.), it is in "all likelihood" less expensive and often easier to perform such a campaign for a new material. While not explicitly stated, this sentiment is also echoed in the sampling standard NS-EN 14899:2006.

Chapter 5

Main Conclusions

1) Section 2.1 proposes a theoretical framework for the nucleation of SiO_2-CaO-Al_2O_3 slag, which can form a foundation for building more in-depth process models for OLR of MG-Si.

2) The proposed theoretical framework predicts that a purge gas with high oxygen content will improve refining efficiency. Since there is an oxidation limit of silicon, the oxygen content in the purge gas can be tailored such that it will promote the formation of small nuclei throughout the bubbles ascent. Higher temperatures are also predicted to increase the oxidation limit, but will also promote SiO formation, thus a critical temperature cut-off for efficient refining exists.

3) Calcia has a much greater effect on slag growth than alumina, which means that the amount of dissolved Ca in the melt is an important control parameter. If the concentration of [Ca] becomes too low, it is expected that the refining will slow down.

4) Section 2.1 also contains experimental work, which showed that there are strong indications that silica is surface active, and that alumina is not surface active in SiO_2-CaO-Al_2O_3 slag.

5) Section 3.1 shows that the mass transfer of Ca and Al exhibit high relative behavioral similarity when the mass transfer occurs by slag/alloy equilibriation. While the mass transfers are of different orders quantitatively, the relative behavioral similarity is present in all the selected slag compositions. A general mass transfer model was used to estimate the total mass transfer coefficient $k_{t,i}$, $k_{t,Ca} \approx 3 \cdot 10^{-6}$ and $k_{t,Al} \approx 1 \cdot 10^{-5}$ [m/s].

6) The mass transfer of B from silicon alloy to slag was found in section 3.2 to not be significantly affected by simultaneous mass transfer of Ca to a 95% confidence. After a holding time of 30 min, the concentrations of both [B] and [Ca] have mostly converged, regardless of initial composition, with B converging towards the L_B predicted by the literature ($\approx$2–2.1).

7) The overall refining behavior seen in both the laboratory-scale experiments and an industrial OLR measurement campaign, both detailed in section 3.3, may be described as:

   – Initially the refining occurs by the formation of a surface slag layer, controlled by the formation of calcia rich SiO_2-CaO-Al_2O_3 slag. If this surface slag layer is not disrupted, then it will hinder any further surface oxidation.

   – During gas purging, refining primarily occurs by slag formation on the gas bubbles, controlled by the formation of new SiO_2-CaO-Al_2O_3 slag.

   – Towards the end of the refining cycle, enough slag has been amassed in the ladle to form a global equilibrium between the bulk slag and alloy. This is seen by a change in the general refining path. It is assumed that this change reflects a final compositional adjustment in the alloy to reach an equilibrium with the bulk slag.

   – Next to all of the overall refining behaviors seen in the laboratory-scale experiments were found to be activity-controlled.

8) A model for locating slag-contaminated samples in industrial measurement campaigns is proposed in section 4.1, with a type I error (false positive) less than 2.5%, and a realistic type II error (false negative) below 15%.

Chapter 6

Future Work

Fundamental Description of SiO_2-CaO-Al_2O_3 Slag Nucleation in OLR

While there are still more theoretical aspects to explore within the proposed theoretical framework, it would be more efficient to experimentally test the predictions made by said framework. The framework makes a large number of predictions on the behavior of the interfacial tension between the slag and alloy σ_{sm}, and the continuation of the work depends to a large part on the value of σ_{sm} at different slag compositions, temperatures, and oxygen amount in the gas bubbles. While the value is not known, the theoretical framework provides several avenues to estimate it. If experiments could be performed which utilized equation 2.9 to estimate σ_{sm}, then the results could be compared with estimates of σ_{sm} from experiments on the behavior from figure 2.10. These coupled experiments would be complex to statistically design, but they are aided by the framework predicting that many of its predictions are not very sensitive to process parameters.

Mass Transfer of Al, Ca, and B Between Silicon and Synthetic SiO_2-CaO-Al_2O_3 Slags

The continuation of this work would benefit from using a crucible material which did not interact significantly with silicon or the slag. It would be interesting to see how this impacted the mass transfer behaviors of both Ca and Al. To further understand the mass transfer kinetics in OLR, the silicon should also be pre-alloyed with different amounts of Ca and Al to see how this changes the mass transfer of these species.

For the mass transfer of B, it would be interesting to try different slags with other charge compensating species. If no dynamic mass transfer effect is seen with respect to B, then it strengthens the discussed hypothesis in section 3.2, that the documented effect by Krystad et al.[66] may not be due to an increase in the apparent interfacial area, but rather the availability of a charge compensating species at the surface.

Oxidative Refining of Metallurgical Grade Silicon: Lab-scale Measurements and Description of Ca and Al Mass Transfer

The effect of temperature on the refining behavior should be the next parameter to investigate systematically. In addition, results of laboratory experiments in this work should be compared with more industrial sample sets.

It would additionally be interesting to explore if Si alloys with higher amounts of impurities like FeSi, which contains large amounts of Al, can see higher refining efficiency if the initial purging is decreased.
While mainly discussed in paper 5, the formation of solid alumina-rich inclusions may be a possible avenue for refining the silicon alloy to very low [Al] concentrations, while retaining higher [Ca] concentrations. This would require the liquidus line to be targeted carefully, necessitating precise temperature control.

Improving the Experiment

The experimental setup worked very well, but there were parts that worked better than others. If the experiments are to be repeated, this section contains some notes on major aspects of the experiment, which may help guide a future redesign:

- A more efficient method of measuring temperature should be adopted, as the method used here lacked any redundancy. In hindsight, a thermocouple inside the wall of the graphite crucible and another one inside/closer to the melt, connected to different readers, would both provide redundancy and allow the temperature signals to be combined for a more accurate temperature measurement.

- Better shielding of the thermocouple should also be considered to increase the lifetime of the thermocouples. Both B- and C-type did not last long in the current setup.

- A better method for keeping the SiC gas lance in place should be found. The main issue lay with the gas tube connected to the lance, and its weight making the lance drift towards one side during purging. This was fixed by hoisting the gas tube above the lance with a crane, but this made it more difficult to handle the lance itself.

- It would also be better if a SiCaAl-alloy was made beforehand and analyzed, such that the alloying step could be omitted, and one would have a better sense of the initial composition. Reasons for wanting to omit the alloying step, is that it takes time to melt the alloying elements, and that it may damage the lance and thermocouple. The big problem however, is to produce an alloy in reasonable quantities without significantly oxidizing it. One way might be to just use a mixture of refined and unrefined industrial alloys, such that less Ca and Al need to be added. In this case it would be very important to perform enough measurements of the mixture beforehand, to ensure homogeneity and to know the composition to the desired degree.

Statistical Model for Locating Micro Slag Droplets in MG-Si Alloy Sample Sets

The proposed model can be expanded if more relations between the mass transfer of [Al] and [Ca] are found, or if more industrial measurement campaigns were published. In fact, the model would benefit greatly from most of the future work proposed in this chapter.

Bibliography

[1] Tangstad, Merete. Ferrosilicon and Silicon Technology. In *Handbook of Ferroalloys: Theory and Technology*, pages 179–220. Elsevier Ltd., Butterworth-Heinemann, 1st edition, 2013. Michael Gasik (Editor).

[2] J. E. A. Maurits. Silicon Production. In *Treatise on Process Metallurgy*, volume 3. Elsevier, 2014. Seshadri Seetharaman (Editor).

[3] Ida Kero, Mari K. Næss, Vegar Andersen, and Gabriella M. Tranell. Refining Kinetics of Selected Elements in the Industrial Silicon Process. *Metallurgical and Materials Transactions B*, 46(3):1186, 2015.

[4] Anders Schei, Johan Kristian Tauset, and Halvard Tveit. *Production of High Silicon Alloys*. Tapir Forlag, Trondheim, 1st edition, 1998.

[5] Erlend Lunnan Bjørnstad and Gabriella Tranell. Nucleation of SiO_2-CaO-Al_2O_3 Slag in Oxidative Ladle Refining of Metallurgical Grade Silicon. *Metallurgical and Materials Transactions B*, 52(3):1392–1412, 2021.

[6] Elena Dal Martello. *Impurity Distribution and Reduction Behaviour of Quartz in the Poduction of High Purity Silicon*. PhD thesis, Norwegian University of Science and Technology, Faculty of Natural Sciences and Technology, Department of Materials Science and Engineering, 2012.

[7] Edin Henrik Myrhaug. *Non-Fossil Reduction Materials in the Silicon Processs: Properties and Behaviour*. PhD thesis, Norwegian University of Science and Technology, Faculty of Natural Sciences and Technology, Department of Materials Science and Engineering, 2003.

[8] Erlend L. Bjørnstad and Gabriella M. Tranell. Investigation of Surface Oxide

Layer of Metallurgical Grade Silicon (MG-Si). In *11th International Conference on Molten Slags, Fluxes and Salts*, 2021. Extended Abstract.

[9] Erlend Lunnan Bjørnstad and Gabriella Tranell. Mass Transfer of Al and Ca Between Silicon and Synthetic SiO_2-CaO-Al_2O_3 Slags. In *Materials Processing Fundamentals 2017*, pages 85–96. Springer, 2017.

[10] Erlend L. Bjørnstad, Gjermund Solbakk, Øyvind Mosevoll, and Gabriella M. Tranell. The Effect of Calcium Alloy Content on the Mass Transfer of Boron Between Silicon and SiO_2-CaO slag. In *11th International Conference on Molten Slags, Fluxes and Salts*, 2021. Extended Abstract.

[11] Erlend Lunnan Bjørnstad, In-Ho Jung, Marie-Aline Van Ende, and Gabriella Tranell. Oxidative Refining of Metallurgical Grade Silicon: Laboratory-scale Measurements and Description of Ca and Al Mass Transfer. Manuscript prepared for publication.

[12] Erlend Lunnan Bjørnstad and Gabriella Tranell. Statistical Model for Locating Micro Slag Droplets in MG-Si Production. In *Silicon for the Chemical Industry XIV*, pages 349–356. The Norwegian Univerdity of Science and Technology, N-7491 Trondheim, Norway, 2018.

[13] Josiah Willard Gibbs. On the Equilibrium of Heterogeneous Substances: pt. 1. *Transactions of the Connecticut Academy of Arts and Sciences*, 3:139, 1874. From the Internet Archive. Donated by the Connecticut Academy of Arts and Sciences; Burndy Library. Downloaded 27.06.2017.

[14] Josiah Willard Gibbs. On the Equilibrium of Heterogeneous Substances: pt. 2. *Transactions of the Connecticut Academy of Arts and Sciences*, 3:180, 1877. From the Internet Archive. Donated by the Connecticut Academy of Arts and Sciences; Burndy Library. Downloaded 27.06.2017.

[15] Jan Erik Olsen, Dadan Darmana, Alireza Ashrafian, and Kai Tang. CFD Modelling of a Reactive Gas Stirred Three Phase Silicon Reactor. In *6th International Conference on CFD in Oil & Gas, Metallurgical and Process Industries*, page 9. SINTEF Materials and Chemistry, Trondheim, Norway, 2008.

[16] Abraham Marmur. Surface Tension and Adsorption Without a Dividing Surface. *Langmuir*, 31(46):12653–12657, 2015.

[17] Dimo Kashchiev. *Nucleation*. Elsevier Science, 1st edition, 2000.

[18] Hanna Vehkamäki. *Classical Nucleation Theory in Multicomponent Systems*. Springer Science & Business Media, 1st edition, 2006.

[19] V. I. Kalikmanov. *Nucleation Theory*, volume 860 of *Lecture Notes in Physics*. Springer, Netherlands, Dordrecht, 2013.

[20] S. M. Thompson, K. E. Gubbins, J. P. R. B. Walton, R. A. R. Chantry, and J. S. Rowlinson. A Molecular Dynamics Study of Liquid Drops. *The Journal of Chemical Physics*, 81(1):530–542, July 1984.

[21] Grant S. Henderson. The Structure of Silicate Melts: a Glass Perspective. *The Canadian Mineralogist*, 43(6):1921–1958, 2005.

[22] Pierre-Gilles De Gennes, Françoise Brochard-Wyart, and David Quéré. *Capillarity and Wetting Phenomena: Drops, Bubbles, Pearls, Waves*. Springer Science & Business Media, 2013.

[23] D. Walker and O. Mullins. Surface Tension of Natural Silicate Melts from 1200–1500°C and Implications for Melt Structure. *Contributions to Mineralogy and Petrology*, 76(4):455–462, 1981.

[24] I. V. Schweigert, K. E. J. Lehtinen, M. J. Carrier, and M. R. Zachariah. Structure and Properties of Silica Nanoclusters at High Temperatures. *Physical Review B*, 65(23), 2002.

[25] Alexandra Roder, Walter Kob, and Kurt Binder. Structure and Dynamics of Amorphous Silica Surfaces. *The Journal of Chemical Physics*, 114(17):7602–7614, May 2001.

[26] G. Vaccaro, G. Buscarino, S. Agnello, A. Sporea, C. Oproiu, D. G. Sporea, and F. M. Gelardi. Structure of Amorphous SiO_2 Nanoparticles Probed through the E_γ Centers. *The Journal of Physical Chemistry C*, 116(1):144–149, January 2012.

[27] Butler, J. A. V. The Thermodynamics of the Surfaces of Solutions. *Proceedings of the Royal Society of London. Series A*, 135(827):348–375, 1932.

[28] Toshihiro Tanaka, Klaus Hack, Takamichi Iida, and Shigeta Hara. Application of Thermodynamic Databases to the Evaluation of Surface Tensions of Molten Alloys, Salt Mixtures and Oxide Mixtures. *Zeitschrift für Metallkunde*, 87(5):380–389, 1996.

[29] T. Tanaka. Surface Properties of Alloys and Ionic Mixtures. *Mineral Processing and Extractive Metallurgy*, 120(4):229–234, November 2011.

[30] N. A. Arutyunyan, A. I. Zaitsev, and N. G. Shaposhnikov. Surface Tension of CaO-Al_2O_3, CaO-SiO_2, and CaO-Al_2O_3-SiO_2 Melts. *Russian Journal of Physical Chemistry A*, 84(1):7–12, 2010.

[31] Masashi Nakamoto, Toshihiro Tanaka, Lauri Holappa, and Marko Hämäläinen. Surface Tension Evaluation of Molten Silicates Containing Surface-Active Components (B_2O_3, CaF_2 or Na_2O). *ISIJ International*, 47(2):6, 2007.

[32] Masashi Nakamoto, Akihito Kiyose, Toshihiro Tanaka, Lauri Holappa, and Marko Hämäläinen. Evaluation of the Surface Tension of Ternary Silicate Melts Containing Al_2O_3, CaO, FeO, MgO or MnO. *ISIJ International*, 47(1):6, 2007.

[33] Timo Fabritius, Jaana Riipi, Mika Järvinen, Olli Mattila, Eetu-Pekka Heikkinen, Aki Kärnä, Jari Kurikkala, Petri Sulasalmi, and Jouko Härkki. Interfacial Phenomena in Metal–Slag–Gas System During AOD Process. *ISIJ International*, 50(6):7, 2010.

[34] Masahito Hanao, Toshihiro Tanaka, Masayuki Kawamoto, and Kouji Takatani. Evaluation of Surface Tension of Molten Slag in Multi-Component Systems. *ISIJ International*, 47(7):5, 2007.

[35] B. J. Keen. *Slag Atlas Part 10*. Verlag Stahleisen GmbH, Dusseldorf, 2nd edition, 1995.

[36] Yoshio Waseda and James M. Toguri. *The Structure and Properties of Oxide Melts*. World Scientific Publishing Co. Pte. Ltd., 1st edition, 1998.

[37] J. O'M. Bockris, J. D. Mackenzie, and J. A. Kitchener. Viscous Flow in Silica and Binary Liquid Silicates. *Transactions of the Faraday Society*, 51:1734, 1955.

[38] F. D. Richardson. *Physical Chemistry of Melts in Metallurgy*. Academic Press, Cambridge, 1st edition, 1974.

[39] Nguyen Ngoc Linh and Vo Van Hoang. Surface Structure and Structural Point Defects of Liquid and Amorphous Aluminosilicate Nanoparticles. *Journal of Physics: Condensed Matter*, 20(26):265005, May 2008. Publisher: IOP Publishing.

[40] David A. Litton and Stephen H. Garofalini. Atomistic Structure of Sodium and Calcium Silicate Intergranular Films in Alumina. *Journal of Materials Research*, 14(4):14, April 1999.

[41] Svein Stølen and Tor Grande. *Chemical Thermodynamics of Materials: Macroscopic and Microscopic Aspects*. Wiley, John Wiley & Sons, Incorporated, Wiley-Blackwell, New York, 1st edition, 2004.

[42] P. Buffat and J-P. Borel. Size Effect on the Melting Temperature of Gold Particles. *Physical Review A*, 13(6):2287–2298, June 1976.

[43] Gao, Fan and Gu, Zhiyong. Melting Temperature of Metallic Nanoparticles. In *Handbook of Nanoparticles*, volume 25, pages 661–690. Springer International Publishing, Switzerland, 1st edition, 2016. M. Aliofkhazraei (ed.).

[44] Andrea Broggi. *Condensation of SiO and CO in Silicon Production*. PhD thesis, Norwegian University of Science and Technology, Faculty of Natural Sciences and Technology, Department of Materials Science and Engineering, 2021.

[45] Mari Kirkebøen Næss. *Mechanisms and Kinetics of Liquid Silicon Oxidation*. PhD thesis, Norwegian University of Science and Technology, Faculty of Natural Sciences and Technology, Department of Materials Science and Engineering, 2013.

[46] L. A. Girifalco and R. J. Good. A Theory for the Estimation of Surface and Interfacial Energies. I. Derivation and Application to Interfacial Tension. *The Journal of Physical Chemistry*, 61(7):904–909, July 1957.

[47] K. C. Mills and B. J. Keene. Physical Properties of BOS Slags. *International Materials Reviews*, 32(1):1–120, January 1987. Publisher: Taylor & Francis.

[48] T. Narushima, K. Matsuzawa, Y. Mukai, and Y. Iguchi. Oxygen Solubility in Liquid Silicon. *Materials Transactions, JIM*, 35(8):522–528, 1994.

[49] A. V. Shishkin and A. S. Basin. Surface Tension of Liquid Silicon. *Theoretical Foundations of Chemical Engineering*, 38(6):660–668, November 2004.

[50] Kenneth C. Mills and Y. C. Su. Review of Surface Tension Data for Metallic Elements and Alloys: Part 1–Pure Metals. *International Materials Reviews*, 51(6):329–351, 2006.

[51] B. J. Keene. A Review of the Surface Tension of Silicon and its Binary Alloys with Reference to Marangoni Flow. *Surface and Interface Analysis*, 10(8):367–383, 1987.

[52] B. J. Keene. Review of Data for the Surface Tension of Pure Metals. *International Materials Reviews*, 38(4):157–192, 1993.

[53] Zhang Fu Yuan, Kusuhiro Mukai, and Wen Lai Huang. Surface Tension and its Temperature Coefficient of Molten Silicon at Different Oxygen Potentials. *Langmuir*, 18(6):2054–2062, 2002.

[54] Aïmen E. Gheribi, Mathieu Vermot des Roches, and Patrice Chartrand. Modelling the Surface Tension of Liquid Metals as a Function of Oxygen Content. *Journal of Non-Crystalline Solids*, 505:154–161, 2019.

[55] S. T. Bromley, M. A. Zwijnenburg, and T. Maschmeyer. Fully Coordinated Silica Nanoclusters:$(SiO_2)_N$ Molecular Rings. *Physical Review Letters*, 90(3):035502, 2003.

[56] C.W. Bale, E. Bélisle, P. Chartrand, S.A. Decterov, G. Eriksson, A.E. Gheribi, K. Hack, I.-H. Jung, Y.-B. Kang, J. Melançon, A.D. Pelton, S. Petersen, C. Robelin, J. Sangster, P. Spencer, and M-A. Van Ende. Reprint of: FactSage thermochemical software and databases, 2010—2016. *Calphad*, 55:1–19, 2016. Christopher W. Bale Symposium - Thermodynamic Applications, Optimizations and Simulations in High Temperature Processes.

[57] Lars Klemet Jakobsson. *Distribution of Boron Between Silicon and CaO-SiO_2, MgO-SiO_2, CaO-MgO-SiO_2 and CaO-Al_2O_3-SiO_2 Slags at 1600°C*. PhD thesis, Norwegian University of Science and Technology, Faculty of Natural Sciences and Technology, Department of Materials Science and Engineering, 2013.

[58] T. Abel Engh. *Principles of Metal Refining*. Oxford University Press, 2nd edition, 1992.

[59] Erlend Lunnan Bjørnstad. Mass Transfer Coefficients and Bubble Sizes in Oxidative Ladle Refining of Silicon. Master's thesis, Norwegian University of Science and Technology, Faculty of Natural Sciences and Technology, Department of Materials Science and Engineering, 2016.

[60] Lars Klemet Jakobsson and Merete Tangstad. Thermodynamic Activities and Distributions of Calcium and Magnesium Between Silicon and CaO-MgO-SiO_2 Slags at 1873 K (1600°C). *Metallurgical and Materials Transactions B*, 46(2):595–605, 2015.

[61] P. V. Riboud and L. D. Lucas. Influence of Mass Transfer Upon Surface Phenomena in Iron and Steelmaking. *Canadian Metallurgical Quarterly*, 20(2):199–208, 1981.

[62] M. A. Rhamdhani, G. A. Brooks, and K. S. Coley. Analysis of Interfacial Area Changes During Spontaneous Emulsification of Metal Droplets in Slag. *Metallurgical and Materials Transactions B*, 37(6):1087–1091, 2006.

[63] Christopher P. Manning and Richard J. Fruehan. The Rate of the Phosphorous Reaction Between Liquid Iron and Slag. *Metallurgical and Materials Transactions B*, 44(1):37–44, 2013.

[64] Andrew Wu, Peter C. Hayes, and Hae-Geon Lee. Silicon and Manganese Transfer in Dynamic Conditions of Carbon-Saturated Liquid Iron Drops Falling through Slag Layer. *ISIJ international*, 38(3):213–219, 1998.

[65] L. D. De Oliveira Campos. *Mass Transfer Coefficients Across Dynamic Liquid Steel/Slag Interface*. PhD thesis, Universite de Bordeaux, 2017.

[66] Egil Krystad, Lars K. Jakobsson, Kai Tang, and Gabriella Tranell. Thermodynamic Behavior and Mass Transfer Kinetics of Boron Between Ferrosilicon and CaO-SiO_2 Slag. *Metallurgical and Materials Transactions B*, 48(5):2574–2582, 2017.

[67] Jeff Kline, Merete Tangstad, and Gabriella Tranell. A Raman Spectroscopic Study of the Structural Modifications Associated with the Addition of Calcium Oxide and Boron Oxide to Silica. *Metallurgical and Materials Transactions B*, 46(1):62–73, 2015.

[68] Jacobson, Nathan S., Lee, Kang N., and Fox, Dennis S. Reactions of Silicon Carbide and Silicon(IV) Oxide at Elevated Temperatures. *Journal of the American Ceramic Society*, 75(6):1603–1611, 1992.

[69] Jacobson, Nathan S. and Opila, E. J. Thermodynamics of Si-C-O System. *Metallurgical Transactions A*, 24A:1212–1214, 1993.

[70] Nathan S. Jacobson and Rapp, Robert A. Thermochemical Degredation Mechanisms for the Reinforced Carbon/Carbon Panels on the Space Shuttle. Scientific 106793, NASA, Ohio, 1995.

[71] Geoffrey K. Sigworth. Thermodynamics of Dilute Liquid Silicon Alloys. *Canadian Metallurgical Quarterly*, 59(3):251–261, July 2020.

[72] Seung Hwan Ahn, Lars Klemet Jakobsson, and Gabriella Tranell. Distribution of Calcium and Aluminum Between Molten Silicon and Silica-Rich CaO-Al_2O_3-SiO_2 Slags at 1823 K (1550°C). *Metallurgical and Materials Transactions B*, 48(1):308–316, 2017.

[73] Kjetil Hildal. *Steam Explosions During Granulation of Si-Rich Alloy.: Effect of Al- and Ca-Additions*. PhD thesis, Norwegian University of Science and Technology, Faculty of Natural Sciences and Technology, Department of Materials Science and Engineering, 2002.

[74] Frank E. Grubbs. Procedures for Detecting Outlying Observations in Samples. *Technometrics*, 11(1):1–21, 1969.

[75] Maurice G. Kendall. Partial Rank Correlation. *Biometrika*, 32(3/4):277–283, 1942.

[76] Karl Pearson. VII. Note on Regression and Inheritance in the Case of two Parents. *Proceedings of the Royal Society of London*, 58(347-352):240–242, 1895.

[77] Maurice G. Kendall. A New Measure of Rank Correlation. *Biometrika*, 30(1/2):81–93, 1938.

[78] Theodore W. Anderson and Donald A. Darling. Asymptotic Theory of Certain" Goodness of Fit" Criteria Based on Stochastic Processes. *The Annals of Mathematical Statistics*, pages 193–212, 1952.

[79] NIST/SEMATECH. e-Handbook of Statistical Methods. https://doi.org/10.18434/M32189, 2021.

[80] Bernard Rosner. Percentage Points for a Generalized ESD Many-Outlier Procedure. *Technometrics*, 25(2):165–172, 1983.

[81] Irving Langmuir. Oil Lenses on Water and the Nature of Monomolecular Expanded Films. *The Journal of Chemical Physics*, 1(11):756–776, 1933.

[82] Neville A. Miller. Investigation of the Tension Mechanisms Responsible for Lens Formation and a New Method for Measuring the Angles of Liquid Lenses. *The Journal of Physical Chemistry*, 45(6):1025–1045, 1941.

[83] Alex Nikolov and Darsh Wasan. Oil Lenses on the Air–Water Surface and the Validity of Neumann's rule. *Advances in Colloid and Interface Science*, 244:174–183, 2017.

[84] Zhen Cao and Andrey V. Dobrynin. Polymeric Droplets on Soft Surfaces: From Neumann's triangle to Young's law. *Macromolecules*, 48(2):443–451, 2015.

[85] W. Kurtz and D. J. Fisher. *Fundamentals of Solidification*. Trans. Tech. Publications, Switzerland, 4th edition, 2005.

[86] Wolf-Dieter Deckwer and Robert W. Field. *Bubble Column Reactors*. Reaktionstechnik in Blasensäulen. Wiley, Chichester, 1992.

[87] Arman Hoseinpur and Jafar Safarian. Mechanisms of Graphite Crucible Degradation in Contact with Si–Al Melts at High Temperatures and Vacuum Conditions. *Vacuum*, 171:108993, 2020.

[88] J. C. F. de Winter. Using the Student's "t"-Test with Extremely Small Sample Sizes. *Practical Assessment, Research & Evaluation*, 18(10), August 2013.

Appendix A

Expressions, Relations, and Models

A.1 Nucleation Condition for Solute Condensation

The nucleation of (SiO_2) on the gas bubbles in OLR of MG-Si occurs by solute condensation, as the silicon alloy becomes supersaturated by [SiO_2]. However, there is not enough thermodynamic data on this reaction currently to solve the nucleation equations. It is therefore desirable to express the nucleation of silica slag with respect to [O] and $\{O_2\}$, which is shown in this section. A more detailed generalized description of this can be found in Kashchiev [17].

Solute condensation is a first-order phase transition, which is often described as the equilibrium between an "old" saturated phase, where the solute and solvent were in equilibrium, and a "new" supersaturated phase, where the solvent is in equilibrium with a condensed phase consisting of the old solute. The chemical potential between these two states $\Delta\mu$ [J] is thus the driving force for the phase transition, where:

$$\mu_{new} < \mu_{old} \;\rightarrow\; \Delta\mu = \mu_{new} - \mu_{old} < 0 \tag{A.1}$$

Here μ_{old} and μ_{new} are the chemical potentials of the old and new phases respectively.
The system will move from the old state to the new one by spontaneous solute condensation as long as $\Delta\mu$ is negative[1]. A new equilibrium is reached when the driving force $\Delta\mu$ becomes zero, leading to:

$$\mu_{old,eq} = \mu_{new,eq} = \mu_{eq} \tag{A.2}$$

To find $\Delta\mu$, one can consider the first-order phase transition:

$$\nu_1 A + \nu_2 B + \cdots = A_{\nu_1} B_{\nu_2} \cdots \tag{A.3}$$

$$\Rightarrow \Pi = \prod_{i=1}^{k} a_i^{\nu_i} \;>\; \Pi_{eq} = \prod_{i=1}^{k} a_{i,eq}^{\nu_i} \tag{A.4}$$

Where a_i is the thermodynamic activity of species i, $(i = 1, 2, ..., k)$, and ν_i is the particle/molar amount of species i to balance the given reaction. $a_{i,eq}(T)$ is the activity of species i at the solute/solvent equilibrium, at the temperature T [K]. Π and Π_{eq} are the actual and equilibrium products of the solute, where at sufficiently low dilution Π_{eq} is the solubility product of the i'th species.

[1] It must be noted that some confusion may arise when comparing nucleation equations from different fields, as by convention certain fields define positive $\Delta\mu$ and ΔG as the criteria for spontaneity. This means that the equations will have opposite signs from what is generally seen.

As long as equation A.4 holds, $\Delta\mu$ will always be negative, allowing μ_{old} to expressed as:

$$\mu_{old} = \sum_{i=1}^{k} \nu_i \mu_{i,old} \tag{A.5}$$

$$= \sum_{i=1}^{k} \left[\nu_i \mu_{i,eq} + k_B T \ln \left(\frac{a_i^{\nu_i}}{a_{i,eq}^{\nu_i}} \right) \right] \tag{A.6}$$

$$= \mu_{eq} + k_B T \ln \left(\frac{\Pi}{\Pi_{eq}} \right) \tag{A.7}$$

Where $\mu_{eq} = \sum_{i=1}^{k} \nu_i \mu_{i,eq}$ is the sum of the chemical potentials of species i at equilibrium, k_B [J/K] is the Boltzmann constant, and $\ln() = \log_e()$ is the natural logarithm.

Kashchiev writes that "μ_{new} is practically a independent"[17, pp.11], giving that:

$$\mu_{new}(\Pi) \approx \mu_{new}(\Pi_{eq}) = \mu_{eq} \tag{A.8}$$

Using this assumption with equations A.1 and A.7 allows $\Delta\mu$ to be expressed as:

$$\Delta\mu\,(\Pi,\ T) = -k_B T \ln \left(\frac{\Pi}{\Pi_{eq}(T)} \right) \tag{A.9}$$

Silica is assumed to form the foundation for the SiO_2-CaO-Al_2O_3 slag phase in OLR. It is the product of oxygen dissolved in the alloy reacting with silicon at the melt/gas interface through reaction A.R1, and SiO reacting with oxygen in the gas at the interface by reaction A.R2. Species in the melt/gas interface are denoted with the superscript *.

$$\text{A.R1)}\ \ [\text{Si}]^* + 2\{\text{O}\}^* \rightarrow [\text{SiO}_2]^*$$

$$\text{A.R2)}\ \ \{\text{SiO}\}^* + \{\text{O}\}^* \rightarrow [\text{SiO}_2]^*$$

Dissolved silica further nucleates by solute condensation at the interface to the slag phase on the bubble substrate through reaction A.R3.

$$\text{A.R3)}\ \ [\text{SiO}_2]^* \rightarrow (\text{SiO}_2)$$

If one assumes that silica is only produced at the metal melt/gas interface on the melt side, then both reactions can be described by:

$$\text{A.R4)}\ \ [\text{Si}]^* + 2[\text{O}]^* = (\text{SiO}_2)$$

This assumes that $\{\text{SiO}\}^*$ dissociates into its constituents, Si and O, as it enters the melt side interface region, along with $\{\text{O}\}^* \rightarrow [\text{O}]^*$, before they react.

For reaction A.R4, equation A.9 can be expressed as:

$$\Delta\mu\left(\Pi,\ T\right) = -k_B T \ln\left(\frac{a_{[Si]^*} a_{[O]^*}^2}{a_{[Si]^*,eq} a_{[O]^*,eq}^2}\right) \tag{A.10}$$

Since [Si] is the bulk solvent phase, one should be able to assume that $a_{[Si]^*} \approx a_{[Si]^*,eq}$, giving:

$$\Delta\mu\left(\Pi,\ T\right) \approx \Delta\mu\left(a_{[O]},\ T\right) = -k_B T \ln\left(\frac{a_{[O]^*}^2}{a_{[O]^*,eq}^2}\right) \tag{A.11}$$

Since the solubility of [O] at 1873 K is in the order of 10^1 ppmw, infinite dilution is assumed: $a_{[O]^*,eq} \approx c_{[O],eq}$, where $c_{[O],eq}$ is the oxygen solubility limit in liquid silicon at a given temperature. $a_{[O]^*}$ is not currently measurable, but since $\{\text{O}_2\} \rightarrow 2[\text{O}]^*$, there should be a measurable $\{\text{O}_2\}$ representative activity for $a_{[O]^*}$, such that:

$$\Delta\mu\left(a_{[O]},\ T\right) \approx \Delta\mu\left(a_{\{O_2\}},\ T\right) = -k_B T \ln\left(\frac{a_{\{O_2\}}}{c_{[O],eq}^2}\right) \tag{A.12}$$

A.2 Geometry of a Lens

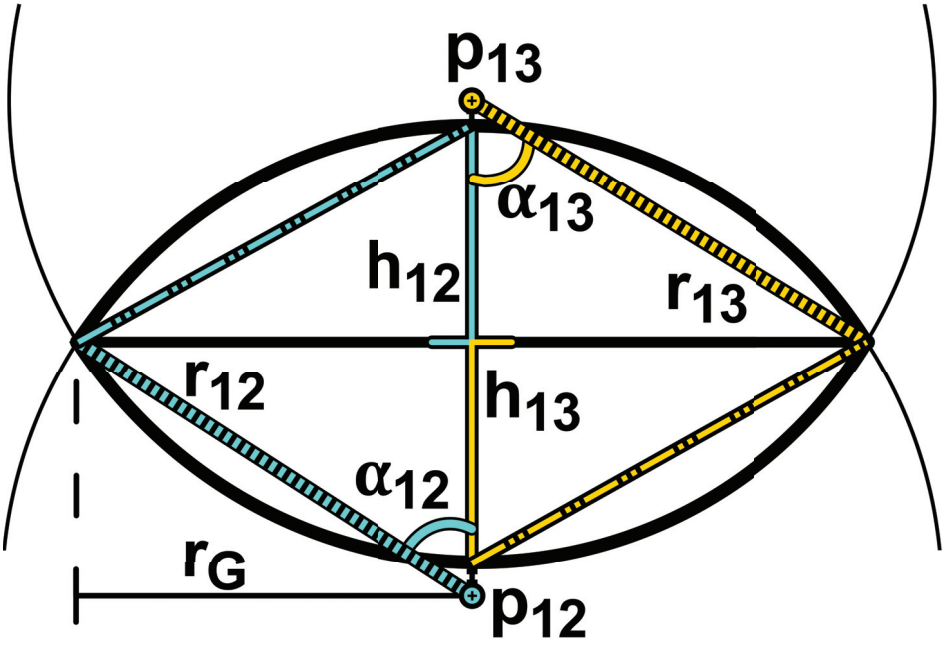

Figure A.1: A 2D cross section of a 3D lens. p_{12} and p_{13} are the centers of the two spheres, with radii r_{12} and r_{13}, whose spherical caps share the same ground radius r_G, together forming a lens. h_{12} and h_{13} are the heights, and α_{12} and α_{13} the contact angles, of their respective spherical cap.

A lens can be seen in figure A.1. It consists of two spherical caps sharing a single ground radius. The volume and surface area (without the ground plane) of each spherical cap is:

$$V_{cap} = \frac{\pi h}{6}\left(3r_G^2 + h^2\right) \tag{A.13}$$

$$= \frac{4\pi}{3}r^3 \cdot \left(\frac{(2+\cos\alpha)\,(1-\cos\alpha)^2}{4}\right) \tag{A.14}$$

$$= V_{Sph} \cdot \psi(\alpha) \tag{A.15}$$

$$A_{cap} = \pi\left(r_G^2 + h^2\right) \tag{A.16}$$

$$= 4\pi r^2 \cdot \left(\frac{(1-\cos\alpha)}{2}\right) \tag{A.17}$$

$$= A_{sph} \cdot \vartheta(\alpha) \tag{A.18}$$

Many relations are only derived for spheres, so it is customary to represent the volume and surface area of a spherical cap with respect to its spherical equivalence, as seen in equations A.15 and A.18. This allows a simple correction factor to be added to many relations, such that they also apply for a spherical cap or lens. The volume and surface area of a lens may thus be written:

$$r_{12}\sin\alpha_{12} = r_{13}\sin\alpha_{13} \tag{A.19}$$

$$V_{lens} = \frac{4\pi}{3}\left(r_{12}^3\cdot\psi(\alpha_{12}) + r_{13}^3\cdot\psi(\alpha_{13})\right) \tag{A.20}$$

$$= \frac{4\pi}{3}r_{12}^3\cdot\left(\psi(\alpha_{12}) + \left(\frac{\sin\alpha_{12}}{\sin\alpha_{13}}\right)^3\psi(\alpha_{13})\right) \tag{A.21}$$

$$= V_{sph,12}\cdot f\left(\alpha_{12},\alpha_{13}\right) \tag{A.22}$$

$$= V_{sph,13}\cdot f\left(\alpha_{13},\alpha_{12}\right) \tag{A.23}$$

$$A_{lens} = 4\pi r_{12}^2\cdot\left(\vartheta(\alpha_{12}) + \left(\frac{\sin\alpha_{12}}{\sin\alpha_{13}}\right)^2\vartheta(\alpha_{13})\right) \tag{A.24}$$

$$= A_{sph,12}\cdot\Xi(\alpha_{12},\alpha_{13}) \tag{A.25}$$

$$= A_{sph,13}\cdot\Xi(\alpha_{13},\alpha_{12}) \tag{A.26}$$

A.3 Relations Between the Interfacial Tensions of a Lens

In this section all angles are displayed in radians.

The relationships between the different interfacial tensions and contact angles in a lens, can be described by Neumann's rule[81][82][83][84], and expressed as a Neumann triangle, shown in figure A.2(b). To be considered a lens, a droplet's contact angles must fall within:

$$0 < \theta_s,\ \theta_g,\ \theta_m < \pi, \qquad 0 < \alpha_{sm},\ \alpha_{sg} < \frac{\pi}{2} \tag{A.27}$$

It is helpful to express the interfacial tensions in figure A.2(a) as functions of the slag's contact angles θ_s, α_{sm}, and α_{sg}, using the relations:

$$\pi = \theta_m + \alpha_{sm},\ \pi = \theta_g + \alpha_{sg},\ \theta_s = \alpha_{sm} + \alpha_{sg} \tag{A.28}$$

Relationships between contact angles and interfacial tensions based on figure A.2(b) can then be extracted utilizing general trigonometry, noting that $\sin(\pi - x) = \sin(x)$ and $\cos(\pi - x) = -\cos(x)$.

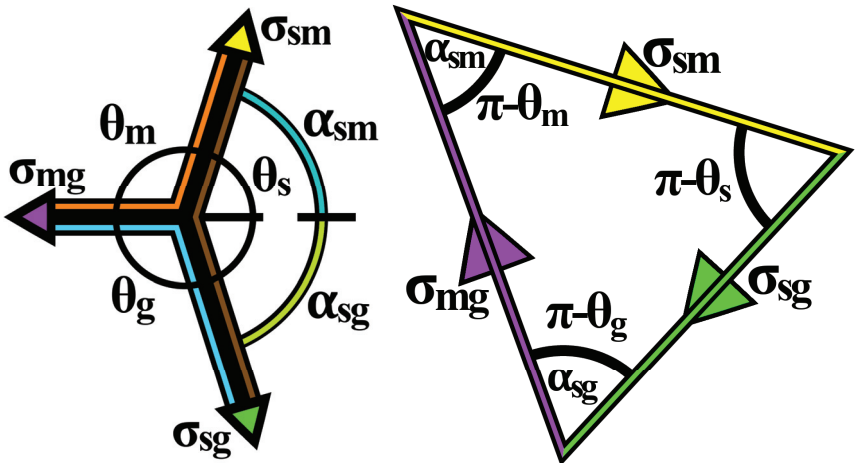

(a) (b)

Figure A.2: a) Contact angles for a lens. **b)** The contact angles from a) expressed as a Neumann triangle (here in radians).

Some important relationships:
The Projection Relations:

$$\sigma_{sm} = \text{-}\sigma_{sg}\cos(\theta_s) + \sigma_{mg}\cos(\alpha_{sm}) \tag{A.29}$$
$$\sigma_{sg} = \text{-}\sigma_{sm}\cos(\theta_s) + \sigma_{mg}\cos(\alpha_{sg}) \tag{A.30}$$
$$\sigma_{mg} = \sigma_{sg}\cos(\alpha_{sg}) + \sigma_{sm}\cos(\alpha_{sm}) \tag{A.31}$$

The Sinusoidal Relationships:

$$\sigma_{sm}\sin(\alpha_{sm}) = \sigma_{sg}\sin(\alpha_{sg}) \tag{A.32}$$
$$\sigma_{sg}\sin(\theta_s) = \sigma_{mg}\sin(\alpha_{sm}) \tag{A.33}$$
$$\sigma_{mg}\sin(\alpha_{sg}) = \sigma_{sm}\sin(\theta_s) \tag{A.34}$$

The Cosine Relationships:

$$\sigma_{sm}^2 = \sigma_{sg}^2 + \sigma_{mg}^2 - 2\sigma_{sg}\sigma_{mg}\cos(\alpha_{sg}) \tag{A.35}$$
$$\sigma_{sg}^2 = \sigma_{sm}^2 + \sigma_{mg}^2 - 2\sigma_{sm}\sigma_{mg}\cos(\alpha_{sm}) \tag{A.36}$$
$$\sigma_{mg}^2 = \sigma_{sm}^2 + \sigma_{sg}^2 + 2\sigma_{sm}\sigma_{sg}\cos(\theta_s) \tag{A.37}$$

Since all of these relationships must be valid for any given state, they can all be evaluated at once, showing that there is a unique value of θ_s, or pairs of values for α_{sm} and α_{sg}, for any given value of σ_{sm}, as shown in figure A.3.

Figure A.3 also shows that α_{sm} has a maximum value for slag nucleation in OLR. This maximum can be shown from the relationships above to always occur at $\theta_s{=}\frac{\pi}{2}$, and is due to σ_{sg}, the opposing length to α_{sm} in figure A.2(b), always being smaller than σ_{sm}, the opposing length to α_{sg}. Note that this is not the general case, but this will always be true for high silica SiO_2-CaO-Al_2O_3 slags, at temperatures relevant in OLR of MG-Si, due to σ_{mg} being higher than σ_{sg} by a wide enough margin.

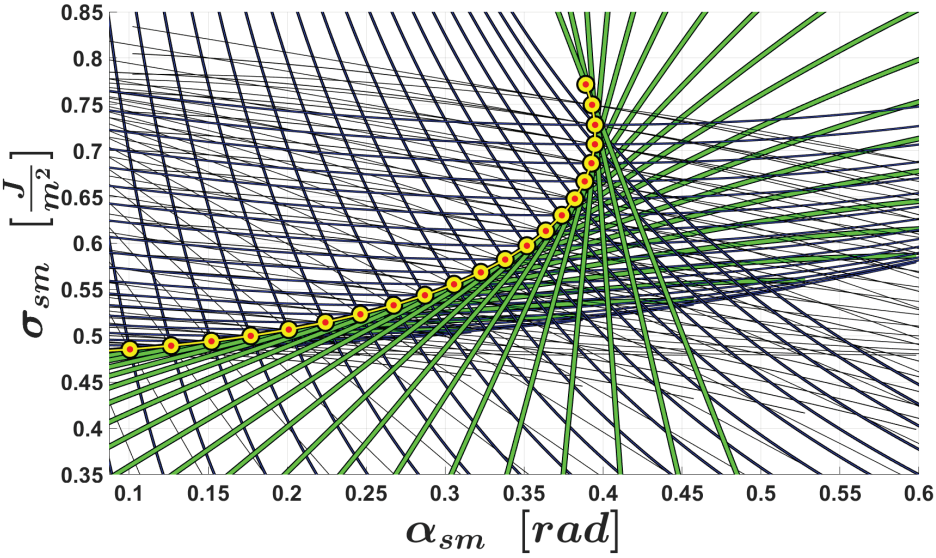

Figure A.3: σ_{sm} as a function of α_{sm} for different values of θ_s. Multiple relations are plotted for each value of θ_s. Circles mark the places where the different relation lines intersect for each θ_s. Figure is generated using parameter values from table 2.1.

A.4 Deriving the Critical Nucleation Equations

The condition for nucleation can be expressed as[85, pp.24]:

$$\Delta G_{tot} = \Delta G_s + \Delta G_V = \sigma_{ij} A_s + \Delta\varphi_p V \tag{A.38}$$

$$= 4\pi r^2 \sigma_{ij} + \frac{4\pi}{3} r^3 \Delta\varphi_p \tag{A.39}$$

Where ΔG_{tot}, ΔG_s, and ΔG_V [J][2] are the total, surface/interfacial, and volumetric Gibbs energies respectively.

[2]The units for Gibbs energy can be changed to [J/mol] by altering the units of $\Delta\varphi_p$ in the later equations. It is not advised to do it here.

σ_{ij} [J/m^2] is the surface ($i{=}j$) or interfacial ($i{\neq}j$) energy, A_s [m^2] is the surface area, while V [m^3] is the phase volume. The nucleation equations are derived for a sphere with radius r [m], and subsequently corrected to fit a lens, as described in A.2. $\Delta\varphi_p$ [J/m^3] is the difference in Gibbs energy between an old state (before nucleation occurs) and some new state per unit volume. The form $\Delta\varphi_p$ takes depends on what drives the nucleation process, like under-cooling in solidification, under-pressure in vapor condensation, and supersaturation in solute condensation.

Nucleation will only occur when the system can support nuclei above some critical size. This can also be expressed as:

$$\frac{d\Delta G_{tot}}{dr} = 8\pi r\sigma_{ij} + 4\pi r^2\Delta\varphi_p \tag{A.40}$$

$$\lim_{\substack{\Delta G_{tot}\to\Delta G^* \\ r\to r^*}} \left(\frac{d\Delta G_{tot}}{dr}\right) = 0 \tag{A.41}$$

$$\Rightarrow r^* = -\frac{2\sigma_{ij}}{\Delta\varphi_p} \tag{A.42}$$

$$\Rightarrow n^* = -\frac{32\pi}{3}\frac{\sigma_{ij}^3}{V_{0,mol}\Delta\varphi_p^3}, \qquad V_{0,mol} = \frac{4\pi}{3}\frac{r^{\star 3}}{n^*} \tag{A.43}$$

$$\Rightarrow \Delta G^* = \frac{16\pi}{3}\frac{\sigma_{ij}^3}{\Delta\varphi_p^2} \tag{A.44}$$

Where the $*$ superscript denotes the critical point at which the system supports nucleation. n [mol] and $V_{0,mol}$ [m^3/mol] denotes molar amount and molar volume respectively. In this work nucleation is driven by the formation of silica, due to the silicon alloy becoming over-saturated with oxygen, and the nucleation is heterogeneous in the form of a lens. This transforms the equations above to:

$$r^* = -\frac{2\sigma_{sm}V_{0,mol}}{\Delta\mu}\sin(\alpha_{sm}) \quad [m] \tag{A.45}$$

$$n^* = -\frac{32\pi}{3}\frac{\sigma_{sm}^3V_{0,mol}^2}{\Delta\mu^3}\cdot f(\alpha_{sm},\alpha_{sg}) \quad [mol] \tag{A.46}$$

$$\Delta G^* = \frac{16\pi}{3}\frac{\sigma_{sm}^3V_{0,mol}^2}{\Delta\mu^2}\cdot f(\alpha_{sm},\alpha_{sg}) \quad [J] \tag{A.47}$$

A.5 Slag to Metal Mass Transfer Model

For the reaction:

$$\text{A.R5)}\ \ (Me) \rightarrow [Me]$$

Mass conservation in the slag and melt can be expressed as:

$$m_s \dot{\omega}_{(Me)} = -k_{t,Me} \overline{\rho}_s A_s \left(\omega_{(Me)} - \omega^{eq}_{(Me)} \right) \tag{A.48}$$

$$m_m \dot{\omega}_{[Me]} = k_{t,Me} \overline{\rho}_m A_s \left(\omega^{eq}_{[Me]} - \omega_{[Me]} \right) \tag{A.49}$$

Here, m [kg] is the bulk mass, $\overline{\rho}$ [kg/m^3] is the bulk density, and ω_{Me} [-] is the bulk mass fraction of species Me, with $\dot{\omega}$ [s^{-1}] denoting the rate of change of said mass fraction. Subscripts s and m denote the slag and silicon metal phase, where (Me) and [Me] denotes that the species Me is in the slag and metal respectively. A_s [m^2] is the contact area between slag and silicon, with $k_{t,Me}$ representing the part of the total resistance against the mass transfer of species Me, which specific to species Me. More details about the specifics of $k_{t,Me}$ can be found in Engh[58, pp.176], Deckwer and Field[86], and Bjørnstad[59].
The mass transfer occurs from the slag to the liquid silicon, thus conservation of mass gives:

$$\Rightarrow -m_s \dot{\omega}_{(Me)} = m_m \dot{\omega}_{[Me]} \tag{A.50}$$

$$\overline{\rho}_s \left(\omega_{(Me)} - \omega^{eq}_{(Me)} \right) = \overline{\rho}_m \left(\omega^{eq}_{[Me]} - \omega_{[Me]} \right) \tag{A.51}$$

$$\omega^{eq}_{[Me]} - \omega_{[Me]} = \frac{\overline{\rho}_s}{\overline{\rho}_m} \left(\omega_{(Me)} - \omega^{eq}_{(Me)} \right) \tag{A.52}$$

And:

$$\Rightarrow m_s \left(\omega^{in}_{(Me)} - \omega_{(Me)} \right) = m_m \left(\omega_{[Me]} - \omega^{in}_{[Me]} \right) \tag{A.53}$$

$$\omega_{(Me)} = \omega^{in}_{(Me)} - \frac{m_m}{m_s} \left(\omega_{[Me]} - \omega^{in}_{[Me]} \right) \tag{A.54}$$

For major slag constituents there are next to no data concerning the reaction A.R5. Thus, the system must be expressed with respect to the oxides in the slag through reaction A.R6.

$$\text{A.R6)}\ \ (Me_x O_y) + \tfrac{y}{2} [Si] \rightarrow x [Me] + \tfrac{y}{2} (SiO_2)$$

The equilibrium concentrations in equation A.52 between the slag and liquid silicon can be related through the thermodynamic equilibrium distribution coefficient for reaction A.R6:

$$K_{Me} = \frac{a^{x}_{[Me]}}{a_{(Me_xO_y)}} \left(\frac{a_{(SiO_2)}}{a_{[Si]}} \right)^{\frac{y}{2}} \tag{A.55}$$

$$= \frac{(c^{eq}_{[Me]} f_{[Me]})^{x}}{\chi^{eq}_{(Me_xO_y)} \gamma_{(Me_xO_y)}} \left(\frac{a_{(SiO_2)}}{a_{[Si]}} \right)^{\frac{y}{2}} \tag{A.56}$$

Here K [-] is the thermodynamic equilibrium distribution coefficient, a [-] is the thermodynamic activity (references states are Raoultian (X°=1) for all species except [Me], which is in the Henrian($[wt\%Me]^{\circ}$=1) reference state), γ and f are the Raoultian and Henrian activity coefficients, with χ and c as the relative mole-fraction and mass-percent to their respective reference state[3]. Thus:

$$\chi_{(Me_xO_y)} = \frac{X_{(Me_xO_y)}}{X^{\circ}_{(Me_xO_y)}} = \frac{1}{X^{\circ}_{(Me_xO_y)}} \frac{\omega_{(Me_xO_y)}/M_{Me_xO_y}}{\sum_j \omega_{(jOX)}/M_{jOX}} \tag{A.57}$$

$$= \Upsilon \omega_{(Me_xO_y)} \tag{A.58}$$

$$\Rightarrow \omega^{eq}_{(Me_xO_y)} = \frac{(100\omega_{[Me]} f_{[Me]})^{x}}{K_{Me} \Upsilon \gamma_{(Me_xO_y)}} \left(\frac{a_{(SiO_2)}}{a_{[Si]}} \right)^{\frac{y}{2}} \tag{A.59}$$

To finally solve equation A.52 the oxide mass fraction in the slag must be related to the species mass fraction in the slag. M [kg/kmol] is the molar mass, and n [kmol] the amount of mols.

$$n_{(Me)} = x n_{(Me_xO_y)} \rightarrow m_{(Me)} = x m_{(Me_xO_y)} \frac{M_{Me}}{M_{Me_xO_y}} \tag{A.60}$$

$$\omega_{(Me)} = \zeta_{Me} \omega_{(Me_xO_y)}, \; \zeta_{Me} = x \frac{M_{Me}}{M_{Me_xO_y}} \tag{A.61}$$

Equations A.52 and A.54 can now be expressed using the oxide properties:

$$\omega^{eq}_{[Me]} - \omega_{[Me]} = \frac{\overline{\rho}_s}{\overline{\rho}_m} \zeta_{Me} \left(\omega_{(Me_xO_y)} - \omega^{eq}_{(Me_xO_y)} \right) \tag{A.62}$$

$$\omega_{(Me_xO_y)} = \omega^{in}_{(Me_xO_y)} - \frac{m_m}{m_s \zeta_{Me}} \left(\omega_{[Me]} - \omega^{in}_{[Me]} \right) \tag{A.63}$$

[3]Thermodynamics has no concept of concentrations with dimensions. Even relative concentrations in physical space, like mass and mole fractions, must be represented relative to the specified reference the thermodynamic parameters refer to. The commonly used reference states all use the value 1 in their parameter space as a reference, thus imputing the concentration will give the correct numeric result, creating the illusion that concentration is what is actually used. Imputing the concentration is a useful simplification, however some caution is advised as this is not always applicable.

To simplify further calculations it is assumed that the slag reaction is on a form where x = 1[4]. For CaO this is already the case, while Al_2O_3 can be converted to $AlO_{1.5}$, assuming that $a_{Al_2O_3}{=}a^2_{AlO_{1.5}}$. This gives:

$$\omega^{eq}_{[Me]} - \omega_{[Me]} = \frac{\overline{\rho}_s}{\overline{\rho}_m}\left(\zeta_{Me}\omega^{in}_{(MeO_y)} + \frac{m_m}{m_s}\omega^{in}_{[Me]} - \beta\omega_{[Me]}\right) \tag{A.64}$$

$$\beta = \frac{m_m}{m_s} + \left(M_{Me}\sum_j \frac{\omega_{(jOX)}}{M_{jOX}}\right)\frac{100 f_{[Me]}}{K_{Me}\gamma_{(MeO_y)}}\left(\frac{a_{(SiO_2)}}{a_{[Si]}}\right)^{\frac{y}{2}} \tag{A.65}$$

The measured final measured concentration $\omega^{\infty}_{[Me]}$ is used as an estimate of $\omega^{eq}_{[Me]}$, as real experiments measure distributions not values, or that the actual system may be slightly different than the ideal case making $\omega^{eq}_{[Me]}$ unreachable. $\omega^{\infty}_{[Me]}$ can be approximated as the measured concentration at the minima of the driving force for mass transfer. This gives:

$$\lim_{\omega_{[Me]}\to\omega^{\infty}_{[Me]}}\left(\omega^{eq}_{[Me]} - \omega_{[Me]}\right) \approx 0 \tag{A.66}$$

$$\Rightarrow \zeta_{Me}\omega^{in}_{(MeO_y)} + \frac{m_m}{m_s}\omega^{in}_{[Me]} = \beta\omega^{\infty}_{[Me]} \tag{A.67}$$

Which can be used in equation A.64 to express the RHS of equation A.52:

$$\omega^{eq}_{[Me]} - \omega_{[Me]} = \frac{\overline{\rho}_s}{\overline{\rho}_m}\beta\left(\omega^{\infty}_{[Me]} - \omega_{[Me]}\right) \tag{A.68}$$

$$\dot{\omega}_{[Me]} = -\frac{k_{t,Me}\overline{\rho}_s A_s}{m_m}\beta\left(\omega_{[Me]} - \omega^{\infty}_{[Me]}\right) \tag{A.69}$$

This is a 1st order differential equation, where integration gives the desired representation:

$$\omega_{[Me]}(t) = \omega^{\infty}_{[Me]}\left(1 - \exp\left(\text{-}(\frac{k_{t,Me}\overline{\rho}_s A_s}{m_m}\beta)t\right)\right) \tag{A.70}$$

$$\beta = \frac{m_m}{m_s} + \left(M_{Me}\sum_j \frac{\omega_{(jOX)}}{M_{jOX}}\right)\frac{100 f_{[Me]}}{K_{Me}\gamma_{(MeO_y)}}\left(\frac{a_{(SiO_2)}}{a_{[Si]}}\right)^{\frac{y}{2}}$$

[4] A common issue when using relations in moles, as the number of moles is not generally conserved. x=1 makes the number of moles equal for Me and MeO_y

A.6 Surface Oxidation

Argument for Why the pre-Purging Refining Effect is Not a Function of Time

Figure A.4 shows the fraction between the measured and target initial [Ca] and [Al] composition from the lab-scale experiments, against the time it took from a fully liquid charge to the initiation of the purge gas. A Runs-test shows that there is no reason to believe that there are any effects due to the measurement order, at a 95% confidence, with parameters seen in table A.1 (answer does not change with normal approximation or using the average, but the parameters will). This is a non-parametric test that checks if a set of data is in a random order by looking at the homogeneity of the set.

Table A.1: Parameters for Runs-test on the normalized initial measurement data against the target. The deviation is here given from the median. Don't reject H_0, that the set is in random order, if $2(1\text{-}P(V \leq v^*)) > \alpha$, where v^* is the number of runs in the given set. Here α=0.05 which is equivalent to a 95% confidence.

	Set	n_-	n_+	v^*	$P(V \leq v^*)$	
Ca	-,-,+,+,+,-,+,-,-,-,+	6	5	6	0.55	Don't Reject H_0
Al	-,-,+,-,-,+,-,-,+,+,+	6	5	6	0.55	Don't Reject H_0

From the figure A.4 it is clear that there is no consistent effect with time, but an F-test was run on the linear regression of every model possible which is a combination of the terms (t^0, t^1, t^2, t^3). An F-test checks if the fitted model is any better than random noise by looking at its variance, like:

$$\text{MSE} = \frac{\text{SSE}}{\nu_{SSE}} = \frac{1}{\nu_{SSE}}((\mathbf{y} - \hat{\mathbf{y}})^T (\mathbf{y} - \hat{\mathbf{y}}))$$

$$\text{MSR} = \frac{\text{SSR}}{\nu_{SSR}} = \frac{1}{\nu_{SSR}}((\hat{\mathbf{y}} - \overline{\mathbf{y}})^T (\hat{\mathbf{y}} - \overline{\mathbf{y}}))$$

$$\text{If } \frac{\text{MSR}}{\text{MSE}} < f_\alpha\left(\nu_{\text{SSE}}, \nu_{\text{SSR}}\right) \text{ Then Reject Regression}$$

$\mathbf{y}$, $\hat{\mathbf{y}}$, and $\overline{\mathbf{y}}$ are the measured, estimated, and mean measurement response vectors. SSE/SSR are the residual/regression sum of square error, with ν as their respective degrees of freedom. MSE is the mean sum of residual square error, which is generally used as an approximation of the model's parameter variance and can also be thought of as representing the noise/variance in the measurement data. MSR is the mean sum of regression square error, which represents how much of the total error (or variance) the regression can account for, and is a variance itself. Thus, one can test if the regression is able to account for the measurement noise. Succeeding this test does not mean that the regression is valid, but it is very useful for quickly sifting out those that absolutely do not work.

None of the fitted models were able to pass the F-test, thus there is no reason to believe that the pre-purge refining effect is a function of time spent before purging. There are however clearly some outliers in figure A.4, but all of these belong to the measurement sets that deviate behaviorally from the rest, so this is to be expected. That the pre-purging refining effect is not a function of time is also helpful in stating that purging has an effect, as it is very clear from the measurement series plots that there is an increased effect when the purge gas is initiated.

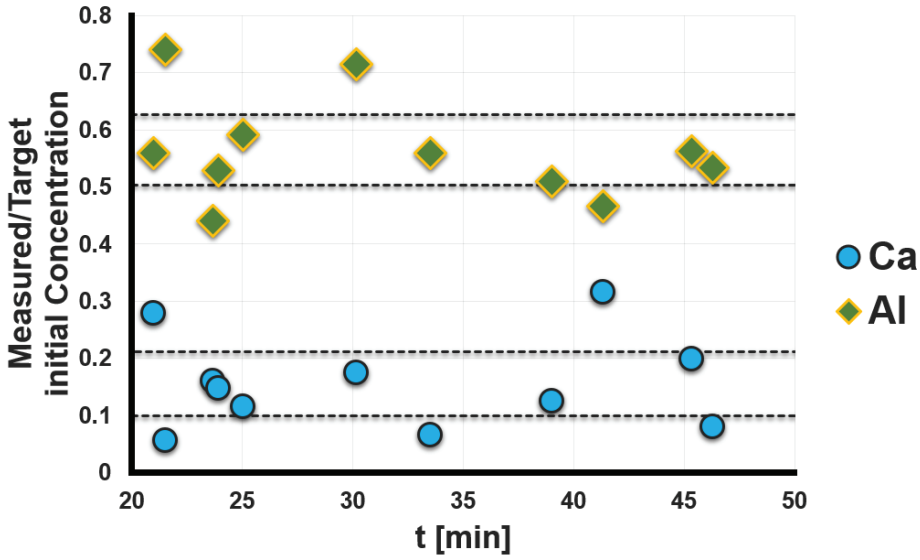

Figure A.4: The fraction between measured and target [Ca] and [Al] concentrations, with respect to the total time from liquid charge to initiation of the purge gas, comprising alloying and subsequent heating. 95% confidence intervals for each species are shown as stippled lines.

Another effect that might impact the pre-purging refining effect is how long the melt was exposed to temperatures below 1873 K, which would be the time between the alloying finished, until purging was initiated. Since this time period is a subset of the time interval already covered the concentrations will not change, but their order will. This is shown in figure A.5, and using the same logic as with figure A.4, it is clear that there also here is no significant effect from different exposure times to lower temperatures on the pre-purging refining effect, in these specific measurement sets.

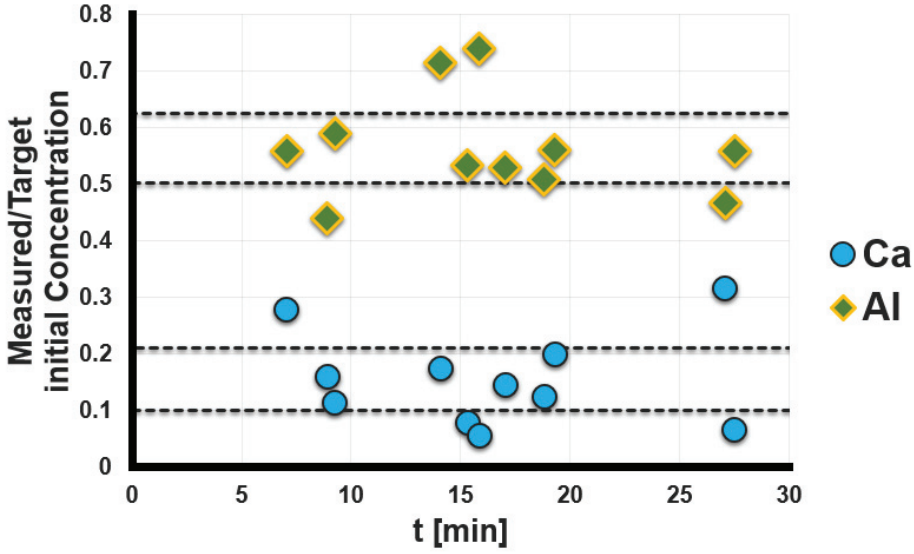

Figure A.5: The fraction between measured and target [Ca] and [Al] concentrations, with respect to the time from alloying ended until initiation of the purge gas (or the "subsequent heating" time). 95% confidence intervals for each species are shown as stippled lines.

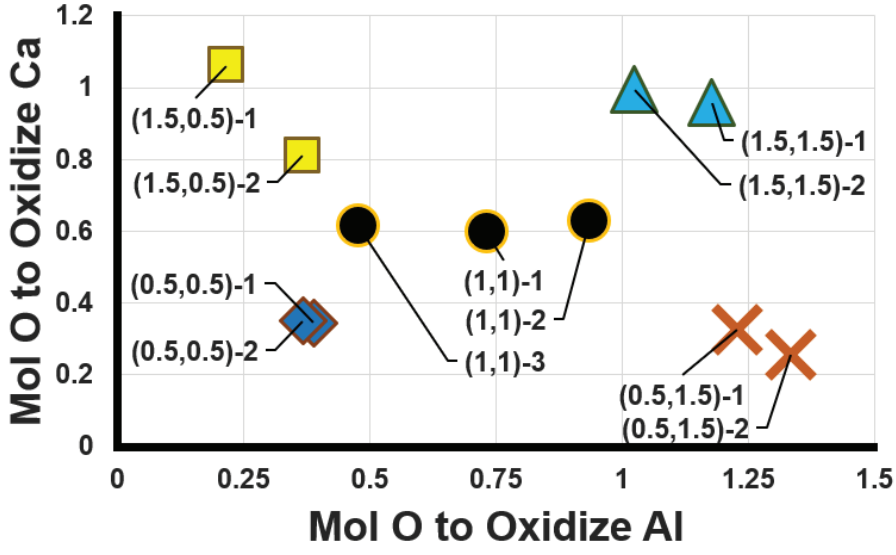

Figure A.6: The amount of [O] [mol] which is required to oxidize the impurities refined in the pre-purging period, for the Al and Ca concentration respectively.

Oxygen From the pre-Purging Refining Effect

It has been shown that the pre-purging refining effect is not a function of the time spend before purging, or the time spent heating after alloying indicating to temperature effect, which implies that the oxidation effect is proportional to the impurity concentration. If the amount of oxygen needed to oxidize the amount of Al and Ca, accounting for the discrepancy between the target and measured initial concentrations, are compared against each other for each set, then this effect becomes clear, as seen in figure A.6. Figure A.6 also indicates that the amount of alloying elements added in each experiment is consistent with that which is expected, due to how consistent figure A.6 is with the experiments 2^2 statistical design.

The figure shows that there seems to be more variance related to the oxygen required to oxidize Al than Ca. This can be shown more clearly if the differential against the mean of each replicate within a given target concentration is normalized with respect to said mean, to compare the relative size of this variation for all target concentrations, like:

$$\frac{n^{ox}_{[O],ij} - \overline{n}^{ox}_{[O],i}}{\overline{n}^{ox}_{[O],i}} \tag{A.71}$$

Here $n^{ox}_{[O],ij}$ [mol] is the amount of oxygen needed to oxidize the discrepancy in species i between the target and measured initial concentration in replicate j, with $\overline{n}^{ox}_{[O],i}$ as the mean over all replicates in a set.

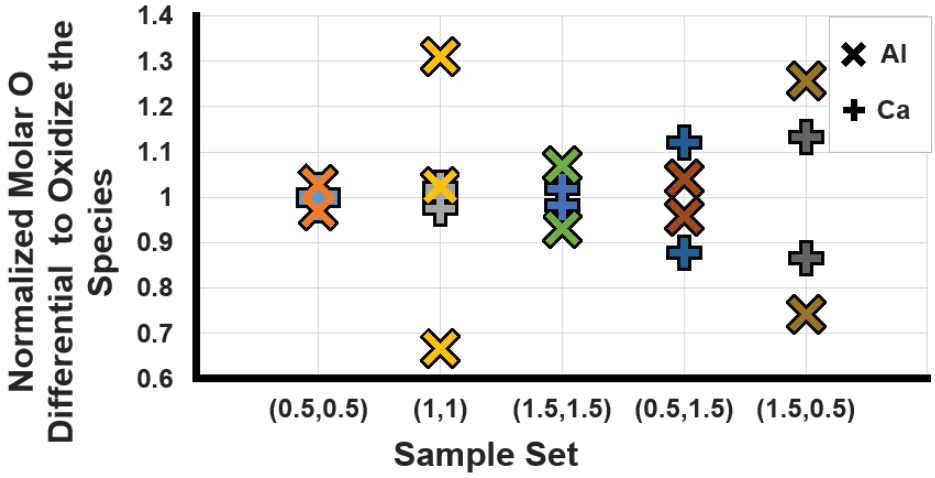

Figure A.7: Solution of equation A.71 for Ca and Al, in each target concentration.

Figure A.7 shows this relative variation, which shows some consistent behaviors. First, in all sets the oxygen amount needed to oxidize the initial concentration difference in Ca is very low and consistent, compared with that of Al. There also seems to be a difference between the sets with an equal target concentration of Al and Ca and those where they differ, but since one of the (1.5,0.5) sets have been found to be an outlier (it did not reach 1873 K before 5 min into gas purging), it is not clear if this is a true effect.

The relative variation in the oxygen amount needed to oxidize the initial concentration difference in Al is also very large for the (1.5,0.5) sets, which can also be attributed to one of the replicates being an outlier. However, this cannot be said in the case of the (1,1) sets, which see the highest relative variation in Al. Since they are very consistent with respect to Ca, this might be due to differences in the oxidation amount of the aluminum-foil before it entered the melt. It is interesting however that these large variations only occurred in this set, but it might also just be due to there being 3 replicates instead of the others with just 2, thus allowing more of the effect to be seen.

Another possibility is that the (1,1) sets start in a portion of the ternary phase diagram where the iso-activity lines of alumina change very drastically, they essentially shift from favoring the iso-concentration line of calcia to that of alumina. This might explain why Al is the only element affected, since it may make the melt composition more sensitive with respect to alumina formation, such that compositional variations, which are not significant in the other sample sets, have a greater effect here. One observation which supports this, is that even if there are initial differences in composition between the replicates, they still show a similar refining behavior during purging, as they then are in an area of the phase diagram where alumina formation plays a lesser role to that of calcia and silica.

Generally, figure A.7 also is another indication that the SiCa-alloy is very consistent, as it implies a low variation with respect to Ca. The (0.5,1.5) sets see a greater variance, but they deviate mostly due to differences in slag forming behavior, as discussed in section 3.3 and paper 5[11]. There are reasons to believe that the aluminum-foil does undergo some surface oxidation, as it sees higher variation, but this needs further testing. Another interesting effect to look into are the oxygen affinities, where the Ellingham diagram states that calcia should get its oxygen before alumina, so the low variation in Ca, may just be because it always gets all the oxygen it desires, while Al needs to wait for its turn. Kinetically, this effect would result in higher variance with respect to Al, but it does not account for the (0.5,1.5) case.

Finally, the absolute pre-purging refining effect must be tackled. The total amount of [O] needed to produce the pre-purging refining effect, is compared to the total amount of [O] needed to oxidize all impurities in the target composition, in figure A.8. Figure A.8 shows that the pre-purging refining effect can be expressed as a linear function of the total [O] needed to oxidize the total target impurity concentration. This clearly shows that the pre-purging refining effect is primarily determined by the impurity composition, and is another indication that the target amount of each impurity was added to the charge.

If the molar amount of Ca and Al are used instead as individual inputs, thus removing the 1.5 modifier from Al (Al forms Al_2O_3, while Ca forms CaO), the regression gives that the two species have weights statistically indistinguishable from each other. This indicates that each Ca and Al atom in the melt contribute equally to the total effect, even though Al needs 1.5 times the number of oxygen atoms to form alumina than Ca to form calcia. That this is the case is not unexpected, as calcia has a higher oxygen potential than alumina, and that it plays a bigger part in facilitating slag formation.

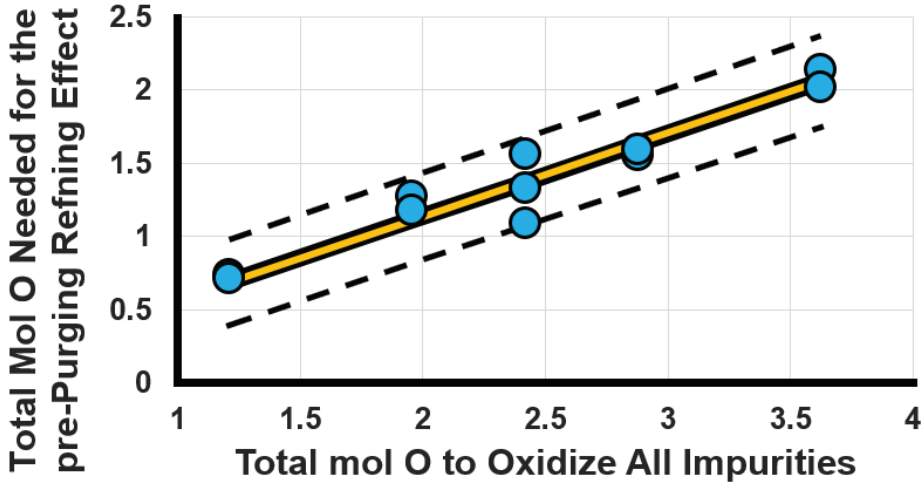

Figure A.8: Linear regression, where $\hat{y}{=}b_1 x$, $b_1{=}0.568$ with 95% CI $[0.534,\ 0.602]$. Full yellow line shows the regression, with its 95% prediction intervals as stippled black lines. From Bjørnstad et al.[11].

Figure A.8 also shows that the amount of [O] which needs to be added to get the pre-purging refining effect is very high. If these amounts are converted into a volumetric flow-rate of synthetic-air ($\{\text{mol\%}O_2\}$=21) [NL/min] (1 bar, 298 K), then the average flow-rate over the period of time where the melt was liquid before purging was initiated, varies from about 0.9 to 5.2 [NL/min].

Thus, this precludes any notions that the pre-purging refining effect is driven by a gas flow similar to that when purging, noting that the purge gas was delivered at 2 [NL/min], since the gas flow rate would need to be too high. The average gas flow rate also changes for each sample set, which could be explained if the contact area between the atmosphere and melt was different in each case, but the crucible opening is constant, indicating that something else must be responsible for the effect.

The properties of this effect are very similar to those found in Hildal[73], who discussed the surfaces of silicon melts in contact with humid air. On silicon melts in contact with air there will form a protective SiO_2 layer, due to a high partial pressure of gaseous oxide at ambient pressures[45]. Hildal shows experimentally that when small amounts of Al and Ca were present in the liquid silicon, a mixed oxide layer was formed instead, displacing the pure SiO_2 layer further away from the surface. This oxide layer would pacify the surface when fully formed. It must be noted that Hildal's quantitative work is not necessarily directly applicable, due to using water as the oxidation source, and only using low alloying amounts of Al and Ca. The (0.5,0.5) sets are close to Hildal's compositions, but the slag composition expected from the pre-purging refining effect is very different to that in Hildal, though since the systems are different one would not expect these compositions to be equal.

That calcia and alumina disrupt the silica surface structure is a common theme throughout this work, and that they also disrupt the protective surface cover of pure silica, provides an effect which is consistent with what has already been found in this work (also being consistent with the theoretical nucleation framework). While more research is needed to say anything definitely, a tentative description of the pre-purging refining effect can be made.

As liquid Si comes into contact with oxygen in the air, a protective silica layer is formed on the melt surface, pacifying it. Al and Ca, whom are both surface active in liquid silicon, react with this layer as it forms, forming a less protective oxide layer, which eventually becomes thick enough to pacify the melt surface. Thus, the pre-purging refining effect comes from the formation of this oxide layer, and is primarily a function of the total impurity amount. The higher the amount of impurities, the more the silica surface structure is damaged, resulting in a thicker surface layer before the surface can be pacified. Calcia has a greater effect on disrupting the surface structure, thus [Ca] more consistently attains the oxygen it needs to oxidize, while the formation of alumina depends on the availability of [Ca] and if it can be charge balanced by calcia. This also agrees with Ca and Al having atom for atom an equal contribution to the effect, even though Al should contribute more.

A.7 Ternary Vectors

This section aims to explain how a straight line in a ternary phase diagram can be described as a ternary vector. The ternary vector can then be normalized, such that its relative change in composition can be compared with other such vectors. While the ternary SCA (SiO_2-CaO-Al_2O_3) phase diagram will be used in this section, the relations are valid for any ternary phase diagram.

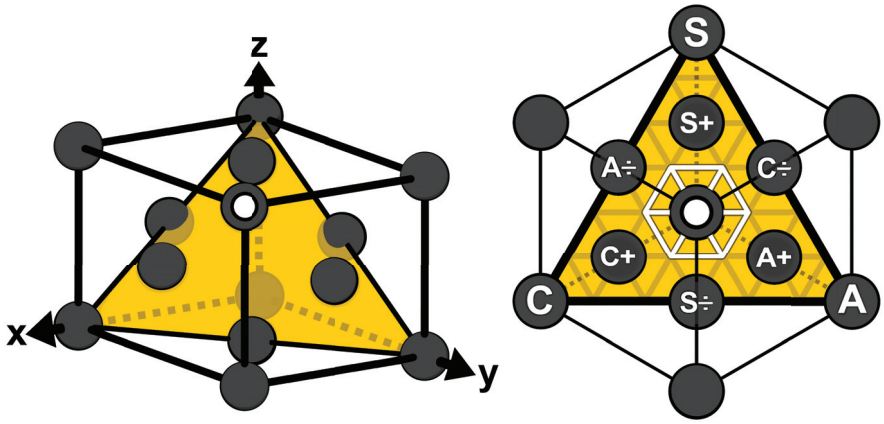

Figure A.9: a) The FCC arrangement in a Cartesian coordinate system (x,y,z) with a bound plane similar to a ternary phase diagram. **b)** a) which has been rotated to align the centers of mass. Different points have been denoted to indicate the silica-calcia-alumina (SCA) phase diagram, and the compositional change that will occur for a given vector rooted at the center of mass. From Bjørnstad et al.[11].

The ternary plane used to create ternary phase diagrams, is a plane in 3D Cartesian space (x,y,z) bound by $1{=}x{+}y{+}z$, and rotated such that the ternary center of mass, the $(\frac{1}{3}, \frac{1}{3}, \frac{1}{3})$-point, and the ternary projection of the Cartesian center of mass, the origin, overlap. A metallurgical analogy to this, is why face centered cubic (FCC) is the cubic close packing (CCP) arrangement. Both FCC and hexagonal close packing (HCP), the only other close packing arrangement in 3D, express similar hexagonal characteristics, which in the case of FCC originates from the exact same rotation and projection used to create ternary phase diagrams, shown in figure A.9.

As with 2D Cartesian vectors, vectors in 2D ternary space can also be compared by normalizing them and displacing them such that they originate at a single point. To simplify the mathematics, the center of mass of generally chosen as this origin point, which is the $(\frac{1}{3}, \frac{1}{3}, \frac{1}{3})$-point in a ternary phase diagram.

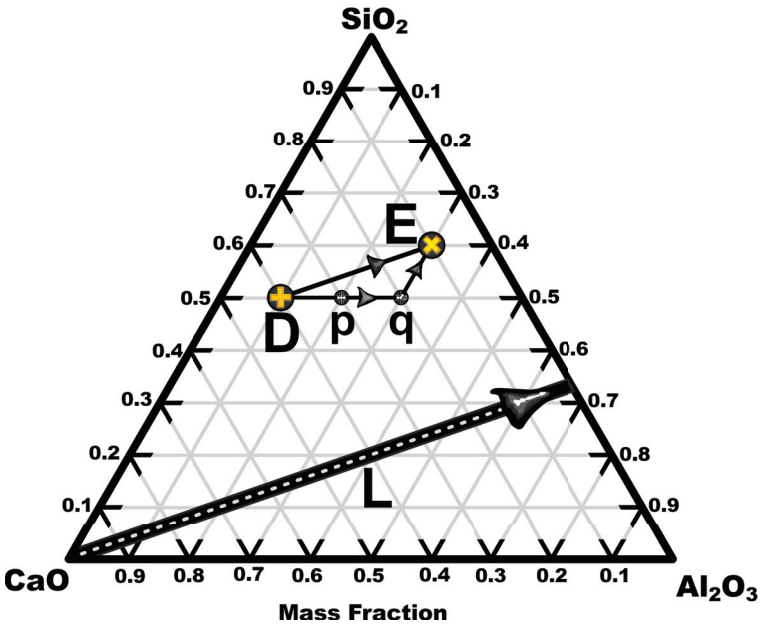

Figure A.10: Ternary SiO_2-CaO-Al_2O_3 phase diagram with ternary vectors.

The point D in figure A.10 represents the composition (S,C,A)[5] = (0.5,0.4,0.1), with the composition in E being (S,C,A) = (0.6,0.1,0.3), thus the vector DE represents a compositional change of Δ(S,C,A) = (+0.1,÷[6]0.3,+0.2). DE can also be expressed as a combination of the vectors Dp=(0,÷0.1,+0.1), pq=(0,÷0.1,+0.1), and qE=(+0.1,÷0.1,0), whom all sum up to (+0.1,÷0.3,+0.2). This shows that the change between two points in ternary space is an invariant property, and that in a ternary phase diagram specifically, all compositional change must always sum to 0, due to the plane being bound by (S+C+A)=1, giving Δ(S+C+A)=0. These properties are crucial, as any change which only involves two of the three species[7] must be equal but opposite (change by an equal amount, but with different signs (+,÷)). More broadly this can be expressed as: an equally sized step in a given direction along any of the iso-concentration lines for a given species, must result in equal but opposite quantitative change in the two other species.

[5] S = SiO_2, C = CaO, A = Al_2O_3.
[6] Here ÷ represents negative.
[7] Occurring along an iso-concentration line.

If all three species take part in the change, then the change must occur such that the species which sees the greatest change, like $\Delta C = \div 0.3$ in DE, must be equal but opposite to the combined change in the two other species, $\Delta S + \Delta A = 0.1 + 0.2 = 0.3$ in DE. The two species which see the least change must also share an equal sign, or else their sum cannot equal that of the species which sees the greater change. This results in there only being 6 combinations of signs for any change in a ternary phase diagram, which are all listed in table A.2, eluding to the hexagonal symmetry seen in figure A.9.

Table A.2: The only allowed combinations of signs for any compositional change in a ternary phase diagram.

Greatest Change		S	C	A
	S	+	÷	÷
		÷	+	+
	C	÷	+	÷
		+	÷	+
	A	÷	÷	+
		+	+	÷

The vector L, represented by the line L in figure A.10, depicts the compositional change $\Delta(S,C,A) = (+0.33..,\div 1,+0.66..) = \frac{1}{3}(+1,\div 3,+2)$. $L = \frac{10}{3}DE$, which means that L and DE express a similar relative change, as their direction[8] are the same. To accentuate this similarity, both L and DE can instead be expressed by the change they depict. Previously, it was noted that the two species which see the least change, designated here as the "subservient species", must share the same sign, and sum up to equal the species which sees the greatest change, here named the "controlling species". For a straight line/vector, any change in the two subservient species will always occur at a set ratio, like how $\Delta A/\Delta S = 2$ in both L and DE. Thus, both L and DE can be expressed as a change in their controlling species, ΔC, and a fraction of the change in their two subservient species, $\Delta A/\Delta S$.

This is always the case due to DE being a segment of L, if L was displaced as in figure A.11. Figure A.11 shows how any point along the line DE can be expressed as a point on the line L, displaced by an amount $\mathbf{\Lambda}$ in the S direction. More generally, any straight line in the ternary phase diagram can be expressed as a displaced segment/part of any other straight line parallel to it.

[8] Combination of the angles relative to the axis when originating at the center of mass, and signs.

Mathematically, it is useful to represent any straight line/vector by its longest parallel line in the ternary phase diagram, which means that Λ can be ignored, as it will always be zero. Like L, the longest straight parallel line/vector will always pass through either (1,0,0), (0,1,0), or (0,0,1), and intersect the (0,C,A), (S,0,A), or (S,C,0) iso-concentration lines. Thus, any line which is parallel to L will always be segment of L, where its intersect with the (S,0,A) line marks the ratio between the subservient species.

A useful convention is to always place the subservient species which sees the greatest change in the numerator, which ensures that the ratio between the subservient species (without Λ), is equal to or greater than 1. This primarily aids in depicting the change, but also simplifies calculations.

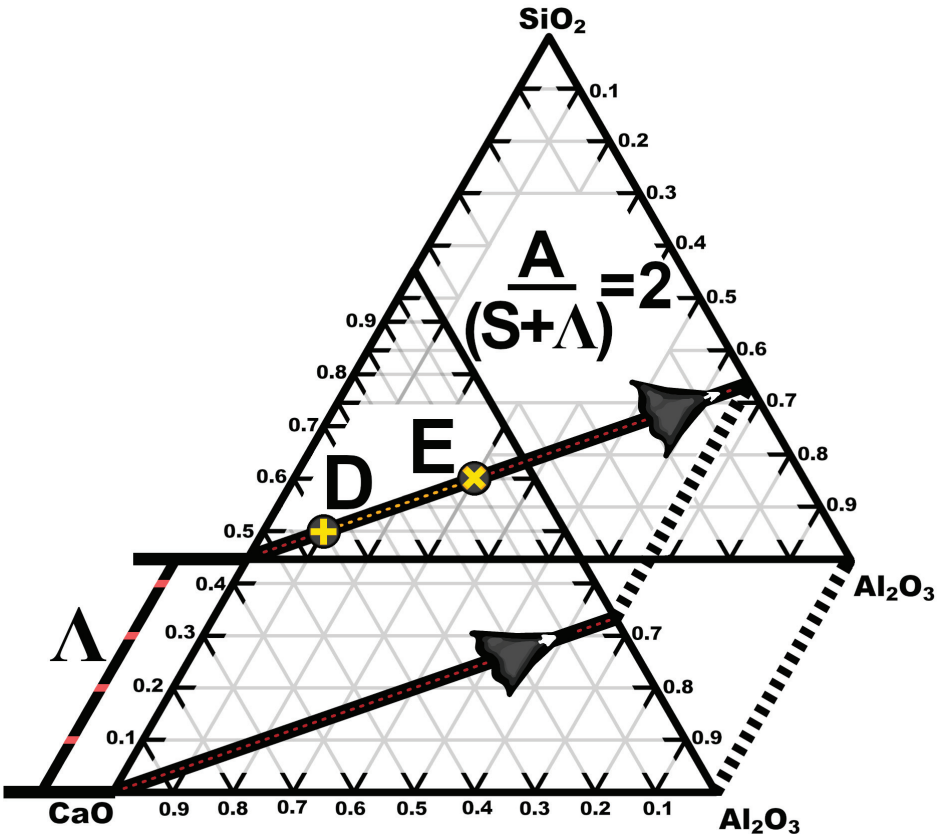

Figure A.11: Shows how DE is a subsection of L, if L was displaced by Λ. The ratio between A and S shows how any point along the line DE can be expressed as a displaced point along the line L.

When comparing the relative change of multiple different vectors, like those in figure A.13(a), their difference becomes more apparent if the vectors are first transformed to their longest parallel vector, and then displaced to originate at the ternary origin point $(\frac{1}{3},\frac{1}{3},\frac{1}{3})$. The vectors can then be scaled to fit a ternary normalization diagram, like that in figure A.13(b). This diagram is a culmination of all the properties previously discussed in this section, and shows which relative compositional change any ternary vector sees. Each hexagonal segment represents one of the 6 allowed combinations of signs from table A.2, one for each of the 3 possible controlling species with one of 2 signs, indicated by the protruding arrowheads on the outer hexagon. The hexagonal segments are subdivided into two parts, with the border providing an indication of the size difference between the subservient species, each seeing the greatest change in its respective part. For instance, ef in figure A.12 is in the (÷C) hexagonal segment and (+S) subsection. ef is close to the S/A=1 line, so any change in C is almost evenly shared by S and A. If ef had pointed closer to the A_0 line, an equal change in C would result in a greater change in S than A, at A_0 any change in C would be equal and opposite in S.

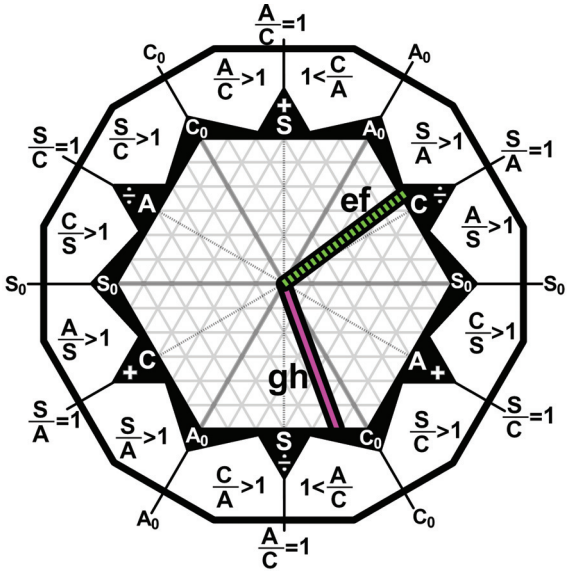

Figure A.12: Ternary normalization diagram. The outer ring contains the fractional relations between the subservient species, displayed on a shorthand form on the inner hexagonal border. Protruding arrows on each hexagonal segment denotes the controlling species and its sign. S_0, C_0, and A_0 denote the iso-concentration lines. Vector ef represents a relative change where the calcia concentration is reduced, which will result in an increase in the silica and alumina concentration, slightly favoring silica. gh represents a relative change which is controlled by reducing the silica content, resulting in an alumina and calcia increase, greatly favoring alumina. From Bjørnstad et al.[11].

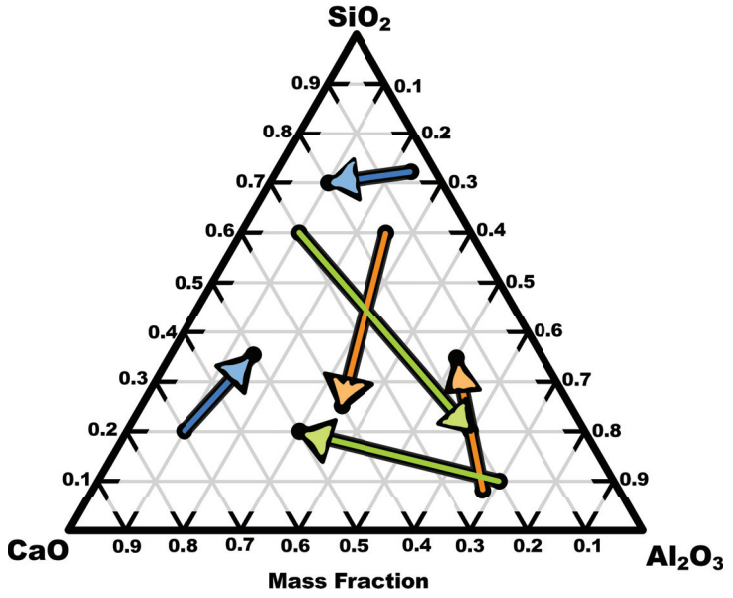

(a)

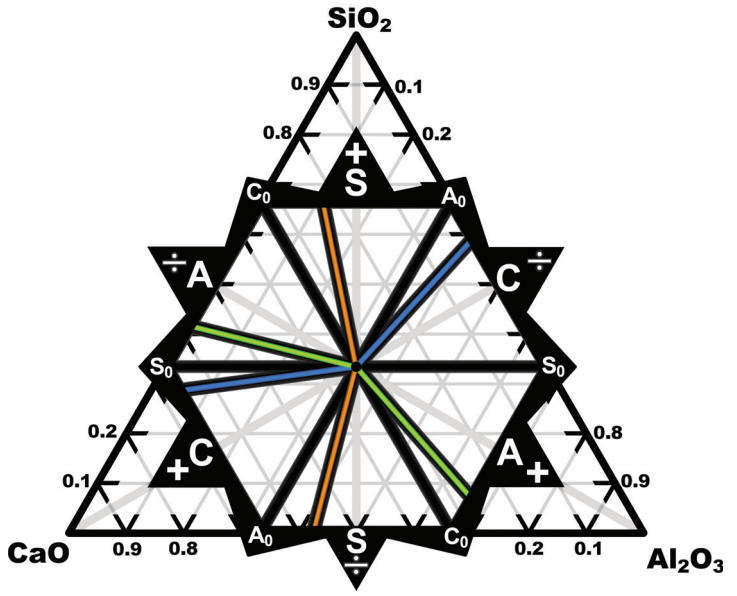

(b)

Figure A.13: a) Several ternary vectors, colored orange, blue, and green depending if silica, calcia, or alumina is its respect controlling species. **b)** Normalized vectors from a) in a ternary normalization diagram.

Appendix B

Measurement Data

B.1 Slag to Si Measurement Data

Table B.1: ICP-MS data of dissolved Ca and Al in Si with their sampling error (relative standard deviation). 2 sub-samples were imaged from each sample in the kinetic series. Here, Ca and Al came from SiO_2-CaO-Al_2O_3 slag (SCA) with the given composition in contact with pure Si at 1873 K for the listed time. * marks dual-scan entries of the same sub-sample, taken by the operator to verify the large disparity between replicates. These data are used in section 3.1.

	SCA-1 = (55,25,20) [wt%]				SCA-2 = (40,25,35) [wt%]			
t [min]	Ca [ppmw]	RSD [%]	Al [ppmw]	RSD [%]	Ca [ppmw]	RSD [%]	Al [ppmw]	RSD [%]
5	4394	0.8	2830	2.1	4423	2	5670	4
5	4946	3.6	3258	3.2	4195	2.1	5261	2.3
10	2030	1.1	1377	4.4	1709	0.6	4333	2.6
10	2195	1.5	1487	1.9	1804	2.5	4094	1
20	2522	4.9	1761	4	4571	1.7	7504	0.5
20	2885	2.5	1975	1.4	4574	3.4	7614	0.5
30	3250	1.4	2287	1.7	1938	2.4	4741	1.1
30	2870	2.9	2016	0.5	2461	1.7	6137	0.1
180	3933	2.3	3273	3.7	4613	2.7	9171	2.3
180	4008	1.3	3152	0.8	4708	3.1	10458	1.6

	SCA-3 = (40,40,20) [wt%]			
t [min]	Ca [ppmw]	RSD [%]	Al [ppmw]	RSD [%]
5	1432	3.1	879	2.3
5	1616	0.2	951	0.8
10	5255	3.6	2951	1.4
10	5285	2.2	3155	1.7
20*	5210	2.7	2766	1.7
20*	5176	0.8	2795	3.2
20	5853	2.4	3136	1.2
30	9900	1.6	5335	1.7
30	9438	2.2	5203	0.9
180	12434	1.8	6255	0.9
180*	19625	0.9	9269	1.1
180*	19960	4.2	9677	3

Table B.2: ICP-MS data Si, Ca, and Al in a SiO_2-CaO-Al_2O_3 slag with their sampling error (relative standard deviation). 2 sub-samples were imaged from each sample in the kinetic series. Amounts of SiO_2, CaO, and Al_2O_3 are calculated from the measured composition. * marks dual-scan entries of the same sub-sample, taken by the operator to verify the large disparity between replicates. These data are used in section 3.1.

	SCA-1	Slag		Target	(55,25,20)	[wt%]
t	Si	RSD	Ca	RSD	Al	RSD
[min]	[ppmw]	[%]	[ppmw]	[%]	[ppmw]	[%]
0	264090	1.9	215207	5.3	121442	3.7
0	242511	5.3	134710	5	70001	6
5	246362	2.8	196315	1	109706	6.4
5*	261817	2.9	195200	2.7	111273	0.9
5*	242588	2.5	200045	2.2	112990	2.2
10	250666	8.5	192056	6	108571	7.4
10	254615	2.2	204149	2.4	113103	2.9
20	242869	1	80518	0.7	24582	1.3
20	244381	4.7	120782	1.5	59741	4
30	259571	2.5	207188	3.5	116880	3.1
30	249681	2.9	200061	1.9	115520	1.3
180	260218	2.6	172132	1.8	89330	1.9
180	239319	7.4	196549	5.7	108878	4.8

t	SiO_2	CaO	Al_2O_3	sum
[min]	[wt%]	[wt%]	[wt%]	[wt%]
0	56.49	30.11	22.95	109.55
0	51.88	18.85	13.23	83.95
5	52.70	27.47	20.73	100.90
5*	56.01	27.31	21.03	104.35
5*	51.89	27.99	21.35	101.23
10	53.62	26.87	20.52	101.01
10	54.47	28.56	21.37	104.40
20	51.95	11.27	4.64	67.87
20	52.28	16.90	11.29	80.47
30	55.53	28.99	22.08	106.60
30	53.41	27.99	21.83	103.23
180	55.67	24.08	16.88	96.63
180	51.19	27.50	20.57	99.27

	SCA-2	Slag		Target	(40,25,35)	[wt%]
t	Si	RSD	Ca	RSD	Al	RSD
[min]	[ppmw]	[%]	[ppmw]	[%]	[ppmw]	[%]
0	166301	0.9	37520	0.6	46344	2.8
0	173216	0.4	39622	1.4	43922	3.1
5	175278	1.4	116890	0.9	115001	2
5	182927	1.9	31755	1.3	37420	3.8
10	169869	2.2	177641	3.6	176497	2.4
10	196868	1.6	109180	4	112564	1.6
20	178295	4.4	117397	0.5	115736	2.1
20	199833	0.9	144432	1.3	146243	0.5
30	166605	1.5	42108	3.1	46365	0.9
30	175140	4.7	20601	6.5	25390	3.9
180	187356	1.6	42215	3.1	45335	2.7
180	180559	1.6	54335	1.5	57887	1.8

t	SiO_2	CaO	Al_2O_3	sum
[min]	[wt%]	[wt%]	[wt%]	[wt%]
0	35.57	5.25	8.76	49.58
0	37.05	5.54	8.30	50.90
5	37.50	16.36	21.73	75.58
5	39.13	4.44	7.07	50.65
10	36.34	24.86	33.35	94.54
10	42.11	15.28	21.27	78.66
20	38.14	16.43	21.87	76.44
20	42.75	20.21	27.63	90.59
30	35.64	5.89	8.76	50.29
30	37.47	2.88	4.80	45.15
180	40.08	5.91	8.57	54.55
180	38.63	7.60	10.94	57.17

	SCA-3	Slag		Target	(40,40,20)	[wt%]
t	Si	RSD	Ca	RSD	Al	RSD
[min]	[ppmw]	[%]	[ppmw]	[%]	[ppmw]	[%]
0	169319	4.9	309068	5.1	105454	7.3
0	178574	2.8	330510	1.9	117594	1.7
5	192962	1.7	289399	6.6	95296	12.2
5	192756	1.5	269406	4.5	89980	2.3
10*	204767	4.6	266231	3.6	91200	2.7
10*	197672	4.9	251443	7.1	85603	7.9
10	181583	3	280964	4.3	95038	4.5
20	181472	2.7	292863	0.8	99922	3.7
20	184725	4.1	282666	4.5	98902	3.8
30	189977	3.1	296331	0.8	101102	2.8
30	191680	0.9	302575	1.4	102752	3.6
180	174452	2.5	305289	0.5	96482	2.4
180	181125	1.8	297783	2.1	100715	0.4

t	SiO_2	CaO	Al_2O_3	sum
[min]	[wt%]	[wt%]	[wt%]	[wt%]
0	36.22	43.24	19.93	99.39
0	38.20	46.24	22.22	106.67
5	41.28	40.49	18.01	99.78
5	41.23	37.70	17.00	95.93
10*	43.80	37.25	17.23	98.29
10*	42.29	35.18	16.18	93.64
10	38.84	39.31	17.96	96.11
20	38.82	40.98	18.88	98.68
20	39.52	39.55	18.69	97.75
30	40.64	41.46	19.10	101.21
30	41.00	42.34	19.42	102.76
180	37.32	42.72	18.23	98.27
180	38.75	41.67	19.03	99.44

Table B.3: This is the data pertaining to the repeatability series on the experiments detailed in section 3.1. ICP-MS data of dissolved Ca and Al in Si with their sampling error (relative standard deviation), with 3 sub-samples imaged from each sample. 3 additional sub-samples were also imaged by Atomic Adsorption Spectroscopy, where the rounded numbers are due to a lower compositional resolution. Here, Ca and Al came from SiO_2-CaO-Al_2O_3 slag (SCA) with the given composition in contact with pure Si at 1873 K for the listed time. * marks dual-scan entries of the same sub-sample, taken by the operator to verify the large disparity between replicates in ICP-MS.

(SCA) = (40,25,35), Replicate Set 1.						
	ICP-MS				Atomic Adsorption Spectroscopy	
t	Ca	RSD	Al	RSD	Ca	Al
[min]	[ppmw]	[%]	[ppmw]	[%]	[ppmw]	[ppmw]
5^1*	341	3.4	938	5.2	330	950
5^1*	386	3.7	976	5		
5	350	2.1	939	1.5	320	940
5^2*	379	5.1	943	5.8		
5^2*	395	4.3	945	3.1	340	920
10	524	1.9	2073	4.9	480	1900
10	466	2.6	1881	4.1	520	1900
10	484	1.8	1853	1.8	500	1900
20	655	4.5	3507	4.7	680	3000
20	669	1.3	3185	6.4	690	3000
20	702	2.9	3348	4.8	700	3000
30	1078	2.7	4539	2.2	1000	4000
30	1137	1.4	4786	3.1	1000	3900
30	1057	6.4	4606	5.3	1000	3900
60	1420	5.2	7065	3.4	1400	4800
60	1506	0.8	6145	4.2	1400	4900
60	1440	2.9	5833	3.1	1400	4900
180	1337	2.3	6036	3.8	1300	5400
180	1271	2.6	6191	2.1	1300	5500
180	1261	1.8	6038	3.2	1200	5200
210	1331	1.8	6246	2.4	1400	5500
210	1345	3.7	6366	2.4	1500	5400
210	1427	4.2	6466	3	1400	5500

(SCA) = (40,25,35), Replicate Set 2.						
	ICP-MS				Atomic Adsorption Spectroscopy	
t [min]	Ca [ppmw]	RSD [%]	Al [ppmw]	RSD [%]	Ca [ppmw]	Al [ppmw]
5	302	1.7	938	4.8	280	910
5	298	2.7	980	7.5	290	900
5	296	0.9	976	1.4	290	940
10	642	5.5	2450	7.9	680	2300
10	672	4	2463	1.6	690	2400
10	647	2.8	2448	7.9	660	2300
20	713	3.4	3522	2.4	690	3200
20	727	1.7	3435	5.7	720	3200
20	816	8.8	3582	4	720	3300
30	778	1.5	3995	2.9	770	3600
30	770	3.2	4240	8.8	770	3800
30	769	2.2	4115	4.5	740	3700
60	1189	3.5	6329	3.2	1100	5500
60	1173	2.9	6146	0.7	1000	5500
60	1144	5.8	6072	1.7	1100	5500
180	1160	2	5696	1.6	1100	4900
180	1121	0.1	5496	6.9	1100	4800
180	1186	5.8	5798	2.1	1100	4900
210	1770	3.9	6696	1.5	1900	6400
210	1731	5.5	7009	6.1	2000	6300
210	1594	4.5	6289	3.4	1900	6300

(SCA) = (40,25,35), Replicate Set 3.						
	ICP-MS				Atomic Adsorption Spectroscopy	
t [min]	Ca [ppmw]	RSD [%]	Al [ppmw]	RSD [%]	Ca [ppmw]	Al [ppmw]
5*	330	1.7	1197	5.5	330	1100
5*	331	2.2	1188	4.1		
5	344	1.4	1167	8	330	1100
5	236	4.1	784	6.2	320	1100
10	535	4.6	2185	6.8	520	2000
10	482	2.4	2111	4.8	540	2000
10	524	6.9	2180	4.4	520	2100
20	861	5.8	3882	4.1	970	3700
20	991	6.5	4267	8.2	990	3700
20	980	3	4552	0.5	920	3600
30	641	3.8	3073	5	650	2900
30	680	4.5	3401	4.9	610	2900
30	674	2.4	3332	2.1	610	2800
60	1203	2.2	5675	6.2	1300	4900
60	1346	2.3	5885	5.3	1400	4900
60	1220	4.2	5676	5.5	1400	4800
180	1059	6.1	5794	3.8	1300	5000
180	1074	4.3	6121	1.9	1400	4900
180	1021	3.9	5703	2.1	1400	4800
210	889	2.8	5673	2.2	940	5100
210	916	3.1	5840	7.6	890	5100
210	939	3.5	5667	4.6	940	5200

Table B.4: Combined mean and variance for the repeatability sets, with respect to each time step. Dual-scan entries for a single sub-sample have been statistically pooled, with the pooed value treated as a single entry.

ICP-MS				
(SCA) = (40,25,35), Replicate Set 1.				
t	$\overline{Ca}$	s^2	$\overline{Al}$	s^2
[min]	[ppmw]	[ppmw^2]	[ppmw]	[ppmw^2]
5	366	427	947	1563
10	491	694	1936	15276
20	675	847	3347	48838
30	1091	3028	4644	41342
60	1455	3782	6348	325500
180	1289	1985	6088	40900
210	1368	4013	6359	35909
(SCA) = (40,25,35), Replicate Set 2.				
t	$\overline{Ca}$	s^2	$\overline{Al}$	s^2
5	299	41	964	2894
10	654	941	2454	25523
20	752	4060	3513	25628
30	772	359	4117	72304
60	1169	2773	6182	29531
180	1156	2464	5663	71438
210	1698	12004	6665	166543
(SCA) = (40,25,35), Replicate Set 3.				
t	$\overline{Ca}$	s^2	$\overline{Al}$	s^2
5	303	2353	1048	39810
10	513	1200	2159	14983
20	944	5967	4234	124597
30	666	859	3269	38772
60	1257	5503	5745	115913
180	1051	3133	5873	57629
210	915	1239	5727	99995

Atomic Adsorption Spectroscopy				
(SCA) = (40,25,35), Replicate Set 1.				
t	$\overline{Ca}$	s^2	$\overline{Al}$	s^2
[min]	[ppmw]	[ppmw^2]	[ppmw]	[ppmw^2]
5	330	100	937	233
10	500	400	1900	0
20	690	100	3000	0
30	1000	0	3933	3333
60	1400	0	4867	3333
180	1267	3333	5367	23333
210	1433	3333	5467	3333
(SCA) = (40,25,35), Replicate Set 2.				
t	$\overline{Ca}$	s^2	$\overline{Al}$	s^2
5	287	33	917	433
10	677	233	2333	3333
20	710	300	3233	3333
30	760	300	3700	10000
60	1067	3333	5500	0
180	1100	0	4867	3333
210	1933	3333	6333	3333
(SCA) = (40,25,35), Replicate Set 3.				
t	$\overline{Ca}$	s^2	$\overline{Al}$	s^2
5	327	33	1100	0
10	527	133	2033	3333
20	960	1300	3667	3333
30	623	533	2867	3333
60	1367	3333	4867	3333
180	1367	3333	4900	10000
210	923	833	5133	3333

Table B.5: Combined mean and variance, with general median, for the combined repeatability sets, with respect to each time step.

Combination of all sets						
			ICP-MS			
t [min]	$\overline{Ca}$ [ppmw]	Median [ppmw]	s^2 [ppmw^2]	$\overline{Al}$ [ppmw]	Median [ppmw]	s^2 [ppmw^2]
5	323	336	1898	986	961	16715
10	553	524	6132	2183	2180	63651
20	790	727	16411	3698	3522	214622
30	843	770	34058	4010	4115	371630
60	1293	1220	18376	6092	6072	221639
180	1165	1160	12013	5875	5798	86744
210	1327	1345	108927	6250	6289	253391
			Atomic Adsorption Spectroscopy			
t	$\overline{Ca}$	Median	s^2	$\overline{Al}$	Median	s^2
5	314	320	443	984	940	6965
10	568	520	6302	2089	2000	35063
20	787	720	15656	3300	3200	78519
30	794	770	24517	3500	3700	215185
60	1278	1400	24691	5078	4900	91358
180	1244	1300	14321	5044	4900	64321
210	1430	1400	172522	5644	5500	259136

B.2 SiB and SiCaB Measurement Data

Table B.6: Measured [B] and [Ca] concentrations by ICP-MS, for two different initial alloy compositions, at different holding times at 1873 K in contact with a 45 (wt%SiO_2) and 55 (wt%CaO) slag. These data belong to section 3.2.

	SiCaB		SiB	
	Set-1	Set-2	Set-1	Set-2
Time [min]	B [ppmw]	B [ppmw]	B [ppmw]	B [ppmw]
5	233	251	312	-
8	218	235	245	280
12	190	172	219	203
20	152	122	152	174
30	106	126	132	114
60	74.4	96.3	119	84.5
60	79.4	94.4	123	88.1
Time [min]	Ca [wt%]	Ca [wt%]	Ca [wt%]	Ca [wt%]
5	0.853	0.632	0.523	-
8	0.684	0.99	0.557	0.454
12	0.831	0.859	0.626	0.726
20	0.806	1.06	0.77	0.624
30	0.903	0.87	0.805	0.944
60	1.05	0.947	0.824	0.747
60	1.23	0.913	0.762	0.876

B.3 SiCa-Alloy

Table B.7: Table containing the amount of Si and $CaSi_2$ in each batch of SiCa-alloy, including their calculated calcium concentration. All samples were cast into ingots except samples 1-1, 1-2, and 1-3 which were rapidly cooled in their respective crucible. Sample 2-1 consisted of two ingots of similar composition which shattered under handling and got mixed. Instead of separating them it was decided to treat them as one sample.

SiCa-alloy Batch	1-1	1-2	1-3	2-1	2-2
m_{Si} [g]	587.02	600.00	600.4	1060.00	533.50
m_{CaSi_2} [g]	42.36	46.31	46.28	131.12	65.95
$[wt\%$Ca]	2.80	2.98	2.98	4.58	4.58
SiCa-alloy Batch	2-3	3-1	3-2	3-3	3-4
m_{Si} [g]	533.00	531.50	531.00	533 .00	530.50
m_{CaSi_2} [g]	65.70	75.38	75.67	75.79	75.65
$[wt\%$Ca]	4.57	5.17	5.19	5.18	5.20
SiCa-alloy Batch	3-5	3-6	3-7		
m_{Si} [g]	532.00	529.50	530.00		
m_{CaSi_2} [g]	75.24	75.31	75.01		
$[wt\%$Ca]	5.16	5.18	5.16		

Here, information about the produced SiCa-alloy is shown in table B.7. The alloy was created by melting $CaSi_2$ and silicon granules in a graphite crucible. This was performed in an induction furnace under an inert atmosphere, here Ar 5.0. Each batch was melted at 1873–1923 K, and then the temperature was lowered to 1773 K, reducing losses to fuming. The alloy was kept at 1773 K for at least 30 min to ensure mixing, before being cast into a water-cooled copper mold placed inside the furnace, ensuring rapid cooling. To reduce losses to the formation of carbides the crucibles were impregnated with an inner SiC layer[87], by first melting a sacrificial batch of only pure silicon in them. Each crucible was used multiple times.

Each batch had a target of 600 to 650 g alloy, with differing weight percent of Ca. Due to the volatility of $CaSi_2$ in contact with water (including moisture in the air), each batch was prepared in a glove-box before controlled transfer to the furnace.

Table B.8: Measured and target [wt%Ca] in ingots. The meta-samples were made by crushing equal amounts of batch 3-1 to 3-5 into a single sample. 3 separate meta-samples were tested.

Batch	Measured [wt%Ca]	Target [wt%Ca]
3-1	6.59	5.17
3-2	3.36	5.19
3-3	3.30	5.18
3-4	3.20	5.20
3-5	4.03	5.16
Meta-1	3.79	
Meta-2	3.48	
Meta-3	4.03	
3-6	3.33	5.18
3-7	4.28	5.16

To evaluate the SiCa-alloy, several ingots which should contain an equal amount of Ca were tested by ICP-MS, seen in table B.8. From the table, it is quite clear that the measured and target [Ca] concentrations are not similar, but there is a high degree of homogeneity between 3 to 3.4 [wt%Ca], with some extreme deviations from these values. The meta-samples were made by combing 0.5g from batches 3-1 to 3-5, and should contain [wt%Ca]$\approx$4.2, based on the individual batch measurements. A 95% confidence interval generated from the meta-samples predicts a mean concentration somewhere within the bounds $\overline{[\text{wt\%Ca}]}\in$[3.08, 4.45], where 4 of the batch samples are far towards the lower end of this bound, 2 are towards the upper end, and 1 is far above the upper bound, with this spread (deviation from the meta-sample mean) not being randomly distributed at a 95% confidence.

A.6 shows that there is strong linear correlation between the initial target composition and surface oxidation in the lab-scale OLR experiments, which indicates that the actual [Ca] content in the initial lab-scale alloy was not significantly different to the initial target Ca concentration. This would not be the case if the SiCa-ingots contained an amount of Ca expected from table B.8. Significant loss of Ca to surface oxidation during casting of the ingots can also be ruled out, as this would cause an imbalance between the surface oxidation effect from Ca and Al, as Ca would already be oxidized, which is not seen. Instead, it is though that the deviation was the result of phase segregation, such that the ingots contain a phase high in Ca and one low in Ca. Large ingot chucks where used during the lab-scale experiments, making any segregation irrelevant, as all Ca would enter the alloy regardless. This would also account for the high homogeneity seen in the lower [wt%Ca] measurements, and the deviations from this, in table B.8.

Figure B.1: Image of the SiCa-ingots.

The lower values represent the phase with low Ca content, while the deviations are the result of different amounts of the phase high in Ca. Thermodynamic calculations were performed in FactSage 7.3[56], with FactPS, FT-oxid, and FT-lite/custom database from paper 5, but no adequate solution was found.

B.4 Lab-Scale Experiments: Estimated Initial Content of Ca and Al, and Refining Measurements.

Table B.9: Estimated initial content of each lab-scale experiment. The concentration of Al and Ca were calculated from the total charge mass m_{tot}^{in} [g], and the calculated mass of Ca and Al in the alloying agents. m_{tot}^{in} includes the SiCa-alloy, silicon, and aluminum foil. Ca content was calculated using pure $CaSi_2$ (χ_{Ca}=0.33..., χ_{Si}=0.66...). All numbers were rounded to the second decimal place.

Experiment	(0.5,0.5)-1	(0.5,1.5)-1	(1,1)-1	(0.5,1.5)-2
m_{tot}^{in}	3003.08	2999.12	3001.00	2999.70
$[wt\%Al]$	0.50	1.50	1.00	1.47
$[wt\%Ca]$	0.51	0.51	1.03	0.51
Experiment	(1,1)-2	(1.5,0.5)-1	(1.5,0.5)-2	(1.5,1.5)-1
m_{tot}^{in}	2999.77	3004.37	2993.08	2999.82
$[wt\%Al]$	1.01	0.50	0.51	1.53
$[wt\%Ca]$	1.00	1.51	1.51	1.47
Experiment	(0.5,0.5)-2	(1.5,1.5)-2	(1,1)-3	
m_{tot}^{in}	2999.55	3058.32	3000.14	
$[wt\%Al]$	0.50	1.47	1.01	
$[wt\%Ca]$	0.47	1.53	1.00	

Table B.10: Ca and Al content from the lab-scale measurements, analyzed by ICP-SFMS. These measurements belong to section 3.3.

(0.5,0.5)				
	Set-1		Set-2	
t [min]	Ca [ppmw]	Al [ppmw]	Ca [ppmw]	Al [ppmw]
0	425	2810	331	2800
0	428	2670	-	-
0	339	2530	-	-
5	142	1920	44.3	2450
7	195	2250	42.1	2650
7	94.6	2010	-	-
7	128	2120	-	-
10	85.3	2050	32.3	2830
15	28.2	1900	48.3	2670
15	38.6	2130	-	-
(0.5,1.5)				
	Set-1		Set-2	
t [min]	Ca [ppmw]	Al [ppmw]	Ca [ppmw]	Al [ppmw]
0	564	6860	2130	9520
0	530	7440	735	9320
0	786	8610	1870	2160
5	183	5840	221	6540
7	132	5080	1030	8040
7	-	-	1100	7900
10	135	5570	1720	8460
15	36.5	4800	152	6410
(1.5,0.5)				
	Set-1		Set-2	
t [min]	Ca [ppmw]	Al [ppmw]	Ca [ppmw]	Al [ppmw]
0	836	3700	4430	2860
0	-	-	3960	2800
0	-	-	4160	2730
5	154	3870	1690	1930
5	193	3800	-	-
7	130	4040	957	1590
7	-	-	1240	1640
7	-	-	1060	1640
10	255	4420	1210	1620
15	287	4420	584	1250

Table B.11: Ca and Al content from the lab-scale measurements, analyzed by ICP-SFMS. These measurements belong to section 3.3.

(1,1)						
	Set-1		Set-2		Set-3	
t [min]	Ca [ppmw]	Al [ppmw]	Ca [ppmw]	Al [ppmw]	Ca [ppmw]	Al [ppmw]
0	2130	5780	1550	4280	1750	7150
0	2070	5830	1650	4520	-	-
0	1770	5250	-	-	-	-
5	283	3540	559	3560	739	5350
7	227	3280	480	3300	698	5350
10	151	3280	276	2820	280	4150
10	1030	3900	-	-	-	-
15	228	3080	391	3070	430	4490

(1.5,1.5)				
	Set-1		Set-2	
t [min]	Ca [ppmw]	Al [ppmw]	Ca [ppmw]	Al [ppmw]
0	2200	7940	1720	8860
5	967	6040	437	7210
7	681	5480	295	6790
10	608	5330	310	5730
15	475	4900	168	6060

B.4.1 Measurement Accuracy of [Ca]

Ca is generally more difficult to measure than [Al]. One part of this, is because the concentration of [Ca] is much lower towards the end of the refining cycle. Figure B.2 shows that there is a clear relation between the concentration of [Ca][1] (effect size), and the relative size of the 95% confidence interval. Of 11 sample point with replicates, 7 had three replicate measurements, with 1 not significantly different than zero at a 95% confidence (they are to the right of the stippled line in figure B.2), and 4 with two replicate measurements, where 2 not significantly different than zero at a 95% confidence.

[1] It is assumed that the replicates points are part of a normal distributed population, making them t-distributed.

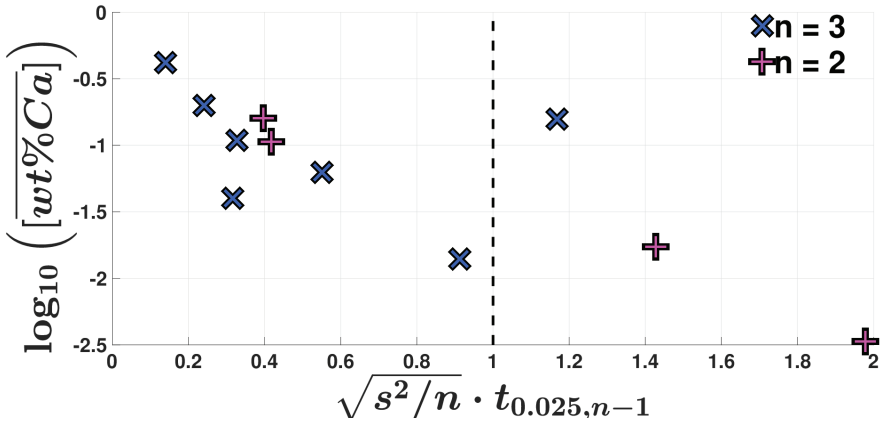

Figure B.2: Mean [Ca] concentrations at sample points with replicates against the relative size of their respective 95% confidence intervals. Sample points are colored and marked according to their number of replicates. If a marker is to the right of the black stippled line then it is not significantly different than zero to a 95% confidence.

Figure B.2 clearly indicates that lower measured [Ca] concentrations are expected to vary more, necessitating higher statistical resolutions, i.e. more samples, at lower [Ca] concentrations. While the laboratory-scale experiments do not focus on measuring specific concentrations very accurately, instead opting for behaviors, the figure shows that it proper to spend a portion of the replicate points in the area where the [Ca] concentration was low, but that even more needed to be spent to accurately describe this area. The figure also states that for future experiments, initial target concentrations which expect to reach low [Ca] concentrations, like (0.5,0.5), need at least 3 replicate measurements to get a decent value for the concentration in the low [Ca] region, but 5 is probably advised[2].

[2]Due to the extremely small[88] sample size, going from 3 to 5 samples allows many new statistical tests to be used, while going from 3 to 4 only gives a slightly better result. This is due to the large statistical improvements in extremely small and small sample size statistics which can be gained by reaching specific sample size benchmarks, making these types of experiments very "feast or famine" with respect to their extractable quantity and quality of information.

Appendix C

Papers

Paper 1

ORIGINAL RESEARCH ARTICLE

Nucleation of SiO_2-CaO-Al_2O_3 Slag in Oxidative Ladle Refining of Metallurgical Grade Silicon

ERLEND L. BJØRNSTAD and GABRIELLA TRANELL

Oxidative ladle refining (OLR) is the most used refining method in industrial production of metallurgical grade silicon. OLR is performed by purging the liquid alloy with oxygen-enhanced air at 1823 K to 1873 K, reacting with silicon and the primary slag forming impurities to a SiO_2-CaO-Al_2O_3 slag. To further increase our capability to control this process, it is paramount to understand how the slag nucleates and forms, and represent it such that it is useful for predicting and controlling the process behavior. This work aims to formulate a comprehensive theoretical description of slag nucleation and formation at nano/microscale using classical macroscale thermodynamics, bridging these spatial regimes. To achieve this, the work argues that silica's liquid structure allows its nuclei to exhibit "well defined" surfaces. Furthermore, silica is predicted to be highly surface active, so if its concentration is high while the slag nucleus is small, the SiO_2-CaO-Al_2O_3 slag should retain silica's surface properties. An experiment confirmed the surface active nature of silica in the SiO_2-CaO-Al_2O_3 system. It was also shown that increasing the slag's calcia concentration has a greater effect on the interfacial tension between the molten slag and liquid alloy than alumina, confirming industrial observations of the coupling between refining rate and relative alloy/slag composition.

https://doi.org/10.1007/s11663-021-02132-7

I. INTRODUCTION

METALLURGICAL grade silicon (MG-Si) sees widespread use as a raw material or additive in many processes and products, such as silicones and aluminum alloys. It is also a precursor for photovoltaic and electronic grade silicon. MG-Si is typically produced by carbothermally reducing quartz in a submerged arc furnace (SAF). Further refining is then performed to customer specification. While any given plants refining scheme might differ, it typically includes oxidative ladle refining (OLR), a process through which the continuously tapped alloy is purged with an air-oxygen mixture. OLR is primarily used to reduce the content of Ca and Al, which enter the process as part of the raw materials. A typical ladle contains over 7 tonnes of molten silicon when full, with a height of 2 to 2.7 m and top width of 1.5 to 1.8 m, as seen in Figure 1. Impurity concentrations of Al and Ca in the melt tapped into the ladle lie typically between 0.5 and 2 wt pct, and is refined to approximately 0.01 to 0.5 [wt pct Ca] and 0.1 to 1.2 [wt pct Al]*, depending on which silicon alloy is being produced. The process as a whole takes between 1 and 2 hours, where further gas purging may continue as necessary to reach the desired impurity composition, after tapping ends. Temperatures typically range from 1500 °C to 1700 °C, where the desired process temperature lies between 1500 °C and 1600 °C. Impurities are transferred to a slag phase, created through reactions between the gas and melt. As the bubbles ascend, [Si] (Si in the melt phase) reacts with $\{O_2\}$ (O_2 in the gas phase) to form (SiO_2) (SiO_2 in the slag phase) and $\{SiO\}$ through equilibrium reactions 2 and 1. Through reaction 2, (SiO_2) nucleates on the bubble surface, initiating slag formation. While the nucleus grows, (SiO_2) will react with the primary slag forming impurities [Al] and [Ca], resulting in a predominantly SiO_2-CaO-Al_2O_3 slag droplet. The relevant reactions are assumed to be as follows:

1. $2[Si] + \{O_2\} = 2\{SiO\}$
2. $[Si] + \{O_2\} = (SiO_2)$
3. $2[Ca] + (SiO_2) = 2(CaO) + [Si]$
4. $4[Al] + 3(SiO_2) = 2(Al_2O_3) + 3[Si]$
5. $2[Al] + 3(CaO) = (Al_2O_3) + 3[Ca]$

*Product data sheets accessed 06.05.20 from suppliers: Elkem(Silicon 99, SiLLOY 130/170), HOSHINE(Silicon Metal(multiple alloys)), and BAIDAO(Silicon Metal(multiple alloys)).

ERLEND L. BJORNSTAD AND GABRIELLA TRANELL are with the Department of Materials Science and Engineering, Norwegian University of Science and Technology, Bergbygget E-133, Alfred Getz vei 2, IMA, NTNU, N-7491 Trondheim, Norway. Contact e-mail: erlend.l.bjornstad@ntnu.no

Manuscript submitted September 18, 2020; February 12, 2021.

Published online: 09 April 2021

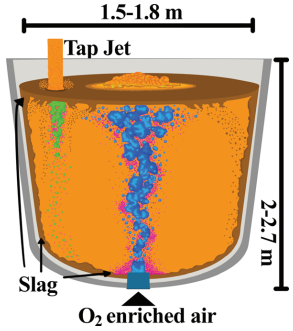

Fig. 1—Ladle refining system including the falling jet. Bubbles of entrapped air are displayed in green while the central bubble column is colored in blue. Slag leaving the bubbles is here displayed in purple, while the settled slag is in brown.

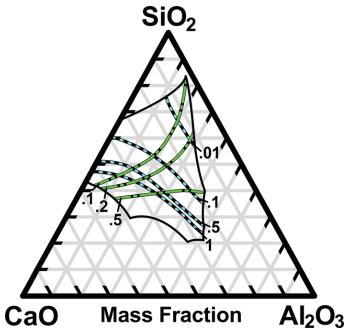

Fig. 2—How the equilibrium concentration of Ca(Blue) and Al(Red) (in wt pct) dissolved in liquid Si changes when in contact with different SiO_2-CaO-Al_2O_3 slags at 1823 K. Calculated from Sigworth[2]

The slag will still contain small concentrations of other oxide-forming impurities, such as Ba, rare-earth elements, Mg, etc.,[1] but as minor components, they are not considered further in this work. To provide an idea of how the two primary slag forming impurities act with changing slag composition, Figure 2 summarized by Sigworth,[2] shows how the equilibrium concentration of the impurities dissolved in liquid silicon changes with the slag composition.

At a certain point the droplet detaches from the ascending bubble, allowing coalescence with other droplets and further reactions with the melt. The slag droplet's path through the melt is determined by its perceived flow field and physical properties/composition, where the slag eventually settles at the ladle floor, walls, or as a floating top slag. While widely used, there are still many aspects of OLR in MG-Si production which are not well described in the literature. Schei *et al.*[3] compiled much of the literature prior to 1998, providing an overview of both system thermodynamics and some important slag properties. Important aspects of slag forming kinetics on the gas bubbles however, were not described. Olsen *et al.*[4] and Ashrafian *et al.*[5] later attempted to describe and model different aspects of the OLR process. While promising, the modeling work suffered from a lack of open experimental data in certain key areas. Kero *et al.*[1] later provided data from an industrial refining campaign, where samples were taken in different ladles during the refining process.

The main piece of information currently missing for OLR pertain to the reaction kinetics between the gas, melt, and slag, and how the slag nucleates and grows on the bubble surface.

Hence, the current work aims to give a cohesive theoretical description of nucleation, species interaction, and slag behavior, supported by experimental work. Collectively, the work forms the basis of a new model framework for the OLR process, starting with the reactions on each individual gas bubble.

Table I. System Parameters from Olsen *et al.*[4]

$X_{\{O_2\},0}$	$X_{\{N_2\},0}$	$T\,[K]$	$\bar{d}_{b,0}\,[m]$	$H\,[m]$
0.5	0.5	1900	0.01	0.69

II. THEORETICAL FRAMEWORK: NUCLEATION AND SLAG FORMATION

As a start, it is useful to determine the maximum amount of slag that can be generated by a single gas bubble. This provides an upper bound, when looking at the size domains relevant for slag nucleation and initial growth. A possible method of handling the scaling issues relevant to transitioning between different size domains, from nano- to macroscale, is subsequently presented.

A. *Slag Generated on Each Bubble*

Olsen *et al.*[4] modeled industrial refining of a 2 tonne ladle, using typical industrial parameters. They estimated a Sauter mean bubble diameter, using a model from Calderbank,[6] between 7 and 10 mm, with a gas flow rate of 45 Nm^3/h.[4] Table I lists some of the model parameters used in the study, together with the bubble diameter used in further calculations.

Here $X_{\{O_2\},0}$, $X_{\{N_2\},0}$ are the initial mole fractions of $\{O_2\}$ and $\{N_2\}$ in the purge gas, $T\,[K]$ is the melt temperature, and $\bar{d}_{b,0}\,[m]$ is the initial Sauter mean bubble diameter. $H\,[m]$ is the melt height over the plug. Assuming an ideal gas, the initial amount of gas molecules in a gas bubble can be expressed as:

$$n_{g,0} = \frac{V_b P_b}{RT}\,[mol] \qquad [1]$$

where $V_b\,[m^3]$ is the initial bubble volume of one bubble, and $R\,[J/molK]$ is the ideal gas constant. P_b is the pressure inside a bubble, which Olsen *et al.* assume

equal to the atmospheric pressure. $\{O_2\}$ reacts to form (SiO_2) and/or $\{SiO\}$, where the amount of each species in moles, $n_{\{SiO\}}$ and $n_{(SiO_2)}$ $[mol]$, can be calculated as a function of the initial oxygen molar fraction in the gas bubbles, here assumed to be equal to that in the purge gas $X_{\{O_2\},0}$.[7]

$$n_{\{SiO\}} = (1 - X_{\{O_2\},0}) n_{g,0} \frac{p_{\{SiO\}}}{P_b - p_{\{SiO\}}} \quad [2]$$

where $p_{\{SiO\}}$, using thermodynamic data from the FACT oxide database,[7] can be expressed as

$$p_{\{SiO\}} \approx \frac{n_{\{SiO\}}}{n_{\{SiO\}} + n_{\{N_2\}} + n_{\{O_2\}}} P_b \quad [3]$$

$$= \left(\frac{\exp\left(11.13 + \frac{39464}{T}\right)}{\exp\left(-23.66 + \frac{113623}{T}\right)} \right)^{\frac{1}{2}} P_b \qquad [Pa] \quad [4]$$

If one assumes that all oxygen in the gas bubble forms $\{SiO\}$ and (SiO_2) then:

$$n_{(SiO_2)} = n_{g,0} X_{\{O_2\},0} - \frac{1}{2} n_{\{SiO\}} \quad [5]$$

Combined, these allow the maximum amount of (SiO_2) produced by a single bubble to be calculated, assuming spherical bubbles. Using $\rho_{[Si]} \approx 2500\, kg/m^3$[8] and $\rho_{(SiO_2)} \approx 2212\, kg/m^3$[4] at 1900 K, together with parameters from Table I, gives $m^{tot}_{(SiO_2)} \approx 0.11$ mg, which corresponds to a sphere with diameter $d^{tot}_{(SiO_2)} \approx 0.46$ mm. It should also be noted, that as the slag composition changes so will its density. Interactions between slag and dissolved [Ca] and [Al] will lead to an increase in both (wt pct CaO) and (wt pct Al_2O_3), which in turn will result in a higher density, thus decreasing the diameter. This means that a slag consisting of pure SiO_2 will always provide the largest diameter possible.

For all molten SiO_2-CaO-Al_2O_3 slag compositions at 1823 K (1550°C), it can be shown that they will not change the earlier diameter of ≈0.46 mm, by more than 0.05 mm. While this represents a size given thermodynamic equilibrium, reaction kinetics and/or flow might affect the droplet size. Still, it provides a useful insight, and shows most notably that the maximum amount of slag one bubble can produce is small compared to the bubble itself, as seen in Figure 3.

It is important to note that $m^{tot}_{(SiO_2)}$ is the maximum mass of (SiO_2) over all slag droplets an individual bubble can produce over its ascent. Thus, it seems reasonable to assume that each individual slag droplet is smaller than this value, most probably by orders of magnitude. This corresponds with analytical observations from the industry, where some of the sampling deviation is attributed to the presence of imperceptible micro-slag droplets in the metal. However, this has not been documented in any scientific publications.

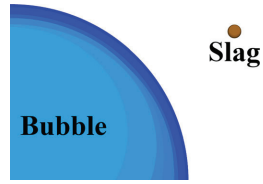

Fig. 3—Size comparison between a bubble and a slag droplet consisting of the total amount of SiO_2 which can be produced by said bubble, using parameters from Table I.

An important note about the slag droplet size estimation is that changing process parameters, within reasonable boundaries, does not have a great impact the size regime. Adding hydrostatic pressure, changing the temperature $T \pm 100$ K/°C, and/or assuming no production and back-filling of the bubbles with SiO ($n_{\{SiO\}}=0$), the total slag droplet diameter will not change significantly. The effect of these changes will result in a change in droplet diameter $\Delta d^{tot}_{(SiO_2)} < 0.04$ mm. Using different literature values for the density of molten silicon $\rho_{[Si]}$ or for silica $\rho_{(SiO_2)}$ does not change the size markedly either. Increasing the initial molar fraction of oxygen in the bubbles $X_{\{O_2\},0} \pm 0.2$ and the bubble size $\bar{d}_{b,0} \pm 5$ mm produce more significant changes, but the total slag droplet diameter is still within $\Delta d^{tot}_{(SiO_2)} < 0.5$ mm.

B. *Slag Nucleation*

The lower spatial boundary considered relevant to slag formation in OLR is assumed to be the slag's initial nucleus size. This size represents the initial condition for nuclei growth, as the system must be able to accommodate oxide nuclei of this size before the slag phase can form and subsequently grow. In this work only heterogeneous nucleation will be covered, as it is assumed that the slag forms on the gas bubble itself. The initial nucleus size is traditionally associated with the nanoscale, where many of the models and assumptions used at the micro/macro domain start to falter. An important aspect for such a model is where one phase ends and a new phase begins, i.e., a surface. Gibbs 9 and 10 divides two phases by placing a dividing surface/plane, separating the phases. This plane is a mathematical construct which cleanly separates each phase into uniquely distinguishable volumes without a gradual transition between the phases, allowing each surface to be clearly defined. Thermodynamic properties like surface tension, phase volume, surface area, etc. are properties of this plane, as these are all properties defined by the surface. Separating phases as described above is called the cluster approach (CA). This approach works well in systems where the surface region represents only a small part of the phase as a whole, but is not necessarily applicable for smaller systems where the surface region will represent a significant portion of the phase. In reality the surface can be viewed as a continuous change in a phase's respective particle density, as it continuously

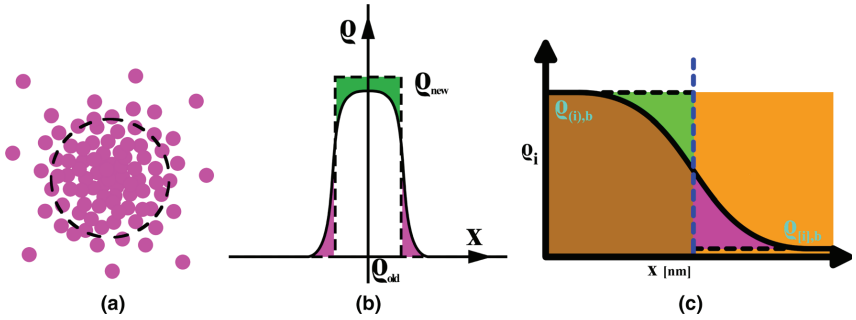

Fig. 4—Schematic descriptions of two approaches to define a surface. (*a*) The cluster approach. Particles shown in pink and the phase's surface is shown by the dotted line. (*b*) Density functional approach. The black line ($\varrho(x)$) is the particle density function of a given species as one moves from one phase to the other. The pink area represent the concentration excluded by the cluster approach (The particles outside of the dotted line in a), and the green area represents the additional concentration added to the cluster to compensate for this. (*c*) Particle density of a species *i* changes as one passes from the bulk of the slag in brown to the melt in orange. The dotted line indicates the equimolar dividing surface.

changes from the bulk density of the first phase to the bulk density of the second. This is called the density functional approach (DFA), and gives a more accurate representation of the surface than CA. Even though phase boundaries can be defined in multiple other ways, one finds that CA and DFA are the ones primarily used.[11] A more comprehensive description of DFA can be found in the literature (Kalikmanov[12], Kashchiev[11]).

Figure 4(b) shows a comparison between these two methods, where the particle density function $\varrho(x)$ is given by the black line, the pink area under the line represents the particles not accounted for by the cluster approach (the ones outside the dotted line in Figure 4(a)), and the green area represents the extra particles added to try to compensate for the ones left out. The problem with DFA is that it is very computationally demanding, requires experimental data which is currently out of reach in regards to the OLR process, and solves problems very differently than classical macroscale thermodynamics. CA on the other hand, has been researched to a much greater extent, requires significantly less computational time,[11] and uses a very similar mindset to that of classical macroscale thermodynamics, like sharing similar parameters/properties. Another benefit of a well defined phase boundary, like in CA, is that the boundaries of a nuclei is clearly defined, which is required for assigning it certain thermodynamic phase properties. These phase properties are to list a few: volume $V\,[m^3]$, surface area $A_s\,[m^2]$, surface σ_{ii} and interfacial energy density $\sigma_{ij}|_{i\neq j}\,[J/m^2]$ (which for liquids is the same as surface and interfacial tension), and particle count $\varsigma\,[\#particles]$. In contrast, DFA's particle density function describes the phase and its transitional regimes as a whole. Seen in this context it makes no sense to assign a phase a surface area for instance, as it is in truth a mathematical construct and not a true physical property. While DFA provides a more accurate depiction of the physical world, it is difficult to combine with other micro/macro theories found in the literature, as its system description and parameters are fundamentally different to those traditionally used (along with its previously noted solvability issues). This makes it easier to compare and integrate CA with other micro/macro theories in the literature, as they share the same parameters and are built with similar mindsets. Thus at the current date, CA is preferred over DFA if possible.

When using CA to describe slag nucleation in OLR, the first challenge comes from CA not necessarily being applicable for nanoscale systems. For CA to be applicable it must first be demonstrated that the slag can be assumed to exhibit a clearly defined surface. This can be rephrased as a surface for which the surface tension σ_{ii} is not a function of cluster size, or:

$$\frac{d\sigma_{ii}}{dr} \approx 0 \qquad [6]$$

Here dr is the change in phase surface curvature which, assuming a given phase geometry like a sphere and a given particle density, can also be expressed by the number of particles in a phase ς_p. A consequence of this is that the surface structure will be consistent regardless of the phase size.

This phenomenon can be visualized by picturing a surface consisting of small triangles, with a given size, approximating a sphere. Triangles can simply be added or removed to change its size without changing the surfaces overarching structure, as long as the sphere is large compared to the triangles themselves. However, if the sphere shrinks too much, the triangles will no longer be able to retain their approximate spherical shape. The surface structure must therefore change to accommodate this change in size, causing it to change its surface tension σ_{ii}. Kashchiev[11] describes the thermodynamic surface tension for a droplet becoming less and less sensitive to changes in its curvature $\Delta\sigma_{ii}(\varsigma_p)$ as it becomes larger. This has also been shown by others,

like the modeling work of Thompson *et al.*[13] From Kashchiev and Thompson et al., $\varsigma_p > 1000$is here assumed as the size a slag nuclei/droplet needs to attain before CA is a generally applicable approximation. This is based on Kashchiev and Thompson *et al.*'s limits pertaining to simple liquids, where the proposed framework is based on the slag exhibiting non-simple behaviors while the nucleus is small.

Schweigert *et al.*[14] have performed molecular modeling of SiO_2 clusters over the range T=1500-2800 K, and found that its surface tension is relatively constant down to 24 SiO_2 molecules, implying that the surface structure does not change significantly with size. Hence, a SiO_2 cluster may then be viewed as an outer surface shell encompassing the bulk. One aspect which must be noted about the results from Schweigert *et al.* is that their value for the surface tension of silica ($\sigma_{SiO_2}([1999\ K, 2300\ K]) \approx [0.58, 0.67]\, J/m^2$) does not fit the literature value ($\sigma_{SiO_2}([1999\ K, 2300\ K]) \approx [0.30, 0.31]\, J/m^2$). This is attributed to the chosen interatomic potential being tuned for a bulk phase and not the surface, but the overall behavior of the cluster should still hold. Work by Roder *et al.*[15] and Vaccaro *et al.*[16] also found a similar shell-like structure in SiO_2 nanoparticles, where Roder *et al.*'s model only covers higher temperatures and particle amounts and Vaccaro *et al.* measures the shell thickness experimentally at room temperature. Since this shell structure is found by multiple groups, it strengthens the notion that silica also has this structure at nanoscale. In OLR, due to the alloy mainly consisting of Si, the slag nuclei is expected to start as pure SiO_2. (SiO_2) will then react with [Ca] and [Al], as the nucleus grows. Until experiments are performed to verify/disprove the molecular modeling results of Schweigert *et al.*[14], it is prudent to assume that the CA can be applied to the initial slag nucleus, if we assume that it consists of pure silica and contains more than 24 SiO_2 molecules, even though it might be a rough approximation. The next challenge comes in placing the dividing surface between the slag and both silicon melt and gas bubble. Thermodynamic phase properties like phase volume** are by default not necessarily equal to their physical counterparts as the CA is internally consistent for any arbitrary dividing surface.[9,10] As such, a dividing surface must be chosen where the calculated thermodynamic properties and physical measurements align so that the theoretical surface is representative of the physical object. This is necessary to ensure that any calculated thermodynamic parameter will match its physical counterpart, as only the physical parameter can be measured.

Figure 4(c) shows one such way of placing the dividing surface, called an equimolar dividing surface. Here, the area in green shows the number of particles which do not get accounted for by placing the dividing surface as shown, similar to the particles outside of the circle in Figure 4(a). To compensate, an equal amount of particles are added to the slag, here shown in pink. This placement of the dividing surface thus conserves the number of particles in each phase, making it equimolar. In multicomponent phases, each individual components density function $\varrho_{p,i}$ will not necessarily align as each species may exhibit different degrees of surface activity, adding extra layers of complexity in placing a representative dividing surface.

As such, if a single species is much more surface active than the others, it might define the surface, meaning this species alone can be used as a guide to place a surface which is more representative of the phase as a whole, like depicted in Figure 5. Figure 5 shows the particle density functions of two species i and j, where species i is surface active while j is not. From the figure, one can see that the equimolar dividing surface given by species i, provides a more representative boundary between the slag and metal melt than the dividing surface from species j. How Al and Ca affect the slag will be discussed further in Section II–C. This section will continue with the nucleation of pure silica nuclei, formulating an expression of the slag's initial nucleus size, assuming CA.

Here it is assumed that the nucleus behaves closer to that of a liquid than a rigid solid, even though the initial nucleus is assumed to consist solely of silica, which melts at 1725°C, and temperatures in OLR are generally in the range of 1500 °C to 1700 °C. Hence, the properties of liquid silica will be used if not otherwise specified. Due to its size regime and the structural comparison/transition of amorphous silica to its liquid form, coupled with

**Volume of the whole system is conserved and does not depend on the dividing surface, only the volume assigned to the specific phase.

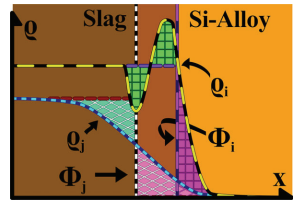

Fig. 5—Particle density functions ($\varrho(x)$) of the surface active species i with lines in black and yellow, and the non surface active species j in blue, where **x** represents distance from the bulk slag phase. Φ_i (purple and pink) and Φ_j (black and white) indicates the equimolar dividing surface.

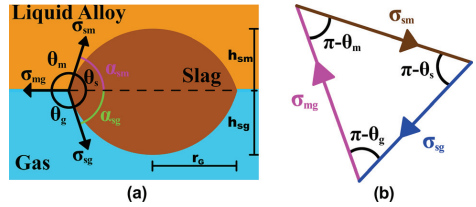

Fig. 6—(*a*) Three-fluid system. Interfacial tensions, σ_{ij}, and contact angles, θ_i, α_{ij}, are given. Droplet radius, r_G, and heights, h_{sm}, h_{sg}, are also shown. (*b*) Neumann Triangle in radians.

the reactions exothermic nature, this assumption is thought to be acceptable, while a similar approach can be performed with a rigid solid nucleus as well.

One could argue that a higher temperature should be used due to the highly exothermic nature of silicon's reactions with oxygen. This is not considered in this work, but if this is the case then it will further strengthen the assumption that silica behaves a liquid and not a rigid solid. Some slight indications that a higher temperature should be used will be seen later when discussing Figure 8. A small molten slag droplet which rests on a gas bubble surface in a metal melt gives a three-fluid system, and is thus assumed to satisfy Neumann's vector relation such that it exhibits a lens shape.[17] Figure 6(a) illustrates the three-fluid system, where it can be seen that the interfacial tension vectors are separated by the phase angle for each phase θ_s, θ_m, and θ_g. The lens can further be divided into two spherical caps, dividing θ_s into contact angles between the slag/melt α_{sm} and gas/slag α_{sg}, with limits:

$$0 < \theta_s < 180^\circ \qquad 0 < (\alpha_{sm}, \alpha_{sg}) < 90^\circ \qquad [7]$$

It is convenient to visualize how the vectors in Figure 6a relate to each other as a triangle, commonly known as a Neumann Triangle and can be seen in Figure 6(b). Using this triangle, one can express how the interfacial tensions relate to each other and the phase angles, like for instance the interfacial tension between slag and melt σ_{sm} can be expressed as:

$$\sigma_{sm} = \sqrt{\sigma_{mg}^2 - \sigma_{sg}^2 \sin^2(\theta_s)} - \sigma_{sg}\cos(\theta_s) \left[\frac{J}{m^2}\right] \qquad [8]$$

An expression for the initial slag nucleus size can then be formulated:

$$n^* = \frac{32\pi}{3}\frac{V_{0,mol}^2 \sigma_{sm}^3}{\Delta\mu^3} f(\alpha_{sm}, \alpha_{sg}) \ [mol] \qquad [9]$$

$$f(\alpha_{sm}, \alpha_{sg}) = \psi(\alpha_{sm}) + \left(\frac{\sin(\alpha_{sm})}{\sin(\alpha_{sg})}\right)^3 \psi(\alpha_{sg}) \qquad [10]$$

$$\psi(\alpha_{ij}) = \frac{(2 + \cos(\alpha_{ij}))(1 - \cos(\alpha_{ij}))^2}{4} \qquad [11]$$

Here, $V_{0,mol}\,[m^3/mol]$ is the molar volume of the species the nuclei consists of at nucleation (here SiO_2), $\Delta\mu\,[J/mol]$ is the thermodynamic chemical potential driving the nucleation, and $f(\alpha_{sm}, \alpha_{sg})$ is a geometric term to account for the fact that we have a lens and not a sphere. How to generate these equations, together with a more in depth coverage of nucleation itself is described by Kashchiev 11.

The driving force for nucleation in the case of OLR can be expressed as a local over-saturation of dissolved oxygen in the melt, as this allows Si to react with oxygen in the first place. This over-saturation can be expressed as the change in chemical potential resulting from the difference in the activity of silica at the oxygen saturation limit in silicon, and the activity of silica when in contact with the gas phase, the bubbles, shown in Figure 7. This will also account for the formation of {SiO}. Assuming that the activity of silicon does not change in the melt, the chemical potential can be expressed as

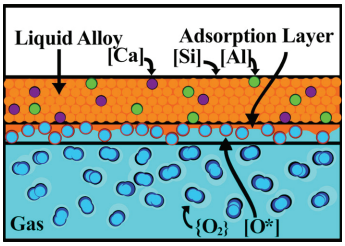

Fig. 7—Schematic representation of the melt/gas interface.

$$\Delta\mu = -RT\ln\left(\frac{a_{\{O_2\}}}{a_{[O]}^2}\right) \qquad [12]$$

$$\lim_{[\text{wtpctO}]\to 0} a_{[O]} = c_{[O],sat} \qquad [13]$$

Here $a_{[O]}$ is the activity of [O], assumed to be equal to the dimensionless oxygen saturation concentration in silicon with respect to 1 wt pct dissolved species in molten Si, $c_{[O],sat}$. $a_{\{O_2\}}$ denotes the activity of oxygen in the gas bubble with respect to a 1 bar reference state. It should be noted that the reason $a_{\{O_2\}}$ is used instead of dimensionless oxygen pressure in the gas $p_{\{O_2\}}$, is due to that the oxygen concentration in the bubbles that the melt sees might not be equal to the bulk oxygen partial pressure of the bubble. Næss [18] concludes from experiments and existing literature that there is a maximum bulk oxygen partial pressure for active oxidation of a still silicon surface of $2{\cdot}10^{-3}$ atm. She also shows that there is a clear distinction between oxygen which is available for silicon to react with, and the oxygen in the bulk gas. From a thermodynamic point of view, this means that one cannot use the common assumption that partial pressure and activity are the same, thus necessitating the use of $a_{\{O_2\}}$ over $p_{\{O_2\}}$.

As thermodynamics is concerned, the number of particles in a nucleus and its geometry are coupled. Thus, if one can express the initial nucleus size like in Eq. [9], there also has to be a way to express the necessary spatial parameters to define the initial nucleus' surface area and volume. For a lens these spatial parameters are its angles, which can be found from Eq. [8], and the lens radius, which is half of the stippled line in Figure 6(a). The initial nucleus size, also called the critical nucleus size, has a critical radius r_G^*, which can be expressed as:

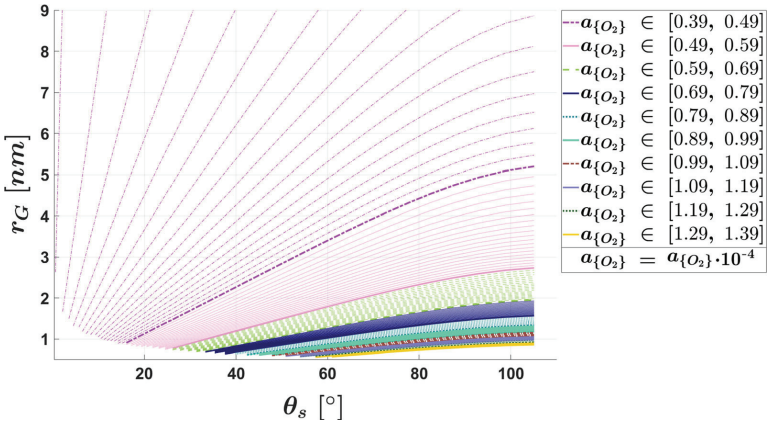

Fig. 8—$r_G^\star$ as a function of the slag's contact angle θ_s and the oxygen activity in the gas $a_{\{O_2\}}$ ($a_{\{O_2\}}$ in the legend must be multiplied by 10^{-4} to get the actual value). Each line represents a different activity, and lines are grouped together by color/line style, where each color/line style represents a span of 10^{-5}. Parameters used can be found in Table II.

$$r_G^\star = -\frac{2\sigma_{sm} V_{0,mol}}{RT \ln\left(c_{[O]}^2 / a_{\{O_2\}}\right)} \sin(\alpha_{sm})\ [m] \qquad [14]$$

Contact angles, like θ_s, are expected to have a specific value in a given system and thermodynamic state, which here is linked to the interfacial tension between slag and alloy σ_{sm} through Eq. [8]. The problem is that neither σ_{sm} nor θ_s are currently known, so the other cannot be calculated directly for given values of σ_{mg} and σ_{sg}. This problem can be somewhat circumvented by looking at the range of all possible values which either σ_{sm} or θ_s may take at a given state, along with how this range of attainable values gets affected as other system properties/parameters change. Sections II–C and II–E delve deeper into how slag composition affects the range of attainable values, while this section will look at how the oxygen activity in the purge gas will restrict the geometries a critical silica nuclei my have. If Eq. [14] is plotted as a function of the slag's total contact angle θ_s for different oxygen activities in the gas $a_{\{O_2\}}$, Figure 8 is generated. Here, each line has a different $a_{\{O_2\}}$, where lines are grouped together by color to increase clarity, with each color representing an oxygen activity span of 10^{-5}, where the span size itself was not chosen for its physical significance, but rather to show the trend more clearly. The white space in the bottom left hand corner is due to a requirement that the nuclei must consist of one or more molecules, and the cut off on the right hand side is due to overstepping the boundaries in Eq. [7]. $3.90{\cdot}10^{-5}$ was chosen as the lowest $a_{\{O_2\}}$ boundary due to it being the lowest oxygen activity which gives SiO_2 clusters consisting of at lest one molecule. It must be noted that $3.90{\cdot}10^{-5}$ is about two order of magnitude lower than the maximum bulk oxygen partial pressure for active oxidation of a still silicon surface ($2{\cdot}10^{-3}$ atm) from Næss 18. This indicates that the oxygen activity can only take values which are between the formation activity and an activity representing the oxygen activity at maximum active oxidation. This is also true for the model used here, as when the oxygen activity becomes too high, only nuclei containing less than one SiO_2 molecule will form, which is not a valid solution. At 1823 K, this happens at $a_{\{O_2\}} \approx 4.85{\cdot}10^{-4}$. The model represented in Figure 8 is valid for activities of the same order of magnitude as that of Næss, but only for temperatures above approximately 2000 K, which coincides with the melting temperature of silica (1999 K). The nature of this connection between the model presented here and the work of Næss is not currently known, but if it exists it might shine some light on how $a_{\{O_2\}}$ behaves, and how it relates to the oxygen partial pressure in the bulk gas.

Figure 8 allows for prediction of the critical nuclei behavior, without necessarily knowing the oxygen activity in the gas $a_{\{O_2\}}$ or the lens shape. As $a_{\{O_2\}}$ increases, Figure 8 predicts that the critical nuclei will take less space on the bubble surface as the radius decreases. Consequently, the possible geometries available for the slag droplet to take, get constrained toward higher contact angles. This results in a configuration where the bubble can support higher populations of slag nuclei, and that each slag droplet can attain a higher volume than it otherwise would, due to exhibiting a sharper convex surface toward the gas and melt.

To Figure 8, lines can be added which indicate the critical radius of a nuclei containing a given number of SiO_2 molecules. This results in Figure 9. Each group of similarly colored lines in Figure 8 represent the same change in the oxygen activity inside of the gas bubble. Line groups at higher $a_{\{O_2\}}$ are closer together forming a

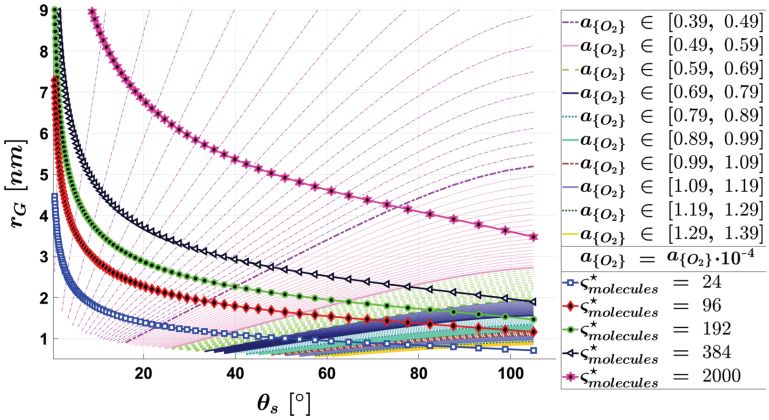

Fig. 9—Figure 8 with lines indicating the number of SiO_2 molecules in the critical nucleus. These lines use densities from Sweigert *et al.* 14 and transforms a sphere with said density into a lens. For a lens r_G is a function of θ_s which is then plotted.

tighter color band, as the critical radius becomes less sensitive to the oxygen activity in the gas with increased activity. This means that a critical nucleus containing a given amount of molecules will have to change its contact angle less to accommodate a higher oxygen activity in the gas $a_{\{O_2\}}$, as seen in Figure 9. Higher oxygen activities also put greater restrictions on the number of molecules in the critical nucleus, its radius, and its allowed angles. From the fourth line grouping (dark blue) and onward, the critical nucleus cannot contain more than 384 molecules, its radius must be less than 2 nm, and the total slag angle θ_s must be larger than 32°. In general Figure 9 predicts that a higher oxygen content in the bubble will result in smaller slag nuclei being formed with steeper contact angles. It thus predicts that increasing the oxygen content in the purge gas, and by extension the oxygen activity in the gas $a_{\{O_2\}}$, should result in an increased refining rate. The amount of oxygen in the purge gas is one of the few industrial control parameters available in OLR, making this connection between oxygen amount and critical nucleus size and geometry valuable not only for research purposes, but also for further industrial process control. It must however be noted that increasing the amount of oxygen in the bubble also has other effects. If there is too much oxygen in the bubbles, then one could picture a scenario where silica is produced too quickly to facilitate a smooth transition from SiO_2 to SiO_2-CaO-Al_2O_3 slag. The high viscosity of silica should make diffusion slower for the impurities, but if the diffusion length is small then this becomes less of an issue. If the slag droplet gets too large however, then this will likely reduce the refining rate instead of increasing it.

C. *"Well Defined" Surfaces in SiO_2-CaO-Al_2O_3 Slags*

The previous section shows how the initial slag nuclei can be described by CA, when it is assumed that it consists of pure silica. As the slag nuclei grows it will react with [Ca] and [Al], forming a SiO_2-CaO-Al_2O_3 slag. If this occurs before the number of particles in the nucleus ς_p becomes higher than 1000, then we must consider if CA is still applicable. In this section we will show that there are clear indications that SiO_2 defines the surface structure of SiO_2-CaO-Al_2O_3 slags, at least at high silica concentrations ($X^{\text{surface}}_{(SiO_2)} \geq 0.9$). Assuming that the nuclei will grow large enough before SiO_2 starts to loose control over the surface seems reasonable, as the availability of [Si] is much higher compared to [Ca] or [Al]. With this assumption, the droplet growth can be scaled, expressed, and defined even as it transitions between different spatial regimes.

The exact concentration at which this transition occurs is currently not known for SiO_2-CaO-Al_2O_3 slags, but Waseda and Toguri 23 states that any addition of alkali metal oxide beyond 10 mol pct will gradually change the fragmented random covalent network of silica into an ionic liquid. This compares well with the experimental work of Bockris *et al.*,24 which states that the silica framework will "collapse" when sufficient metal oxide is added, which they write is in the rage of 10-12 mol pct. Bockris *et al.,* 24 also provides a possible method for how the collapse occurs, which is later expanded on in Richardson 25 by including more of the then available literature.

While liquids, unlike solids, do not show long range structure they still exhibit short range, and in some instances intermediate range, structure. The intermediate range structure exhibited by molten silica, like the one shown by Waseda and Toguri, is presumably the reason for why the silica surface can be described as "well defined", satisfying Eq. [6]. That silica retains this property even at nanoscale, indicates that the surface structure is very favorable, which in turn implies that it is at an energy state not that much higher than the bulk molecules. Silica's relatively low surface tension also supports this, as surface tension can also be expressed as the energy difference between the surface and bulk.

Systems will tend toward minimizing its energy state, so if a phase consists of multiple species, then a lower surface energy state can be achieved by allowing the species with the lowest surface energy state to be positioned at the surface. Thermodynamically, this is represented by a surface activity, and causes a different species concentration at the surface compared to the bulk phase. Surface activity can be quantified by looking at how each species affects the total surface energy density/surface tension of the slag σ_s. σ_s can be estimated using a model based upon the Butler equation from Tanaka 26, solving the equation set:

$$\sigma_s = \sigma_i^\circ + \frac{RT}{\overline{A}_i} \ln\left(\frac{a_i^s}{a_i^b}\right) \quad [15]$$

Here $\overline{A}_i\,[m^2/mol]$ is the surface molar coverage for species i, and a_i is the species Raoultian activity with a pure species in mole fraction as its reference state, where b or s in the superscript designate either surface or bulk respectively. Nakamoto *et al.* 27 and 28], Fabritius *et al.* 29 and Hanao *et al.* 30 have shown that this model approximates the surface tension σ_s for different ternary slag compositions consisting of SiO_2, Al_2O_3, CaO, FeO, MgO, and MnO quite well.

It must be noted that in the desired temperature range T = 1500 °C to 1700 °C the pure slag components will not be liquid, but the model treats them as such. For reference, SiO_2 melts around $1727^\circ C$, and both CaO and Al_2O_3 melt at different temperatures higher than $2000^\circ C$. The specifics of the model and its viability is discussed extensively in the respective referenced literature.

It is well documented that the structures and properties of oxide melts are controlled by the concentration and potency of its network-formers and -modifiers. Silica is a potent network-forming oxide, imposing structure in the melt. Calcia on the other hand, is a strong network-modifier, breaking down the melt structure, while alumina is an amphoteric oxide, behaves either as a network-former or -modifier depending on slag composition. Silica imposes a structure consisting of more or less coupled SiO_4^{4-} monomers, whose degree of polymerization depends on the surrounding slag. In the slag, alumina can reach its lowest energy state by acting as if it was silica. By sharing one Ca^{2+} ion between two Al^{3+} ions, charge neutrality is reached, while also allowing each Al^{3+} ion to act as if it were Al^{4+}, mimicking Si^{4+}. Other structures for Al^{3+} are also possible, but they require higher energy states. Calcia acts only to disrupt the silica structure. As silica imposes structure, increasing properties like dynamic viscosity and lowering the diffusion rate, calcia will disrupt said structure, and in turn lower the slag viscosity and increase the diffusion rate. Calcia thus plays a vital role in forming the SiO_2-CaO-Al_2O_3 slag, as it provides new Al and Ca ions easier access to the bulk slag, while also facilitating the uptake of Al^{3+} ions by allowing a lower energy structural configuration. Alumina can also disrupt the structure of silica if the relative concentration of calcia is low, but is a much less disruptive than calcia.

These structural behaviors can also be seen by solving Eq. [15], as shown in Figure 10. The iso-tension lines were calculated by solving Eq. [15] at a given σ_s and $X^b_{(SiO_2)}$. As $\sum X_i = 1$ is true for both surface and bulk concentrations, this allows the equation set to be solved with three unknowns ($X^s_{(CaO)}$, $X^b_{(CaO)}$, $X^s_{(SiO_2)}$) and three equations. Expressions for species surface tension σ_i° and surface molar coverage $\overline{A}_i$ were taken from Arutyunyan *et al.* 31.

Figure 10(a) shows that the bulk concentration of calcia has a much greater impact on the surface structure than that of alumina, even though σ_s is most sensitive to the slag's bulk silica concentration. This is seen by how the iso-tension lines follow paths which all fall between the iso-concentration lines of silica and calcia, which states that the iso-tension lines follow constant calcia to silica ratios in the bulk. The lines are however not completely straight, and which ratios they follow differ, but the trend is quite clear to see. In Figure 10(b) it can also be seen that the surface composition reflects this trend, but here the concentration of silica is even more dominant. This trend is consistent with the theory, as if Al^{3+} gets to act as Al^{4+} in the slag, it will only cause the slag structure to deviate slightly from that of pure silica, which should only cause a slight increase in the energy state and thus the slag surface tension σ_s. Significant deviations in σ_s are only shown when greater amounts of alumina are added. Calcia is the principal network-modifier, so its effect on the surface should overshadow that of alumina. However, increasing the concentration of any of the species at the cost of silica will have the greatest effect.

When Figures 10(a) and (b) are seen side by side, it shows that the slag's bulk composition can change quite drastically, while only causing minor changes in surface concentration. Since the surface concentration of silica changes less than that of the bulk when calcia and alumina are added, indicates that silica is surface active while alumina and calcia are not. In Eq. [15] the reference surface tension for species i σ_i° and $RT/\overline{A}_i$ will be positive values. $\sigma^\circ_{(CaO)}$ and $\sigma^\circ_{(Al_2O_3)}$ both will be higher than σ_s, while $\sigma^\circ_{(SiO_2)}$ is smaller, at 1873 K. The only way to satisfy the equation set is then for:

$$a^s_{(SiO_2)} > a^b_{(SiO_2)},\ a^s_{(CaO)} < a^b_{(CaO)},\ a^s_{(Al_2O_3)} < a^b_{(Al_2O_3)} \quad [16]$$

If $a_i^s > a_i^b$ the species must be surface active, leading to it possessing a higher surface presence than its bulk concentration would imply. $a_i^s < a_i^b$ on the other hand causes the species to withdraw from the surface and congregate in the bulk. From this it is quite clear the model predicts that silica is highly surface active, while both calcia and alumina prefer the bulk slag. Figures 10(a) and (b) show that this allows the slag to retain a surface concentration of more than 90 mol pct silica, even though the silica concentration in the bulk slag is much lower. This allows the slag to retain its "well defined" surface over a wide range of bulk compositions, allowing the approximation to still be valid even though different slag nuclei may experience

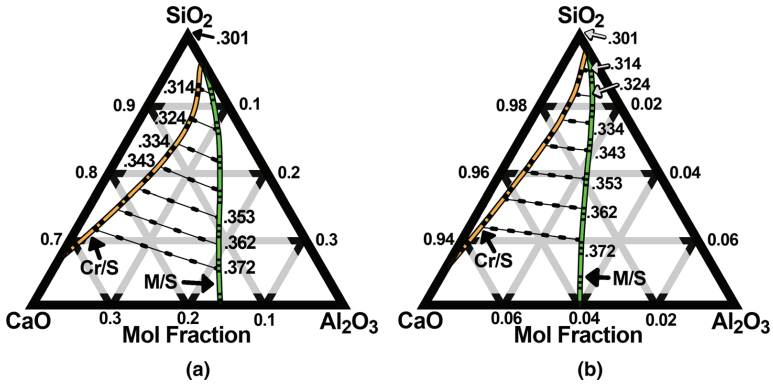

Fig. 10—Slag surface tension σ_s [J/m^2] at different surface/bulk slag concentrations, calculated with the model from Tanaka 26 at 1873 K. The iso-tension lines cover the concentrations where the slag is liquid, and is flanked by the cristobalite/slag(liq) (Cr/S) line and the mullite/slag(liq) (M/S) line. (*a*) σ_s at different bulk slag concentrations. (*b*) Shows the surface concentrations corresponding with the iso-tension lines and Cr/S, M/S lines in a).

compositional variations before they reaches a size of 1000 particles. Showing that the "well defined" surface is resistant to compositional variation is critical, as a high sensitivity would limit its practical use due to the high variance associated with high temperature processes.

Some notes on the model used in this section and a comparison with other authors: Arutyunyan *et al.* 31 models the slag's surface tension σ_s for CaO-Al_2O_3, CaO-SiO_2, and SiO_2-CaO-Al_2O_3 melts, with respect to concentration and temperature. They additionally compare their results with experimental data from multiple other authors. While the spread in experimental values are quite significant, they share similar trends with Tanaka's 26 model. Increasing the amount of calcia and/or alumina in the bulk slag, increases σ_s both in the case of CaO-SiO_2 and SiO_2-CaO-Al_2O_3. Tanaka's model was also compared with values from a slag atlas.[32] Here the seven listed experimental values with $X^b_{(SiO_2)}$ above 0.6 would overshoot the modeled values by between 0.0022 and 0.0627 J/m^2 at a 95 pct confidence. Arutyunyan *et al.* 31 also has a positive $d\sigma_s/dT$ for CaO-SiO_2 and SiO_2-CaO-Al_2O_3, but only for high concentrations of SiO_2. $d\sigma_s/dT$ will then become negative as the amount of calcia and alumina combined get too large. Still, at high concentrations of silica their model also alludes to silica defining the surface, which results in the silicon alloy perceiving the slag surface as only consisting of silica until the concentrations of alumina and calcia become high enough to start influencing the surface concentration, and thus the surface structure, themselves.

D. *Slag Growth*

Interfacial tension is in general affected by chemical reactions through effects like surface convection and Marangoni effects. If one has a pure silica slag droplet on a non-reactive gas substrate in a liquid silicon alloy, one would expect the contact surface between the slag and alloy to reduce its curvature as to increase the contact area. This can be seen as the surface spreading the burden of reaction over as large of an area as possible, by reducing surface curvature. A higher curvature can be retained once the droplet gets close to equilibrium with its surroundings.

For the system relevant to this work, this may not be case. As the gas bubble enters the silicon alloy, oxygen from the gas will over-saturate the silicon locally, which in turn will next to instantaneously form silica, which goes on to form the critical nuclei. The bubble will then be covered by small silica nuclei which act as seeds for further slag growth, however the greater their surface coverage the lower the oxygen flux between gas and liquid alloy will be. While it is convenient to think of the addition of calcia and alumina in the form of reactions, as shown in reaction 3 and 4 , this might not represent the whole story. On the silica surface there will be certain points where an oxygen atom will stick out of the surface ring structure, as can be seen in Roder *et al.* 15, Schweigert *et al.* 14, and Vaccaro *et al.* 16. Following the logic in Bromley *et al.* 33 these points should be the primary reaction centers, and additionally provide an attachment point for new silica molecules. When these oxygen atoms react with a particle the surface must deform to more firmly bind it to the structure. In the case of the impurities there are interesting ways

Table II. Values Used to Generate Fig. 8

$V_{0,mol}\ [\frac{m^3}{mol}]$	$27.516(1+(T-1773)\cdot 10^{-4})\cdot 10^{-6}$	[19]
$\log_{10}(c_{[O]}\ [\frac{wt\%O}{1wt\%O}])$	$-\frac{4620}{T}+0.332$	[20]
$\sigma_{sg}\ [\frac{J}{m^2}]$	$(243.2+0.031T)\cdot 10^{-3}$	[21]
$\sigma_{mg}\ [\frac{J}{m^2}]$	$0.82-3\cdot 10^{-4}(T-1685)$	[22]
T [K]	1823	

Marangoni effects may cause the surface to locally fold, delivering the impurity away from the surface while simultaneously exposing new oxygen atoms.

In this work we argue that the slag nuclei will grow so rapidly, due to the low solubility of oxygen in silicon (see Table II), that any reduction in curvature from reactions between the slag and impurities is negligible. Instead, as the nucleus grows new silica molecules will use the underlying structure as a scaffold to further expand upon. [Ca] and [Al] will react with the surface, and in doing so disrupting said scaffold increasing the surface's energy state. This continuous growth will thus allow calcia and alumina to quickly enter the bulk slag while still affecting the surface structure. It will also spread them more evenly throughout the slag, lessening the need for diffusion, Marangoni effects, and allowing alumina to more quickly take its low energy configuration, while also solving potential ionic drag issues related to the local charge balance. It is further conjectured that since silica has an exceptionally favorable surface structure, this continuous growth provides a situation which is more similar to that at equilibrium, than that at which the curvature decreases. This also means that the "well defined" surface assumption still holds, and that the general thermophysical properties can be used. Here calcia and alumina get to affect the geometry by modifying the structure, like in the equilibrium case, but as their addition occurs over the whole growth cycle this will not cause the sudden changes needed for a large decrease in curvature. It must be noted, that for a slag nuclei/droplet to get ejected from the bubble surface it must either detach itself from the bubble substrate, which requires a very large curvature, or extend far enough from the bubble surface to get ripped of by the flow field, which gets stronger further away from the bubble surface. Size and curvature are thus important properties, as they both contribute to how far a nuclei/droplet may extend itself away from the bubble surface. A problem with the low curvature case, is that the slag nuclei/droplet would need to reach equilibrium with the surrounding alloy to allow higher curvatures. To compensate for shifts in the local alloy composition, and thus the slag's target equilibrium composition, it also seems likely that the nuclei/droplet would need to grow very large before its curvature could be increased. Since these events must happen in sequence, any external event/effect which negatively impacts the rate at which either event occurs will equally affect the process as a whole.

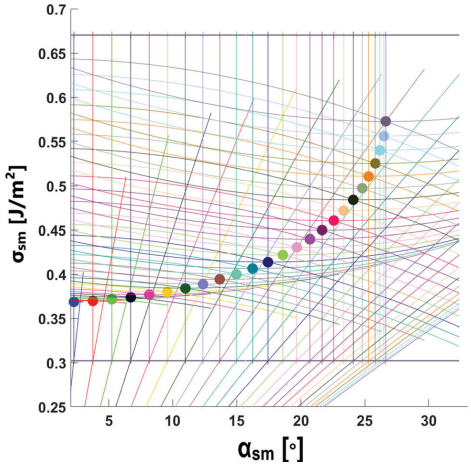

Fig. 11—Plot of different relationships between a triangles sides and angles from Fig. 6b, where the interfacial tension between slag and melt σ_{sm} is a function of the wetting angle between slag and melt α_{sm}. Valid solutions are marked with circles. $\theta_s \in [5, 179]^\circ$, $\alpha_{sm} = \arcsin((\sigma_{sg}/\sigma_{mg})\sin(\theta_s))$. Valid solutions of σ_{sg}, σ_{mg} are approximated as σ_s°, $\sigma_m^\circ(1900K)$, and uses the same expressions as in Table II.

It must be noted that this behavior should vary as the bubble travels through the ladle. In industrial ladles it is common to find what is colloquially called a "sponge" or a "mushroom". This is a collection/structure of slag found quite close to/on the porous plug, which is high in calcia. Calcia has a higher oxygen affinity than alumina, which suggest that just as the gas enters the melt there will be formed a large amount of slag very quickly. As the bubble ascends it will gradually get depleted of oxygen which will decrease the oxygen flux toward the alloy, slowing down or even stopping the production of new slag. This is however mitigated somewhat by there being a maximum bulk oxygen partial pressure for active oxidation of the silicon surface, as concluded by Næss 18. This works in the favor of the rapid growth hypothesis, as it means that the gas bubble has a limit to how quickly oxygen can be depleted, such that the rapid growth can occur over larger parts of the bubbles ascent. Local and ladle wide depletion of impurities is also a factor which will impede slag growth, and will be discussed further in the next section.

It must be stated that this is a hypothesis, as the authors have not found these complex interactions satisfactorily explored in the current literature to validate it until further work has been conducted. This work will continue to explore the effect of calcia and alumina on the slags geometry as if the proposed conjecture is true, as it sheds light on several interesting behaviors.

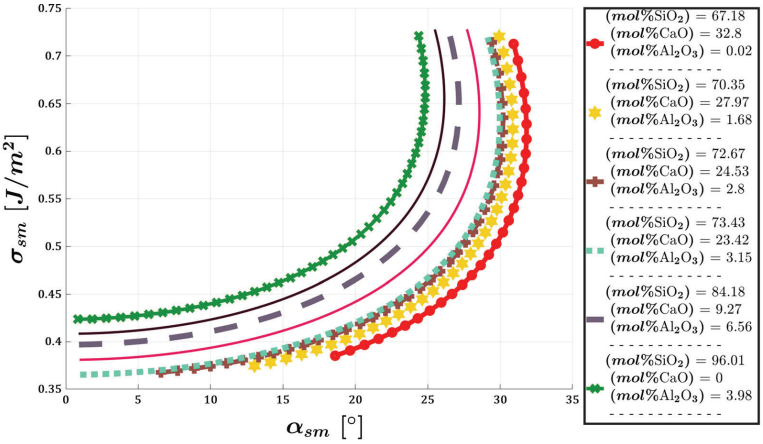

Fig. 12—Interfacial tension between slag and melt as a function of contact angle and bulk slag composition along the cristobalite/slag(liq) line. Similar procedure as Fig. 11, but σ_{sg} is found from the model described in Section II–C and T = 1873 K. σ_{mg} was set equal to 0.73 J/m^2.

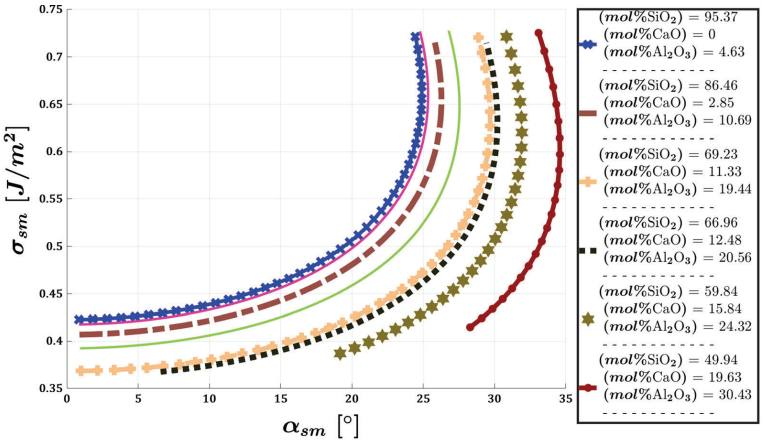

Fig. 13—Interfacial tension between slag and melt as a function of contact angle and bulk slag composition along the mullite/slag(liq) line. Similar procedure as Fig. 11, but σ_{sg} is found from the model described in Section II–C and T = 1873 K. σ_{mg} was set equal to 0.73 J/m^2.

E. *Slag Droplet Geometry*

Much of this work has been dedicated to why it seems prudent to assume that the SiO_2-CaO-Al_2O_3 slag droplet can be assumed to have a "well defined" surface. This subsection concerns itself with what consequences this has for the slag droplet geometry as the slag concentration changes.

Equation 8 is but one of the ways to show how the different wetting angles (θ_s, θ_m, θ_g, α_{sm}, α_{sg}) and interfacial tensions (σ_{sm}, σ_{sg}, σ_{mg}) in Figure 6(a) and 6(b) relate to each other, by the relationship between the sides and angles of a triangle. It can also be shown that for any value of the slag's primary wetting angle θ_s, there will only be one valid solution for the secondary wetting angles between slag/melt α_{sm} and slag/gas α_{sg}. A solution is only valid when every relationship is satisfied, and this can be found by plotting them against each other and identifying where they all intersect, as seen in Figure 11. If the same methodology is used as in Figure 11, but $\sigma_{sg} \approx \sigma_s$ is found from the model described in Section II–C, then the slag composition can also be added as a parameter. To our knowledge, there is no clear indication in the current literature that the surface

structure of SiO_2-CaO-Al_2O_3 slag or liquid Si, drastically changes when these two phases are in contact with each other, or when they are individually in contact with a gas containing oxygen for that matter. It thus seems reasonable to assume that the value of the interfacial tension between slag and melt lies in between the surface tension values of the slag and melt, $\sigma_s < \sigma_{sm} < \sigma_m$. If this is assumed then one gets Figures 12 and 13 .

The expression for the melt's surface tension σ_m, here assuming $\sigma_m \approx \sigma_{mg}$, in Table II by Shishkin and Basin 22 is not recommended for use above 1830 K. σ_m was here set as 0.73 J/m^2, as this value seems to be more in line with the data shown in their article at this temperature, than what their expression gives. The melt's surface tension was intentionally set toward the higher end of those shown in Shishkin and Basin, as the constricting effect, which will be discussed shortly, becomes more pronounced the lower σ_m is.

Figures 12 and 13 show that increasing the amount of calcia and alumina in the slag causes the slag droplet to protrude further into the melt. The more a droplet protrudes into the metal melt, the faster it will start to get affected by the flow field, and thus it is likely that this should lead to the slag leaving the bubble faster, making room for new slag to form, and as such increase the refining rate. They also show that calcia will increase the contact angle more than alumina. As previously noted, calcia is critical for allowing alumina to attain its preferred structure in the slag, which when included with the previous points, makes the importance of calcia in the operation of OLR become quite apparent. Based on this, it becomes apparent that for smooth operation of OLR it is important to make sure that there always is enough calcium available to produce a slag which can efficiently extract dissolved aluminum in the melt, and provide a favorable slag droplet geometry. An important consequence of applying the constraint on the value of the slag/melt interfacial tension σ_{sm}, is that the possible valid values the wetting angle α_{sm} can take become smaller as the slag's silica concentration decreases. This means that even if there is currently not enough information available to solve the problem fully, it is still possible to make predictions of how the different parameters affect the slag droplet's geometry due to this constriction of possible solutions. It is also valuable to look at how the contact angle between the slag and gas changes, as can be seen in Figure 14. The most important observation from Figure 14 is that the possible solutions the wetting angle α_{sg} can take are constrained to steeper angles as the silica concentration decreases. Assuming a constant volume in the slag droplet, the contact area between the gas bubble and slag droplet will decrease as the droplet extends further into the melt. In turn, this strengthens the earlier statement that calcia is critical for the refining rate, as it should become easier for the slag droplet to detach from the gas bubble if its contact area becomes smaller. The overall model behavior does not change as long as $\sigma_s \leq \sigma_{sm} \leq \sigma_m$. Shishkin and Basin 22 have performed an extensive meta study on the surface tension of silicon σ_m. From their work it can be seen that there is quite a large variance in the literature values on the surface tension of silicon. What can be said is that $\sigma_m \in [0.68, 0.8]\,[J/m^2]$, T=1800-1900K is most likely the case. The range tested was T=1773-1973K, as this is considered possible temperatures in OLR. As long as the slag's surface tension σ_s is kept constant, decreasing the melt's surface tension σ_m will cause the system to push toward steeper wetting angles between the slag and silicon melt α_{sm}, while an increase favors shallow angles. Changing σ_s will cause similar effects as it is the distance between σ_s and σ_m which dictates the behavior. Niu *et al.* 34, Yuan *et al.* 35, Hibiya *et al.* 36, and Shishkin and Basin 22 describe how dissolved oxygen in the melt [O] affects the melt surface tension σ_m at different T. An

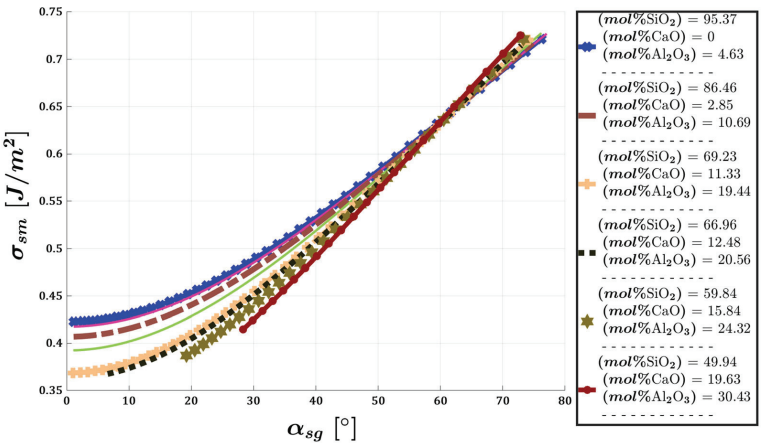

Fig. 14—Similar to Fig. 13, but the interfacial tension between slag and melt σ_{sm} is now expressed as a function of the wetting angle between slag and gas α_{sg}.

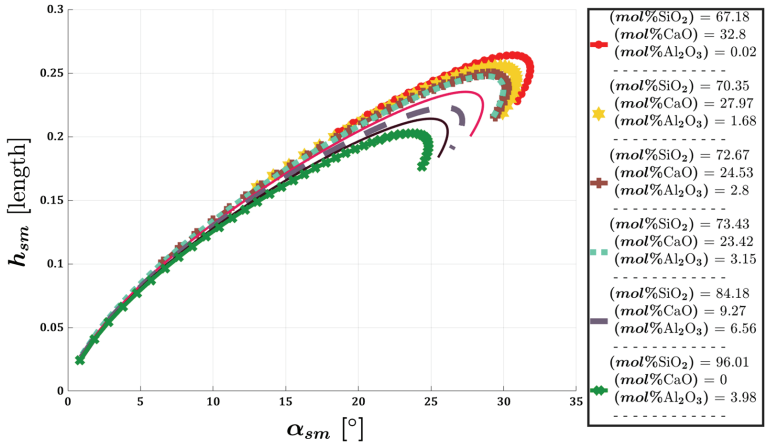

Fig. 15—Height of the slag droplet between the slag and melt h_{sm} as a function of wetting angle between slag and melt α_{sm} and slag composition following the cristobalite/slag(liq) line. The slag droplet is assumed to have a constant volume of 1 with an arbitrary cubed length unit.

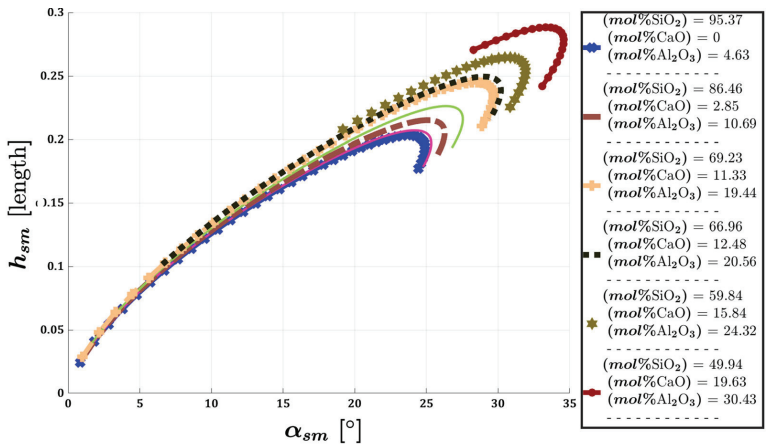

Fig. 16—Height of the slag droplet between the slag and melt h_{sm} as a function of wetting angle between slag and melt α_{sm} and slag composition following the mullite/slag(liq) line. The slag droplet is assumed to have a constant volume of 1 with an arbitrary cubed length unit.

increase in the melt's dissolved oxygen concentration will result in a decrease in its surface tension σ_m, until the oxygen saturation limit $\omega_{[O],sat}$ is reached. Yuan *et al.* [35] additionally presents experimental data on how silicon's surface tension σ_m varies when molten silicon is subjected to an atmosphere where the oxygen partial pressure is higher than its saturation pressure $p_{O_2} > p_{O_2,sat}$, using argon as the bulk gas. As p_{O_2} increases, σ_m increases slightly, with some indications that it will flatten out. The authors write that this is most likely due to SiO_2 formation on the surface, which can be seen from their samples. The drop in the melt's surface tension σ_m, seen in Yuan *et al.* 35, Niu *et al.* 34, and Hibiya *et al.* 36 is quite large, $\sigma_m(T) \approx 0.94\sigma_m(T)|_{[O]_{sat}}$ T=1693-1773K, approximately an 6 pct drop in σ_m at full oxygen saturation is observed. For the slag it is assumed that as [Si] reacts with $\{O_2\}$, the kinetics of (SiO_2) and $\{SiO\}$ formation is fast, allowing close to local equilibrium between (SiO_2) and $\{SiO\}$ at their contact surface. This is a reasonable assumption, since the slag droplet height is

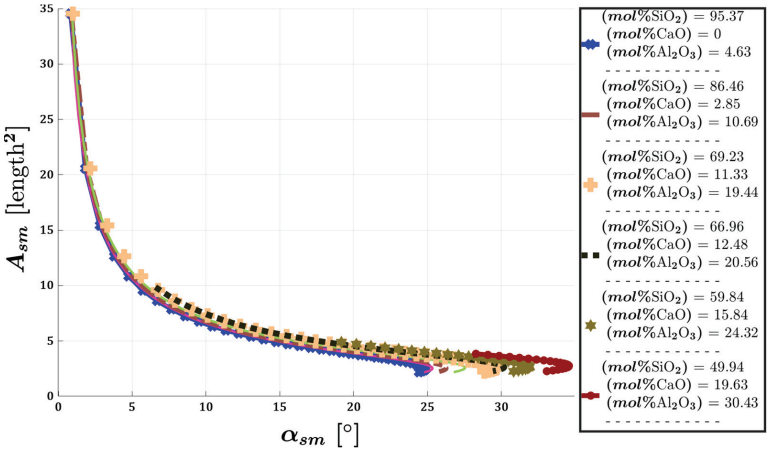

Fig. 17—Contact area between slag and melt A_{sm} as a function of wetting angle between slag and melt α_{sm} along the mullite/slag(liq) line. The slag droplet is assumed to have a constant volume of 1 with an arbitrary cubed length unit.

quite small, and both reactions between [Si] and $\{O_2\}$ occur close to the droplet. Both the slag and melt phase are in contact with the gas phase, so the primary change in interfacial tension should come from surface active species in the gas.

As [Ca] and [Al] react to form Al_2O_3 and CaO slag species, the equilibrium between the slag and $\{SiO\}$ is altered. We have not found any literature concerning how σ_s changes depending on $p_{\{O_2\}}$, at high T. Continuing from Figure 12 and 13 , if the droplet in question is assigned a constant volume $V_{lens}=1[\text{length}^3]$ (here "length" denotes an arbitrary length unit), the changes in contact area and height between the slag and melt h_{sm}, as a function of the wetting angle α_{sm} and slag composition can be calculated. This is shown in Figures 15, 16, and 17 , illustrating how the slag droplet protrudes into the melt.

Seen together, they provide a clearer picture of what occurs on the bubbles, which can be summed up as follows: Assuming a pure (SiO_2) nuclei is the initial slag state, the pure silica droplet (SiO_2) can exhibit very shallow wetting angles between the slag and melt α_{sm}. This allows the silica droplet to spread out over the bubble surface, providing a large contact area between the slag and melt A_{sm}. As a result, even if diffusion is difficult, due to the high viscosity of SiO_2, a high reaction rate between (SiO_2) and the impurities can still be attained. This is further facilitated by a low height between the slag and melt h_{sm}, which leads to a small diffusion length, previously noted in Section II−B. As the slag droplet grows it will react with [Ca] and [Al], increasing the concentration of (Al_2O_3) and (CaO), causing the droplet to contract radially, favoring steeper wetting angles between both the melt and gas.

Table III. Concentration of [Wt Pct Al] and [Wt Pct Ca] in the Unrefined Industrial Alloy Measured by Inductively Coupled Plasma Mass Spectroscopy (ICP-MS). The Sample Mean and Standard Deviation are Given in [Wt Pct], Based on a Set of 3 Sub-samples

Impurity	Sample Mean	Sample Standard Deviation
Al	0.332	0.095
Ca	0.269	0.118

This reduces the contact area between the slag and the gas bubble, while simultaneously causing the slag to protrude further into the melt, making it easier for whole/or parts of the droplet to get ripped off by the flow. It plausible that the slag droplet is not all detached at once, where only the part which protrudes into the melt itself gets swept away by the flow field. The part left behind will then start to grow again, continuing the cycle, but how plausible this is depends on many factors like slag viscosity and the flow field experienced by the extremities of slag droplet.

An industrial observation is that if the amount of dissolved calcium becomes too low, refining stops. This may be explained by how calcia dictates the behavior of alumina in the slag, which in turn dictates the slag geometry. Aluminosilicates do also have a very high viscosity, which should hamper diffusion, and such the reaction rate. Even though the droplet will have a large contact area with the melt it will still cling to the bubble surface, and with a high viscosity it can never get to the point where the droplet gets pulled off before the gas bubble leaves the melt.

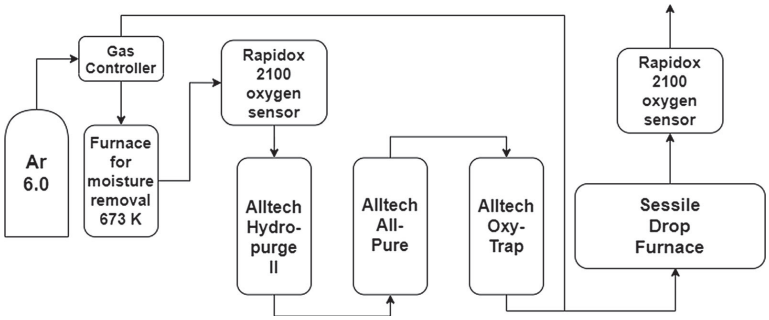

Fig. 18—Flowchart depicting the oxygen scrubbing system with the experimental setup.

III. EXPERIMENTAL WORK

As shown in the theoretical description, many of the predicted behavioral trends are not very sensitive to small changes in system properties. An example of this is the interfacial tension between the slag and melt, σ_{sm}, in Section II–E always behaves in a similar manner in the relevant temperature and slag concentration ranges. As a supplement to the theoretical description of slag nucleation and growth, the initial formation of SiO_2-Al_2O_3-CaO slag from an industrial silicon alloy in contact with oxygen was investigated experimentally. The experiment was designed to explore the distribution of different oxides in the slag, as SiO_2 is expected to be surface active while Al_2O_3 and CaO are not.

A. *Materials*

An approximately 1.5 mm cube was cut from an unrefined industrial alloy with composition listed in Table III. Afterwards the cube was cleaned with acetone and ethanol to remove any contamination from the cutting fluid, and left over night in a heating cabinet at 120°C to remove any excess moisture.

B. *Procedure*

The sample was placed on a ISO-88 graphite substrate in a sessile drop furnace under an Ar 6.0 atmosphere (less than 1 ppmX impurities), where the argon was first run through an oxygen scrubbing system. This oxygen scrubbing system consisted first of a graphite tube furnace at 673 K (400°C), which heated the gas and allows some of the moisture to escape and condense before the gas is fed through an Alltech Hydropurge II moisture trap. Since Ar 6.0 was used, this step was arguably redundant, as the initial amount of moisture in the gas (less than 0.5 ppmX[37]) should not be sufficient to exceed the moisture taps capacity. Next, the gas is fed through Alltech's ALL-Pure™ Nitrogen Purifier and Oxy-Trap module. The ALL-Pure™ gas purifier is a multi-purification system which contains an oxygen, moisture, and hydrocarbon purification module, where the Oxy-Trap further reduces the oxygen concentration. A partial pressures less than 10^{-16} bar O_2 was measured with a Rapidox 2100 oxygen sensor placed at the furnace gas outlet. The experimental setup is shown in Figure 18. Figure 8 predicts that if the oxygen activity in the gas is less than $3.90 \cdot 10^{-5}$ then no new slag will form. Even though activities of gaseous species and their partial pressures are not necessarily equal, the difference in this case is considered so large that it can safely be assumed that the oxygen partial pressure in the furnace is too low to form slag nuclei. Formation of {SiO} was not considered, as any amount produced would be small and swept away by the argon flow. The furnace is then heated to 1873 K (1600°C) over 20 minutes, and held there for 15 min. After spending 5 min at 1873 K (1600°C) the sample was exposed to 1 min of un-scrubbed Ar 6.0, to provide enough oxygen to promote slag formation. After 15 min at 1873 K the furnace was turned off, and the sample was subjected to rapid cooling to room temperature. The sample was then stored in an desiccator and sent for imaging. Light surface cleaning with one drop of acetone and ethanol, with heating the sample to remove moisture, were performed right before the imaging started.

C. *Imaging and Analysis of Reacted Samples*

The surface of the sample was then imaged in a scanning electron microscope (SEM), and a small cross-section was selected and extracted with a focused ion beam emitter (FIB). Since the silicon alloy was saturated with carbon, first from the industrial process and later from the substrate, there was large patches of SiC on the silicon surface. From the SEM images it was documented that slag was present on the surface of both the metal and SiC phase, shown in Figure 19(b). A cross-section was therefore selected such, that it covered both the silicon and SiC phases, as the SiC phase is very distinct, making it easier to distinguish where the SiC phase ends and the slag phase begins than between the slag and Si. The selected cross-section was covered with a layer of carbon and gallium to protect the surface during further handling, seen outlined in blue in Figure 19(a). A FEI Helios G4 FIB emitting gallium

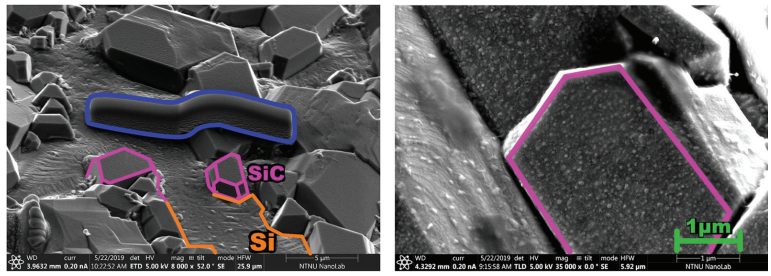

Fig. 19—(*a*) SEM image of the silicon surface. SiC crystals outlined in pink and Si phase outlined in orange. Selected cross-section is covered by a protective layer of carbon and gallium, outlined in blue. (*b*) SEM image of a SiC face outlined in pink. The rough surface texture indicates that there is another phase, here slag, on top of the SiC surface.

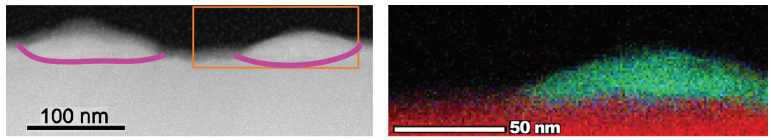

Fig. 20—(*a*) STEM image of two slag droplets on the SiC surface. Pink lines indicate the SiC/slag interface. (*b*) RGB concentration map of the area inside the orange box in a). Si(EELS) is red, Al(EELS) is green, and Blue is Ca(EDS).

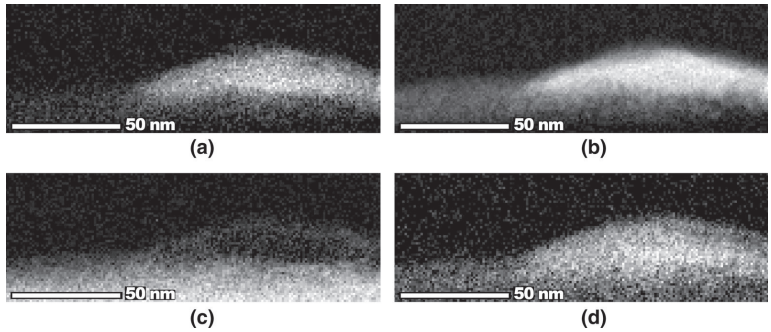

Fig. 21—EELS maps of (*a*) aluminum, (*b*) oxygen, (*c*) silicon, and (*d*) calcium.

ions, was used to extract and thin the sample to electron transparency (approx. 200 nm). TEM/STEM (scanning transmission electron microscopy) imaging and chemical mapping was performed with a probe/image aberration-corrected JEOL ARM-200F cold field emission gun microscope, operated at 200 kV. In STEM, the probe current was approximately 300 pA with a convergence angle of 27 mrad and collection angles between 67-118 mrad. Electron energy loss spectroscopy (EELS) was collected simultaneously with the energy-dispersive X-ray spectra (EDS). EELS was run using a GIF Quantum with a dispersion of 1 eV, collection angle of 67 mrad, with a 20 ms dwell time, while EDS was conducted using a JEOL Centuro detector.

D. *Results*

On the SiC surface, small spherical cap shaped slag droplets were imaged, shown in Figure 20(a). The leftmost droplet was not fully cut through, so chemical mapping is only provided for the rightmost droplet, where Figure 20(b) shows an RGB map of said slag

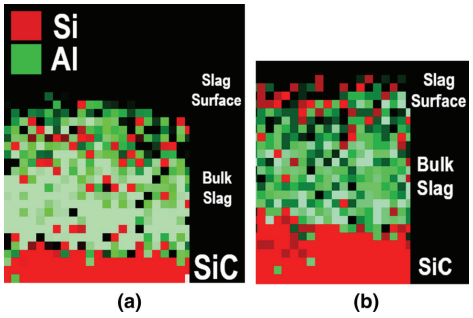

Fig. 22—(*a*) EELS map retaining only the strongest concentration signal for Al(Green) and Si(Red) in the middle portion of the slag droplet in Fig. 21. The sidebar shows where the slag surface, center, and SiC are located. (*b*) EDS map of the same area as in (a). Al is colored in green and Si in red.

droplet. Figure 21(a) and 21(b) shows the individual concentration maps of Al and O respectively. Comparisons of the strongest signals from Si and Al can be found in Figures 22(a) and 22(b), extracted from the EELS and EDS maps of the elements respectively. These figures were generated by greatly increasing the contrast in Figure 21(a) and 21(c), and their EDS counterparts not shown here, retaining only the strongest signals from each element. The silicon map was then superimposed on the aluminum map in each case, resulting in Figures 22(a) and 22(b).

Figure 22(a) displays the middle portion of the slag droplet, where a brighter color represents a higher concentration of each species, and the color pallet of the EELS maps of aluminum and silicon, Figures 21(a) and 21(c), have been changed to green and red respectively. In the case of aluminum, Figure 22(a) shows its highest concentration at the center of the slag droplet, indicated by the light green color, and that it decreases toward the slag surface, as it transitions toward darker shades of green. Silicon, displayed in red, has a weaker EELS signal in the slag than Al, seen by comparing Figures 21(c) and 21(a). When the strongest silicon signal in the slag droplet is extracted, one gets the red parts of Figure 22(a). Here, the strongest silicon signal in the slag is at the slag surface, as there are more red squares at the slag surface than in the bulk. The same behavior is also found in the EDS map, if it is subjected to a similar treatment as Figure 20(a), shown in Figure 22(b).

E. *Discussion of the Experimental Work*

Figures 22(a) and 22(b) support the theoretical claims that silica is surface active while alumina is not. By comparing the different concentration maps in Figure 21, it is expected that Ca has a concentration profile close to that of Al in the slag. The high amount of noise present in Figure 21(d) makes it unsuitable for the same type of image manipulation used to create Figures 22(a) and 22(b), so it was omitted. Primarily EELS, and less so EDS, has some difficulties distinguishing between Ca and C, due to their energy peaks being close together, which is the reason why SiC seemingly contains Ca in Figures 20(b) and 21(d). However, the rest of the elements have energy peaks so far apart that one can clearly distinguish between them. While the elements can be easily distinguished from each other, there would seem to be very little silicon in the slag, as seen in Figure 21(c). This is assumed to be a result of the imaging method used. It is thought that the silicon signal emitted by the SiC is so much stronger than that from the slag, overshadowing the silicon signal from the slag. This is a known problem which might occur when using EELS and EDS in TEM, as these analysis methods are better suited for finding which elements are present rather than quantifying them. The concentration maps in Figure 21 are thus useful for comparing the relative spatial concentration of each element, but should not be used to compare absolute concentration of different elements.

IV. SUMMARY AND CONCLUSIONS

The results and conclusions of the theoretical and experimental work in this study can be summarized as follows:

1) This work presents a theoretical framework, which expresses nucleation and growth of SiO_2-CaO-Al_2O_3 slag droplets on oxygen-rich gas bubbles related to refining of MG-Si, using classical macroscale thermodynamics.

   The theoretical framework describes how nanoscale processes like slag nucleation and its initial growth, can be expressed using classical macroscale thermodynamics, and forms a foundation for modeling refining of MG-Si.

2) The low surface tension and high surface activity of silica is the key which allows nucleation and growth of SiO_2-CaO-Al_2O_3 slag droplets to be described using classical macroscale thermodynamics.

   Silica's strong surface structure, represented by its low surface tension, makes it a special case, where the surface can be considered as "well defined", even when a silica nuclei consists of a small number of molecules. That the surface can be considered "well defined" is essential, as this is generally what classical macroscale thermodynamics sees as a surface, and fundamentally will not work without it. Since silica is highly surface active, the theoretical framework states that the surface will always be "well defined" as long as silica defines the surface. Thus, as long as the concentrations of calcia and alumina are low during the slag droplet's initial growth stage (until the number of particles in the slag exceed 1000), it is assumed to retain its "well defined" surface. Above

this, classical macroscale thermodynamics is considered to be generally applicable. How accurate the assumption that the slag droplet retains its "well defined" surface is currently not known, but a high nucleation rate and low availability of impurity elements compared to silicon to form the slag, favors this assumption.

3) The framework may be used to predict the viability of refining for different melt compositions and bubble oxygen concentrations, resulting from different slag droplet composition, droplet geometries and properties at different spatial regimes. This also allows calculation and/or verification of refining parameters which are difficult to find experimentally.

   A key feature of the proposed theoretical framework is that it provides a framework for describing the slag droplet as it grows between different spatial regimes which is continuous. By being continuous, all properties relating to the slag growth are linked together regardless of which spatial regime they are measured in, and they can be expressed by the same classical macroscale thermodynamics. This allows for instance experimental results on the solubility of oxygen in molten silicon at different oxygen partial pressures, to be more easily implemented into industrial refining models, thus shortening the path between academic research and its industrial application. Another example, is that macroscale experiments can be used to provide information about nanoscale phenomena, where the macroscale experiments are often much less resource intensive and more readily available.

4) The model framework predicts, in accordance with industrial observations, that the concentration of Ca in the Si melt and oxygen concentration in the gas bubbles are important parameters for the effectiveness of the Si refining process. It has also been shown experimentally that there are strong indications that silica is surface active, and that alumina is not surface active in SiO_2-CaO-Al_2O_3 slag.

V. FUTURE WORK

In on-going work, the reaction kinetics between air/Ar gas and Si-alloys of different composition is explored experimentally. An iterative thermodynamic modeling approach is used to expand the slag formation framework into a model able to predict the refining behavior in industrial vessels. In the future we would also like to use the proposed framework to estimate the interfacial tension between silicon and SiO_2-CaO-Al_2O_3 slags experimentally. The framework expresses the interfacial tension as a function of multiple individually measurable parameters, this makes it possible to create experimental setups where multiple parameters are measured at once, to attain the necessary statistical.

ACKNOWLEDGMENTS

This publication has been funded by the SFI Metal Production, (Centre for Research-based Innovation, 237738). The authors gratefully acknowledge the financial support from the Research Council of Norway and the partners of the SFI Metal Production. The Research Council of Norway is acknowledged for the support to the Norwegian Micro- and Nano-Fabrication Facility, NorFab, project number 295864/F50.

CONFLICT OF INTEREST

The authors declare that they have no conflict of interest.

FUNDING

Open access funding provided by NTNU Norwegian University of Science and Technology (incl St. Olavs Hospital - Trondheim University Hospital).

LIST OF SYMBOLS

SPECIES PHASE LOCATION

[El]	Species El is in the alloy phase
(El)	Species El is in the slag phase
{El}	Species El is in the gas phase

LATIN SCRIPT

A_s	Surf. area	[m^2]
$\overline{A}_i$	Surf. molar coverage	[m^2/mol]
a	Activity	[–]

Ref.	Dissolved [1 wt pct]Gaseous [1 bar]Pure sol/liq [100 mol pct]
c	Dimensionless wt pct [wt pct/1 wt pct]
d	Diameter [m]
$\overline{d}_0$	Init. Sauter d [m]
H	Height [m]
h	Droplet height [m]
m	Mass [kg]
n	Moles [mol]
$n^\star$	Critical n [mol]
P	Total pressure [Pa], [bar]
p	Partial pressure [Pa], [bar]
R	Gas constant [J/(molK)]
r_G	Droplet radius [m]
$r_G^\star$	Critical rG [m]
T	Temperature [K], [°C]
V	Volume [m^3]
V_m	Molar volume [m^3/mol]
X	Mole fraction [–]
x	Distance [m]

GREEK SCRIPT

α	Contact angle [°, rad]
Δ	Differential [–]
$\Delta\mu$	Chemical potential [J/mol]
ω	Mass fraction [–]
ρ	Density [kg/m^3]
ϱ	Particle density [particles/m^3]
σ_i	Surface tension [J/m^2]
σ_{ij}	Interfacial tension [J/m^2]
ς_p	Particle amount
ς	Critical particle amount
θ	Contact angle [°, rad]

SUBSCRIPTS

g	Gas
s	Slag
m	Alloy melt
b	Bubble
sat	Saturated
lens	The whole lens

SUPERSCRIPT

b	Bulk
s	Surface

ABBREVIATIONS

MG-Si	Metallurgical grade Si
OLR	Oxidative ladle refining
CA	Cluster Approach
DFA	Density functional approach

REFERENCES

1. I. Kero, M.K. Næss, V. Andersen, and G.M. Tranell: *Metall. Mater. Trans. B*, 2015, vol. 46, pp. 1186–94.
2. G.K. Sigworth: *Can. Metall. Q.*, 2020, vol. 59, pp. 251–61.
3. A. Schei, J.K. Tauset, and H. Tveit: *Production of High Silicon Alloys*, 1st ed., Trondheim, Tapir Forlag, 1998, pp. 233–73.
4. J. E. Olsen, D. Darmana, A. Ashrafian, K. Tang, 6th International Conference on CFD in Oil & Gas and Metallurgical and Process Industries, Trondheim, Norway, Conference Proceedings, 2008.
5. A. Ashrafian, S.T. Johansen, S. Gaal, B. Andresen, 6th International Conference on CFD in Oil & Gas and Metallurgical and Process Industries, Trondheim, Norway, Conference Proceedings, 2008.
6. P.H. Calderbank: *Trans. Inst. Chem. Eng*, 1958, vol. 36, pp. 433–40.
7. K. Tang, Report No. F8532, SINTEF Materials and Chemistry, Trondheim, (2007).
8. M. J. Assael, I. J. Armyra, J. Brillo, S.V. Stankus, J. Wu, W.A. Wakeham. J. Phys. Chem. Ref. Data. 2012. vol. 41, pp. 033101-1 to 033101-16.
9. J.W. Gibbs. Trans. Conn. Acad. Arts Sci. 1874, vol. 3, https://archive.org/details/Onequilibriumhe00Gibb, Accessed (27 June 2017).
10. J.W. Gibbs. Trans. Conn. Acad. Arts Sci., 1877, vol. 3, https://archive.org/details/Onequilibriumhe00GibbA, Accessed (27 June 2017).
11. D. Kashchiev: *Nucleation*, 1st ed., Butterworth-Heinemann, Oxford, 2000, pp. 9–112.
12. I.V. Kalikmanov: *Nucleation Theory*, 1st ed., Springer, Dordrecht, 2013, pp. 55–70.
13. S.M. Thompson, K.E. Gubbins, J.P.R.B. Walton, R.A.R. Chantry, and J.S. Rowlinson: *J. Chem. Phys*, 1984, vol. 81, pp. 530–42.
14. I.V. Schweigert, K.E.J. Lehtinen, M.J. Carrier, M.R. Zachariah: Phys. Rev. B, vol. 65, pp. 235410-1 to 235410-9 (2002).
15. A. Roder, W. Kob, and K. Binder: *J. Chem. Phys*, 2001, vol. 114, pp. 7602–14.
16. G. Vaccaro, G. Buscarino, S. Agnello, A. Sporea, C. Oproiu, D.G. Sporea, and F.M. Gelardi: *J. Phys. Chem. C*, 2012, vol. 116, pp. 144–49.
17. P.G. De Gennes, F. Brochard-Wyart, D. Quéré. *Capillarity and Wetting Phenomena*, Translation of 1st ed. to English by A. Reisinger, Springer Science & Business Media, New York, 2004, pp. 54-56.
18. M.K.Næss, IMA NTNU. *Mechanisms and Kinetics of Liquid Silicon Oxidation*, PhD. Thesis, Trondheim, (2013).
19. K.C. Mills and B.J. Keene: *Int. Mater. Rev.*, 1987, vol. 32, pp. 1–120.
20. T. Narushima, K. Matsuzawa, Y. Mukai, Y. Iguchi: Mater. Trans. JIM, vol. 35, pp. 522–28 (1994).
21. T. Tanaka, K. Hack, T. Iida, and S. Hara: *Z. Metallkd.*, 1996, vol. 87, pp. 380–89.
22. A.V. Shishkin and A.S. Basin: *Theor. Found. Chem. Eng.*, 2004, vol. 38, pp. 660–68.
23. Y. Waseda, J.M. Toguri. *The Structure and Properties of Oxide Melts*, 1st ed., World Scientific Publishing Co. Pte. Ltd., pp. 5–7 (1998).
24. J.O'M. Bockris, J.D. Mackenzie, J.A. Kitchener. Trans. Faraday Soc. 1955, vol. 51, pp. 1734–47.
25. F.D. Richardson: *Physical Chemistry of Melts in Metallurgy*, 1st ed., Academic Press, Cambridge, 1974, pp. 92–99.
26. T. Tanaka: *Miner. Process. Extr. Metall.*, 2011, vol. 120, pp. 229–34.
27. M. Nakamoto, T. Tanaka, L. Holappa, and M. Hämäläinen: *ISIJ Int.*, 2007, vol. 47, pp. 211–16.
28. M. Nakamoto, A. Kiyose, T. Tanaka, L. Holappa, and M. Hämäläinen: *ISIJ Int.*, 2007, vol. 47, pp. 38–43.
29. T. Fabritius, J. Riipi, M. Järvinen, O. Mattila, E.-P. Heikkinen, A. Kärnä, J. Kurikkala, P. Sulasalmi, and J. Härkki: *ISIJ Int.*, 2010, vol. 50, pp. 797–803.

30. M. Hanao, T. Tanaka, M. Kawamoto, and K. Takatani: *ISIJ Int*., 2007, vol. 47, pp. 935–39.
31. N.A. Arutyunyan, A.I. Zaitsev, and N.G. Shaposhnikov: *Russ. J. Phys. Chem. A*, 2010, vol. 84, pp. 7–12.
32. B.J. Keen: *Slag Atlas Part 10*, 2nd ed., Verlag Stahleisen GmbH, Dusseldorf, 1995, p. 430.
33. S.T. Bromley, M.A. Zwijnenburg, Th. Maschmeyer. Phys. Rev. Lett., vol. 90, pp. 035502 1-4 (2003).
34. Z. Niu, K. Mukai, Y. Shiraishi, T. Hibiya, K. Kakimoto, and M. Koyama: *J. Jpn. Assoc. Cryst. Growth*., 1997, vol. 24, pp. 369–78.
35. Z.F. Yuan, K. Mukai, and W.L. Huang: *Langmuir*, 2002, vol. 18, pp. 2054–62.
36. T. Hibiya, S. Nakamura, K. Mukai, Z.-G. Niu, N. Imaishi, S.-I. Nishizawa, S.-I. Yoda, M. Koyama. Philos. Trans. R. Soc. A vol. 356, pp. 899–909 (1998).
37. Linde AG. Promotional Datasheet: HiQ® Specialty Gases Finder Argon. Accessed 04 Aug 2020.

Paper 2

The 11th Molten Slags, Fluxes and Salts [MOLTEN 2020]
May 25-29, 2020, Seoul, Korea

Nucleation of SiO_2-Al_2O_3-CaO slag in the oxidative refining process for Metallurgical Grade Silicon (MG-Si)

Erlend L. Bjørnstad[1*] and Gabriella M. Tranell[1]

[1]Norwegian University of Science and Technology, Trondheim, Norway

Abstract: Oxidative ladle refining (OLR) is used as a primary refining step for removal of dissolved Ca and Al in the production of metallurgical grade silicon alloys. Greater control over this process could be exerted with more fundamental knowledge of the physio-chemical mechanisms governing the nucleation and mass transfer of elements between alloy and SiO_2-Al_2O_3-CaO slag. Two identical unrefined industrial silicon alloy samples were melted in a low oxygen environment ($p_{O2} < 10^{-15}$ ppmV) and kept for 15 min at 1873 K (1600ºC). One of the two samples was subsequently exposed to Ar 6.0, containing approximately 1 ppmV oxygen, for 1 minute at 1873 K, reacting with any oxygen present in the gas. After melting/exposure, both samples were quickly cooled to room temperature. Both samples were further analyzed by transmission electron microscopy (TEM) and auger electron spectroscopy (AES), to investigate the phases on the alloy surface and their composition respectively. The results showed two very different surfaces. The sample exposed to an oxygen containing atmosphere contained well-defined, nano-sized slag droplets where differences in Al, Ca and Si distribution within the slag droplets were seen, indicating that Al is not surface active.

I. INTRODUCTION

Metallurgical grade silicon (MG-Si) is a material used in a range of applications; from alloying element in aluminum to a precursor for silicones and high purity silicon for electronics and solar cell production. MG-Si is produced by carbothermal reduction of quartz in an electric furnace (SAF), and further refined and crushed. The refining step most commonly consists of oxidative ladle refining (OLR) as Si is tapped from the furnace into a ladle, where it is purged by oxygen-enhanced air through a bottom mounted porous plug. The porous plug generates a bubble column, where the oxygen in the bubbles will react with the melt and its primary slag forming impurities, Ca and Al, forming a SiO_2-Al_2O_3-CaO slag phase according to reactions 1-3.

1) $Si_{(l)} + O_{2(g)} = SiO_{2(slag)}$ **2)** $2\underline{Ca} + SiO_{2(slag)} = 2CaO_{(slag)} + Si_{(l)}$ **3)** $4\underline{Al} + 3SiO_{2(slag)} = 2Al_2O_{3(slag)} + 3Si_{(l)}$

Important to achieving greater process control in OLR, is understanding how the slag nucleates, grows, and changes its behavior as oxygen comes into contact with unrefined silicon of different initial compositions. It would be of industrial value if the framework describing these nano-scale phenomena would be compatible with existing thermodynamic macro-models. These are in general incompatible due to how Gibbs defines a surface [1]. An important contribution to the coupling between macro- and nano-scale phenomena would be to establish if the slag surface properties determined by macro-scale thermodynamics hold true also at the nano-scale. This work hence aims to investigate experimentally the initial stages of slag formation/growth when unrefined silicon is exposed to an atmosphere with very low concentrations of oxygen.

2. EXPERIMENTAL

Two 1.5mm cubes were cut from a sample taken from an unrefined industrial alloy. They were then placed on graphite substrates in a sessile drop furnace, brought up to 1873 K at a rate of 900 K/min, held there for 15 minutes, and subsequently rapidly cooled to room temperature. The atmosphere in the furnace consisted of oxygen scrubbed Ar 6.0, where the oxygen partial pressure was measured to be $p_{O2} < 10^{-15}$ ppmV using a Rapidox 2100 oxygen sensor. After 5 minutes at 1873 K, one of the samples was subjected to 1 minute of un-scrubbed Ar 6.0 to allow controlled oxidation. A small surface cross-sectional piece from each reacted sample was extracted using a focused ion beam (FIB), with a protective layer of a carbon-gallium mixture to ensure no surface damage, and then thinned to electron transparency using a FEI Helios G4. The samples were further imaged using a transmission electron

* erlend.l.bjornstad@ntnu.no, +47 95760328

microscope (TEM), and elemental concentrations were analyzed with electron energy loss spectroscopy (EELS) and simultaneous energy-dispersive X-ray spectra (EDS). Either EELS or EDS were chosen for each specific element depending on the quality of their respective signal.

3. RESULTS AND DISCUSSION

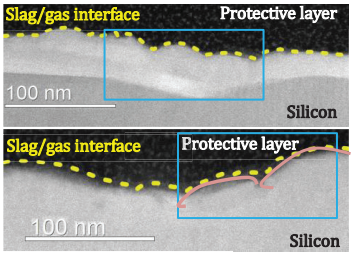

Fig. 1. TEM images of the (upper) un-exposed and (lower) exposed sample surfaces. Slag/gas interface marked with yellow dotted line. Two of the droplets are outlined in pink in the exposed sample. The protective gallium-carbon layer forms the dark backdrop. Light blue boxes indicating the sampling area for fig. 2-3.

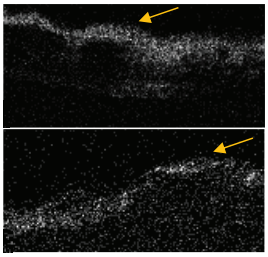

Fig. 2. EDS image of Al in the (upper) un-exposed and (lower) exposed sample, image area is marked in light blue in fig. 1. Concentration of an element is indicated by higher brightness. Orange arrows indicate good spots to see contrast in fig. 2-3.

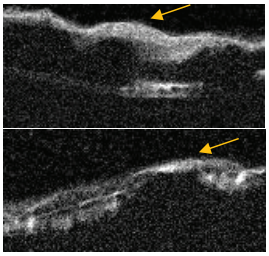

Fig. 3. EELS image O in the (upper) un-exposed and (lower) exposed sample, image area is marked in light blue in fig. 1. Concentration of an element is indicated by higher brightness. Orange arrows indicate good spots to see contrast in fig. 2-3

Fig. 1 shows the TEM images of the un-exposed and exposed sample surfaces respectively, and fig. 2-3 show their Al and O concentrations, where EDS or EELS was used depending on signal quality. From fig. 1-3 we observe that even if the sample was not exposed to extra oxygen during melting, there is still enough bound oxygen on the sample surface itself to form a slag layer with an approximate thickness of 10 nm. The exposed case, in contrast, illustrate slag shaped as individual droplets, where 2 of these are indicated in pink in fig. 1. This indicates a different geometric slag configuration when the surface is subjected to oxygen. i.e. the surface slag film becomes unstable due to slag forming reactions at the interface, changing the slag composition and with it, its surface tension. The elemental mapping of the slag droplets in figs 2-3 show a stronger prevalence of O than Al at the slag surface. As determined by earlier research the slag surface tension is highly dependent on the composition of the SiO_2-Al_2O_3-CaO slag [2]. While SiO_2 is a strongly surface-active compound, the model by Nakamoto et al. [3] predicts that Al_2O_3 is not surface active. The slag nuclei observed in the current study corroborates the non-surface active behavior of Al_2O_3, even in small spatial regimes. This was also seen for Ca/CaO, but due to the proximity of C and Ca intensity peaks, this carries a higher uncertainty as the images contain vastly more noise. The industrial implication of this is that when Ca and Al come into contact with the slag, it may not see the slags bulk concentration, but one containing a higher concentration in SiO_2. When there is more oxidation the slag also changes its geometry, likely due to a change in slag composition and amount, leading to a change in geometry.

4. CONCLUSION

Two unrefined silicon samples were subjected to different oxygen atmospheres when molten at 1873 K. When observed in TEM it was found that the slag changes its geometry, increasing contact area, when exposed to oxygen, and that Al_2O_3 is not surface active, as opposed to SiO_2.

Acknowledgements: This work has been funded by SFI Metal Production, (Center for Research-based Innovation, 237738), and NorFab, (Norwegian Micro- and Nano-Fabrication Facility, 245963/F50).

References

[1] Kashchiev D.: Nucleation, Butterworth-Heinemann Burlington (2000)
[2] Schei A., Tuset J. K., Tveit H.: Production of high Silicon alloys, Tapir forlag Trondheim (1998)
[3] Nakamoto M., Kiyose A., Tanaka T., Holappa L., Hämäläinen M.: ISIJ International 47 (2007), pp. 38–43

Paper 3

Mass Transfer of Al and Ca Between Silicon and Synthetic SiO_2-CaO-Al_2O_3 Slags

Erlend Lunnan Bjørnstad and Gabriella Tranell

Abstract The mass transfer of *Al* and *Ca* between silicon and synthetic $SiO_2 - CaO - Al_2O_3$ slags of varying composition has been investigated, using different experimental set-ups. Samples were kept at $1600°C$, varying the holding times in an individual crucible kinetic series set-up or sampled at given sample intervals in a larger crucible set-up. Solute concentrations of *Al* and *Ca* in *Si* and slags were found by ICP-MS. This work compares these results to observations from industrial Si refining measurement campaigns. A model for interpreting kinetic mass transfer phenomena observed for parallel *Al* and *Ca* mass transfer between slag and *Si*, is also discussed.

1 Introduction

Metallurgical grade silicon(>96% *Si*) [1] is used as a raw material in aluminum alloy production, silicones, the electronics industry and in renewable energy technologies. The demand for products with a high degree of accuracy, with respect to the composition of impurities, has increased drastically over the last decade. An example of this is the high purity product needed to supply the manufacturing of solar energy technologies. High purity is of utmost importance since even low concentrations of impurities could harm the semiconductor properties of silicon, thus limiting its use in solar panels. To better control the composition of the final product refining steps are added to the production process. Understanding the refining process is vital to stay competitive and continue to meet the demands of today, but also the demand of tomorrow.

The typical industrial metallurgical production route for silicon consists of carbothermic reduction of quartz in an electric arc furnace. A majority of the impurities including *Al*, *Ca*, *P*, *B* and *Fe* enter the system through the carbon sources, like coal, charcoal and wood chips. To control the level of impurities in the final product the melt is tapped from the furnace into a ladle to undergo oxidative ladle refining. Oxidative ladle refining is conducted by continuously purging the ladle with oxygen enriched air. After a series of reactions the main impurities, *Ca* and *Al*, will go to an immiscible oxide phase, a slag, which later can be separated from the melt. Understanding the transport and kinetic properties of this process is crucial to exert a more precise control over the products final composition.

Extensive work has already been performed mapping the thermodynamics of the system, however there has been comparatively few studies investigating the mass transfer and reaction kinetics. This work aims to investigate the mass transfer of *Al* and *Ca* between *Si* and $SiO_2 - CaO - Al_2O_3$ slags. Two experiments were performed, but only one yielded publishable results. It also looks at a basic refining model [2] and compares it to the experimental data found by this work, and the industrial data from Kero et al. [3].

2 Process Overview

As the melt is tapped from the furnace into the ladle the refining process is performed continuously, and

Erlend Lunnan Bjørnstad, PhD Candidate
Department of Materials Science and Engineering, Norwegian University of Science and Technology, Alfred Getz vei 2, NO-7491, Trondheim, Norway, e-mail: erlend.l.bjornstad@ntnu.no

Gabriella Tranell, Professor
Department of Materials Science and Engineering, Norwegian University of Science and Technology, Alfred Getz vei 2, NO-7491, Trondheim, Norway, e-mail: gabriella.tranell@ntnu.no

continues for a set amount of time after the ladle is full. The purge gas is introduced through a porous plug located at the bottom of the ladle. This creates a bubble column rising through the ladle, driving a flow while mixing the melt. On its ascent the O_2 in the bubbles will react with Si to form SiO_2 and $SiO_{(g)}$. $SiO_{(g)}$ will be transported into the bubble saturating the gas phase, while SiO_2 will nucleate at the bubble interface. Tang [4] writes that SiO_2 forms a droplet on the surface, while Schei et al. [5] writes that it can form a film around the bubble. SiO_2 then reacts with the impurities in the melt, primarily Al and Ca, to form a predominantly $SiO_2 - CaO - Al_2O_3$ slag. When the slag is formed there will be a driving force to approach equilibrium between the present phases driving a mass transport to the slag so their respective equilibrium concentration can be reached. Since the temperature of the system is high it is often assumed that the reactions can be considered instantaneous [6]. As the diffusion of species in the metal is faster than in the slag, the rate determining step for the transport of Al and Ca is considered to be the transport in the slag [3, 4, 6]. To sum up the overall reactions can be expressed as:

1. $Si + O_2 = SiO_2$
2. $Si + \frac{1}{2}O_2 = SiO_{(g)}$
3. $2\underline{Ca} + SiO_2 = 2CaO + Si$
4. $4\underline{Al} + 3SiO_2 = 3Si + 2Al_2O_3$
5. $3CaO + 2\underline{Al} = 3\underline{Ca} + Al_2O_3$

with figure 1 illustrating the whole process.

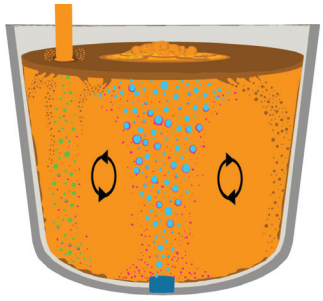

Fig. 1 The whole system including the falling jet. Bubbles of entrapped air are displayed in green.

To express the system it has been proposed to use a standard [2] batch reactor model [3]. By applying two-film theory to the interface the molar transfer for species i, N_i, from the metal to slag can be expressed:

$$N_i|_{m\to s} = \frac{k_{i,m}\rho_m}{M_i}(\omega_{i,m} - \omega^\star_{i,m}) = \frac{k_{i,s}\rho_s}{M_i}(\omega^\star_{i,s} - \omega_{i,s}) \ [\frac{kmol}{m^2\ s}] \tag{1}$$

where $k_{i,p}$ $[\frac{m}{s}]$ is the mass transfer coefficient for species i in phase p, ρ_p $[\frac{kg}{m^3}]$ is the density of phase p, and M_i $[\frac{kg}{kmol}]$ denotes the molar mass of species i. $\omega_{i,p}$ denotes here the mass fraction of species i in phase p, and the superscript * expresses that it is at the interface. Due to the complexity of determining the mass transfer coefficient, k_i, $k_{i,m}$ and $k_{i,s}$ may be combined in an overall mass transfer coefficient $k_{i,t}$ [2].

$$\frac{1}{k_{i,t}\rho_m} = \left(\frac{1}{k_{i,m}\rho_m} + \frac{\gamma_i}{k_{i,s}\rho_s K_i f_i}\right) \tag{2}$$

where K_i denotes the equilibrium constant $K_i = \frac{\omega^\star_{i,s}\gamma_i}{\omega^\star_{i,m} f_i}$ between the two phases for species i. Here γ_i is the raultion activity coefficient for the oxide of species i and f_i is the henrian activity coefficient of species i in the melt. By assuming that the slag and metal is completely mixed the mass balance can be expressed as [2]:

$$-m_m \frac{d\omega_{i,m}}{dt} = k_{i,t}\rho_m A_s(\omega_{i,m} - \omega^{eq}_{i,m}) \tag{3}$$

Here m_p $[kg]$ is the mass of phase p, and A_s $[m^2]$ is the reaction area. In equation 3 $\omega^{eq}_{i,m}$ is the hypothetical concentration in the metal at equilibrium with the actual concentration in the slag $\omega_{i,s}$ given by $\omega^{eq}_{i,m} K_i f_i = \gamma_i \omega_{i,s}$. Assuming that $\omega_{i,s}|_{t=0} = 0$ and $\lim_{t\to\infty} \omega_{i,m} = \omega^\infty_{i,m}$ equation 3 can be written as:

$$\int_{\omega^{in}_{i,m}}^{\omega_{i,m}} \frac{d\omega_{i,m}}{\omega_{i,m} - \omega^\infty_{i,m}} = -\int_0^t \frac{k_{i,t}\rho_m A_s}{m_m}\left(1 + \frac{\gamma_i m_m}{K_i f_i m_s}\right) dt \tag{4}$$

Equation 4 poses a problem due to most of the parameters on the RHS are functions with respect to time [3]. There is also an additional problem in the

fact that ladle refining of silicon is done while tapping and therefore cannot be considered a true batch process for its full duration. Kero et al. [3] writes that allowing the *RHS* in equation 4 to be constant with respect to time will still give an equation which can be useful in comparing the refining kinetics in this system. This is due to the fact that m_m, m_s, A_s and ρ_m all change in the same way with respect to time for every species in the melt allowing it to serve as a crude approximation, according to Kero et al.

Cussler [7] has gathered multiple expressions for k and from this it can be seen that some common dependencies are $k = f(\rho, U, L, D, \sigma, \mu)$. Here U $[\frac{m}{s}]$ is the terminal rise velocity, L $[m]$ is some characteristic length, D $[\frac{m^2}{s}]$ is the diffusion coefficient, σ $[\frac{J}{m^2}]$ is the surface energy density, and μ $[\frac{kg}{m\,s}]$ is the dynamic viscosity. This states that k is a property depending not only on the thermophysical properties of the phases involved, but also on the flow and geometries. If these properties can be considered constant or their behavior similar then $k_{i,t}$ might be considered constant, or similar in behavior as well.

An interesting point when looking at equation 4 is that the exponential transient behavior of the *RHS*, after integration, is shared with the much more complex CFD models from Ashrafian et al. [6] and Olsen et al. [8] on the same system. In addition it shows a decent fit with the industrial sample set from Kero et al. [3], as seen in figure 2, for many elements, like *Ca*.

The experiments performed in this work differ from the industrial case in that a clean metal is used instead of a slag. This leads to the transport of *Al* and *Ca* from the slag, with a known slag concentration, to the clean metal. However, the mass transfer behavior should not be affected by this as the steps of transport are the same in both cases. Clean metal is used due to it being considerably easier to create a synthetic slag with an accurate composition, than doping pure silicon with specific amounts of *Ca* and *Al*. By applying the same theory as used earlier on this system, with a *RHS* which is not a function of time, gives:

$$\omega_{i,m}(t) = \omega_{i,m}^{\infty}\left[1 - exp\left(-\frac{k_{i,t}\rho_s A_s}{m_m}\left(\frac{K_i f_i}{\gamma_i} + \frac{m_m}{m_s}\right)t\right)\right] \quad (5)$$

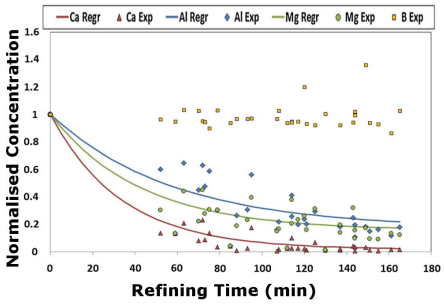

Fig. 2 Normalized *Ca*, *Al*, *Mg* and *B* concentrations as functions of time. From Kero et al. [3]. Printed with permission under the Creative Commons Attribution License as stated in Kero et al. [3].

3 Experiment

The apparatus used during the experiment was a graphite tube furnace of an inhouse design, shown in figure 3. The furnace was kept under an argon atmosphere at 1.15-1.3 bar to ensure that neither the sample or the graphite was in contact with an oxidizing atmosphere in the hot zone. Two B-type thermocouples were used. The one inserted from the top regulated the temperature, while the second was used as an insurance. This furnace was used due to its special crucible insertion and withdrawal system. It allows the operator to insert and extract samples while the furnace is still running and kept inert. This keeps disturbances to the furnace atmosphere to a minimum, allowing for all the samples in one series to be subjected to as similar conditions as possible.

12g of silicon pellets were put into 15 IG-110 graphite crucibles with dimensions Ø30mm/22x45mm and an inner height of 40mm. The silicon pellets were premelted to minimize inconsistencies in contact area between metal and slag. This gave a smoother surface morphology with a contact area approximately equal to the crucible opening. The furnace was evacuated to $\leq$ 0.3mbar and refilled with 5.0 argon. Heating to 1600°C was started after the internal furnace pressure reached 1.2bar, at a rate of 40$\frac{K}{min}$. Each crucible was held in

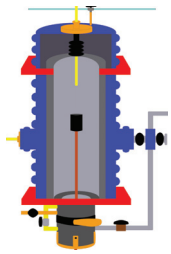

Fig. 3 Graphite tube furnace

the hotzone for 7min before quenching. The holding time at the chamber separation mechanism was 5min for the first series, but was later increased to 7min due to the withdrawal rods heat. 11g of slag was then added to each crucible, with compositions listed in table 1. Three different slags were used with five samples in each slag series, totaling 15 samples. Five time steps were chosen and they were 5, 10, 20, 30 and 180 min. The first four time steps measure the mass transfer kinetics, while the 180min sample was expected to reach equilibrium concentration as proposed by Jakobsson [9]. The same procedure as used above was performed for each sample set. To keep the experimental conditions as constant as possible each sample set was run on the same day and kept in a desiccator after cooling to avoid contamination.

Table 1 Intended slag concentrations.

Slag ID	SiO_2 $[wt\%]$	CaO $[wt\%]$	Al_2O_3 $[wt\%]$
CSA255520	55	25	20
CSA254035	40	25	35
CSA404020	40	40	20

The silicon used in this experiment had a purity of at least 8N. Initial master slags were made from commercial oxides with a purity of $\geq 99.5\%$. Homogeneity was achieved by mixing the oxides in different proportions, melting, quenching and crushing, with the last three steps repeated at least twice. The master slags contained approximately $0.1wt\%$ Fe_2O_3, with the total initial concentration of all other measured oxides $\geq$ $0.1wt\%$. By mixing the master slags at different proportions the desired slag compositions were obtained. These can be seen in table 1. To ensure homogeneity the new slag mixtures were heated to 1873K, kept there for one hour, before quenched and crushed. The mass loss after heating was only measurable for the 180 min samples where the mass loss was close to 0.6% due to reactions with the crucible.

Before analysis the graphite crucible was removed and the slag and metal separated. Great care was taken to ensure that no metal was present in the slag samples and no slag in the metal samples. As to not contaminate the final product pieces were discarded rather than kept. Over $95wt\%$ of the metal and at least $60wt\%$ of the slag was kept after separation. After separation the metal samples were crushed to a fine powder using a tungsten carbide disk mill. The slag samples they were crushed with a polytetrafluoroethylene ball mill.

Both metal and slag were analyzed by ICP-MS to find the concentration of *Ca* and *Al* in the metal, and to check for contaminants in the slag. This was done by the HR-ICP-MS lab at the Department of Chemistry at NTNU, with the instrument type Element 2 from Thermo Electronics. Two sub-samples, between 25-45mg, were taken from each sample and dissolved in a 1.5mL ultra pure 68% HNO_3 + 0.5mL 40% HF mixture. After dissolution the samples are diluted, with deionized water, to a final volume between 216-220mL, giving 0.1M HNO_3 and 0.23% v/v HF. Three samples of NIST metallurgical silicon standard reference, three standard slag references and three blank samples were analyzed together with the sub samples.

4 Results

In terms of analytical accuracy figures 4, 5 and 6 show the experimental results with a 95% confidence level. There were no other major contaminants found in any of the slag samples beyond what was already noted. The measured values for each sub-sample by ICP-MS are average values from the detector and

are delivered with their own relative standard deviation(RSD). Due to this inherent uncertainty the STD values are calculated by taking the root of the sum of the variance between sub-samples and the average between the sub-samples own variance. This is expressed in equation 6, where the sub-expressions are from the ASTM standard for basic statistics E2586-14.

$$STD = \sqrt{\frac{n\left(\sum_{i=1}^{n} x_i^2\right) - \left(\sum_{i=1}^{n} x_i\right)^2}{n(n-1)} + \frac{\sum_{j=1}^{n}\left(\frac{x_j RSD_j}{100}\right)^2}{n}} \tag{6}$$

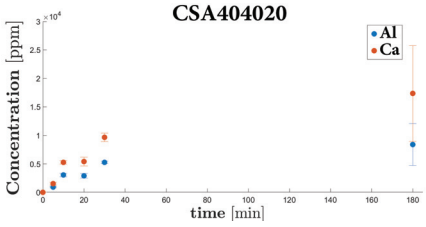

Fig. 4 CSA404020 sample with errorbars set at 95% confidence level.

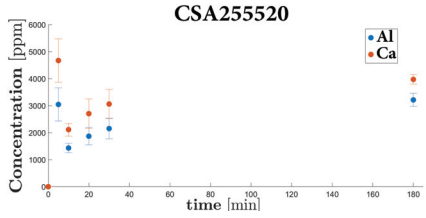

Fig. 5 CSA255520 sample with errorbars set at 95% confidence level.

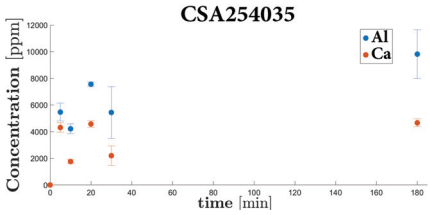

Fig. 6 CSA254035 sample with errorbars set at 95% confidence level.

5 Discussion

The experimental method used here has earlier been used by Jakobsson [9], and the method is simple to execute. This method is beneficial due to the fact that there is no flow in the crucible, and the reaction surface should be close to constant. Since the quench is immediate after leaving the hotzone it can be assumed that very little mass transfer happens during cooling giving higher accuracy. One problem with this method is that there is a high loss of slag when separating the two phases, due to the porosity of the slag when machining away the crucible. It is crucial that there are no small pieces of metal in the slag making the loss unavoidable if they are separated by hand. Another experiment using a a crucible with an inner diameter of 70mm and outer height of 150mm was also performed, but there were considerable difficulty associated with the sampling. Glass tubes with an inner diameter of 4mm were used inserted trough a graphite tube inserted into the melt. The problem was that considerable amounts of slag entered the sampling tube blocking the metal from entering. This problem is thought to be linked to the high viscosity of the slag and its surface tension. The amount of metal recovered was too small for any reliable analysis. An induction furnace was used for this experiment which induces flows among other things, making it less accurate for predicting specific properties, but it should be useful as another way of generating data to check and validate findings from other experimental methods. It is recommended that another method for sampling is used however.

5.1 Samples

If the 180min entries from figures 4, 5 and 6 are compared with equilibrium values calculated by FactSage it can be seen that they are not consistent with the calculated values. Table 2 lists the FactSage and experimental 180min entries. The Factsage values are calculated using the Fact Oxide- and Fact Light Metals database, at $1600^{\circ}C$.

Table 2 *Al* and *Ca* concentrations, in $[ppm]$, calculated by FactSage, using the Fact Oxide- and Fact Light Metals database, at $1600^{\circ}C$, in equilibrium with $SiO_2 - CaO - Al_2O_3$ slags, with the experimental values.

Sample	CSA404020	CSA255520	CSA254035
Al_{calc}	3900	1000	4500
Al_{exp}	8400	3212	9814
Ca_{calc}	1900	100	280
Ca_{exp}	17339	3970	4660

From figures 4, 5 and 6 it can be seen that while there are some sub-sample pairs which exhibit high degree of variance, the sample setts as a whole there looks to be a high degree of homogeneity between the two sub-samples. This excludes a consistent non-representative sampling of the final product as the culprit for this deviation. The deviation could come from not retrieving enough of the phase in question when separating metal and slag. This might be a reasonable train of thought if the problem lie in the slag, but not for the metal. Another step that might affect the samples could be contamination by the slag when crushing. This does not hold water since the metal and slag were crushed by two different machines.

Operational factors concerning the procedure or the materials used are next in line. The procedure and materials have been tried and tested previously by Jakobsson [9]. Jakobsson did not look at kinetic aspects however so it could be that inserting a cold sample into the hot furnace, and the extra heating associated with this causes some deviations in the early samples. Since the deviation is also found in the later samples this is not considered likely to be the cause of the drastic effect seen here. If this has a large impact then the initial mass transfer should be lower due to a lower temperature, and not much higher as seen from two of the samples. It should be noted that Jakobsson's [9] samples show much better agreement for Al then for Ca when compared with the literature.

Next it would be logical to look at the analysis method. ICP-MS is a common method employed when looking for trace elements in metals and slags. The preparation might cause problems due to the fact that HF reacts with *Si* and *Ca*. NIST proposes using property data from Chase [10] for CaF_2 and Lyman and Noda [11] for SiF_4. From these it can be seen that SiF_4 is more volatile than CaF_2, so *Si* should react first. Jakobsson [9] found that the *Si* loss was not significant, but if the mixture that was used for all of the samples did cause a loss of *Si* then this could explain the high concentration of *Al* and *Ca*. The calibration mixture for the ICP-MS machine could also be off. When looking at the NIST standard samples the the analysis has a low variance for *Al* while the variance of *Ca* is much higher. From this evaluation it seems that calibration problems, or dissolution of the samples might have caused problems when viewing the exact values for the impurities. If this is the case then while the values might be off they should all deviate by approximately the same amount allowing one to view the relative concentration behavior. *Al* does not react strongly with HF, compared to *Si* and *Ca*, and the analysis showed consistent values comparing for the NIST standard. Due to this the behavior of *Al* discussed further.

5.2 Behavior of $\underline{Al}$

If one takes the term assumed constant in equation 5, $\frac{k_{i,t}\rho_s A_s}{m_m}\left(\frac{K_i f_i}{\gamma_i}+\frac{m_m}{m_s}\right)$, and views it in context of the experiment performed some assumptions can be made. A_s should be close to constant if one assumes that the quenching is instantaneous, only allowing reactions at $1600^{\circ}C$. m_m and m_s can also be considered constant as the mass of the crucible did not change to any large degree from before and after the experiment.

The concentration of the slag should not change drastically under the experiment allowing for ρ_s and $\frac{K_i f_i}{\gamma_i}$ to also be roughly considered constant. $k_{i,t}$ is then the only parameter left. Sample set CSA404020 shows a behavior akin to the one expected if $k_{i,t}$ is constant. The other samples setts show large deviations from this behavior, and call for a $k_{i,t}$ that changes drastically with respect to time. For this to fit it must allow multiple changes of magnitude with respect to time, to allow for the peaks seen in the experimental data. Since $\lim_{t\to\infty} \omega_i = \omega_i^\infty$, the behavior of $k_{i,t}$ must additionally be of such a form that $\left(\int_0^t k_{i,t}dt\right)|_{t\to\infty} \to \infty$. This does not seem likely based on the fact that the phase parameters do not change this drastically to commend this. Fluid flow and geometry changes could have contributed, but there is no significant fluid flow, and the geometries should be constant. Slag viscosity is something that has been looked at and the slag viscosity for the sample setts are shown in table 3, calculated using the viscosity model proposed by Kondratiev and Jak [12].

Table 3 Slag viscosity calculated from the viscosity model proposed of Kondratiev and Jak [12].

Sample	CSA404020	CSA255520	CSA254035
μ_s $[Pa\ s]$	0.4135	4.0363	1.5086

Using the same model for small changes in slag concentration shows that the slag viscosity does not change much there either. One thing which is interesting however is that the sample set with the lowest viscosity behaves more akin to the base model, while the sample set with the highest viscosity has the largest initial deviation. This can be seen in figure 7, where the concentration of *Al* has been normalized with respect to the 180min sample. From figure 7 it can be seen that if the 5min sample for the sample set CSA255520 was removed as being an outlier then the behavior of the sample looks somewhat like the batch model [2]. The problem with this still is that the relative initial mass transfer rate from the experimental data is higher with increasing slag viscosity. If all the plot points are considered then it looks like the points oscillate around the curve

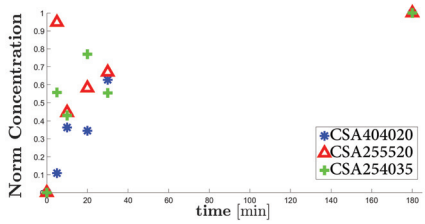

Fig. 7 Normalized concentration of *Al* with respect to the 180min sample for each sample set respectively.

expected from this model. This relationship is also shared with the industrial data for *Al* from Kero et al. [3]. The industrial data in figure 2 show that *Ca*'s behavior closely resembles the batch model, while *Al* has a behavior more akin to the experimental data found here. Since the traditional batch model does not take into consideration the effect the distribution equation between *Ca* and *Al*, reaction 5.), this might allow for the behavior seen here. While it is highly speculative it might still be considered.

If one assumes that the metal initially contains no *Al* and *Ca* then the initial mass transfer should be high due to the ease at which the impurity atoms can move across the reaction interface. When the impurity atoms then enter the metal they can quickly diffuse into the bulk away from the reaction surface allowing new atoms to take their place. This leads to reaction 5.) becoming unbalanced, which in turn should increase the probability of the offending species atoms to move from the metal into the slag. For this to happen the offending species atoms need to be present at the metal interface in a large enough concentration to restore the balance dictated by reaction 5.). As the concentration of impurity atoms increases the impurity atoms movements become more constrained increasing the probability that an impurity atom is present at the metal interface. If this is the case then it is not unreasonable that the impurity concentrations might overshoot their expected value. A higher slag viscosity should lower the rate at which the impurity atoms diffuse in the slag, which in turn should increase the residence time of an impurity atom at the slag interface before it can diffuse

into the bulk slag. It follows that reaction 5.) should then act slower in slags with a higher viscosity allowing a bigger overshoot of impurities in the metal. When the concentration of impurities in the metal becomes high enough it may in turn be favorable to move into the slag causing a new overshoot in the slag. If this occurs continuously where each iteration causes an overshoot which is lower than the previous it can be expressed as an oscillating behavior. For each oscillation there should be a higher readily amount of particles at the interface decreasing the overshoot amount of the species. This thought is somewhat interesting as when one superimposes a damped harmonic motion on to the batch model it provides a better fit for the experimental values, but there is not enough data to support this theory, and with itself it brings other problems.

6 Conclusions

This work has performed experiments investigating the mass transfer kinetics between *Si* and three synthetic $SiO_2 - CaO - Al_2O_3$ slags, with respect to *Al* and *Ca*, for different time steps at $1600°C$. Different experimental setups were performed, but only one yielded reliable results. The experimental results were found to be differ greatly from the expected behavior and values found in the literature. This was discussed, and it was found that while the values might not be valid the relative behavior of especially *Al* was safe to consider. The behavior was then viewed in light of a traditional batch reactor model [2], and compared to industrial data for oxidative ladle refining from Kero et al. [3]. It was found that *Al* exhibits a behavior which can not be expressed by the batch model alone, and some thoughts on this was shared. To give any definitive answer more experiments need to be performed to be able to say anything for certain.

7 Further Work

Experiments looking at the reproducibility of the experiments performed in this work are now under way, with further experiments looking at bigger crucibles in the works. For the bigger crucibles more novel sampling techniques are being investigated to allow for a more reliable sampling. Additionally some modeling work is being done to investigate the theoretical behavior of the impurities at a slag/metal interface as individual particles witch respect to their movement and reactions.

References

1. Treatise on Process Metallurgy, vol. 1:Process Fundamentals (Ringgold Inc, 2014)
2. T. Abel Engh, *Principles of Metal Refining*, 2nd ed. (Oxford University Pres, 1992).
3. Ida Kero et al., "Refining Kinetics of Selected Elements in the Industrial Silicon Process", *Metallurgical and Materials Transactions B*, 46 (2015),1186-1194.
4. Kai Tang, "*Thermodynamic Analysis of Oxidative Ladle Refining of Silicon Melt Including Models for Thermophysical Properties of the Silicon Melt and* $SiO_2 - Al_2O_3 - CaO$ *Slag*" (Report F8532, SINTEF Materials and Chemistry, 2007)
5. Anders Schei, Johan Kristian Tauset and Halvard Tveit, *Production of High Silicon Alloys*, 1st ed. (Tapir Forlag, 1998).
6. Alireza Ashrafian et al., "*A Reactor Model For Ladle Refining of Silicon Metal*" (6th International Conference on CFD in Oil and Gas, Metallurgical and Process Industries, SINTEF/NTNU, Trondheim, Norway, 10-12 June 2008).
7. E. L. Cussler, *Diffusion : Mass Transfer in Fluid Systems*, 2nd ed. (Cambridge University Press, 1997).
8. Jan Erik Olsen et al., "*CFD Modelling of a Reactive Gas Stirred Three Phase Silicon Reactor*" (6th International Conference on CFD in Oil and Gas, Metallurgical and Process Industries, SINTEF/NTNU, Trondheim, Norway, 10-12 June 2008).
9. Lars Klemet Jakobsson, "*Distribution of Boron Between Silicon and* $CaO\text{-}SiO_2$, $MgO\text{-}SiO_2$, $CaO\text{-}MgO\text{-}SiO_2$ *and* $CaO\text{-}Al_2O_3\text{-}SiO_2$ *Slags at* $1600°C$" (PhD. Thesis, Norwegian University of Science and Technology, 2013).
10. M. W. Chase Jr, "Tables, NIST-JANAF Thermochemical", *J. Phys. Chem. Ref. Data*", 1998.
11. John L. Lyman and Tetsuji Noda, "*Thermochemical Properties of* Si_2F_6 *and* SiF_4 *in Gas and Condensed*

Phases", Journal of Physical and Chemical Reference Data, 30(2001), 165-186.

12. Alex Kondratiev and Evgueni Jak, "A Quasi-chemical Viscosity Model for Fully Liquid Slags in the $Al_2O_3 - CaO - FeO - SiO_2$ System", *Metallurgical and Materials Transactions B*, 36 (2005), 623-638.

Paper 4

The 11th Molten Slags, Fluxes, and Salts [MOLTEN 2020]
May 25-29, 2020, Seoul, Korea

The effect of calcium alloy content on the mass transfer of boron between silicon and SiO_2-CaO slag

E. L. Bjørnstad[1*], G. Solbakk[1], Ø. Mosevoll[1] and G. M. Tranell[1]
[1]Norwegian University of Science and Technology, Trondheim, Norway

Abstract: The rate and extent of impurity transfer between silicon and slag is of importance to different oxidative slag treatments of silicon alloys. It has previously been shown that the transfer of major elements between slag and metal phases may create a dynamic interface which enhances the transfer rate of other minor elements between these phases. This work investigates the effect of Ca on the kinetic behavior of boron transfer between silicon and calcium silicate slags. Boron-doped Si- with and without dissolved Ca (0 or 0.7wt%) - was kept in contact with calcium silicate slag, in a graphite crucible, under inert atmosphere for different durations at 1873 K (1600°C). Following reaction, boron concentrations in metal and slag were analyzed using inductively coupled plasma mass spectrometry. Results show that the rate of B mass transfer from slag to Si is not significantly affected by the initial content- and transfer of Ca between Si and slag.

1. INTRODUCTION

It is well documented that during high temperature liquid metal/liquid slag reactions, dynamic interfacial phenomena such as interfacial turbulence, emulsification and subsequent changes in apparent interfacial area may occur [1-5]. Such phenomena may significantly affect the mass transfer of species between these phases. Industrial slag refining of high purity liquid silicon, aimed at partial removal of dissolved boron, is commonly performed with a SiO_2-CaO slag. At the interface between such a slag and molten silicon, simultaneous mass transfer of Ca, B and Si will occur. The current study investigates if and how the mass transfer of Ca affects the mass transfer of B between molten Si and SiO_2-CaO slag.

2. EXPERIMENTAL

A SiO_2-CaO masterslag (45:55 mass ratio) was prepared by repeated melting and grinding of pure oxides. Two different silicon alloys containing 300ppm B and 360 ppm B were synthetised, where the former of the two was additionally alloyed with 0.7 wt% Ca, a concentration close to the equilibrium Ca concentration of Si in contact with the said slag[6]. Four kinetic experiment series (2 x 2 parallels), using 10 g of either silicon alloy and 10 g slag were carried out in a graphite crucible in a vertical graphite tube furnace at 1873K (1600°C), under an Ar 5.0 atmosphere. Prior to the experiments, the silicon alloy had been melted in the crucible by itself to ensure a well-defined contact surface. After cooling, slag was added, giving two clearly defined phases, separated by a known initial contact area. The crucible was introduced into the hot zone of the furnace at temperature via a bottom-mounted pedestal and kept at 1873K for a given time (5, 8, 12, 20, 30 or 60 min respectively) before being rapidly pulled out of the hot zone and cooled to room temperature. Slag and metal were carefully separated and crushed before analyzed by ICP-MS for B and Ca content.

3. RESULTS AND DISCUSSION

The contents of B and Ca in the Si alloy as a function of time for each of the two starting alloys and their respective parallels, are illustrated in Figure. 1. As illustrated by Figure 1a, the Ca mass transfer from the slag to metal is initially very rapid for the Ca-free starting alloy, stabilising around 0.8 wt% Ca after approximately 30 minutes. The alloy starting with 0.7% Ca shows significantly more fluctuations in Ca concentration, but generally increases slowly over the kinetic period. Figure 1b shows that the mass transfer of boron from silicon to slag decays exponentially with time, where the alloy concentration, [B], converge towards equilibrium after approximately 30 min for both alloys, corresponding to the behaviour (in the opposite direction) of Ca. This behaviour has been previously documented [7] where [B] can be expressed by the equation:

*erlend.l.bjornstad@ntnu.no, +47 95760328

$$[ppm\ B] = [ppm\ B]_{eq} + \left([ppm\ B]_{in} - [ppm\ B]_{eq}\right) \cdot \exp\left(-\frac{t}{\tau}\right),$$

$$\tau = \frac{m_{melt}}{k_t \rho_{melt} A_S \left(1 + \frac{\gamma_B m_{slag}}{f_B K m_{slag}}\right)}$$

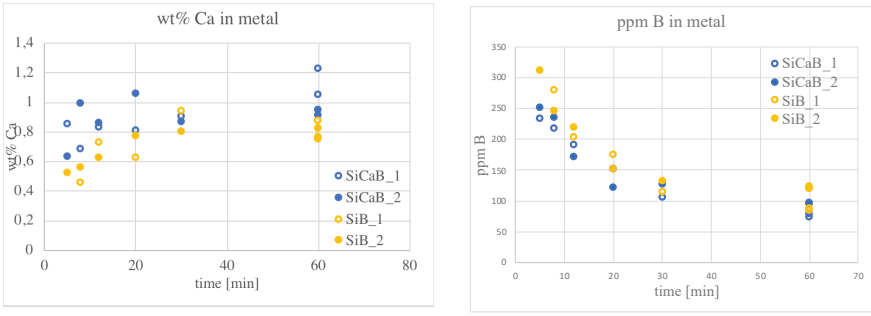

Fig 1. *(a, left)* Concentration of Ca in the alloy as functionof time. *(b, right)* Concentration of B in the Si alloy as function of time

By individual fitting to this equation, the B mass transfer was shown to follow the same behaviour for both the Ca-free and Ca-containing alloy, with the only statistically significant difference being their initial boron concentrations. These results indicate that the mass transfer of B is not significantly affected by the potential interfacial changes created by the transfer of Ca across the interface, although it is an order of magnitude higher in concentration than boron. Introduction of boron into the slag network as B_2O_3 requires charge compensation by Ca [8], but due to the relatively low concentration of B_2O_3 it appears not to be measurably affected by the dynamics of Ca. Assuming no boron losses from the system, the final B content in the silicon around 100-120 ppm indicate that the the slag should contain approximately 200-240 ppm boron, illustrating that equilibrium is approached given that the accepted boron distribution coefficient, ($L_B = C_{B,\ slag}/\ C_{B,\ Si}$) is approximately 2-2.1 for the CaO-SiO_2 system at 1600°C [6].

4. CONCLUSIONS

The effect of Ca on the kinetics of boron mass transfer from Si to a 55wt%CaO-45wt%SiO_2 slag was investigated experimentally. It was found that the boron transfer is not significiantly affected by Ca being simultaneously transferred from the slag to metal at an order of magnitude higher massflux, in the current system. The distribution of both boron and calcium between slag and alloy appear to stabilise at values corresponding to those reported in literature after 30 minutes reaction time.

Acknowledgements: This work has been [partly funded by the SFI Metal Production, (Centre for Research-based Innovation, 237738). The authors gratefully acknowledge the financial support from the Research Council of Norway and the partners of the SFI Metal Production.

REFERENCES

[1] Riboud, P.V. and Lucas, L.D.: Can. Metall. Q., 20, 198; 199-208.
[2] Rhamdhani, M.A, Brooks, G.A. and Coley, K.S: Met. and Mat. Trans B, 36B, 2005; 219-227
[3] De Oliveira Campos, L.D. PhD Thesis, Université de Bordeaux, 2017
[4] Manning, C.P. and Fruehan, R.J.: Met. and Mat. Trans B, 44B, 2013; 37-44
[5] Wu, A., Hayes, P.C. and Lee, H-G; ISIJ International, 38, 1998; 213-219
[6] Jakobsson, L.K.: PhD Thesis, NTNU, 2013
[7]Krystad, E., Jakobsson, L.K.,Tang, K. And Tranell, G.: Met. and Mat. Trans B, 48B, 2017; 2574-2582
[8] Kline, J, Tangstad, M. and Tranell, G: Met. and Mat. Trans B, 46B, 2015; 62-73

Paper 5

This paper is awaiting publication and is not included in NTNU Open

Paper 6

Statistical Model for Locating Micro Slag Droplets in MG-Si production

Erlend Lunnan Bjørnstad[1)], and Gabriella Tranell[2)]
1) PhD Candidate, SFI Metal Production, IMA, NTNU, Trondheim
2) Professor, SFI Metal Production, IMA, NTNU, Trondheim

Abstract

Representative metal sampling in the oxidative ladle refining(OLR) of MG-Si is challenging, creating difficulties for industry and researchers alike in describing the system. One of the problems associated with this comes from the contamination of micro slag droplets(MSD). This work proposes a model for finding metal samples contaminated by micro slag droplets OLR, when only a small number of samples are available for each ladle. To achieve this, the behaviour of [Ca] and [Al] from different ladles are compared to allow for greater statistical resolution. The model has been tested on published data sets, and simulated sets with different population variance, and has been found to represent the system adequately, with a type I and II error less than 10%.

Introduction

Metallurgical grade silicon(MG-Si), is a widely used silicon source in many industries, ranging from aluminum alloy production to photovoltaics. It is produced by carbothermic reduction of quartz in a submerged arc furnace, and undergoes further refining to meet customer specifications. Oxidative ladle refining(OLR) is one these refining processes. In OLR, the melt is tapped into a ladle, which is purged with oxygen enriched air, through a bottom mounted porous plug, as seen in figure 1. The oxygen reacts with the melt, forming an immiscible slag phase, which will contain an equilibrium amount of oxide forming impurities. While a large range of minor oxide-forming impurities are present, the primary slag forming impurities are [Ca] and [Al], giving a predominantly SiO_2-CaO-Al_2O_3 slag. To specify that a species El is in the metal it is written in square brackets, [El]. When customer specification has been reached, the melt will continue to casting, while the slag is removed. While performing OLR it is customary to take product samples during the process, to ensure compliance with customer demands.

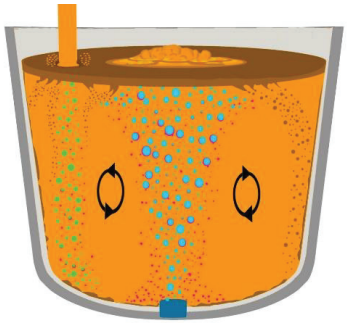

Figure 1: OLR, with gas bubbles in blue, and slag droplets in pink.

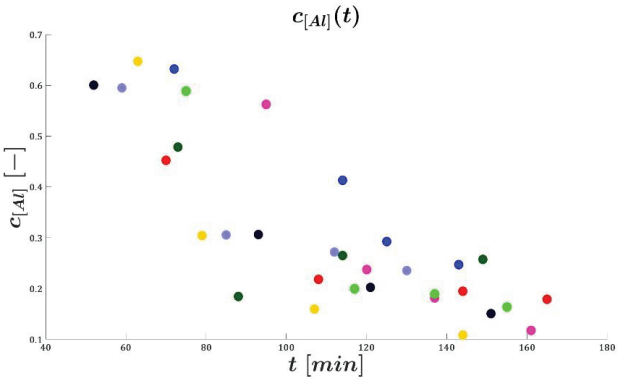

Figure 2: Normalized [Al] concentration, with respect to the initial value, as a function of time.

Sampling however, poses many challenges. High temperatures, ranging from 1823-1923K(1550-1650°C), and an aggressive environment, limits the number of available sampling techniques, and in addition necessitates extensive EHS procedures. Representative sampling poses additional challenges, as a ladle can contain upwards of 7tonns of Si-melt. In addition, there is a moderate chance that micro slag droplets will be present in the sample. These micro slag droplets(MSDs) contaminate the sample, but due to the high uncertainty present in small sample sizes, it can be difficult to distinguish slag-contaminated, and non-contaminated samples. While there exists well studied outlier analysis procedures, like the general extreme Studentized deviate(ESD) many outlier procedure, they are often not applicable due to the limited sample size [1]. This is not only an issue facing the industry, but also researchers working with this process.

By utilizing information regarding the expected refining behavior of the primary slag forming impurities, [Ca] and [Al], and assumed sampling behavior, this work proposes a model for locating slag-contaminated samples in OLR of MG-Si. The aim of the model is to provide a useful approximation for the system currently at hand, where inconsistent sampling intervals and high uncertainties are frequent. Thus higher errors are expected, as not enough information is currently provided to perform a more thorough analysis. This model was evaluated using industrial data sets analyzed by Kero et al. [2], and simulated sample sets with different population variance. Due to limited experimental data and fundamental knowledge, this model is currently limited to samples taken after the ladle is 50% full.

Figure 2 shows the normalized [Al] concentration, with respect to the initial value, $c_{[Al]}$, from Kero et al. [2]. Here the initial point is not shown, as the sets are transformed such that the initial concentration is 1, at time 0. The expected behavior can be approximated as a simple transient decay, with the refined concentration as its steady state. An example of this is the red and yellow ladle in figure 2. $c_{[Ca]}$ will behave similarly.

Expected Behaviors and Assumptions

A common theme in experimental analysis is that the less one knows about a systems behavior the more samples are needed to describe it. While the actual number of necessary samples will depend on system variance, desired resolution, effect size, etc..., this theme is especially important when describing data sets containing small sample sizes. To visualize this fact, one can think of sampling 5 out of 10^5 people, where 1% of the population has red hair. The probability that no one in the sample has red hair is ≈95%. This experiment is not able to see the effect(red hair), let alone give any indication of the effect size(1%). Now, if the occurrence of red hair is increased to 60%, the probabilities that 0, 2, 3, or 4 people, out of 5 sampled, have red hair are respectively ≈<1%, 23%, 34%, and 26%. Here one is expected to see the effect, and additionally the sample can give a rough estimate of the actual effect size(3/5=0.6). Consider the 1% case once more, but now it is known that almost all of the red haired people live in a single city with a population of 2000. The chance of getting a number of red haired people, out of 5 possible, can be seen in table 1.

Table 1: Probability of getting *x* red haired people out of 5 total, in a population of 2000, where 1000 have red hair.

x	0	1	2	3	4	5
p(x) [%]	3	16	31	31	16	3

With this extra knowledge it is now possible to see and estimate the effect. This is an example of the fact that knowledge of a system can allow one to measure effects that could not otherwise be measured. It is also shown that a small sample size cannot see or estimate small effect sizes, since one cannot attain the necessary statistical resolution. The weight fractions of [Ca] and [Al], $\omega_{[Ca]}$, $\omega_{[Al]}[-]$, are in the order of 10^{-3} in a typical tapped MG-Si, after the ladle is half full. $\omega_{[Ca]}$ and $\omega_{[Al]}$ are considered small, compared to their respective counterpart oxides in the slag. Therefore, it is assumed that MSDs contamination has a large effect on the metal analysis. In principle this means that small deviations can be disregarded. It is additionally assumed that the deviation will always be positive, when compared to similar non-contaminated metal samples. This assumption states that the lowest measured $\omega_{[Ca]}$, $\omega_{[Al]}$ values at any given point in time are more likely to represent the population than the highest. In turn, this allows one to compare the samples to the measured minimum, rather than the average. As previously assumed, the slag contains large amounts of both Al and Ca. This means that a sample containing MSDs, can be assumed to show large deviations in both $\omega_{[Ca]}$ and $\omega_{[Al]}$. If the variance is high, then there will naturally be a large spread in the refining curves. This assumption allows one to better distinguish between this natural spread, and MSDs contamination. One can still mark a non-contaminated sample as contaminated, if both concentrations have a naturally high positive deviation, giving a false positive or type I error. However, this assumption will later be shown to greatly reduce these errors, justifying its inclusion.

The assumptions up until this point have all been quite general, but they are not enough to get a proper model. Next, comes therefore some assumptions which are more specific, to allow for a better system description. In figure 2, each ladle is only sampled a few times. Additionally, the samples are not taken at similar absolute times, with regards to refining initialization, but rather at process breakpoints, like 50% full ladle, or full ladle. While the absolute sampling times are, in most cases, not widely different, they still cause scatter when comparing different ladles. Comparing the behavior of $\omega_{[Ca]}$ and $\omega_{[Al]}$ in

different ladles would be of great benefit, as the increased sample size greatly increases the statistical resolution. To decide which ladles/batches behave similarly it is assumed that, the combination of m similar sample sets, from N total sets, starting at 50% full ladle and normalized with respect to the actual initial concentration, will contain a set of k points, each the minima of their respective absolute time interval τ_i.

$$\vartheta_{[El],i} = \min(c_{[El]}(t_j)), \quad t_j \in \tau_i, \quad \tau_i = t_i \pm \Delta t_i, \quad i = 1,2,...,k \tag{1}$$

These points will adequately follow a model on the form:

$$\hat{\vartheta}_{[El]}(t) = \hat{\omega}_{[El],\min}(t) / \omega^{in}_{[El]} = \theta_1 + (\theta_2 - \theta_1)\exp(-\theta_3 t) \tag{2}$$

For this model specifically, time is shifted to the left by the first measured point at 50% full ladle, making this the new initial point. The first time interval will then have t_1-Δt_1=$t_{0,min}$=0. This is to help the regression. $\theta_{1\text{-}3}$ are all fitted values, but for the model to be adequate one should roughly have $\theta_1 \approx c_{[El],min}(k)$, $\theta_2 \approx c_{[El],min}(1)$, and $\theta_3 \in [0\ 1]$. Equation 2 is a simplified version of the batch refining equation found in Engh [3], and while it does not represent the whole refining process adequately, it can approximate the current time interval well enough to be of use. If all points in a set are marked as contaminated, except for the final points or the final points tend towards the general equilibrium concentration, then the set is not considered to be similar with the rest. This essentially states that similar sample sets show approximately the same behaviors within a given time interval.

With the previous observation, it can also be noted that even with dissimilar sampling times there will be a point where $c_{[Ca]}, c_{[Al]} \approx c^{\infty}_{[Ca]}, c^{\infty}_{[Al]}$. Even if these points are scattered over a wide time interval they can still be assumed to represent the same population value. This provides a greater sample size to perform tests on. It is then assumed that the actual variance is the same over the whole refining curve. Finally, it is assumed that the initial value, which is normalized against, is not contaminated. If this is the case, then the set should have a large negative deviation, with regards to the other ladles. Final list of assumptions:

1. MSDs contamination has a large effect on the metal analysis.
2. MSDs contamination will produce a positive deviation in $c_{[Ca]}$ and $c_{[Al]}$.
3. Contamination by MSDs will be seen with respect to both Al and Ca.
4. $c_{[El],min}(i)$ can be adequately fitted to equation 2.
5. Even if scattered over a large time interval, $c_{[Ca]}, c_{[Al]} \approx c^{\infty}_{[Ca]}, c^{\infty}_{[Al]}$ all represent the same population value.
6. The actual variance is the same over the whole refining curve.
7. The value normalized against contains no slag.

Model

First, all of the sample sets are normalized with respect to their respective initial value and sorted by time. Starting at a time, after/at 50% full ladle, all of the values within a specified time interval are checked to find the smallest among them, before moving

forward a given distance and checking again. It is advised to use smaller time steps, and to allow the intervals to overlap, so that multiple points are considered in every time interval. This should lower the chance of getting a minimum point at odds with the other minima. For the data from Kero et al. [2] a step size υ=5min, with the interval Δt=10min was used. t_i can then be written as:

$$t_i = t_{0,\min} + \upsilon \cdot i \tag{3}$$

According to assumption 4, the minima are fitted to equation 2, by the fminunc function in MATLAB R2016b. From this function one can find which points are close to equilibrium. This step could potentially be substituted by visual inspection of the data if one desires. For the set considered here the last 10 points are used.

Next the 95% confidence interval(CI), using the t-distribution with respect to the mean, is calculated for the equilibrium points. If the CI does not contain the smallest equilibrium point, then the point with the largest positive deviation is discarded, and the CI is recalculated. Here assumption 2 is used, as it is assumed that the minimum is a better description of the true values. This is performed until the CI contains the minimum.

Then an interval equal to the CI is placed on top of the minimum values already found for each respective time interval, as such:

$$\varphi_{[El],i} = \vartheta_{[El],i} + \max(CI) - \min(CI) \tag{4}$$

Every point which lies above the line drawn by $\varphi_{[El],i}$ is marked as a potential outlier. For a point to be marked as contaminated, it must lie above both $\varphi_{[Ca],i}$ and $\varphi_{[Al],i}$. If most of a set is marked as contaminated, then it is considered not similar to the rest.

The model on the data from Kero et al. [2] can be seen in figures 3 and 4. Here the blue sample set is not considered similar to the rest. The samples which are marked as outliers are the first points in the pink and green ladle, together with the last point in the dark green ladle.

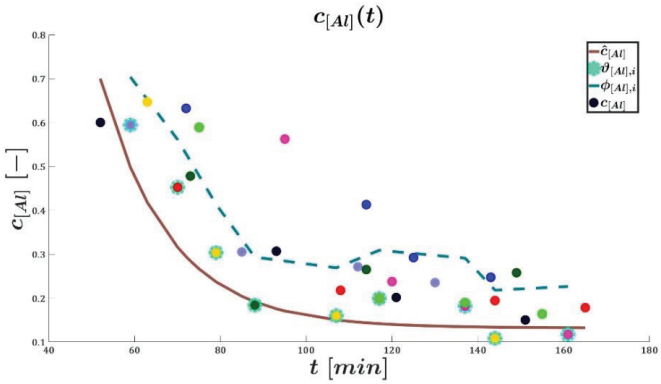

Figure 3: Data from Kero et al. [2] for [Al]. Different colored dots indicate different ladles.

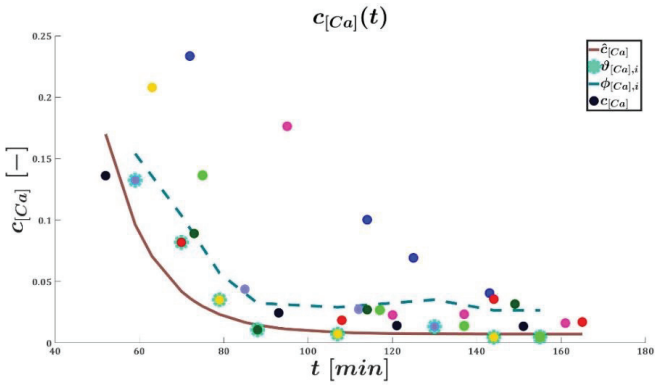

Figure 4: Data from Kero et al.[2] for [Ca]. Different colored dots indicate different ladles.

Simulated Sets

To test the model simulated sets were generated using equation 2 with $\theta_{[Ca]}$=[6.1e-3, 0.17, 8.34e-2] and $\theta_{[Al]}$=[0.15, 0.7, 6.23e-2]. Each point was given a normally distributed displacement around the line with a standard deviation $\sigma_{[Al]} \in [0.02, 0.06]$ where $\sigma_{[Ca]}=0.5\sigma_{[Al]}$, by Matlab R2016b's normrnd function. Within each generated set $\sigma_{[Al]}$ was kept constant. Each point for $c_{[Al]}$ had a specific contamination chance, and thus was displaced further by a random integer between 10 and 50, which was then multiplied by 10^{-2}. $c_{[Ca]}$ has half of the displacement of $c_{[Al]}$. The contamination chances tested were 5, 10, 15, 20, 25, and 30%. When running a simple time series from 0 to 100 minutes, with one point for each minute, including 0, and υ=2.5, Δt=5min, one gets the errors seen in figure 5. It can be seen from figure 5 that the model performance is heavily affected by the contamination chance.

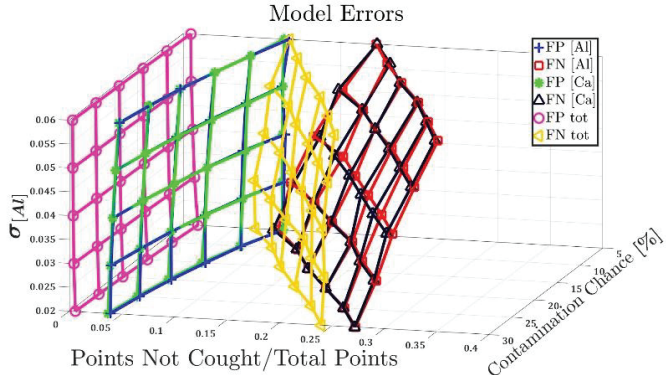

Figure 5: Model Errors. False Negative(FN) and False Positive(FP) for [Al], [Ca], and when they are combined. Each point is generated from 10^5 sets. The last 10 points in each set generated the CI.

This is due to the large variance one gets when there are many contaminated points in the points used to generate the CI. The figure also shows that assumption 3 is quite valuable, as it lowers the error considerably. For a single species one can get the case where a minima does not belong far down the distributions tail. This shifts $\varphi_{[El]}$, making it non-representative. However, the chance is quite small that this occurs in both species. Another problem which might occur is that the rapid change in the initial part of the curve is not fully represented, due to large v and/or Δt. This can be seen quite easily and fixed however. Figures 6 and 7 show different behaviors for the simulated sets.

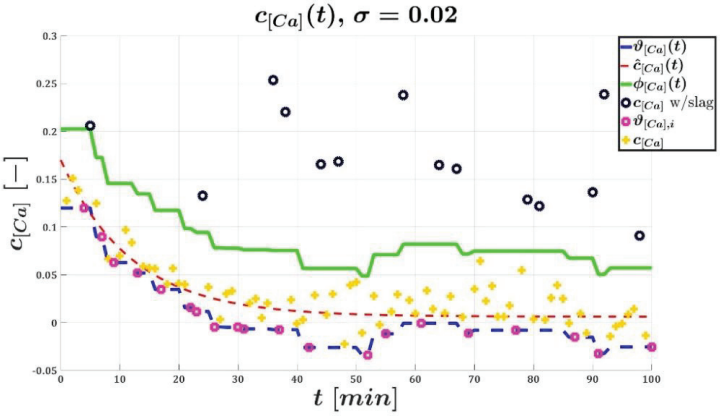

Figure 6: Simulated set of [Ca] with no model error.

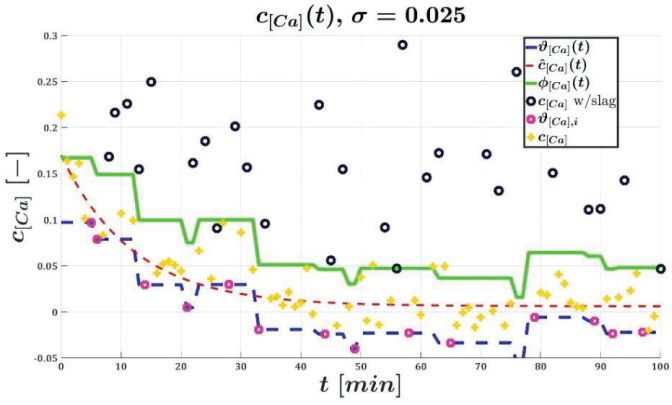

Figure 7: Simulated set of [Ca] with some model error.

Discussion

The proposed model is apt at finding which points are contaminated by MSDs. As seen from figures 3 and 4, all obvious points, like the first point for the light green and pink ladles, lie above the line, and are therefore marked as contaminated. The blue ladle is marked as not similar to the rest, as only one of its points is not above the line for both [Al] and [Ca]. It also does not allow one to remove points which might be considered an outlier at first glance, like the first yellow point. From $c_{[Ca]}$ alone, it might be tempting to discard the point, but this model states that it should be kept. If the sample set from which it generates the CI itself is heavily contaminated, then its performance worsens considerably, as seen in figure 5. This performance drop is primarily due to φ becoming too large, increasing the number of false negatives. If one sees that the final points clearly contains a large group of contaminated samples, it is advised to remove these before running the model. The theory in the proposed model can additionally be expanded on if new relations between the species are found. Sampling designs made to achieve a better representation of a ladle as a whole would also help massively, but this would require each industrial site to change their sampling routines. Due to the small sample size, any positive change would strengthen the set considerably. Further work will be performed to look at how to make the model less sensitive to each minima, but rather uses their joint behavior. Additionally, new relationships between the species will be looked for to add further behavioral restrictions.

Conclusion

A model for determining MSDs contamination in MG-Si has been proposed. It has tested on experimental [Ca] and [Al] data from Kero et al. [2], and simulated sets. From this, it has been found that the model is able to aptly find MSDs contaminated samples.

Acknowledgements

This work has been funded by SFI Metal Production, (Center for Research-based Innovation, 237738). This author gratefully acknowledges the financial support from the Norwegian Research Council and partners of SFI Metal Production.

References

[1] Bernard Rosner. Percentage Points for a Generalized ESD Many-Outlier Procedure. *Technometrics*, 25(2), 1983, p165.

[2] Ida Kero, Mari K. Nass, Vegar Andersen, and Gabriella M. Tranell. Refining kinetics of selected elements in the industrial silicon process. *Metallurgical and Materials Transactions B*, 46(3), 2015, p1186.

[3] T.Abel Engh. *Principles of Metal Refining*. Oxford University Press, 2 edition, 1992.